Acid and Base Gas Exposure and Solvent Effects on Metal-Organic Framework Structure and Gas Adsorption Properties

A Dissertation
Presented to
The Academic Faculty

By

William Pratt Mounfield, III

In Partial Fulfillment
of the Requirements for the Degree
Doctor of Philosophy in Chemical Engineering

Georgia Institute of Technology

December 2016

Acid and Base Gas Exposure and Solvent Effects on Metal-Organic Framework Structure and Gas Adsorption Properties

Approved by:

Dr. Krista S. Walton, Advisor
School of Chemical & Biomolecular Engineering
Georgia Institute of Technology

Dr. Michael A. Filler
School of Chemical & Biomolecular Engineering
Georgia Institute of Technology

Dr. Ryan P. Lively
School of Chemical & Biomolecular Engineering
Georgia Institute of Technology

Dr. David S. Sholl
School of Chemical & Biomolecular Engineering
Georgia Institute of Technology

Dr. Angus P. Wilkinson
School of Chemistry and Biochemistry
Georgia Institute of Technology

Date Approved: October, 27, 2016

ACKNOWLEDGEMENTS

I express my deepest thanks to my advisor, Dr. Krista S. Walton. Your technical and personal guidance throughout my Ph.D. journey has been invaluable. You challenged me to find my passion and to not allow setbacks to cause me to lose focus. I appreciate and value your trust in allowing me to serve as the group safety officer. Your example of working hard and having fun is something I continually strive to achieve.

I am deeply appreciative of the valuable guidance provided by my committee members, Dr. Michael A. Filler, Dr. Ryan P. Lively, Dr. David S. Sholl, and Dr. Angus P. Wilkinson. Thank you for pushing me to refine my proposal and deepen my research work.

I thank my collaborators at Oak Ridge National Lab, Dr. Uma Tumuluri and Dr. Zili Wu. It was a pleasure working alongside you in the UNCAGE-ME EFRC. Thank you, Chu Han, for supporting and making my ideas come to life with your computational simulations.

I am grateful to the Army Research Office for support of Chapters 3 and 6 under PECASE Award W911NF-10-0079 and ARO Contract W911NF-10-0076. I am also grateful to the Center for Understanding and Control of Acid Gas-Induced Evolution of Materials for Energy (UNCAGE-ME), an Energy Frontier Research Center funded by U.S. Department of Energy, Office of Science, Basic Energy Sciences for support of Chapters 4 and 5 under Award #DE-SC0012577.

I thank the Walton Group members, Dr. Katrina Stults, Dr. Yang Cai, Ken Onubogu, Dr. Greg Cmarik, Dr. Chris Murdock, Dr. Tim Duerinck, Erika Garcia-Gutierrez, Dr. Sudhir Sharma, Yutao Gong, Jake Deneff, Lalit Darunte, Julian Hungerford, Jay Joshi, and Colton Moran for valuable discussions throughout my Ph.D. I

express my gratitude to Dr. Nicholas Burtch, Dr. Himanshu Jasuja, Dr. Yi Huang, Dr. Michael Mangarella, Dr. Karen Tulig, Dr. Cody Morelock, Dr. Ian Walton, Rod Sefton, Eli Carter, Yang Jiao, and Michael Dutzer for discussions both serious and not. I offer my sincere thanks to my office mate, Dr. Bogna Grabicka, for our many discussions and all of the lovely puppies that have brightened my days in the office.

Finally, I thank my mother, Dr. Luegina C. Mounfield, and my father, Dr. Wm. Pratt Mounfield, Jr., for encouraging me to follow my dreams, and Dr. Micaela Taborga Claure, who has been by my side these past four years-an example of grace, perseverance, and determination.

William Pratt Mounfield, III, 10/15/2016

TABLE OF CONTENTS

LIST OF TABLES

LIST OF FIGURES

LIST OF SYMBOLS AND ABBREVIATIONS

BET	Brunauer-Emett-Teller
BJH	Barret-Joyner Halenda Model
DFT	Density Functional Theory
DRIFTS	Diffuse Reflectance Infrared Transmission Spectroscopy
-d	Metal-Organic Framework-derived oxide
GC	Gas Chromatograph
IR	Infrared Spectroscopy
MMO	Mixed Metal Oxide
MOF	Metal-Organic Framework
NMR	Nuclear Magnetic Resonance
ORNL	Oak Ridge National Laboratory
P&ID	Plumbing and Istrumentation Diagram
PXRD	Powder X-ray Diffraction
STEM	Scanning Transmission Electron Microscopy
TEM	Transmission Electron Microscopy
TPD	Temperature Programmed Desorption
XPS	X-ray Photonelectron Spectroscopy
XRD	X-ray Diffraction

SUMMARY

Metal-organic frameworks (MOFs) are strong candidates for a large number of industrial adsorption and separation applications due to their tunable chemical properties. However, to move these materials forward toward commercialization a deeper understanding of their synthesis, interaction with process stream components, and formation of functional forms is needed. Chapter 1 introduces the current state of the art in these areas while Chapter 2 provides a discussion of the specific materials chosen for the studies conducted in this dissertation.

Chapter 3 contains a discussion of the synthesis solvent effects using dimethylformamide (DMF) as the solvent for synthesizing MIL-53(Al). This well-known breathing MOF is typically prepared using hydrothermal methods. The two materials synthesized in DMF at 120 °C and 220 °C show measureable deviations from the breathing behavior exhibited by the material synthesized hydrothermally. Powder X-ray diffraction confirmed that MIL-53(Al) synthesized in DMF at 120 °C remains in the large-pore form under all conditions, while the other material synthesized at 220 °C undergoes a more gradual breathing transition than is observed for MIL-53(Al) prepared by traditional methods. Solid-state NMR was used to elucidate additional structural information and gain insight into the role synthesis solvent plays on breathing behavior. The CO_2 and water adsorption of these large-pore stabilized materials were studied, and the differences in adsorption behavior compared to MIL-53(Al) prepared by traditional methods was discussed.

In Chapter 4, adsorbed species and the structural effects of acid gases were investigated on MOFs and MOF derived oxides. MOF-derived oxides were prepared to give insight into adsorbed species on MOFs by connecting to the literature that exists for adsorbed species on metal oxides. These MOF-derived oxides retain the overall

morphology of the parent MOF, allowing direct comparison of the effect of morphology and the metal coordination environment on adsorbed species and acid gas stability of MOF, MOF-derived oxide, and traditionally synthesized metal oxide. A cerium-based MOF with open-metal sites, CeBTC, and the Ti-based MIL-125 were chosen to prepare MOF-derived oxides. IR studies show that adsorbed species during SO_2 and CO_2 adsorption on the MOF materials could be directly correlated to species observed on the MOF-derived and traditional oxides. In addition, the adsorbed species on the MOF-derived oxides differed from traditional oxides due to their different morphology and retained porosity. SEM and TEM images taken before and after CO_2/SO_2 adsorption experiments revealed degradation of all materials giving visual insight into the degradation mechanism after acid gas exposure.

In Chapter 5, the degradation discovered in Chapter 4 for MIL-125 was studied in detail. MIL-125 and MIL-125-NH_2 were investigated with SO_2 exposure in dry, humid, and aqueous environments. MIL-125 was found to be unstable in both humid and aqueous acidic environments, while MIL-125-NH_2 was stable under these exposure conditions, showing no change in textural properties or visual degradation, as observed through SEM. Both materials were stable in the presence of water and dry SO_2, suggesting that the reaction of these molecules to form an acidic species is likely a key factor in the degradation of MIL-125. In situ IR experiments confirmed the presence of sulfite species, supporting the hypothesis that the presence of an acidic sulfur species likely leads to the degradation of the MIL-125 structure. Computational investigation of several potential reaction mechanisms in MIL-125 indicated reactions involving the bisulfite ion are favored over reactions with water or SO_2. DFT simulations support the observation that MIL-125-NH_2 is stable in humid conditions, as all reactions are less favorable with the functionalized framework compared to the unfunctionalized framework.

In Chapter 6, a hydrotalcite-derived MgAl oxide (MMO) was evaluated in combination with the metal-organic frameworks (MOFs) UiO-66 and UiO-66-NH2 for the adsorption of ammonia. Analysis of the materials' textural properties after ammonia breakthrough adsorption revealed no change in the PXRD patterns or FTIR spectra; however, a slight decrease in surface area was observed, consistent with the hypothesized presence of strongly adsorbed species after adsorption. UiO-66:MMO and UiO-66-NH2:MMO composites maintained ammonia adsorption capacity under dry conditions. An almost two-fold increase in humid ammonia capacity was observed for the UiO-66:MMO composite, far beyond that expected through a linear combination of the two materials' capacities. The synergistic effect observed in humid conditions was further investigated with water adsorption experiments, which suggested the effect is the result of the high water affinity of MMO.

Finally, the major conclusions of this dissertation are summarized and potential studies and directions are outlined in Chapter 7. This dissertation advances the MOF field in several areas: (1) understanding of solvent effects in MIL-53(Al) for increasing CO_2 adsorption capacity, (2) increasing the knowledge base for SO_2 adsorption on MOFs by correlation of adsorbed species with MOF-derived and traditional metal oxides, (3) advancing the fundamental understanding of MOF degradation mechanisms during SO_2 exposure through a combined experimental and computational study, and (4) providing an example of a synergistic binding material for ammonia capture.

CHAPTER 1

INTRODUCTION

The rising level of carbon dioxide emissions from the combustion of coal, oil and natural gas is one of the most pressing environmental issues for today's society. With these CO_2 emission sources comprising nearly 80% of worldwide emissions, and with total global emissions on the rise,[1,2] the need for high-performance, low-cost sorbent materials is ever growing. Although an ideal solution would be the transition to cleaner energy production, the large dependence on energy from fossil fuels requires the development of efficient carbon capture and sequestration (CCS) methods for existing emission sources for an immediate impact on global CO_2 emission. Current aqueous alkanolamine sorbents, although having a large regeneration energy penalty of 20-40% for capture of 90% of CO_2 emissions, are still considered the state of the art carbon capture solution for modern power plants.[2-4] Solids adsorbents have garnered much interest as CO_2 adsorbents as they offer the ability to reduce the regeneration penalty that plagues modern amine scrubbers due to their much lower heat capacities.[1,3]

Zeolites are one such group of solid microporous, crystalline adsorbents that have been adopted in several industrial applications.[3-8] Zeolites are comprised of tetrahedral primary building units, MO_4, where M is an aluminum or silicon atom, which share a corner with other primary building units to form secondary building units that result in the well-defined zeolite structure. Zeolites' high chemical and thermal stability makes them ideal for natural gas upgrading and post-combustion CO_2 capture,[5,9-11] and; therefore, studies into improvement of their adsorption properties as well as investigations of their synthesis chemistry have been made.[5,9,12,13] Zeolites have shown

promise for use in CCS applications, and the combination of these porous solid adsorbents with traditional amine materials holds promise for the construction of unique materials with improved CO_2 capture properties.

Another class of porous crystalline solids with selective gas adsorption properties that exceed that of the highest-performing zeolites is metal-organic frameworks (MOFs). These inorganic-organic hybrid materials have shown promise for a wide range of applications in adsorption separations and catalysis,[3,6,8,14-17] owing to their high surface areas, vast selection of metal sources and organic linkers, and tunable chemical properties. A large number of MOFs have been synthesized to date, compared with only a few zeolites despite the relative infancy of the MOF field. Furthermore, the wide variety of metals and organic linkers leads to innumerable combinations for new MOFs. Although a study of the feasible combinations for novel MOF synthesis identified 137,000 potential structures,[18] the need for an understanding of MOF synthesis remains clear. The development of the chemical intuition necessary for targeted experimental synthesis of novel structures would revolutionize the field of adsorption and allow access to the enormous array of chemical and structural properties of these materials.

1.1 Synthesis Modification for Modified Gas Adsorption Properties

Certain MOFs offer unique separation applications due to their ability to ‘breathe’, i.e., undergoing a structural transformation in the presence of certain guest molecules.[19-23] MIL-53 is one of the most well-known MOFs that exhibits this breathing transition during specific guest molecule adsorption and has been studied extensively since its discovery in 2002.[24-32] Traditionally synthesized in water, MIL-53(Al) is comprised of $AlO_4(OH)_2$ corner-sharing octahedral chains connected by terephthalate groups to form a three-dimensional structure with 8.5 Å pores.[25] This hydrothermally synthesized material assembles in the narrow pore (np) form and undergoes a

well-known breathing transition upon adsorption of CO_2. However, it does not breathe in the presence of molecules such as methane and is known to maintain structural stability upon exposure to water vapor.

Despite the wide research into its breathing behaviors, there has been much less attention given to understanding the effect of solvent on the synthesis and breathing behavior of MIL-53(Al). Liu et al.[33] reported a modified MIL-53(Al) synthesis in which an ionic liquid was used as the solvent instead of water. This study showed that, as a consequence of performing the synthesis in an ionic liquid, which is a larger molecule than water, MIL-53(Al) assembles in its large pore (lp) form and does not appear to undergo the expected breathing transition during CO_2 adsorption. DMF (*n,n*-dimethylformamide) is commonly used in the synthesis of certain materials in the MIL series such as the amine-functionalized MIL-53(Al)[34], as well as its polymorph MIL-101(Al)-NH_2.[35] In addition, a study on the synthesis of the non-porous MIL-69[36] found that the use of DMF as solvent in place of water allowed the formation of a new porous material, DUT-4.[37] Recently, a computational and experimental study of the amine-functionalized MIL-53(Al), MIL-101(Al) system investigated the effect of replacing water with DMF during synthesis and found DMF was essential for synthesis of the amine functionalized MIL-101(Al) material.[38] However, despite its wide use in this and many other MOF syntheses, there has not been a study on the effect of DMF on the synthesis and breathing behavior of MIL-53(Al).

1.2 Effects of Acid Gas Adsorption on Stability and Gas Adsorption Properties

Developing gas adsorption systems and catalytic applications for a wide range of industries has garnered much research attention in the field of porous materials.[3,5,6,8,14-17,39] Materials that are designed with promising capabilities for applications such as CO_2 capture are often unable to retain their performance in the

presence of harsh acid gases that exist in many industrial applications.[40] To advance the development of industrially viable porous materials, a better understanding of the effects of these acid gases is required.

Metal-organic frameworks (MOFs) have emerged as a promising class of materials for acid gas separations and catalysis.[3,16,41,42] MOFs are characterized by metal clusters and organic linkers, large surface areas, and tunable chemical properties that make them excellent candidates for these applications. Recent work has also identified MOFs as excellent templates for producing MOF-derived unique, porous, structured metal oxides[43-48] that may offer improved acid gas separation and catalytic properties in comparison to their MOF or traditionally synthesized oxide (oxide) counterparts. Furthermore, these MOF-derived oxides can be used to study adsorbed species on MOFs by creating a bridge to the fundamental understanding of adsorbed species on metal oxides, which have been widely studied using infrared spectroscopy,[49-55] Raman spectroscopy,[56,57] and temperature programmed desorption[58] techniques. CeO_2, for example, is widely used as a catalyst in the automotive industry,[59-62] and several studies have investigated the reduction in catalytic performance CeO_2-based catalysts can suffer upon exposure to even low concentrations of SO_2 present in exhaust gases.[63-67] TiO_2 is also widely used in catalysis[68-70] and photocatalysis,[71] and the effect of exposure to various acid gases has been studied.[72-74] In conjunction with these studies, a MOF-derived CeO_2 or TiO_2 will allow the investigation of adsorbed species and effects of acid gas exposure with those observed for a parent cerium or titanium-based MOF. Therefore, these fundamental studies on metal oxides serve as an excellent foundation to design the investigation of the effect of acid gases on MOFs using MOF-derived oxides.

1.3 Developing Mechanistic Understanding of MOF Degradation Processes

MOFs are often designed with promising capabilities for applications such as CO_2 capture, yet are unable to retain their performance in the presence of other process components such as water and acid gases, which exist in many industrial applications.[40,75-77] In recent years, significant effort has been placed on understanding the behavior and stability of MOF materials in the presence of water.[78-81] Burtch et al. classified MOF materials into four categories ranging from thermodynamically stable, the most water-stable, to those materials that are unstable in the presence of even small amounts of moisture.[79]

While it is necessary to understand the stability of MOF materials in aqueous and humid environments, to further the development of industrially viable MOF materials, a better understanding of the effects of acid gases and those gases in combination with water is also required. Acid gas adsorption has been investigated over a range of MOF materials; however, the focus is usually on adsorption performance without discussion of material stability. In a study of the acid gas stability for several MOFs by Han et al., a lower activation temperature resulted in the retention of CO_2 and N_2 adsorption capacity for Cu-HF after 5 days of SO_2 or NO_2 exposure compared to a loss of capacity with a higher activation temperature and 2 days of exposure.[40] Britt et al. reported the breakthrough capacity of several MOF materials in comparison with BPL carbon for several toxic gases, including SO_2 and CO, but a study of the textural properties of the adsorbents after exposure was not performed.[82] Hamon et al. found H_2S adsorption in MIL-100 and MIL-101 variants to be irreversible either due to degradation or strong adsorption of H_2S molecules, while the smaller-pore MIL-53 and MIL-47 exhibited reversible adsorption of the acid gas and displayed no effect on excess methane adsorption after exposure.[83] In a follow-up study, the authors investigated the adsorption sites for H_2S adsorption in MIL-53 and MIL-47 with a combined IR spectroscopy—

computational approach.[84] Vaesen et al. studied the titanium-based MIL-125 and amine-functionalized MIL-125-NH_2 for co-adsorption of CO_2 and H_2S from biogas and natural gas and found both materials exhibited high H_2S/CH_4 and CO_2/CH_4 selectivity and no loss in CH_4 capacity after dry H_2S exposure.[85]

Developing a mechanistic understanding of degradation in MOFs would contribute to efforts to produce materials with improved water stability[79] or stability in more complex environments. DeCoste et al. hypothesized that the degradation and instability of Mg-MOF-74 in humid environments stemmed from a high concentration of open-metal sites that promote water clustering near the metal-ligand bond.[86] Zuluaga et al. further explored this mechanism in MOF-74 and showed the water dissociation reaction and coordination of OH groups at the metal center leads to the observed breakdown of the framework.[81] Zhang et al. utilized computational techniques to characterize water-induced point defects in ZIF-8, finding that at sufficient time scales, dangling linker vacancies could be induced at room temperature, but the creation of linker vacancies was unlikely to occur.[87] The broader roles of defects in the stability of MOFs have been summarized recently by Lively and Sholl.[88] Studies by Petit et al. have proposed acid gas degradation mechanisms, similar to those discussed above, for an open-metal site MOF, Cu-BTC, in a graphite-oxide composite in the presence of NO_2 and H_2S.[89,90] The authors propose a two-step pathway where the gas molecule first binds to the open copper site then displaces the 1,3,5-benzenetricarboxylic acid (BTC) ligand, resulting in a loss of porosity. The authors also investigated MOF-5 and MIL-100(Fe) in the presence of these adsorbates, and suggested the lack of open-metal sites allows retention of adsorption performance and porosity after exposure.[89] Pang et al. recently used a combined experimental and computational approach to examine the higher stability of the (100) crystallographic facet over that of the (110) facet of ZIF-8 in aqueous SO_2 solutions.[91] Overall, few studies into MOF degradation mechanisms in the

presence of acid gases exist, and there is a need for studies combining the effects of water and acid gases to elucidate these mechanisms.

1.4 Investigation of Complementary Binding Materials for Toxic Gas Adsorption

Developing sorbents for the adsorption of toxic chemicals has garnered much research attention in the field of porous materials. Impregnated activated carbons[92-97] have been widely explored for toxic gas adsorption applications, whereas metal-organic frameworks (MOFs) have emerged as a promising class of materials for removal of toxic gases such as ammonia.[82,98,99] In addition, several studies have focused on investigating different classes of materials to produce MOF composites in an effort to synthesize more water-stable materials, increase adsorption uptake, or produce a functional form (*e.g.* pellets, thin films, membranes).[89,100-106]

While it is necessary for adsorption applications to produce these engineered functional forms, it is often at the cost of reduced adsorption performance or modification of the material's textural properties. One method of producing these functional forms is through pelletization of MOF powders, often drastically reducing surface area. Kim et al. reported the effect of pelletization at several pressures for the MOF, CuBTC, observing a reduction in surface area of over 45% at 10 MPa.[107] Peterson et al. studied the same MOF and showed that while pelletized CuBTC showed a reduction in surface area, ammonia breakthrough capacity was retained, while for UiO-66, surface area was maintained when pressed, but octane loading decreased.[108] In a follow-up study, Peterson et al. found that the amine-functionalized UiO-66 lost surface area as pelletization pressure increased and this loss in surface area was directly correlated with a loss in ammonia capacity.[109]

Another method for producing functional forms is the incorporation of a binding material (metal hydroxides,[105] polymers,[104,107,110] etc.) into composites with MOF

powders to increase the mechanical strength of the pellet or form the material into a membrane. Peterson et al. studied CuBTC-zirconium hydroxide composites for ammonia adsorption and saw in conjunction with reduced surface area the incorporation of increasing amounts of zirconium hydroxide drastically decreased adsorption capacity for ammonia in dry conditions, but only slightly decreased in wet conditions with incorporation of 75 wt % hydroxide.[105] Kim et al. observed that the use of poly(vinyl alcohol) in a 15 wt % solution with CuBTC, resulted in more than a 40% decrease in surface area from the pristine powder and over a 45% decrease in CO_2 capacity.[107] Ren et al. showed that adding sucrose as a binder with UiO-66 and forming pellets resulted in more than a 50% reduction in surface area and a large decrease in the hydrogen storage capacity over the MOF in powder form.[111] Denny et al. recently reported composites using a hydrophobic polymer (PVDF) and several MOFs that were formed into MOF mixed-matrix membranes; each membrane displayed drastically lower surface area than the powdered MOF materials likely due to significant pore blockage by the polymer.[110] DeCoste et al. focused on one of these membranes, PVDF and CuBTC, for ammonia adsorption studies and observed with increasing polymer wt % ammonia capacity was lowered accordingly.[104] Overall, the pelletization of MOFs resulted in a decrease in surface area likely due to pore collapse, as well as a general reduced adsorption capacity. The incorporation of polymers or other binders in MOF composites also resulted in a significant loss of surface area and a corresponding loss in capacity.

1.5 Dissertation Scope

The overall goal of this Ph.D. dissertation is to investigate the effects of guest molecules during both synthesis and adsorption with a variety of MOF materials to drive future improvement of MOF stability for industrial applications in harsh conditions. To achieve this goal, the following objectives were completed:

1. Investigate the effect of synthesis solvent on the structure and adsorption properties of MIL-53(Al) and determine structure-property relationships
2. Investigate the effect of acid gas adsorption on the stability and adsorption properties of MIL-125 and CeBTC and their derived oxides and determine a mechanism of acid gas degradation for MIL-125
3. Investigate the promotion of synergistic effects in UiO-66 composites through the use of hydrotalcite-derived MgAl metal oxide (MMO) binding materials

The completion of these objectives advances the understanding of MOF material properties. Understanding the effects of synthesis solvent on MIL-53(Al) structural properties provides an avenue to switch between polymorphs or change a material's adsorption properties. In addition, the understanding of acid gas interactions with CeBTC and MIL-125 developed in Chapters 4 and 5 gives insight into potential routes for the design of stable MOF materials for harsh industrial applications. Chapter 6 uses chemical intuition to provide a platform for functional MOF composites with increased adsorption capacity for ammonia capture applications. Chapter 7 presents future challenges and scientific questions that can be addressed to further the development of MOF materials.

1.6 References

(1) Mason, J. A.; Sumida, K.; Herm, Z. R.; Krishna, R.; Long, J. R. *Energy & Environmental Science* **2011**, *4*, 3030.

(2) Choi, S.; Drese, J. H.; Jones, C. W. *ChemSusChem* **2009**, *2*, 796.

(3) Sumida, K.; Rogow, D. L.; Mason, J. A.; McDonald, T. M.; Bloch, E. D.; Herm, Z. R.; Bae, T. H.; Long, J. R. *Chem. Rev.* **2012**, *112*, 724.

(4) Li, J.-R.; Ma, Y.; McCarthy, M. C.; Sculley, J.; Yu, J.; Jeong, H.-K.; Balbuena, P. B.; Zhou, H.-C. *Coord. Chem. Rev.* **2011**, *255*, 1791.

(5) Yilmaz, B.; Trukhan, N.; Müller, U. *Chinese J. Catal.* **2012**, *33*, 3.

(6) Czaja, A. U.; Trukhan, N.; Müller, U. *Chem. Soc. Rev.* **2009**, *38*, 1284.

(7) Farrusseng, D.; Aguado, S.; Pinel, C. *Angewandte Chemie International Edition* **2009**, *48*, 7502.

(8) Li, J. R.; Kuppler, R. J.; Zhou, H. C. *Chem. Soc. Rev.* **2009**, *38*, 1477.

(9) Martin, R. L.; Willems, T. F.; Lin, L. C.; Kim, J.; Swisher, J. A.; Smit, B.; Haranczyk, M. *ChemPhysChem* **2012**, *13*, 3595.

(10) Othman, M. R.; Rasid, N. M.; Fernando, W. J. N. *Chem. Eng. Sci.* **2006**, *61*, 1555.

(11) Li, G.; Xiao, P.; Webley, P.; Zhang, J.; Singh, R.; Marshall, M. *Adsorption* **2008**, *14*, 415.

(12) Hayashi, H.; Cote, A. P.; Furukawa, H.; O'Keeffe, M.; Yaghi, O. M. *Nat. Mater.* **2007**, *6*, 501.

(13) Kim, J.; Lin, L. C.; Martin, R. L.; Swisher, J. A.; Haranczyk, M.; Smit, B. *Langmuir* **2012**, *28*, 11914.

(14) Keskin, S.; van Heest, T. M.; Sholl, D. S. *ChemSusChem* **2010**, *3*, 879.

(15) Samanta, A.; Zhao, A.; Shimizu, G. K. H.; Sarkar, P.; Gupta, R. *Ind. Eng. Chem. Res.* **2012**, *51*, 1438.

(16) Lee, J.; Farha, O. K.; Roberts, J.; Scheidt, K. A.; Nguyen, S. T.; Hupp, J. T. *Chem. Soc. Rev.* **2009**, *38*, 1450.

(17) Rezaei, F.; Rownaghi, A. A.; Monjezi, S.; Lively, R. P.; Jones, C. W. *Energy Fuels* **2015**, *29*, 5467.

(18) Sikora, B. J.; Wilmer, C. E.; Greenfield, M. L.; Snurr, R. Q. *Chem. Sci.* **2012**, *3*, 2217.

(19) Sarkisov, L.; Martin, R. L.; Haranczyk, M.; Smit, B. *J. Am. Chem. Soc.* **2014**, *136*, 2228.

(20) Llewellyn, P. L.; Bourrelly, S.; Serre, C.; Filinchuk, Y.; Férey, G. *Angew. Chem.* **2006**, *45*, 7751.

(21) Férey, G.; Serre, C. *Chem. Soc. Rev.* **2009**, *38*, 1380.

(22) Mu, B.; Li, F.; Huang, Y. G.; Walton, K. S. *J. Mater. Chem.* **2012**, *22*, 10172.

(23) Serre, C.; Millange, F.; Surblé, S.; Férey, G. *Angew. Chem.* **2004**, *43*, 6285.

(24) Serre, C.; Millange, F.; Thouvenot, C.; Noguès, M.; Marsolier, G.; Louër, D.; Férey, G. *J. Am. Chem. Soc.* **2002**, *124*, 13519.

(25) Loiseau, T.; Serre, C.; Huguenard, C.; Fink, G.; Taulelle, F.; Henry, M.; Bataille, T.; Férey, G. *Chem-Eur J* **2004**, *10*, 1373.

(26) Bourrelly, S.; Llewellyn, P. L.; Serre, C.; Millange, F.; Loiseau, T.; Férey, G. *J. Am. Chem. Soc.* **2005**, *127*, 13519.

(27) Serre, C.; Bourrelly, S.; Vimont, A.; Ramsahye, N. A.; Maurin, G.; Llewellyn, P. L.; Daturi, M.; Filinchuk, Y.; Leynaud, O.; Barnes, P.; Férey, G. *Adv. Mater.* **2007**, *19*, 2246.

(28) Rallapalli, P.; Prasanth, K. P.; Patil, D.; Somani, R. S.; Jasra, R. V.; Bajaj, H. C. *J. Porous Mater.* **2010**, *18*, 205.

(29) Walton, R. I.; Munn, A. S.; Guillou, N.; Millange, F. *Chem-Eur J* **2011**, *17*, 7069.

(30) Coudert, F.-X.; Boutin, A.; Fuchs, A. H.; Neimark, A. V. *J. Phys. Chem. Lett.* **2013**, *4*, 3198.

(31) Liu, Y.; Her, J. H.; Dailly, A.; Ramirez-Cuesta, A. J.; Neumann, D. A.; Brown, C. M. *J. Am. Chem. Soc.* **2008**, *130*, 11813.

(32) Trung, T. K.; Trens, P.; Tanchoux, N.; Bourrelly, S.; Llewellyn, P. L.; Loera-Serna, S.; Serre, C.; Loiseau, T.; Fajula, F.; Férey, G. *J. Am. Chem. Soc.* **2008**, *130*, 16926.

(33) Liu, J.; Zhang, F.; Zou, X.; Yu, G.; Zhao, N.; Fan, S.; Zhu, G. *Chem. Commun.* **2013**, *49*, 7430.

(34) Couck, S.; Denayer, J. F.; Baron, G. V.; Rémy, T.; Gascon, J.; Kapteijn, F. *J. Am. Chem. Soc.* **2009**, *131*, 6326.

(35) Serra-Crespo, P.; Ramos-Fernandez, E. V.; Gascon, J.; Kapteijn, F. *Chem. Mater.* **2011**, *23*, 2565.

(36) Loiseau, T.; Mellot-Draznieks, C.; Muguerra, H.; Férey, G.; Haouas, M.; Taulelle, F. *C. R. Chim.* **2005**, *8*, 765.

(37) Senkovska, I.; Hoffmann, F.; Fröba, M.; Getzschmann, J.; Böhlmann, W.; Kaskel, S. *Micro. Meso. Mater.* **2009**, *122*, 93.

(38) Goesten, M. G.; Magusin, P. C.; Pidko, E. A.; Mezari, B.; Hensen, E. J.; Kapteijn, F.; Gascon, J. *Inorg. Chem.* **2014**, *53*, 882.

(39) Meek, S. T.; Greathouse, J. A.; Allendorf, M. D. *Adv. Mater.* **2011**, *23*, 249.

(40) Han, S. G.; Huang, Y. G.; Watanabe, T.; Nair, S.; Walton, K. S.; Sholl, D. S.; Meredith, J. C. *Micro. Meso. Mater.* **2013**, *173*, 86.

(41) Thallapally, P. K.; Motkuri, R. K.; Fernandez, C. A.; McGrail, B. P.; Behrooz, G. S. *Inorg. Chem.* **2010**, *49*, 4909.

(42) Cui, J.; Wong, Y.-L.; Zeller, M.; Hunter, A. D.; Xu, Z. *Angewandte Chemie International Edition* **2014**, *53*, 14438.

(43) Chaikittisilp, W.; Torad, N. L.; Li, C.; Imura, M.; Suzuki, N.; Ishihara, S.; Ariga, K.; Yamauchi, Y. *Chem-Eur J* **2014**, *20*, 4217.

(44) Wang, Z. Q.; Li, X.; Xu, H.; Yang, Y.; Cui, Y. J.; Pan, H. G.; Wang, Z. Y.; Chen, B. L.; Qian, G. D. *J. Mater. Chem. A* **2014**, *2*, 12571.

(45) Im, J. H.; Kang, E.; Yang, S. J.; Park, H. J.; Kim, J.; Park, C. R. *Bull. Korean Chem. Soc.* **2014**, *35*, 2477.

(46) Liu, D. D.; Dai, F. N.; Li, X. H.; Liang, J. L.; Liu, Y. Q.; Liu, C. G. *RSC Adv.* **2015**, *5*, 15182.

(47) Khaletskaya, K.; Pougin, A.; Medishetty, R.; Rosler, C.; Wiktor, C.; Strunk, J.; Fischer, R. A. *Chem. Mater.* **2015**, *27*, 7248.

(48) Liu, D.; Dai, F.; Liu, H.; Liu, Y.; Liu, C. *Mater. Lett.* **2015**, *139*, 7.

(49) Dunn, J. P.; Jehng, J.-M.; Kim, D. S.; Briand, L. E.; Stenger, H. G.; Wachs, I. E. *J. Phys. Chem. B* **1998**, *102*, 6212.

(50) Luo, T.; Gorte, R. J. *Appl. Catal., B* **2004**, *53*, 77.

(51) Luo, T.; Vohs, J. M.; Gorte, R. J. *J. Catal.* **2002**, *210*, 397.

(52) Bazin, P.; Saur, O.; Lavalley, J. C.; Blanchard, G.; Visciglio, V.; Touret, O. *Appl. Catal., B* **1997**, *13*, 265.

(53) Mino, L.; Spoto, G.; Ferrari, A. M. *J. Phys. Chem. C* **2014**, *118*, 25016.

(54) Setvin, M.; Buchholz, M.; Hou, W.; Zhang, C.; Stöger, B.; Hulva, J.; Simschitz, T.; Shi, X.; Pavelec, J.; Parkinson, G. S.; Xu, M.; Wang, Y.; Schmid, M.; Wöll, C.; Selloni, A.; Diebold, U. *J. Phys. Chem. C* **2015**, *119*, 21044.

(55) Orsenigo, C.; Lietti, L.; Tronconi, E.; Forzatti, P.; Bregani, F. *Ind. Eng. Chem. Res.* **1998**, *37*, 2350.

(56) Flouty, R.; Abi Aad, E.; Siffert, S.; Aboukais, A.; Aboukaïs, A. *J. Therm. Anal. Calorim.* **2003**, *73*, 727.

(57) Twu, J.; Chuang, C. J.; Chang, K. I.; Yang, C. H.; Chen, K. H. *Appl. Catal., B* **1997**, *12*, 309.

(58) Rodriguez, J.; Rodriguez, T.; Jirsak, A.; Freitag, J.; Hanson, J.; Larese, S.; Chaturvedi *Catal. Lett.* **1999**, *62*, 113.

(59) Kašpar, J.; Fornasiero, P.; Graziani, M. *Catal. Today* **1999**, *50*, 285.

(60) Farrauto, R. J.; Heck, R. M. *Catal. Today* **1999**, *51*, 351.

(61) Trovarelli, A.; de Leitenburg, C.; Boaro, M.; Dolcetti, G. *Catal. Today* **1999**, *50*, 353.

(62) Kašpar, J.; Fornasiero, P.; Hickey, N. *Catal. Today* **2003**, *77*, 419.

(63) Hilaire, S.; Sharma, S.; Gorte, R. J.; Vohs, J. M.; Jen, H. W. *Catal. Lett.* **2000**, *70*, 131.

(64) Kolli, T.; Huuhtanen, M.; Hallikainen, A.; Kallinen, K.; Keiski, R. L. *Catal. Lett.* **2009**, *127*, 49.

(65) Wang, Y.; Li, X.; Zhan, L.; Li, C.; Qiao, W.; Ling, L. *Ind. Eng. Chem. Res.* **2015**, *54*, 2274.

(66) Park, E.; Kim, M.; Jung, H.; Chin, S.; Jurng, J. *ACS Catal.* **2013**, *3*, 1518.

(67) Liu, J.; Li, X. Y.; Zhao, Q. D.; Hao, C.; Wang, S. B.; Tade, M. *ACS Catal.* **2014**, *4*, 2426.

(68) Fujishima, A.; Honda, K. *Nature* **1972**, *238*, 37.

(69) Linsebigler, A. L.; Lu, G.; Yates, J. T. *Chem. Rev.* **1995**, *95*, 735.

(70) Zhang, X.; Pei, Z.; Ning, X.; Lu, H.; Huang, H. *RSC Adv.* **2015**, *5*, 79192.

(71) Thompson, T. L.; Yates, J. T. *Chem. Rev.* **2006**, *106*, 4428.

(72) Xu, W.; He, H.; Yu, Y. *J. Phys. Chem. C* **2009**, *113*, 4426.

(73) Jiang, B. Q.; Wu, Z. B.; Liu, Y.; Lee, S. C.; Ho, W. K. *J. Phys. Chem. C* **2010**, *114*, 4961.

(74) Notoya, F.; Su, C.; Sasaoka, E.; Nojima, S. *Ind. Eng. Chem. Res.* **2001**, *40*, 3732.

(75) Barea, E.; Montoro, C.; Navarro, J. A. R. *Chem. Soc. Rev.* **2014**, *43*, 5419.

(76) Tan, K.; Zuluaga, S.; Gong, Q.; Gao, Y.; Nijem, N.; Li, J.; Thonhauser, T.; Chabal, Y. J. *Chem. Mater.* **2015**, *27*, 2203.

(77) Mounfield III, W. P.; Tumuluri, U.; Jiao, Y.; Li, M.; Dai, S.; Wu, Z.; Walton, K. S. *Micro. Meso. Mater.* **2016**, *227*, 65.

(78) Jasuja, H.; Burtch, N. C.; Huang, Y. G.; Cai, Y.; Walton, K. S. *Langmuir* **2013**, *29*, 633.

(79) Burtch, N. C.; Jasuja, H.; Walton, K. S. *Chem. Rev.* **2014**, *114*, 10575.

(80) Jiao, Y.; Morelock, C. R.; Burtch, N. C.; Mounfield III, W. P.; Hungerford, J. T.; Walton, K. S. *Ind. Eng. Chem. Res.* **2015**, *54*, 12408.

(81) Zuluaga, S.; Fuentes-Fernandez, E. M.-A.; Tan, K.; Xu, F.; Li, J.; Chabal, Y. J.; Thonhauser, T. *J. Mater. Chem. A* **2016**, *4*, 5176.

(82) Britt, D.; Tranchemontagne, D.; Yaghi, O. M. *Proc. Natl. Acad. Sci. U. S. A.* **2008**, *105*, 11623.

(83) Hamon, L.; Serre, C.; Devic, T.; Loiseau, T.; Millange, F.; Férey, G. r.; Weireld, G. D. *J. Am. Chem. Soc.* **2009**, *131*, 8775.

(84) Hamon, L.; Leclerc, H.; Ghoufi, A.; Oliviero, L.; Travert, A.; Lavalley, J.-C.; Devic, T.; Serre, C.; Férey, G. r.; De Weireld, G.; Vimont, A.; Maurin, G. *J. Phys. Chem. C* **2011**, *115*, 2047.

(85) Vaesen, S.; Guillerm, V.; Yang, Q.; Wiersum, A. D.; Marszalek, B.; Gil, B.; Vimont, A.; Daturi, M.; Devic, T.; Llewellyn, P. L.; Serre, C.; Maurin, G.; De Weireld, G. *Chem. Commun.* **2013**, *49*, 10082.

(86) DeCoste, J. B.; Peterson, G. W.; Schindler, B. J.; Killops, K. L.; Browe, M. A.; Mahle, J. J. *J. Mater. Chem. A* **2013**, *1*, 11922.

(87) Zhang, C.; Han, C.; Sholl, D. S.; Schmidt, J. R. *J. Phys. Chem. Lett.* **2016**, *7*, 459.

(88) Sholl, D. S.; Lively, R. P. *J. Phys. Chem. Lett.* **2015**, *6*, 3437.

(89) Petit, C.; Bandosz, T. J. *Dalton Trans.* **2012**, *41*, 4027.

(90) Petit, C.; Levasseur, B.; Mendoza, B.; Bandosz, T. J. *Micro. Meso. Mater.* **2012**, *154*, 107.

(91) Pang, S. H.; Han, C.; Sholl, D. S.; Jones, C. W.; Lively, R. P. *Chem. Mater.* **2016**.

(92) Smith, J. W. H.; Westreich, P.; Croll, L. M.; Reynolds, J. H.; Dahn, J. R. *J. Colloid Interface Sci.* **2009**, *337*, 313.

(93) Seredych, M.; Mahle, J.; Peterson, G.; Bandosz, T. J. *J. Phys. Chem. C* **2010**, *114*, 6527.

(94) Petit, C.; Peterson, G. W.; Mahle, J.; Bandosz, T. J. *Carbon* **2010**, *48*, 1779.

(95) Petit, C.; Karwacki, C.; Peterson, G.; Bandosz, T. J. *J. Phys. Chem. C* **2007**, *111*, 12705.

(96) Mahle, J. J.; Peterson, G. W.; Schindler, B. J.; Smith, P. B.; Rossin, J. A.; Wagner, G. W. *J. Phys. Chem. C* **2010**, *114*, 20083.

(97) Peterson, G. W.; Rossin, J. A.; Smith, P. B.; Wagner, G. W. *Carbon* **2010**, *48*, 81.

(98) DeCoste, J. B.; Peterson, G. W. *Chem. Rev.* **2014**, *114*, 5695.

(99) Glover, T. G.; Peterson, G. W.; Schindler, B. J.; Britt, D.; Yaghi, O. *Chem. Eng. Sci.* **2011**, *66*, 163.

(100) Hermes, S.; Zacher, D.; Baunemann, A.; Wöll, C.; Fischer, R. A. *Chem. Mater.* **2007**, *19*, 2168.

(101) Shekhah, O.; Roques, N.; Mugnaini, V.; Munuera, C.; Ocal, C.; Veciana, J.; Wöll, C. *Langmuir* **2008**, *24*, 6640.

(102) Jahan, M.; Bao, Q.; Yang, J.-X.; Loh, K. P. *J. Am. Chem. Soc.* **2010**, *132*, 14487.

(103) Petit, C.; Huang, L.; Jagiello, J.; Kenvin, J.; Gubbins, K. E.; Bandosz, T. J. *Langmuir* **2011**, *27*, 13043.

(104) DeCoste, J. B.; Denny, J. M. S.; Peterson, G. W.; Mahle, J. J.; Cohen, S. M. *Chem. Sci.* **2016**.

(105) Peterson, G. W.; Rossin, J. A.; DeCoste, J. B.; Killops, K. L.; Browe, M.; Valdes, E.; Jones, P. *Ind. Eng. Chem. Res.* **2013**, *52*, 5462.

(106) Bashkova, S.; Bandosz, T. J. *J. Colloid Interface Sci.* **2014**, *417*, 109.

(107) Kim, J.; Kim, S.-H.; Yang, S.-T.; Ahn, W.-S. *Micro. Meso. Mater.* **2012**, *161*, 48.

(108) Peterson, G. W.; DeCoste, J. B.; Glover, T. G.; Huang, Y.; Jasuja, H.; Walton, K. S. *Micro. Meso. Mater.* **2013**, *179*, 48.

(109) Peterson, G. W.; DeCoste, J. B.; Fatollahi-Fard, F.; Britt, D. K. *Ind. Eng. Chem. Res.* **2014**, *53*, 701.

(110) Denny, M. S.; Cohen, S. M. *Angew. Chem.* **2015**, *127*, 9157.

(111) Ren, J.; Musyoka, N. M.; Langmi, H. W.; Swartbooi, A.; North, B. C.; Mathe, M. *Int. J. Hydrogen Energy* **2015**, *40*, 4617.

CHAPTER 2

MATERIALS AND METHODS

MOF and metal oxide materials were prepared as stated in the experimental sections at the beginning of each chapter. Syntheses of known MOFs were modified for higher yield and quality with literature syntheses cited accordingly. Characterization and adsorption methods were chosen for each study individually, and are presented at the beginning of each chapter for ease of reference. This chapter explains the motivation behind the material choice for each study.

2.1 Materials for Investigation of Synthesis Solvent Effects

As discussed in Chapter 1, MIL-53 is widely known for breathing behavior during guest molecule adsorption and has been the subject of numerous studies.[1-9] Despite the many studies of its breathing behaviors, there are few investigations seeking to understand the effect of solvent on the synthesis and breathing behavior of MIL-53(Al). MIL-53 and its functionalized analogues possess several polymorphs namely MIL-68,[10] MIL-88B,[11] MIL-101,[12-14] CAU-1,[15] CAU-3,[16] and CAU-6.[17] The synthesis of these polymorphs has been accomplished, as noted in the literature, through varying several reaction conditions: temperature, time, concentration, and solvent. However, many of these conditions are similar except for a change in synthesis solvent, and it was hypothesized that keeping other conditions constant and varying the solvent would lead to the synthesis of a different structure.

It was hypothesized that use of DMF as the synthesis solvent, which is known to induce a large-pore transition in MIL-53(Al), would produce a large-pore stabilized MIL-53(Al). MIL-53 exists in a large-pore stabilized form with a vanadium metal center

known as MIL-47.[18] This hypothesis was initially supported by a study showing the replacement of water with DMF during synthesis had a similar effect transforming the non-porous aluminum MIL-69[19] to a new porous material, DUT-4.[20]

2.2 Materials for Investigation of Acid Gas Effects

Many MOFs display strong adsorption properties in single component CO_2 adsorption experiments in efforts to identify materials for flue gas capture; however, as discussed in Chapter 1, several additional components in these types of application streams lead to the degradation of MOFs. Therefore, understanding the interaction of acid gases with specific MOF materials may allow the design of improved and stable MOFs. MIL-125 has been studied for the co-adsorption of CO_2 and H_2S from biogas and natural gas and was found to have high H_2S/CH_4 and CO_2/CH_4 selectivity with no loss in capacity after dry H_2S exposure.[21] Therefore, MIL-125 was chosen as an initial candidate for studying acid gas adsorbed species and their effect on gas adsorption and framework stability.

Furthermore, MIL-125 has been identified as an excellent template for producing MOF-derived unique, porous, structured TiO_2.[22-27] TiO_2 is widely used in catalysis[28-30] and photocatalysis,[31] and the effect of exposure to various acid gases has been studied.[32-34] Work currently underway at ORNL investigates the effect of structure on the catalytic properties of TiO_2 nanoshapes. The derived TiO_2 allows for potential future correlations and conclusions to be made between these nanoshapes and the work conducted in Chapter 4. Similar work has been conducted on CeO_2 nanoshapes as CeO_2 is widely used as a catalyst in the automotive industry,[35-38] and these studies have investigated the reduction in catalytic performance CeO_2-based catalysts can suffer upon exposure to even low concentrations of SO_2 present in exhaust gases.[39-43]

CeBTC, a cerium-based MOF, was chosen to prepare a CeO_2-d derived oxide for comparison with CeO_2 wires prepared and studied in previous nanoshape studies,[44] A MOF-derived CeO_2 or TiO_2 allows the investigation of adsorbed species and effects of acid gas exposure on these metal oxides. Furthermore, these MOF-derived oxides can be used to study adsorbed species on the parent MOFs by creating a bridge to the fundamental understanding of adsorbed species on metal oxides, which have been widely studied using infrared spectroscopy[45-51], Raman spectroscopy[52,53], and temperature programmed desorption[54] techniques.

Adsorbed species were examined for each MOF-derived oxide and compared with an oxide as well as the parent MOF to gain insight into the similarities in these species across morphologies and coordination environments. It was expected that exposure to SO_2 would result in a decrease in the amount of adsorbed CO_2 species for all samples and the nature of adsorbed species for the MOF-derived oxide samples due to retention of SO_2 species at potential adsorption sites and the degradation and loss of those sites.

In Chapter 4, degradation in the presence of SO_2 was observed for MIL-125, through a loss of surface area, powder X-ray pattern, and the visual appearance of cavities in the particles. Chapter 5 focuses on an experimental and computational investigation of the degradation mechanism in MIL-125 to gain a deeper understanding of the degradation process and inform future efforts increasing the stability of this and other MOF materials.

The amine functionalized MIL-125 was chosen for investigation in conjunction with the unfunctionalized MIL-125. MIL-125-NH_2 has displayed promising H_2S adsorption and stability in H_2S environments.[21] Furthermore, the addition of the amine functionality has shown to improve greatly the stability of MIL-125 in the presence of water vapor[55-57] and will allow for the investigation into

the effect of ligand functionalization on acid gas stability and degradation mechanism.

2.3 Materials for Investigation of Beneficial Binding Materials

UiO-66 has been identified as a strong candidate for many applications. In order to move this material forward from lab scale tests, the formation of pellets or other functional forms is necessary. It has been shown that addition of traditional binding materials results in a loss in overall adsorption capacity, reducing the effectiveness of the MOF adsorbent. The loss in capacity can be attributed in several cases to intended properties, such as increased hydrophobicity to increase water stability.

Several studies have focused on investigating different classes of materials to produce MOF composites in an effort to synthesize more water-stable materials, increase adsorption uptake, or produce a functional form (*e.g.* pellets, thin films, membranes).[58-65] While it is necessary for adsorption applications to produce these engineered functional forms, it is often at the cost of reduced adsorption performance or modification of the material's textural properties. One method of producing these functional forms is through pelletization of MOF powders, often drastically reducing surface area. Another method for producing functional forms is the incorporation of a binding material (metal hydroxides,[64] polymers,[63,66,67] etc.) into composites with MOF powders to increase the mechanical strength of the pellet or form the material into a membrane.

Metal-organic frameworks (MOFs) have emerged as a promising class of materials for removal of toxic gases such as ammonia.[68-70] One well known application for UiO-66 is as an ammonia capture material; however, the materials affinity for water hinders its performance in wet conditions. UiO-66 and the amine functionalized UiO-66-NH_2 were chosen as the MOF materials for the ammonia breakthrough

experiments as they have displayed promising adsorption under dry and humid conditions as well as exhibiting good stability in the harsh ammonia environment.[71,72]

Hydotalcite-derived MgAl oxide (MMO) with acid-base pairs, has been shown to be a useful stable support material in catalysis,[73-76] and possesses acid-base sites that would be useful in the adsorption of acid/base gases. Due to its acid-base sites[77] and known transformation to meixnerite during rehydration,[78] it is hypothesized that MMO/MOF composites will possess additional ammonia capacity. The material also is a useful adsorbent in humid environments due to its strong affinity for water. Therefore, it was hypothesized that a functional composite of MOF (UiO-66) and this mixed oxide would produce a functional form that possessed equal or greater adsorption capacity to that of the MOF material in both dry and humid adsorption applications alone by leveraging cooperative adsorption interactions and by preventing the adsorption of water within the MOF framework.

2.4 Conclusions

While the materials chosen for investigation in this dissertation are a small subset of the vast number of MOF materials, they represent materials that are well characterized in initial and basic laboratory studies. Therefore, these materials provide an excellent platform to build a body of knowledge upon that may be applied in the future to many other MOFs. The discoveries made by modifying the synthesis of MIL-53 could be applied to several of its polymorphs, MIL-101 or MIL-68, for example, which are also widely studied and possess promising characteristics for adsorption and catalysis applications.[13,14,79-83] The understanding of MOF-acid gas interactions developed herein offers a starting point for future studies involving other MOFs, and the degradation mechanism developed for MIL-125 is hypothesized to be applicable to a wide number of

MOFs containing the same linker. Finally, the approach of choosing a binding material that increases the adsorption capacity of a MOF composite could drive a different path to the production of functional forms for industrial applications.

2.5 References

(1) Serre, C.; Millange, F.; Thouvenot, C.; Noguès, M.; Marsolier, G.; Louër, D.; Férey, G. *J. Am. Chem. Soc.* **2002**, *124*, 13519.

(2) Loiseau, T.; Serre, C.; Huguenard, C.; Fink, G.; Taulelle, F.; Henry, M.; Bataille, T.; Férey, G. *Chem-Eur J* **2004**, *10*, 1373.

(3) Bourrelly, S.; Llewellyn, P. L.; Serre, C.; Millange, F.; Loiseau, T.; Férey, G. *J. Am. Chem. Soc.* **2005**, *127*, 13519.

(4) Serre, C.; Bourrelly, S.; Vimont, A.; Ramsahye, N. A.; Maurin, G.; Llewellyn, P. L.; Daturi, M.; Filinchuk, Y.; Leynaud, O.; Barnes, P.; Férey, G. *Adv. Mater.* **2007**, *19*, 2246.

(5) Rallapalli, P.; Prasanth, K. P.; Patil, D.; Somani, R. S.; Jasra, R. V.; Bajaj, H. C. *J. Porous Mater.* **2010**, *18*, 205.

(6) Walton, R. I.; Munn, A. S.; Guillou, N.; Millange, F. *Chem-Eur J* **2011**, *17*, 7069.

(7) Coudert, F.-X.; Boutin, A.; Fuchs, A. H.; Neimark, A. V. *J. Phys. Chem. Lett.* **2013**, *4*, 3198.

(8) Liu, Y.; Her, J. H.; Dailly, A.; Ramirez-Cuesta, A. J.; Neumann, D. A.; Brown, C. M. *J. Am. Chem. Soc.* **2008**, *130*, 11813.

(9) Trung, T. K.; Trens, P.; Tanchoux, N.; Bourrelly, S.; Llewellyn, P. L.; Loera-Serna, S.; Serre, C.; Loiseau, T.; Fajula, F.; Férey, G. *J. Am. Chem. Soc.* **2008**, *130*, 16926.

(10) Yang, Q.; Vaesen, S.; Ragon, F.; Wiersum, A. D.; Wu, D.; Lago, A.; Devic, T.; Martineau, C.; Taulelle, F.; Llewellyn, P. L.; Jobic, H.; Zhong, C.; Serre, C.; De Weireld, G.; Maurin, G. *Angewandte Chemie International Edition* **2013**, *52*, 10316.

(11) Serre, C.; Millange, F.; Surblé, S.; Férey, G. *Angewandte Chemie International Edition* **2004**, *43*, 6285.

(12) Biswas, S.; Couck, S.; Grzywa, M.; Denayer, J. F. M.; Volkmer, D.; Van Der Voort, P. *Eur. J. Inorg. Chem.* **2012**, *2012*, 2481.

(13) Hartmann, M.; Fischer, M. *Micro. Meso. Mater.* **2012**, *164*, 38.

(14) Bhattacharjee, S.; Chen, C.; Ahn, W.-S. *RSC Adv.* **2014**.

(15) Ahnfeldt, T.; Guillou, N.; Gunzelmann, D.; Margiolaki, I.; Loiseau, T.; Férey, G.; Senker, J.; Stock, N. *Angewandte Chemie International Edition* **2009**, *48*, 5163.

(16) Reinsch, H.; Feyand, M.; Ahnfeldt, T.; Stock, N. *Dalton Trans.* **2012**, *41*, 4164.

(17) Reinsch, H.; Marszalek, B.; Wack, J.; Senker, J.; Gil, B.; Stock, N. *Chem. Commun.* **2012**, *48*, 9486.

(18) Barthelet, K.; Marrot, J.; Riou, D.; Férey, G. *Angew. Chem.* **2002**, *41*, 281.

(19) Loiseau, T.; Mellot-Draznieks, C.; Muguerra, H.; Férey, G.; Haouas, M.; Taulelle, F. *C. R. Chim.* **2005**, *8*, 765.

(20) Senkovska, I.; Hoffmann, F.; Fröba, M.; Getzschmann, J.; Böhlmann, W.; Kaskel, S. *Micro. Meso. Mater.* **2009**, *122*, 93.

(21) Vaesen, S.; Guillerm, V.; Yang, Q.; Wiersum, A. D.; Marszalek, B.; Gil, B.; Vimont, A.; Daturi, M.; Devic, T.; Llewellyn, P. L.; Serre, C.; Maurin, G.; De Weireld, G. *Chem. Commun.* **2013**, *49*, 10082.

(22) Chaikittisilp, W.; Torad, N. L.; Li, C.; Imura, M.; Suzuki, N.; Ishihara, S.; Ariga, K.; Yamauchi, Y. *Chem-Eur J* **2014**, *20*, 4217.

(23) Wang, Z. Q.; Li, X.; Xu, H.; Yang, Y.; Cui, Y. J.; Pan, H. G.; Wang, Z. Y.; Chen, B. L.; Qian, G. D. *J. Mater. Chem. A* **2014**, *2*, 12571.

(24) Im, J. H.; Kang, E.; Yang, S. J.; Park, H. J.; Kim, J.; Park, C. R. *Bull. Korean Chem. Soc.* **2014**, *35*, 2477.

(25) Liu, D. D.; Dai, F. N.; Li, X. H.; Liang, J. L.; Liu, Y. Q.; Liu, C. G. *RSC Adv.* **2015**, *5*, 15182.

(26) Khaletskaya, K.; Pougin, A.; Medishetty, R.; Rosler, C.; Wiktor, C.; Strunk, J.; Fischer, R. A. *Chem. Mater.* **2015**, *27*, 7248.

(27) Liu, D.; Dai, F.; Liu, H.; Liu, Y.; Liu, C. *Mater. Lett.* **2015**, *139*, 7.

(28) Fujishima, A.; Honda, K. *Nature* **1972**, *238*, 37.

(29) Linsebigler, A. L.; Lu, G.; Yates, J. T. *Chem. Rev.* **1995**, *95*, 735.

(30) Zhang, X.; Pei, Z.; Ning, X.; Lu, H.; Huang, H. *RSC Adv.* **2015**, *5*, 79192.

(31) Thompson, T. L.; Yates, J. T. *Chem. Rev.* **2006**, *106*, 4428.

(32) Xu, W.; He, H.; Yu, Y. *J. Phys. Chem. C* **2009**, *113*, 4426.

(33) Jiang, B. Q.; Wu, Z. B.; Liu, Y.; Lee, S. C.; Ho, W. K. *J. Phys. Chem. C* **2010**, *114*, 4961.

(34) Notoya, F.; Su, C.; Sasaoka, E.; Nojima, S. *Ind. Eng. Chem. Res.* **2001**, *40*, 3732.

(35) Kašpar, J.; Fornasiero, P.; Graziani, M. *Catal. Today* **1999**, *50*, 285.

(36) Farrauto, R. J.; Heck, R. M. *Catal. Today* **1999**, *51*, 351.

(37) Trovarelli, A.; de Leitenburg, C.; Boaro, M.; Dolcetti, G. *Catal. Today* **1999**, *50*, 353.

(38) Kašpar, J.; Fornasiero, P.; Hickey, N. *Catal. Today* **2003**, *77*, 419.

(39) Hilaire, S.; Sharma, S.; Gorte, R. J.; Vohs, J. M.; Jen, H. W. *Catal. Lett.* **2000**, *70*, 131.

(40) Kolli, T.; Huuhtanen, M.; Hallikainen, A.; Kallinen, K.; Keiski, R. L. *Catal. Lett.* **2009**, *127*, 49.

(41) Wang, Y.; Li, X.; Zhan, L.; Li, C.; Qiao, W.; Ling, L. *Ind. Eng. Chem. Res.* **2015**, *54*, 2274.

(42) Park, E.; Kim, M.; Jung, H.; Chin, S.; Jurng, J. *ACS Catal.* **2013**, *3*, 1518.

(43) Liu, J.; Li, X. Y.; Zhao, Q. D.; Hao, C.; Wang, S. B.; Tade, M. *ACS Catal.* **2014**, *4*, 2426.

(44) Wu, Z.; Li, M.; Howe, J.; Meyer, H. M.; Overbury, S. H. *Langmuir* **2010**, *26*, 16595.

(45) Dunn, J. P.; Jehng, J.-M.; Kim, D. S.; Briand, L. E.; Stenger, H. G.; Wachs, I. E. *J. Phys. Chem. B* **1998**, *102*, 6212.

(46) Luo, T.; Gorte, R. J. *Appl. Catal., B* **2004**, *53*, 77.

(47) Luo, T.; Vohs, J. M.; Gorte, R. J. *J. Catal.* **2002**, *210*, 397.

(48) Bazin, P.; Saur, O.; Lavalley, J. C.; Blanchard, G.; Visciglio, V.; Touret, O. *Appl. Catal., B* **1997**, *13*, 265.

(49) Mino, L.; Spoto, G.; Ferrari, A. M. *J. Phys. Chem. C* **2014**, *118*, 25016.

(50) Setvin, M.; Buchholz, M.; Hou, W.; Zhang, C.; Stöger, B.; Hulva, J.; Simschitz, T.; Shi, X.; Pavelec, J.; Parkinson, G. S.; Xu, M.; Wang, Y.; Schmid, M.; Wöll, C.; Selloni, A.; Diebold, U. *J. Phys. Chem. C* **2015**, *119*, 21044.

(51) Orsenigo, C.; Lietti, L.; Tronconi, E.; Forzatti, P.; Bregani, F. *Ind. Eng. Chem. Res.* **1998**, *37*, 2350.

(52) Flouty, R.; Abi Aad, E.; Siffert, S.; Aboukais, A.; Aboukaïs, A. *J. Therm. Anal. Calorim.* **2003**, *73*, 727.

(53) Twu, J.; Chuang, C. J.; Chang, K. I.; Yang, C. H.; Chen, K. H. *Appl. Catal., B* **1997**, *12*, 309.

(54) Rodriguez, J.; Rodriguez, T.; Jirsak, A.; Freitag, J.; Hanson, J.; Larese, S.; Chaturvedi *Catal. Lett.* **1999**, *62*, 113.

(55) Jeremias, F.; Lozan, V.; Henninger, S. K.; Janiak, C. *Dalton Trans.* **2013**, *42*, 15967.

(56) Kim, S.-N.; Kim, J.; Kim, H.-Y.; Cho, H.-Y.; Ahn, W.-S. *Catal. Today* **2013**, *204*, 85.

(57) Canivet, J.; Bonnefoy, J.; Daniel, C.; Legrand, A.; Coasne, B.; Farrusseng, D. *New J. Chem.* **2014**, *38*, 3102.

(58) Hermes, S.; Zacher, D.; Baunemann, A.; Wöll, C.; Fischer, R. A. *Chem. Mater.* **2007**, *19*, 2168.

(59) Shekhah, O.; Roques, N.; Mugnaini, V.; Munuera, C.; Ocal, C.; Veciana, J.; Wöll, C. *Langmuir* **2008**, *24*, 6640.

(60) Jahan, M.; Bao, Q.; Yang, J.-X.; Loh, K. P. *J. Am. Chem. Soc.* **2010**, *132*, 14487.

(61) Petit, C.; Huang, L.; Jagiello, J.; Kenvin, J.; Gubbins, K. E.; Bandosz, T. J. *Langmuir* **2011**, *27*, 13043.

(62) Petit, C.; Bandosz, T. J. *Dalton Trans.* **2012**, *41*, 4027.

(63) DeCoste, J. B.; Denny, J. M. S.; Peterson, G. W.; Mahle, J. J.; Cohen, S. M. *Chem. Sci.* **2016**.

(64) Peterson, G. W.; Rossin, J. A.; DeCoste, J. B.; Killops, K. L.; Browe, M.; Valdes, E.; Jones, P. *Ind. Eng. Chem. Res.* **2013**, *52*, 5462.

(65) Bashkova, S.; Bandosz, T. J. *J. Colloid Interface Sci.* **2014**, *417*, 109.

(66) Kim, J.; Kim, S.-H.; Yang, S.-T.; Ahn, W.-S. *Micro. Meso. Mater.* **2012**, *161*, 48.

(67) Denny, M. S.; Cohen, S. M. *Angew. Chem.* **2015**, *127*, 9157.

(68) DeCoste, J. B.; Peterson, G. W. *Chem. Rev.* **2014**, *114*, 5695.

(69) Britt, D.; Tranchemontagne, D.; Yaghi, O. M. *Proc. Natl. Acad. Sci. U. S. A.* **2008**, *105*, 11623.

(70) Glover, T. G.; Peterson, G. W.; Schindler, B. J.; Britt, D.; Yaghi, O. *Chem. Eng. Sci.* **2011**, *66*, 163.

(71) Jasuja, H.; Peterson, G. W.; Decoste, J. B.; Browe, M. A.; Walton, K. S. *Chem. Eng. Sci.* **2015**, *124*, 118.

(72) Peterson, G. W.; DeCoste, J. B.; Fatollahi-Fard, F.; Britt, D. K. *Ind. Eng. Chem. Res.* **2014**, *53*, 701.

(73) Taborga Claure, M.; Chai, S.-H.; Dai, S.; Unocic, K. A.; Alamgir, F. M.; Agrawal, P. K.; Jones, C. W. *J. Catal.* **2015**, *324*, 88.

(74) Taborga Claure, M.; Morrill, M. R.; Goh, J. W.; Chai, S.-H.; Dai, S.; Agrawal, P. K.; Jones, C. W. *Catal. Sci. Technol.* **2016**.

(75) Morrill, M. R.; Thao, N. T.; Shou, H.; Davis, R. J.; Barton, D. G.; Ferrari, D.; Agrawal, P. K.; Jones, C. W. *ACS Catal.* **2013**, *3*, 1665.

(76) Morrill, M. R.; Thao, N. T.; Agrawal, P. K.; Jones, C. W.; Davis, R. J.; Shou, H.; Barton, D. G.; Ferrari, D. *Catal. Lett.* **2012**, *142*, 875.

(77) Kozlowski, J. T.; Davis, R. J. *ACS Catal.* **2013**, *3*, 1588.

(78) Perez-Ramirez, J.; Abello, S.; van der Pers, N. M. *Chem.--Eur. J.* **2007**, *13*, 870.

(79) Mitchell, L.; Gonzalez-Santiago, B.; Mowat, J. P. S.; Gunn, M. E.; Williamson, P.; Acerbi, N.; Clarke, M. L.; Wright, P. A. *Catalysis Science & Technology* **2013**, *3*, 606.

(80) Serra-Crespo, P.; Ramos-Fernandez, E. V.; Gascon, J.; Kapteijn, F. *Chem. Mater.* **2011**, *23*, 2565.

(81) Yang, Q.; Vaesen, S.; Vishnuvarthan, M.; Ragon, F.; Serre, C.; Vimont, A.; Daturi, M.; De Weireld, G.; Maurin, G. *J. Mater. Chem.* **2012**, *22*, 10210.

(82) Lescouet, T.; Vitillo, J. G.; Bordiga, S.; Canivet, J.; Farrusseng, D. *Dalton Trans.* **2013**, *42*, 8249.

(83) Volkringer, C.; Meddouri, M.; Loiseau, T.; Guillou, N.; Marrot, J.; Férey, G.; Haouas, M.; Taulelle, F.; Audebrand, N.; Latroche, M. *Inorg. Chem.* **2008**, *47*, 11892.

CHAPTER 3

EFFECT OF SYNTHESIS SOLVENT ON MIL-53(Al)

As discussed in Chapter 1, developing an understanding of MOF synthesis would advance the field of adsorption and allow access to the enormous array of chemical and structural properties of these materials. Understanding the effect that synthesis solvent has on the structure and adsorption properties of a well-known MOF will be the main emphasis of this chapter. This Chapter was adapted from W.P. Mounfield, III; K.S. Walton, "Effect of Synthesis Solvent on Breathing Behavior of MIL-53(Al)," Journal of Colloid and Interface Science, 447, Copyright 2015, with permission from Elsevier. DOI: 10.1016/j.jcis.2015.01.027.

In this chapter, two solvothermal synthesis methods are presented for MIL-53(Al) with DMF as the solvent. The synthesis at lower temperature results in a material that is stabilized in the large-pore (lp) form, similar to the non-breathing vanadium analogue, MIL-47(V), [1,2] and exhibits higher CO_2 adsorption in the 1-20 bar pressure range and lower water adsorption at humidity levels less than 50 %RH in comparison to that of the breathing material synthesized by traditional routes. The synthesis at higher temperature results in a material that is stabilized in the lp form, but exhibits a swift breathing transition with higher CO_2 adsorption across the entire pressure range and much lower water adsorption at all humidity levels in comparison to that of the breathing material synthesized by traditional routes as well as the lower temperature, lp stabilized material presented in this study.

3.1 Experimental Section

Synthesis of MIL-53(Al)$_{sDMF120}$. The synthesis of MIL-53(Al)$_{sDMF120}$ (sDMF$_{120}$) was performed by mixing aluminum nitrate nonahydrate ($Al(NO_3)_3 \cdot 9H_2O$) and benzene-1,4-dicarboxylic acid (C_6H_4-1,4-($CO_2H)_2$) (referred to as BDC hereafter) in a 1:2.25 molar ratio. The reagents were added to 30 mL DMF (*n,n*-dimethylformamide) and stirred for 30 minutes until all solids were dissolved. The mixture was placed in a 60 mL glass vial and reacted at isothermal conditions of 120 °C for 72 hours. The resulting milky-white solid was gravity-filtered, washed with DMF three times and washed finally with methanol once. The final product was dried in air overnight.

Synthesis of MIL-53(Al)$_{sDMF220}$. The synthesis of MIL-53(Al)$_{sDMF220}$ (sDMF$_{220}$) was performed by mixing $Al(NO_3)_3 \cdot 9H_2O$ and BDC in a 1:2.25 molar ratio. The reagents were added to 30 mL DMF and stirred for 30 minutes until all solids were dissolved. The mixture was placed in a sealed 20 mL Teflon-lined reactor and reacted at isothermal conditions of 220 °C for 72 hours. The resulting white solid was gravity-filtered, washed with DMF three times and washed finally with methanol once. The final product was dried in air overnight.

Synthesis of MIL-53(Al)$_{sH2O}$. The synthesis of MIL-53(Al)$_{sH2O}$ (sH_2O) was performed following the procedure found in literature.[3] 1.30 g $Al(NO_3)_3 \cdot 9H_2O$ and 0.288 g BDC were stirred for 30 minutes in 5 mL H_2O and placed in a 23 mL Teflon-lined stainless steel autoclave for 72 hours at 220 °C. The resulting white product was gravity filtered and washed with water three times. Powder X-ray diffraction and nitrogen adsorption analysis were performed on the resulting white solid. Unreacted BDC was found in the pores, and an extraction process from literature was adapted to remove this leftover material.[4] The filtered product was placed in 10 mL DMF in a 23 mL Teflon-lined stainless steel autoclave overnight at 150 °C. The resulting product was filtered with DMF and dried in air overnight.

Powder X-ray diffraction. Powder X-ray diffraction patterns were recorded on an X'Pert X-ray PANalytical diffractometer with an X'accelerator module using Cu Kα (λ = 1.5418 Å) radiation at room temperature, with a step size of 0.02˚ in two theta (2θ). All attempts at obtaining single crystal X-ray diffraction data were unsuccessful.

N_2 physisorption. Nitrogen physisorption isotherms were measured at 77 K for samples activated at 473 K for 16h before and after water exposure using the Quadrasorb system from Quantachrome instruments (Figure 3.A.2). Nitrogen adsorption analysis was performed on all resulting products, and surface areas were determined by applying BET theory over a range of data points applicable to microporous materials.[5] N_2 isotherms showed typical Type I behavior as per the IUPAC classification.

Gas adsorption. An Intelligent Gravimetric Analyzer (IGA-1 series, Hiden Analytical Ltd.) was used to collect pure gas (CO_2, CH_4, N_2) adsorption isotherms at 293 K and pressures up to 20 bar (Figure 3.2, 3.A.3). Samples were activated in situ at 473 K under vacuum until no further weight loss was observed. After activation, the system was maintained under vacuum, and the temperature was adjusted to the desired value. A sample size of approximately 25 mg was used for the measurements, and a maximum equilibration time of 40 minutes was used for each point in the isotherm.

Water adsorption. An Intelligent Gravimetric Analyzer (IGA-3 series, Hiden Analytical Ltd.) was used to obtain water vapor adsorption isotherms at 293 K (Figure 3.5). A sample size of approximately 35 mg was used for collecting the water vapor adsorption isotherm. Dry air was used as the carrier gas, with a percentage being bubbled through a vessel filled with deionized water. Two mass flow controllers were used to vary the ratio of saturated air and dry air so that the relative humidity (%RH) could be controlled. Due to water condensation in the equipment at higher humidities, experiments were conducted up to 80 %RH. The total gas flow rate was set at 200 cm^3/min, and each adsorption/desorption step was allowed a maximum time of 24 h to

approach equilibrium. Samples were activated in situ at 473 K under vacuum until no further weight loss was observed before starting the experiment. Samples were regenerated by heating at 473 K under vacuum for 16 h after the water adsorption isotherm measurement prior to BET analysis.

FTIR spectroscopy. FTIR spectra were recorded on a Bruker Vertex 70, equipped with a DTGS detector in transmission geometry. Samples were prepared in a 1:100 sample:KBr pellet. The spectra were collected with an accumulation of 24 scans and a resolution of 4 cm^{-1}. A flow of N_2 at 20 mL min^{-1} was maintained during the measurement. The spectra were recorded at room temperature without any pre-treatment of the samples.

Solid-state NMR spectroscopy. ^{27}Al, ^{13}C, and ^{1}H NMR spectra were recorded on a Bruker Avance III spectrometer with a 9.4T magnetic field operating at 400 MHz using an automated procedure for analysis. A 4mm Bruker MAS probe with a ZrO_2 rotor spinning at 12 kHz was used in the ^{1}H and ^{27}Al MAS NMR studies. ^{27}Al MAS NMR spectra were recorded over 4096 scans on a simple block decay single-pulse excitation of 0.6 µs pulse duration with a repetition delay of 500 ms. Deconvolution of the ^{27}Al NMR spectra was performed using Bruker TopSpin 3.2.

3.2 Results and Discussion

Due to the larger kinetic diameter in comparison to water, 5.5 Å versus 2.6 Å,[6] and its known ability to induce a large-pore structural transition,[7] DMF offers the ability to stabilize the lp form of MIL-53(Al) much like CO_2, which possesses a kinetic diameter of 3.6 Å. Recently, there has been work on alternative synthesis using an ionic liquid as the solvent in place of water for increasing the hydrophobicity of MIL-53.[8] The ionic liquid possesses a kinetic diameter similar to DMF, illustrated in Figure 3.A.5. Therefore, in accordance with the findings of Liu et al.[8] and Senkovska et al.,[9] we hypothesize that the

size of the solvent molecule directs the synthesis such that DMF prevents the formation of the np literature framework, as illustrated in Scheme 1(b), where DMF molecules in orthogonal and parallel orientations are seen to block the pores and occupy a much larger space than a water molecule, previously illustrated by Loiseau et al. [3] As seen by Senkovska et al. for DMF synthesis of MIL-69,[9] the framework must assemble in the lp form in the presence of DMF to accommodate the larger solvent molecule[10] as shown in Scheme 1(a), and when synthesized at lower temperatures (120 °C) is unable to undergo the breathing transition shown for dehydration/hydration/cooling of MIL-53(Al) materials prepared by published procedures.[3] Interestingly, synthesis at higher temperatures (220 °C) results in a material that is able to undergo a slight breathing transition similar to that observed for MIL-53(Al) in literature.[3]

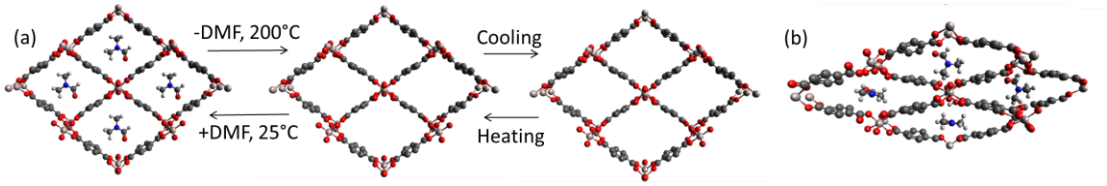

Scheme 3.1. Illustration of (a) removal of DMF from pores of MIL-53(Al)sDMF and stability of lp form after cooling to room temperature (b) DMF molecules occupying pore space of MIL-53(Al)sH2O in orthogonal and parallel orientations.

BET analysis was performed on each of the resulting products, and it was determined that the unreacted BDC was removed from the sH_2O material by the DMF extraction process and no calcination step was necessary. Further, the extraction step allows for one of the highest reported BET surface areas for MIL-53(Al), 1410 m^2/g, much higher than previously reported literature values.[3,11-13] In comparison, $sDMF_{120/220}$ possess activated surface areas of 1472 m^2/g, and 1570 m^2/g, respectively. In order to determine the degree to which the three materials were activated, the theoretical surface area was calculated and compared to the experimental surface area results.[14] As all surface areas are nearing the theoretical value of 1630 m^2/g, it was believed that the

materials were sufficiently activated. However, analysis of FTIR spectra (Figure 3.1) for $sDMF_{220}$ showed the presence of a spectral peak at 1660 cm^{-1} attributed to ν(C=O) in DMF molecules that remain trapped in the material; an observation made in other MOFs when using DMF in place of H_2O as the synthesis solvent.[15] Several washing steps with methanol were repeated in an attempt to remove the DMF molecules from the framework; however, it was found that these repeated washing steps did not remove the trapped species, suggesting these molecules are coordinated to the metal center or to the benzene ring of the ligand. Although there are some coordinated DMF molecules in the material, the observed high surface area indicates that these molecules are few in number and should not reduce the material's gas adsorption capability.

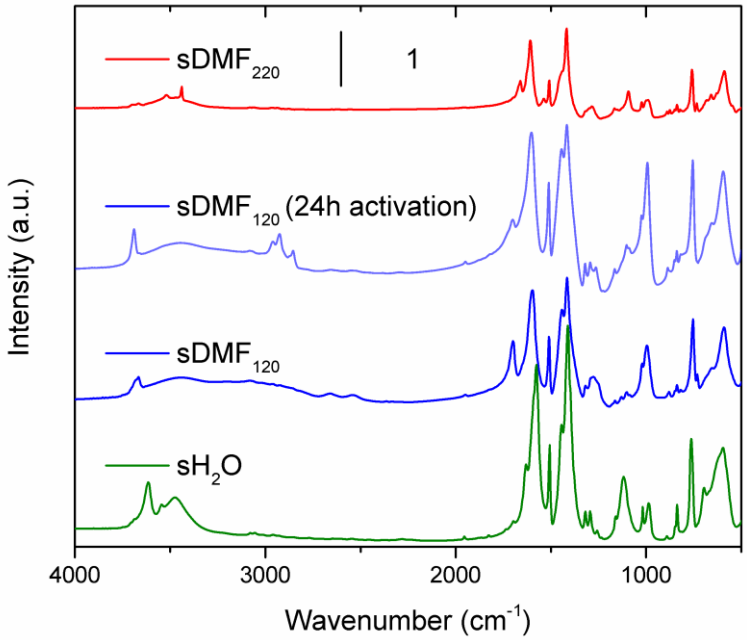

Figure 3.1. FTIR spectra of activated MIL-53(Al)sH_2O (sH_2O, green), activated MIL-53(Al)$_{sDMF120}$ ($sDMF_{120}$, blue), MIL-53(Al)$_{sDMF120}$ ($sDMF_{120}$ 24h, light blue) activated for 24 hours at 300 °C after six DMF washes, activated MIL-53(Al)$_{sDMF220}$ ($sDMF_{220}$, red).

Analysis of FTIR spectra for $sDMF_{120}$ showed the presence of a spectral peak at 1701 cm^{-1} attributed to ν(COOH) in terephthalate linkers in the material. Several washing steps with DMF were repeated in an attempt to remove any free, unreacted BDC

molecules from the framework; however, these repeated washing steps did not eliminate the presence of the spectral peak in the FTIR spectra. In order to confirm the peak was not due to free BDC molecules trapped in $sDMF_{120}$, the material was again washed six times with DMF, once with methanol, and activated at 300 °C for 24 hours. A BET analysis confirmed a complete structural collapse of the material and the continued presence of the spectral peak at 1706 cm^{-1} indicates a free carboxylic group of BDC still exists within the material and cannot be removed through activation. Furthermore, the continued presence of this group after numerous activation procedures, suggests that this peak is not, in fact, due to trapped BDC molecules, but rather an indication of the defects of the material, uncoordinated linkers that contribute to the framework's inability to undergo a structural transition.

Irretrievably trapped terephthalate molecules are not observed for the $sDMF_{220}$ material; the absence of a peak near 1700 cm^{-1} in Figure 3.1, confirms complete removal of unreacted BDC molecules.[16-19] As DMF molecules cannot be completely removed from $sDMF_{220}$ through the activation procedure described, and the framework undergoes a complete but gradual breathing transition, the framework appears to assemble into a slightly larger form than the literature framework due to the larger solvent molecule. This hypothesis is supported by the slightly larger cell parameters observed with LeBail refinement (Figure 3.A.8, Table 3.A.1). Adsorbed water molecules in sH_2O material account for the spectral band observed at 1629 cm^{-1}.

Powder X-ray diffraction (PXRD) was used to verify the structures of the three MIL-53(Al) micro-crystalline powders. Figure 3.2 shows that the sample synthesized with DMF at low temperatures, designated as MIL-53$(Al)_{sDMF120}$, exhibits broad, well-resolved peaks, indicating small crystallites, as seen in the recent work with ionothermal synthesis.[8] After activation, it is evident that MIL-53$(Al)_{sDMF120}$ is present in only the large-pore (lp) form.[3] The stability of MIL-53$(Al)_{sDMF120}$ in the lp form is quite unlike the

MIL-53(Al) sample synthesized with water, designated MIL-53(Al)$_{sH2O}$, as seen when referencing its as-synthesized XRD pattern, Figure 3.2(3). After extraction of remaining BDC molecules from the pores of the sample, and subsequent activation, it is clear that the MIL-53(Al)$_{sH2O}$ sample is present in the narrow-pore (np) form.[3] The material synthesized at higher temperatures in DMF, designated as MIL-53(Al)$_{sDMF220}$, exhibits an

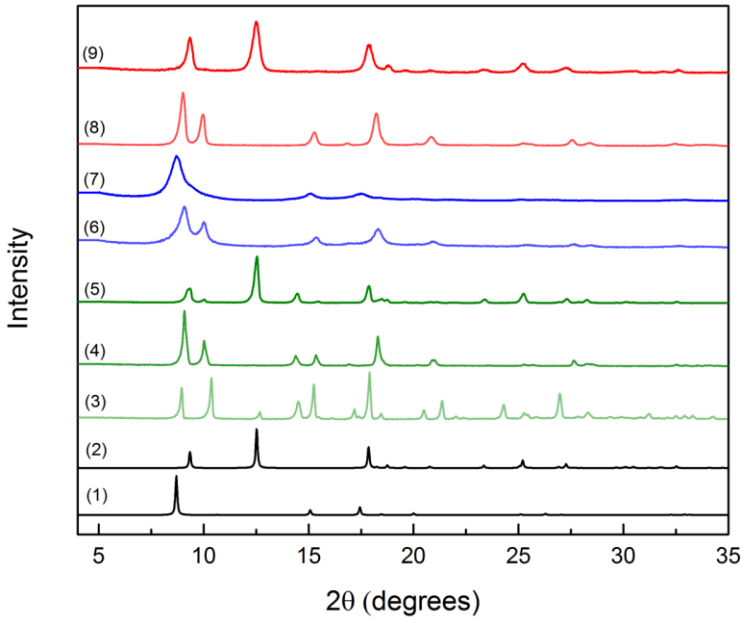

Figure 3.2. PXRD patterns of (1) large-pore form, (2) narrow-pore form, (3) as-synthesized MIL-53(Al)$_{sH2O}$, (4) extracted MIL-53(Al)$_{sH2O}$, (5) activated MIL-53(Al)$_{sH2O}$, (6) as-synthesized MIL-53(Al)$_{sDMF120}$, (7) activated MIL-53(Al)$_{sDMF120}$, (8) as-synthesized MIL-53(Al)$_{sDMF220}$, (9) activated MIL-53(Al)$_{sDMF220}$.

as-synthesized pattern similar to MIL-53(Al)$_{sH2O}$ after extraction with DMF, where both materials are present in the lp form. However, after activation, unlike the material synthesized in DMF at 120°C, MIL-53(Al)$_{sDMF220}$ is present in the np form, similar to MIL-53(Al)$_{sH2O}$. In conjunction with the presence of DMF in the IR spectra from the activated MIL-53(Al)$_{sDMF220}$ sample, we hypothesized that the material would be able to undergo a complete structural transition similar to the literature framework but that the transition would be affected by the coordinated DMF molecules; a hypothesis that is tested with gas adsorption experiments later in the text. The LeBail refinement

performed on the PXRD pattern for MIL-53(Al)$_{sDMF220}$ reveals the material exists in a structural form that is slightly larger than the traditional material's np form. After intermittent exposure to laboratory atmosphere, ~50 %RH, there was no observed change in the samples' XRD pattern, as seen in Figure 3.A.4.

A combination of ^{27}Al, ^{13}C, and ^{1}H MAS NMR was used to elucidate further structural information for the three MIL-53(Al) micro-crystalline powders. The ^{13}C MAS NMR spectra of sH_2O and sDMF$_{220}$ in Figure 3.A.6 exhibit three lines at δ = 130, 137, and 175 ppm, where the signal at δ = 174 ppm can be identified as the carboxylic group interacting with a water molecule. The ^{13}C MAS NMR spectra are quite similar for these materials and no clear difference with regards to structural properties under hydrated conditions can be discerned. However, ^{1}H MAS NMR has been used previously to evaluate the hydration of MIL-53(Al) compounds,[3,20] and it allows the determination of the relative hydrophobicity of the materials. The signal at δ = 3 ppm in the ^{1}H MAS NMR spectra in Figure 3.3 for sDMF$_{120}$, sDMF$_{220}$, and sH_2O is indicative of the formation of weak hydrogen bonds between water molecules and neighboring oxygen atoms of the organic linkers. The increased intensity of this signal in sH_2O clearly illustrates the traditionally synthesized sample is hydrated to a greater degree when exposed to laboratory air than the samples synthesized in DMF at high temperature. In addition, the absence of the water signal at 6.1 ppm in the sDMF$_{120}$ spectrum indicates a very low degree of hydration due to the materials permanent state in the large pore form.

To further analyze the MIL-53(Al) materials' structural properties, ^{27}Al MAS NMR was performed on activated samples and compared to samples in the presence of DMF. The ^{27}Al spectra for activated sDMF$_{120}$ exhibits a quadrupolar pattern with δ^{27}Al = 3.3 ppm, C_Q = 8.2 MHz, η_Q = 0.2, sDMF$_{220}$ features a well-defined quadrupolar pattern with δ^{27}Al = 3.6 ppm, C_Q = 8.4 MHz, η_Q = 0.13, while the spectrum for sH_2O exhibits a quadrupolar pattern with δ^{27}Al = 2.9 ppm, C_Q = 8.1 MHz, η_Q = 0.08 and no trace of any

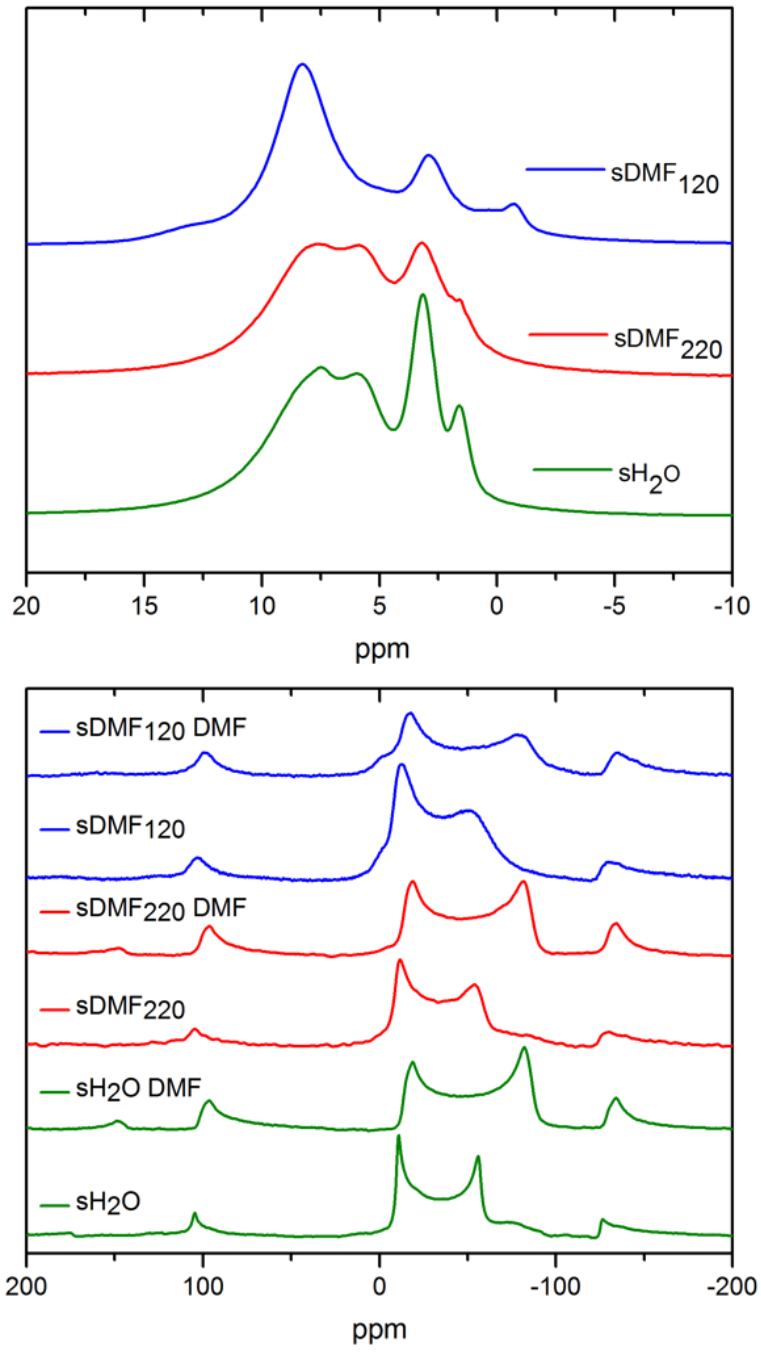

Figure 3.3. (top) ^{1}H, and (bottom) ^{27}Al MAS NMR spectra for $sDMF_{120}$ (blue), $sDMF_{220}$ (red), and sH_2O (green).

other aluminum-containing phase, confirming there is no remaining amorphous $Al(OH)_3$. In order to analyze the breathing transition of $sDMF_{220}$ and sH_2O, the activated materials were saturated with DMF to place them in their lp form. The ^{27}Al MAS spectrum for

$sDMF_{120}$ features a single quadrupolar pattern with $\delta^{27}Al$ = 11 ppm, C_Q = 10.1 MHz, η_Q = 0.16, $sDMF_{220}$ features a quadrupolar pattern with $\delta^{27}Al$ = 5 ppm, C_Q = 10.1 MHz, η_Q = 0.098, while the spectrum for sH_2O exhibits a quadrupolar pattern with $\delta^{27}Al$ = 3.6 ppm, C_Q = 10.1 MHz, η_Q = 0.1. The smaller increase in the quadrupolar coupling constant upon saturation with DMF for $sDMF_{220}$, 8.4~10.1, and $sDMF_{120}$, 8.2~10.1 compared to the increase in C_Q for sH_2O, 8.1~10.1, can be attributed to a decrease in the strain on the $AlO_4(OH)_2$ octahedra in the materials synthesized in DMF. As the octahedra experience less strain in the materials synthesized in DMF, they are able to gradually transition from closed to open pore forms in the case of $sDMF_{220}$, or remain in the open pore form permanently in the case of $sDMF_{120}$ as is confirmed with CO_2 adsorption experiments.

After analyzing the PXRD and solid-state NMR results and concluding the $MIL\text{-}53(Al)_{sDMF120/220}$ samples are unique MIL-53(Al) materials, further investigation of their structure and behavior was made with high pressure, pure-component CO_2 and CH_4 adsorption experiments. The CO_2 and CH_4 adsorption isotherms for $sDMF_{120}$ shown in Figure 3.4 exhibit Type I isotherms with no hysteresis. CO_2 is more strongly adsorbed than CH_4 as it has a higher quadrupole moment than the nonpolar methane. The CH_4 adsorption isotherms for sH_2O and $sDMF_{220}$ shown in Figure 3.4 also exhibit Type I behavior. The CO_2 adsorption isotherm for sH_2O exhibits strong Type IV behavior with large hysteresis upon desorption, which is characteristic of the traditional breathing behavior seen in literature.[2] The CO_2 isotherm for $sDMF_{220}$ exhibits a weak Type IV behavior with small hysteresis upon desorption characteristic of a gradual structural transition, lacking the step-like change observed for CO_2 adsorption in sH_2O, resulting in the observation of only a slight breathing behavior. The observation of this gradual breathing behavior during CO_2 adsorption combined with the results from ^{27}Al NMR showing reduced strain on the octahedral metal centers while in the lp form supports the

hypothesis presented previously that the $sDMF_{220}$ material is indeed able to undergo a complete structural transition, but with a more gradual movement between open and closed forms. The known presence of coordinated DMF molecules in the framework from FTIR analysis suggests that these molecules stabilize the lp form during CO_2 adsorption, allowing for the gradual transition between pore forms. In addition, the presence of the material in the np form after activation suggests the number of coordinated DMF molecules is not enough to induce a transition to the lp form without guest adsorption.

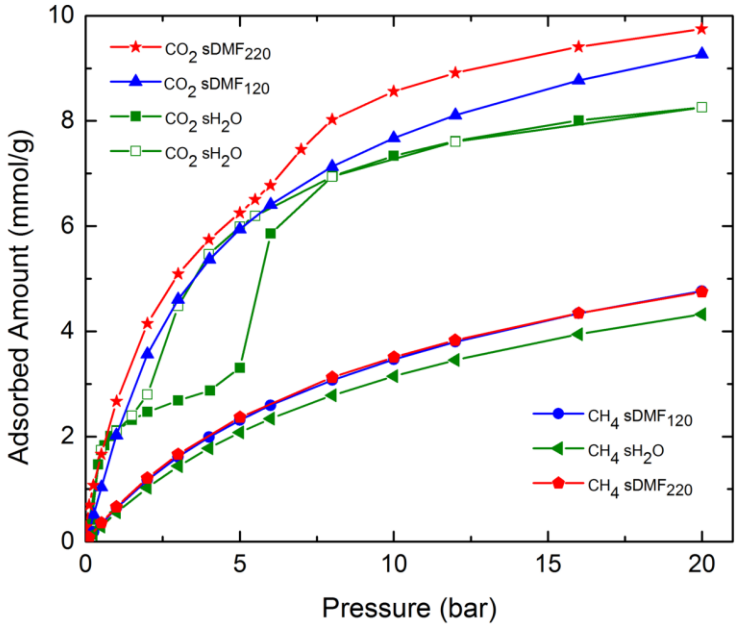

Figure 3.4. CO_2 and CH_4 adsorption isotherms at 25°C for $sDMF_{220}$ (red stars and pentagons), $sDMF_{120}$ (blue triangles and circles) and sH_2O (green squares and left triangles) as a function of pressure ranging from 0-20 bar. Desorption isotherms are omitted except for sH_2O (open green squares), which shows large hysteresis.

The CO_2 and CH_4 adsorption observed for sH_2O, 8.2 mmol/g and 4.3 mmol/g, match that found in the literature, while the overall CO_2 loading for $sDMF_{120}$ is more than 1 mmol/g higher than sH_2O, 9.3 mmol/g. The CH_4 loading is only slightly increased by

0.5 mmol/g to 4.8 mmol/g. The CO_2 loading for $sDMF_{220}$ is more than 1.5 mmol/g higher than sH_2O, 9.8 mmol/g, while the CH_4 loading is the same as $sDMF_{120}$, 4.8 mmol/g. However, a much greater increase over sH_2O is observed for both materials synthesized in DMF in the 1-5 bar region. It is in this region that sH_2O is still present in the np form, and is unable to have additional significant adsorption, while $sDMF_{120}$ is stabilized in the lp form and has continued adsorption throughout this region. It is evident from the adsorption data that the $sDMF_{120}$ material is indeed present in the lp form throughout adsorption of CO_2 as it closely follows the desorption curve for sH_2O in the 2-5 bar region, where the sH_2O material is still present in the lp form before relaxing to the np form as the pressure drops below 2 bar. Contrary to the observations for the material synthesized at low temperatures in DMF in this intermediate pressure region, $sDMF_{220}$ undergoes a gradual structural transition to the lp form, as seen in Figure 3.4 rather than the step breathing transition observed in the sH_2O material, allowing for greatly increased adsorption throughout the region. The coordinated DMF molecules allow retention of the breathing ability of the framework and greatly increased CO_2 adsorption capacity in the transition region. Due to the large increase in CO_2 adsorption with a negligible increase in CH_4 adsorption in this region, the $sDMF_{220}$ and $sDMF_{120}$ materials offer a three-fold increase in working capacity for processes run in the 1-5 bar region, 3.6 mmol/g vs 1.2 mmol/g, in addition to increased CO_2 adsorption at 1 bar for $sDMF_{220}$, 2.7 mmol/g vs 2.1 mmol/g.

Due to the discovery of the non-breathing behavior of $sDMF_{120}$, and the gradual breathing behavior of $sDMF_{220}$ a further investigation of the materials' performance in the presence of water was performed in comparison to that of sH_2O. Water adsorption isotherms were obtained at 1 bar with relative humidity ranging from 0-90 %RH. The water adsorption isotherm for the MIL-53(Al) material synthesized by traditional water synthesis shown in Figure 3.5 (sH_2O) exhibits type I behavior typical of a small pore

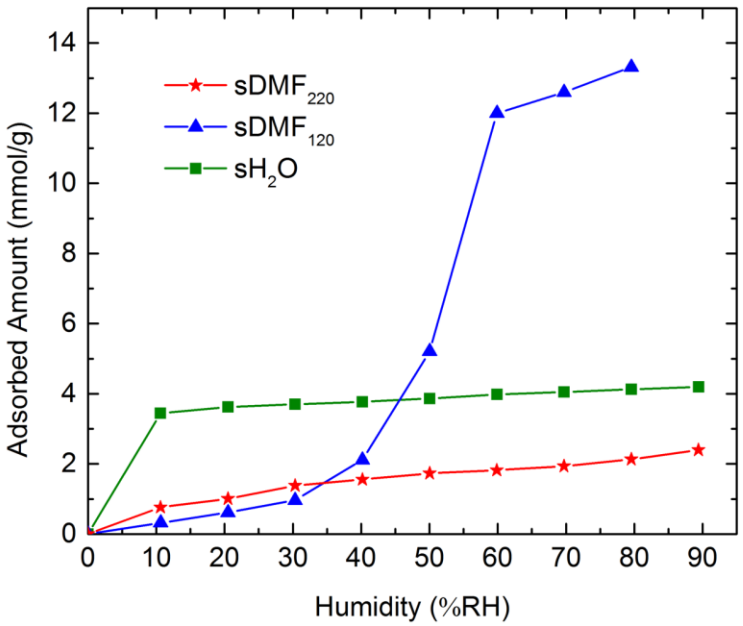

Figure 3.5. H_2O adsorption isotherms at 25°C and 1 bar for $sDMF_{120}$ (blue circles), $sDMF_{220}$ (red squares) and sH_2O (green stars) as a function of relative humidity.

material with very little increase in loading after the initial adsorption of 4 mmol/g at 10 %RH. The material synthesized at 120°C in DMF, $sDMF_{120}$, however, exhibits a type V isotherm characteristic of a large-pore material, with very low initial loading until >50 %RH. $sDMF_{120}$ adsorbs less than 1 mmol/g of water vapor until the humidity rises above 30 %RH, and maintains a lower loading than sH_2O until 50 %RH. This low adsorption along with the absence of any change in PXRD pattern (Figure 3.A.4) or BET surface area after routine exposure to laboratory atmosphere of similar humidity level leads us to believe that the material is stable in humid conditions less than 50 %RH. The material synthesized at 220°C in DMF, $sDMF_{220}$, however, exhibits an approximately linear isotherm, with very low loading across the entire range of humidity. $sDMF_{220}$ adsorbs less than 2 mmol/g of water vapor at 90 %RH, less than half the loading of sH_2O at the same humidity level. The FTIR spectra indicate DMF molecules remain after activation and $sDMF_{220}$ possesses a gradual breathing behavior during CO_2 adsorption. It is likely that the few coordinated DMF molecules prevent or reduce water adsorption around

their locations in the framework resulting in low water adsorption and increased hydrophobicity, as well as continued low adsorption in the high humidity range similar to sH_2O with the np form preventing the clustering and adsorption of large amounts of water seen in $sDMF_{120}$. Similar exposure to laboratory air did not yield any change in the PXRD pattern or BET surface area of $sDMF_{220}$ as was expected from the ^1H NMR results demonstrating its greater hydrophobicity in room conditions than sH_2O.

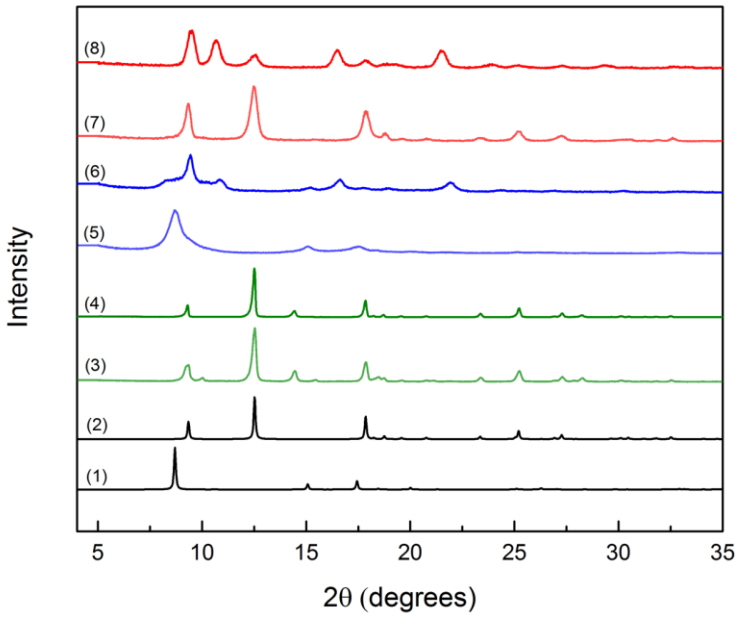

Figure 3.6. XRD patterns of (1) large-pore form, (2) narrow-pore form, (3) activated MIL-53(Al)$_{sH2O}$, (4) post water adsorption MIL-53(Al)$_{sH2O}$, (5) activated MIL-53(Al)$_{sDMF120}$, (6) post water adsorption MIL-53(Al)$_{sDMF120}$, (7) activated MIL-53(Al)$_{sDMF220}$, (8) post water adsorption MIL-53(Al)$_{sDMF220}$.

In addition, we are able to gain insight into the water stability of the lp and np conformations of MIL-53(Al). It is evident that the continued water stability at higher relative humidity levels of the traditionally synthesized material stems from the immediate and complete pore filling with low water adsorption at initial humidity levels due to the presence of inaccessible areas of the pore volume while in the np form. Conversely, while $sDMF_{120}$ is in the lp form, water experiences weak interactions with the pore surface at low humidity levels, as illustrated by the low initial adsorption until 50

%RH. However, as seen in experimental and computational studies of the effects of water on other MOFs,[21-23] beyond this point water clusters form and fill the pore, interacting more with the metal-ligand bond and leading to a breakdown of the structure as the material begins to adsorb large amounts of water, with an ultimate loading of 13.3 mmol/g. In addition, the presence of defects, indicated by FTIR analysis of this material, allows easy access to the metal-ligand bond and subsequent collapse of the structure. The large increase in adsorption in $sDMF_{120}$ corresponding to a breakdown of the MOF structure is confirmed through comparison of PXRD patterns before and after water adsorption experiments shown in Figure 3.6, and BET surface areas before and after water adsorption experiments. It is evident that a large change has occurred in the structure of $sDMF_{120}$ as the structure no longer resembles the activated pattern or the simulated lp or np form patterns and the BET surface area was reduced from 1472 m^2/g to 370 m^2/g.

$sDMF_{220}$, while appearing to behave similarly to sH_2O, is found to not be water stable, with the pattern after water adsorption experiments closely resembling its as-synthesized pattern shown in Figure 3.2 (8), suggesting there are free BDC and $Al(OH)_x$ molecules present after being removed by attacking water molecules. The reduction of the BET surface area from 1570 m^2/g to 402 m^2/g confirms the breakdown of the framework in the presence of high humidity. The instability of this material, although present in a narrow-pore form, suggests that the coordinated DMF molecules may induce the observed larger np form, which allows for enough water to be absorbed to degrade the material. On the other hand, there is little change in the PXRD pattern for MIL-53$(Al)_{sH2O}$ after water adsorption, with the pattern closely resembling the activated pattern as well as the simulated np form. In addition, BET analysis showed a negligible change in surface area before and after water adsorption for MIL-53$(Al)_{sH2O}$, 1410 m^2/g to 1408 m^2/g, confirming the water stability of the material while in the np form. These

results lead to the hypothesis that traditionally synthesized MIL-53(Al) materials as well as the large-pore stabilized materials are susceptible to water effects at high humidity levels while in pore forms any larger than the traditional np form, which would have a negative impact on CO_2 adsorption applications at higher pressures, where all types of these materials would be present in the large-pore form.

3.3 Conclusions

In conclusion, we have reported solvothermal syntheses of large-pore stabilized MIL-53(Al) MOFs that do not possess the standard breathing behavior found in literature. Synthesis at 120 °C in DMF produces a material with no breathing behavior, while synthesis at 220 °C in DMF results in a material with a gradual, slight breathing behavior. The different breathing behavior or lack thereof and increased stability of the large-pore form allows for a large increase in CO_2 adsorption in the 1-5 bar region, and overall loading for the large-pore only material, and a large increase throughout the entire pressure range for the gradually breathing MOF. Water adsorption studies of the materials synthesized in DMF at 120 °C, $sDMF_{120}$, and 220 °C, $sDMF_{220}$, suggest that at humidity levels less than 50 %RH, the materials are stable and have much lower water loading than the material synthesized in water, sH_2O. It is evident that choice of synthesis solvent can have a significant impact on the resulting structure. Understanding and modulating the breathing behavior of metal-organic frameworks offers unique opportunities for enhancing applications in gas adsorption, chemical sensing, and other areas of interest.

3.3 References

(1) Barthelet, K.; Marrot, J.; Riou, D.; Férey, G. *Angew. Chem.* **2002**, *41*, 281.

(2) Bourrelly, S.; Llewellyn, P. L.; Serre, C.; Millange, F.; Loiseau, T.; Férey, G. *J. Am. Chem. Soc.* **2005**, *127*, 13519.

(3) Loiseau, T.; Serre, C.; Huguenard, C.; Fink, G.; Taulelle, F.; Henry, M.; Bataille, T.; Férey, G. *Chem-Eur J* **2004**, *10*, 1373.

(4) Serre, C.; Bourrelly, S.; Vimont, A.; Ramsahye, N. A.; Maurin, G.; Llewellyn, P. L.; Daturi, M.; Filinchuk, Y.; Leynaud, O.; Barnes, P.; Férey, G. *Adv. Mater.* **2007**, *19*, 2246.

(5) Walton, K. S.; Snurr, R. Q. *J. Am. Chem. Soc.* **2007**, *129*, 8552.

(6) ten Elshof, J. E.; Abadal, C. R.; Sekulić, J.; Chowdhury, S. R.; Blank, D. H. A. *Micro. Meso. Mater.* **2003**, *65*, 197.

(7) Biswas, S.; Ahnfeldt, T.; Stock, N. *Inorg. Chem.* **2011**, *50*, 9518.

(8) Liu, J.; Zhang, F.; Zou, X.; Yu, G.; Zhao, N.; Fan, S.; Zhu, G. *Chem. Commun.* **2013**, *49*, 7430.

(9) Senkovska, I.; Hoffmann, F.; Fröba, M.; Getzschmann, J.; Böhlmann, W.; Kaskel, S. *Micro. Meso. Mater.* **2009**, *122*, 93.

(10) Serre, C.; Millange, F.; Thouvenot, C.; Noguès, M.; Marsolier, G.; Louër, D.; Férey, G. *J. Am. Chem. Soc.* **2002**, *124*, 13519.

(11) Rallapalli, P.; Patil, D.; Prasanth, K. P.; Somani, R. S.; Jasra, R. V.; Bajaj, H. C. *J. Porous Mater.* **2009**, *17*, 523.

(12) Rallapalli, P.; Prasanth, K. P.; Patil, D.; Somani, R. S.; Jasra, R. V.; Bajaj, H. C. *J. Porous Mater.* **2010**, *18*, 205.

(13) Patil, D. V.; Rallapalli, P. B. S.; Dangi, G. P.; Tayade, R. J.; Somani, R. S.; Bajaj, H. C. *Ind. Eng. Chem. Res.* **2011**, *50*, 10516.

(14) Düren, T.; Millange, F.; Férey, G.; Walton, K. S.; Snurr, R. Q. *J. Phys. Chem. C* **2007**, *111*, 15350.

(15) Tynan, E.; Jensen, P.; Kruger, P. E.; Lees, A. C. *Chem. Commun.* **2004**, 776.

(16) Moon, H. R.; Kobayashi, N.; Suh, M. P. *Inorg. Chem.* **2006**, *45*, 8672.

(17) Park, M.; Moon, D.; Yoon, J. W.; Chang, J. S.; Lah, M. S. *Chem. Commun.* **2009**, 2026.

(18) Mu, B.; Huang, Y. G.; Walton, K. S. *CrystEngComm* **2010**, *12*, 2347.

(19) Jasuja, H.; Walton, K. S. *J. Phys. Chem. C* **2013**, *117*, 7062.

(20) Jiang, Y. J.; Huang, J.; Marx, S.; Kleist, W.; Hunger, M.; Baiker, A. *J. Phys. Chem. Lett.* **2010**, *1*, 2886.

(21) Tan, K.; Nijem, N.; Canepa, P.; Gong, Q.; Li, J.; Thonhauser, T.; Chabal, Y. J. *Chem. Mater.* **2012**, *24*, 3153.

(22) Bellarosa, L.; Calero, S.; López, N. *Phys. Chem. Chem. Phys.* **2012**, *14*, 7240.

(23) De Toni, M.; Jonchiere, R.; Pullumbi, P.; Coudert, F. X.; Fuchs, A. H. *ChemPhysChem* **2012**, *13*, 3497.

APPENDIX 3.A

MIL-53(Al) CHARACTERIZATION

Experimental Section

Chemicals: Aluminum nitrate nonahydrate ($Al(NO_3)_3 \cdot 9H_2O$, Sigma Aldrich, 99%), benzene-1,4-dicarboxylic acid (C_6H_4-1,4-$(CO_2H)_2$, Sigma Aldrich, 98%), DMF (*n,n*-dimethylformamide, Sigma Aldrich, 99%), and deionized water were used as received.

Characterization

Thermo gravimetric analysis (TGA) was carried out in the temperature range of 30-710 ˚C on a NETZSCH STA 449 F1 Jupiter® under helium with a heating rate of 5 ˚C / min and flow rate of 20 mL/min.

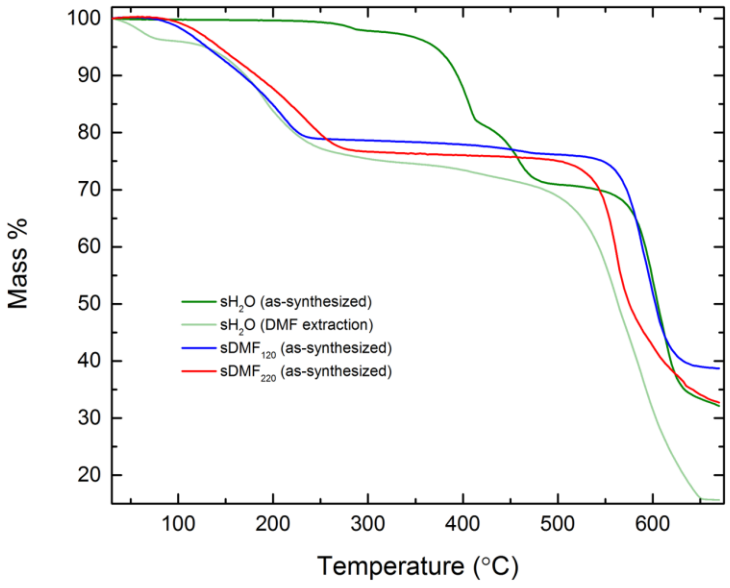

Figure 3.A.1. TGA curves of $MIL\text{-}53(Al)_{sH2O}$ (sH_2O) as-synthesized and after DMF extraction, $MIL\text{-}53(Al)_{sDMF,120}$ ($sDMF_{120}$) as-synthesized, and $MIL\text{-}53(Al)_{sDMF,220}$ ($sDMF_{220}$) as-synthesized.

The TGA curve for sH_2O as-synthesized exhibits two main events between room temperature and 700 °C. The first between 275-450 °C is the departure of free terephthalic acid, while the second, above 500 °C corresponds to the elimination of the terephthalate linkers from the framework. The TGA curve for sH_2O after DMF extraction exhibits three main events between room temperature and 700 °C. The first between 70-140 °C is the departure of water molecules, while the second, between 150-250 °C is the departure of DMF, the third event above 500 °C corresponds to the elimination of the terephthalate linkers from the framework. A slow release of DMF molecules from the extraction process is seen between 250-500 °C. The large difference in final mass % is due to the presence of water (~5 %) and excess DMF (~10 %) in the initial sample. The TGA curve for $sDMF_{120}$ exhibits two main events between room temperature and 700 °C. The first between 100-250 °C is the departure of DMF molecules, while the second, above 500 °C corresponds to the elimination of the terephthalate linkers from the framework. The TGA curve for $sDMF_{220}$ exhibits two main events between room temperature and 700 °C. The first between 100-260 °C is the departure of DMF molecules, while the second, above 500 °C corresponds to the elimination of the terephthalate linkers from the framework.

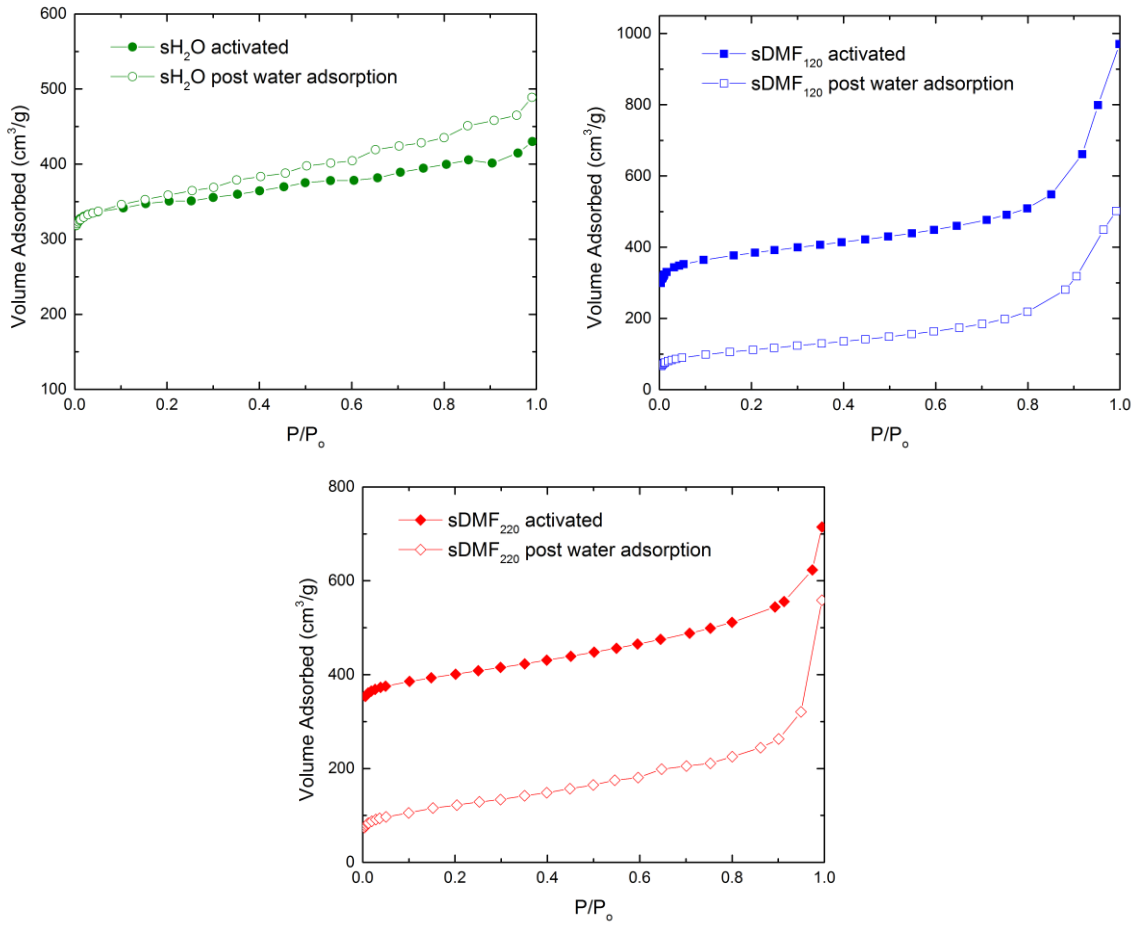

Figure 3.A.2. N_2 adsorption data for MIL-53(Al)$_{ht}$ (sH_2O) before and after water adsorption, MIL-53(Al)$_{sDMF120}$ ($sDMF_{120}$) before and after water adsorption, and MIL-53(Al)$_{sDMF220}$ ($sDMF_{220}$) before and after water adsorption. P/P_0 = 0.003-0.999

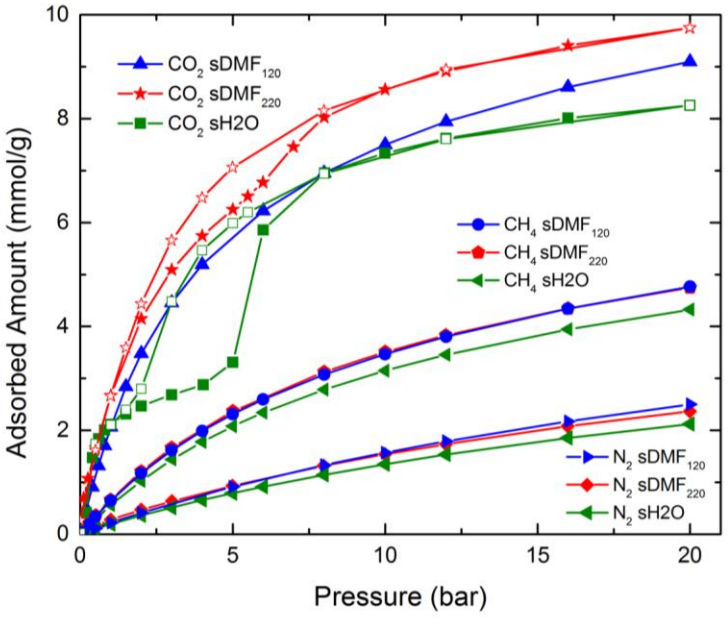

Figure 3.A.3. CO_2, CH_4, and N_2 adsorption isotherms for MIL-53(Al)$_{sH2O}$ (sH_2O), MIL-53(Al)$_{sDMF120}$ ($sDMF_{120}$), and MIL-53(Al)$_{sDMF220}$ ($sDMF_{220}$). Desorption isotherms are shown for $sDMF_{220}$ and sH_2O with open symbols.

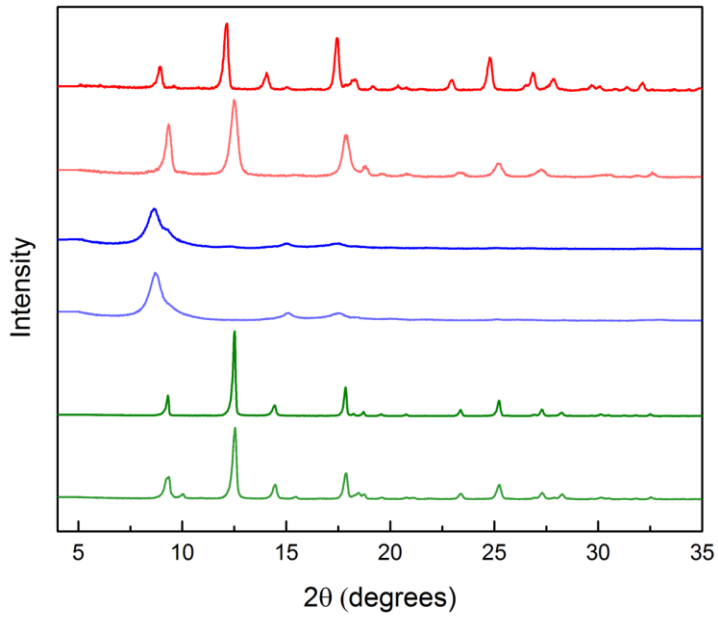

Figure 3.A.4. XRD pattern of MIL-53(Al)$_{sH2O}$ (sH_2O) before (light green) and after water adsorption (green), MIL-53(Al)$_{sDMF120}$ ($sDMF_{120}$) before (light blue) and after (blue) exposure to room humidity air (~50 %RH), and MIL-53(Al)$_{sDMF220}$ ($sDMF_{220}$) before (light red) and after (red) exposure to room humidity air (~50 %RH).

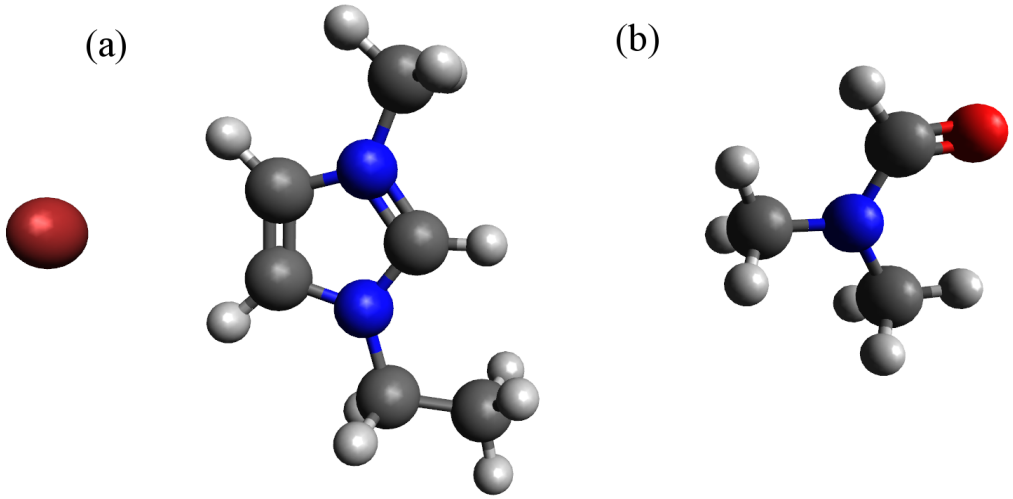

Figure 3.A.5. Size comparison of (a) 1,3-methyl-imidazolium bromine and (b) DMF.

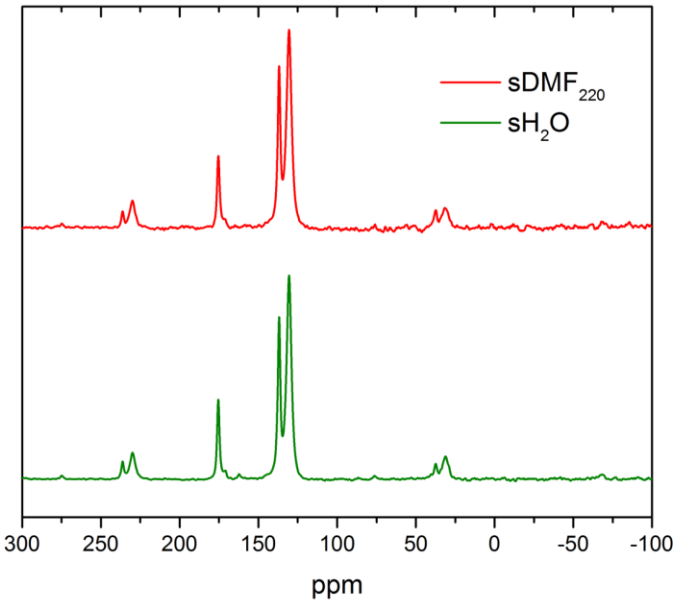

Figure 3.A.6. ^{13}C NMR spectra for MIL-53(Al)$_{sH2O}$ (sH_2O) and MIL-53(Al)$_{sDMF220}$ ($sDMF_{220}$).

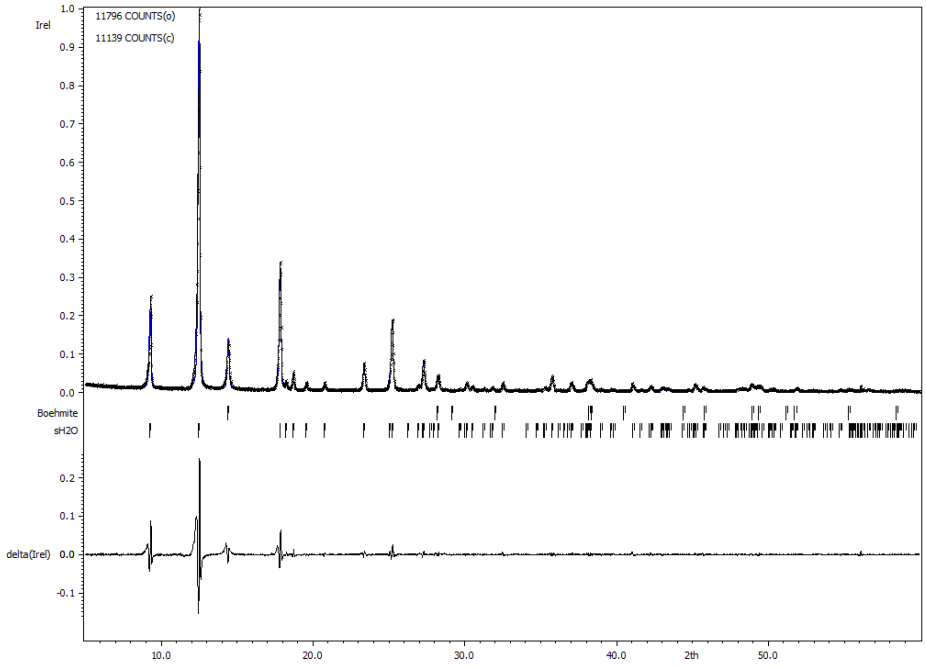

Figure 3.A.7. LeBail refinement for MIL-53(Al)$_{sH2O}$ (sH$_2$O).

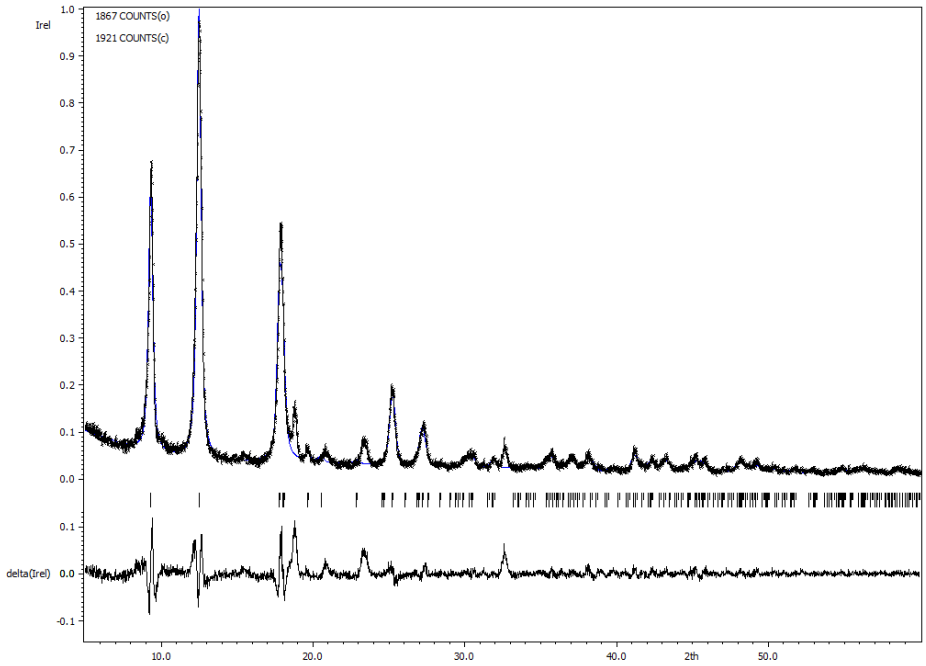

Figure 3.A.8. LeBail refinement for MIL-53(Al)$_{sDMF220}$ (sDMF$_{220}$).

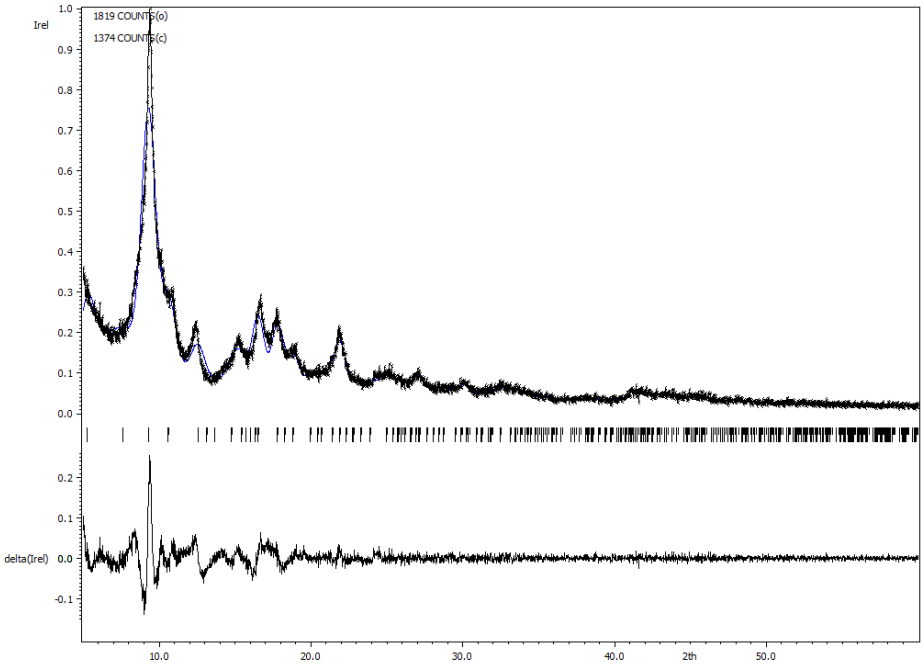

Figure 3.A.9. LeBail refinement for MIL-53(Al)$_{sDMF120}$ (sDMF$_{120}$).

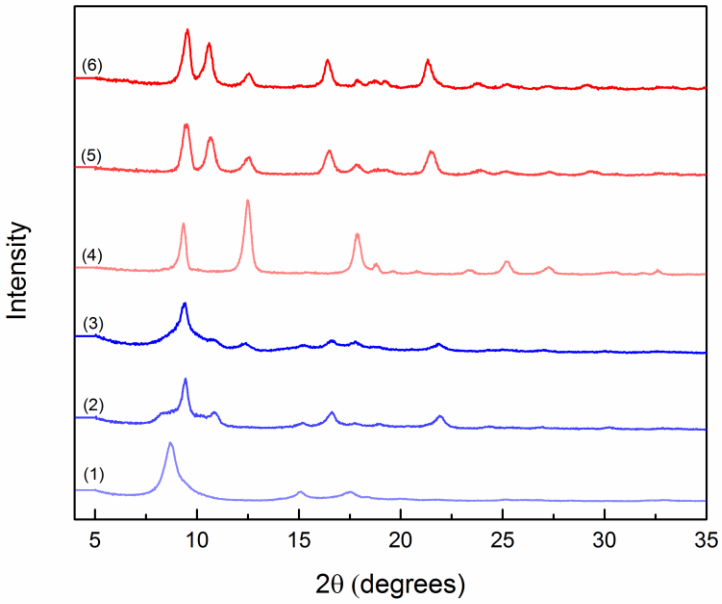

Figure 3.A.10. XRD patterns of (1) activated MIL-53(Al)$_{sDMF120}$, (2) post water adsorption MIL-53(Al)$_{sDMF120}$, (3) regenerated MIL-53(Al)$_{sDMF120}$ after water adsorption, (4) activated MIL-53(Al)$_{sDMF220}$, (5) post water adsorption MIL-53(Al)$_{sDMF220}$, (6) regenerated MIL-53(Al)$_{sDMF220}$ after water adsorption.

Table 3.A.1. Cell parameters calculated from LeBail refinements for MIL-53(Al)$_{sH2O}$ (sH_2O), MIL-53(Al)$_{sDMF220}$ ($sDMF_{220}$), and MIL-53(Al)$_{sDMF120}$ ($sDMF_{120}$), and literature values for the large (*ht*) and narrow (*lt*) pore configurations.

[1]T. Loiseau, et al., Chem-Eur J, 2004, 10, 1373

Material	sH_2O	$sDMF_{220}$	$sDMF_{120}$	MIL-53$_{ht}$ (Al)[1]	MIL-*53*$_{lt}$ (Al)[1]
Crystal system	Monoclinic	Monoclinic	Orthorhombic	Orthorhombic	Monoclinic
Space group	*Cc*	*Cc*	*Imma*	*Imma*	*Cc*
a [Å]	19.487	20.877	6.97	6.6085	19.513
b [Å]	7.5838	7.98	16.47	16.675	7.612
c [Å]	6.5606	6.623	11.40	12.813	6.576
β [°]	104.24	104.24			104.24
R_p	15.80	13.11	9.77	13.7	11.4
R_{wp}	21.08	17.90	12.28	17.0	15.1

For MIL-53(Al)$_{sH2O}$ (sH_2O) and MIL-53(Al)$_{sDMF220}$ ($sDMF_{220}$), the cell parameters of MIL-53(Al)$_{lt}$ from T. Loiseau, et al., Chem-Eur. J., 2004, 10, 1373 were used as a starting point for LeBail refinement. For MIL-53(Al)$_{sDMF,120}$ ($sDMF_{120}$) the cell parameters of MIL-53(Al)$_{ht}$ from T. Loiseau, et al., Chem-Eur. J., 2004, 10, 1373 were used as a starting point for LeBail refinement. The refinement was performed in the software package Jana2006. The determined cell parameters are presented in Table 3.A.1. It was determined for the sH_2O material that a secondary phase of boehmite was present.

CHAPTER 4

ROLE OF DEFECTS AND METAL COORDINATION ON ADSORPTION OF ACID GASES IN MOFS AND METAL OXIDES

The understanding of the effects of synthesis solvent on MOF adsorption and structural properties, discussed in the previous chapter, allows the design and tailoring of these materials for specific applications. To advance MOF materials beyond single-component laboratory performance studies, a better understanding of their performance in multicomponent and often harsh conditions is required. Understanding the effects of harsh acid gases, widely present in many industrial applications, on MOF materials and establishing a route for identifying adsorbed species through correlation with MOF-derived oxides is the main focus of this chapter. This Chapter was adapted from W.P. Mounfield, III; U. Tumuluri; Y. Jiao; M. Li; S. Dai; Z. Wu; K.S. Walton, "Role of Defects and Metal Coordination on Adsorption of Acid Gases in MOFs and Metal Oxides: An In Situ IR Spectroscopic Study" Microporous and Mesoporous Materials, 227, 65-75 DOI**:** 10.1016/j.micromeso.2016.02.023. In Chapter 4, U.T. aided in in situ IR data analysis, Y.J. collected SEM images, and M.L. synthesized CeO_2-wires.

In this chapter, adsorption of acid gases, including CO_2 and SO_2, on several classes of materials was investigated using in situ IR spectroscopy coupled with mass spectrometric techniques. Adsorbed species were examined for each MOF-derived oxide and compared with an oxide as well as the parent MOF to gain insight into the similarities in these species across morphologies and coordination environments. Two sets of samples were chosen for comparison, a cerium series: CeBTC, a cerium-based MOF, CeO_2-d derived from CeBTC, and

CeO_2 wires, prepared and studied in previous studies,[1] and a titanium series: MIL-125, a titanium-based MOF that has shown promising acid gas removal properties,[2,3] TiO_2-d derived from MIL-125, and a bulk mixed-phase TiO_2. In addition to IR spectroscopic studies, the effect of acid gas exposure was also explored through SEM and TEM imaging before and after acid gas exposure, as well as structure analysis via XRD before and after in situ measurements. Water adsorption experiments were coupled with SEM and TEM imaging to investigate material stability and the similarity of the degradation mechanism during water and acid gas exposure. It is expected that exposure to SO_2 would result in a decrease in the amount of adsorbed CO_2 species for all samples and also the nature of adsorbed species for the MOF-derived oxide samples due to retention of SO_2 species at potential adsorption sites and the degradation and loss of those sites. In addition, the visual degradation observed with SEM and TEM for MOF and MOF-derived oxide samples after exposure to SO_2 or H_2O gave insight into the degradation mechanism of these samples.

4.1 Experimental Section

Synthesis of CeBTC. The synthesis of CeBTC was performed using a similar procedure to that reported previously by Mu, et al.[4] $Ce(NO_3)_3 \cdot 6H_2O$ (9.6 mmol) and 1,3,5 benzene tricarboxylic acid (BTC) (8 mmol) were added to 30 mL of *n,n*-dimethylformamide (DMF) in a 60 mL scintillation vial. The vials were heated in an isothermal oven at 120 °C for 24 hours. The resultant beige product was rinsed with DMF three times followed by one methanol wash.

Synthesis of MIL-125. The synthesis of MIL-125 was performed by adding benzene dicarboxylic acid (BDC) (2.75 mmol) to a mixture of DMF (6.5 mL) and methanol (6.5 mL). Acetic acid (22.5 mmol, 1.4 mL) was added to the mixture

before the addition of titanium isopropoxide (0.75 mmol, 0.22 mL) to prevent the titanium precursor from hydrolyzing when added to the solution. The solution was placed in a 60 mL scintillation vial and heated in an isothermal oven at 110 °C for 24 hours. The resultant white product was rinsed with DMF three times followed by methanol one time.

Synthesis of MOF-derived oxides. Porous anatase TiO_2 and porous CeO_2 were prepared using the method described in a previous study for preparation of porous TiO_2 from MIL-125.[5] MIL-125 or CeBTC was placed in a ceramic crucible and calcined at 350 °C for 6 hours in air. The resulting oxide was recovered and stored in a desiccator until the materials were characterized.

TiO_2 Bulk. Bulk mixed-phase TiO_2 was obtained from City Chemical (T7346-500GM) and used as received with no further purification or treatment.

CeO_2 wires. The preparation of CeO_2 wires has been described in detail elsewhere.[1] The morphology of CeO_2 was controlled by varying the pH, temperature and duration of the reaction. $Ce(NO_3)_3{\cdot}6H_2O$ and NaOH were used as precursors for CeO_2 wires. The light yellow precipitate was centrifuged after the hydrothermal synthesis, and washed with deionized water and ethanol three times. The Na impurities were removed by base-acid wash, which was discussed in detail in previous work. The base-acid washed products were dried in vacuum overnight and then calcined at 400 ^oC in air for 4 hours.

Powder X-ray diffraction. Powder X-ray diffraction patterns were recorded on an X'Pert X-ray PANalytical diffractometer with an X'accelerator module using Cu Kα (λ = 1.5418 Å) radiation at room temperature, with a step size of 0.02˚ in two theta (2θ).

N_2 physisorption. Nitrogen physisorption isotherms were measured at 77 K for samples activated at 473 K for 12 h under vacuum using the Quadrasorb

system from Quantachrome instruments. Nitrogen adsorption analysis was performed on all resulting products, and surface areas for the MOFs were determined by applying BET theory over a range of data points applicable to microporous materials.[6] N_2 isotherms showed typical Type I behavior as per the IUPAC classification.

In situ IR and Raman spectroscopy. The MOF-derived and oxide materials were pretreated at 300 ˚C at the rate of 10 ˚C/min and held for 1 hr in He flow at 50 cm^3/min. The MOF materials were activated ex situ under vacuum at 150 ˚C for MIL-125 and 250 ˚C for CeBTC. MIL-125 was pretreated at 150 ˚C to avoid degradation of the sample, and CeBTC was pretreated at 300 ˚C at the rate of 10 ˚C/min and held for 1 hr in He flow at 50 cm^3/min. The in situ spectroscopic studies consist of three cycles in succession on the same sample, two CO_2 cycles, one before and one after an SO_2 cycle. Each cycle consisted of the following steps (i) adsorption, (ii) He purge, and (iii) temperature programmed desorption (TPD). During the first step of the first and third cycles, CO_2 adsorption, the material was exposed to 2% CO_2/He flow at 50 cm^3/min for 15 min at 25 ˚C. During the first step of the second cycle, SO_2 adsorption, the material was exposed to 15 ppm SO_2/He flow at 50 cm^3/min for 15 min at 25 ˚C. During the second step of each cycle, the He Purge, the residual gas was purged by He flow at 50 cm^3/min for 10 min at 25 ˚C. For the final step of each cycle temperature programmed desorption was performed, during which the material was heated to 300 ˚C at the rate of 10 ˚C/min; the temperature of the material was held at 300 ˚C for 30 min, followed by cooling the material to 25 ˚C at the rate of 10 ˚C/min. For MIL-125 the temperature chosen for TPD matched that of its activation, 150 ˚C, instead of 300 ˚C used for all other samples to prevent degradation of the material during heating.

IR spectra were collected continuously through the entire measurement cycle using a Thermo Nicolet Nexus 670 spectrometer in Diffuse Reflectance mode (DRIFTs), the outlet gases from the DRIFTs cell (Pike Technologies HC-900) were analyzed using a quadrupole mass spectrometer (Omnistar GSD-301 O_2, Pfeiffer Vacuum). Absorbance spectra during SO_2 adsorption were calculated as $Abs = -log(I/Io)$, where I is the single beam spectrum during adsorption and I_o is the single beam spectrum before adsorption.

The Raman measurements were performed with a catalytic Raman reactor (Linkam CCR1000) using in-house built multiple-wavelengths Raman system[7] that includes laser excitations at λ=325 and 532 nm. Raman scattering was collected using fiber optics connected directly to the spectrograph stage of the triple Raman spectrometer (Princeton Instruments Acton Trivista 555). Samples pretreatment and SO_2 adsorption were carried out similarly as in the IR studies.

Scanning Electron Microscopy. Samples were imaged on a Zeiss Ultra60 FE-SEM instrument with a high-efficiency in-lens SE detector at a working distance of 7-8 mm and accelerating voltage of 5 kV. The samples were sonicated for 10 s in methanol and then dispersed on a flat Al sample holder with two-sided adhesive conductive carbon tape. Prior to SEM observations, samples were coated with carbon for 30 s at 4.4 V using a Cressington 108A Carbon Coater to exclude the charging effect. Several images were captured for each sample with varying levels of magnifications.

Transmission Electron Microscopy. TEM images were obtained using a Hitachi HT7700 operated at 120keV. The samples were deposited on a lacy carbon copper grid by suspending less than 1 mg of material in methanol and dropcasting the suspension on the grid.

Water Vapor and CO_2 Adsorption. A 3Flex Surface Characterization Analyzer from Micromeritics was used to collect water vapor isotherms at 22 ˚C for all samples. Isotherms were collected after in situ IR experiments with fresh, unexposed sample. Prior to water adsorption measurements, CeBTC was activated in a Smart VacPrep degasser at 300 ˚C for 12 hours under dynamic vacuum, MIL-125 was activated at 175 ˚C for 12 hours under dynamic vacuum, and all metal oxides were activated at 150 ˚C for 12 hours under dynamic vacuum. All water vapor isotherms were measured to $P/P_0 = 0.95$ to avoid water condensation.

CO_2 isotherms were collected on MIL-125, TiO_2-d, and CeBTC on fresh sample as well as samples after in situ IR experiments. Prior to adsorption measurements, CeBTC was activated in a Smart VacPrep degasser at 300 ˚C for 12 hours under dynamic vacuum, MIL-125 was activated at 150 ˚C for 12 hours under dynamic vacuum, and TiO_2-d was activated at 150 ˚C for 12 hours under dynamic vacuum. All isotherms were measured with $P_0 = 760$ mmHg.

4.2 Results and Discussion

4.2.1 Characterization of pristine materials

Powder X-ray diffraction (PXRD) was used to verify the structures of the MOFs and the oxides. Figure 4.A.1 shows that the as-synthesized patterns for CeBTC and MIL-125 match the simulated patterns generated from literature.[8,9] The MOF-derived CeO_2, and CeO_2 wires match the simulated ceria pattern (JCPDS Card No. 34-394), confirming the MOF-derived oxide possesses the same crystal structure as the CeO_2 wires, albeit a different morphology. Derived TiO_2 is synthesized in the anatase phase (JCPDS Card No. 21-1272), while the bulk TiO_2 is present as a mixture of rutile (JCPDS Card No. 88-1175) and anatase

phases. In addition, elemental analysis was performed on the derived oxide materials to verify that all carbonaceous material had been removed. Less than 0.5 wt.% carbon remained for each sample, 0.44 for CeO_2-d and 0.39 for TiO_2-d, indicating complete removal of the organic linkers during preparation.

Table 4.1. BET surface areas for samples as-synthesized, after in situ IR experiments (Post IR), and after water adsorption experiments (Post H_2O).

Material	SA_{BET} (m2/g)	SA_{BET} (m^2/g) Post IR	SA_{BET} (m^2/g) Post H_2O
CeBTC	752	0	52
CeO_2-d	138	124	117
CeO_2 wires	107	104	108
MIL-125(Ti)	1392	190	398
TiO_2-d	133	47	51
TiO_2 bulk	49	54	47

After confirming the crystalline structure of all materials, N_2 physisorption was performed on each sample to determine the surface area and also elucidate the retained porosity of the MOF-derived oxides, which is a key feature of MOF-templated oxides in literature.[10] The MOF BET surface areas, shown in Table 4.1, were similar to those found in literature; 1392 m^2/g for MIL-125 and 752 m^2/g for CeBTC.[8,9] After preparation through calcination of MIL-125, TiO_2-d possesses mesopores with sizes ranging between 2-4 nm, while bulk TiO_2 displays a distribution of micro, meso and macropores as seen in the pore size distribution shown in Figure 4.A.2. The mesopores present in the TiO_2-d are the result of various degrees of connectivity arising during calcination between the 1.25 nm pores present in MIL-125. CeO_2-d shows a larger abundance of micropores than CeO_2 wires, due to a degree of retained pore structure from the CeBTC parent material, though both show a distribution of macro, meso, and micropores. The TiO_2-d and CeO_2-d displayed markedly higher surface areas, 133

and 138 m^2/g, than the traditionally prepared oxides, 49 and 107 m^2/g, respectively. It is important to note that both of the MOF-derived oxides possess a large number of particle defects, such as cracks and voids, leading to an increase in surface area, which will be investigated further with SEM in a later section. These porous MOF-derived oxides will not only provide the basis for understanding acid gas adsorption on MOFs, but also insight into the effect of morphology and defects on material stability in MOFs and MOF-derived oxides.

4.2.2 Structure of SO_x species from SO_2 adsorption

Figure 4.1 shows the IR spectra during SO_2 adsorption on CeBTC, CeO_2-d, and CeO_2 wires at room temperature as a function of time. SO_2 adsorption on ceria is well-studied and the IR spectra shown in Figure 4.1(c) for the CeO_2 wires exhibits characteristic peaks at 1424, 1340, 1233, 1194, 1064, 1018, and 897 cm^{-1} indicating the formation of surface sulfates[11-19] while peaks at 1018 and 989 cm^{-1} indicating the formation of surface sulfites [20,21] during SO_2 adsorption. The broad IR band at 1064 cm^{-1} appearing upon the start of SO_2 adsorption also indicates the presence of surface sulfate species.[18] In addition, the spectra also exhibit characteristic negative peaks at 1398, 1289, and 1218 cm^{-1} indicating the perturbation of previously adsorbed surface carbonates [22-24] by adsorbed SO_2. It is interesting to note that there is no increase in MS intensity to indicate CO_2 evolving during SO_2 adsorption, suggesting that few carbonates are displaced completely from the surface and rather the majority remain bound to the surface. This hypothesis is supported by the release of CO_2 during SO_2 TPD shown in Figure 4.A.3, where these strongly bound species are not evolved until temperatures above 150 ˚C, with a maximum intensity observed at 225 ˚C. These remnant carbonate species are likely explained by the high number of defects

present in the material. To characterize the abundance of these defect sites, the ratio of the defects (600 cm^{-1}) to the bulk (465 cm^{-1}) in the Raman spectra shown in Figure 4.A.4 was calculated in Table 4.A.1.[1] The ratio of defects to bulk for CeO_2 wires drops 6.7% after exposure to SO_2, suggesting the continued presence of SO_x species occupying defect sites.

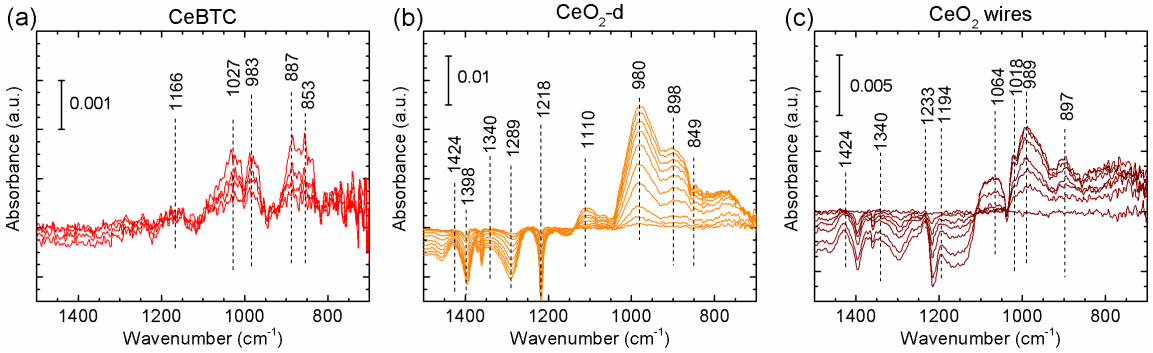

Figure 4.1. IR spectra during 15 minutes of SO_2 adsorption on CeBTC, CeO_2-d, and CeO_2 wires at 25 ˚C.

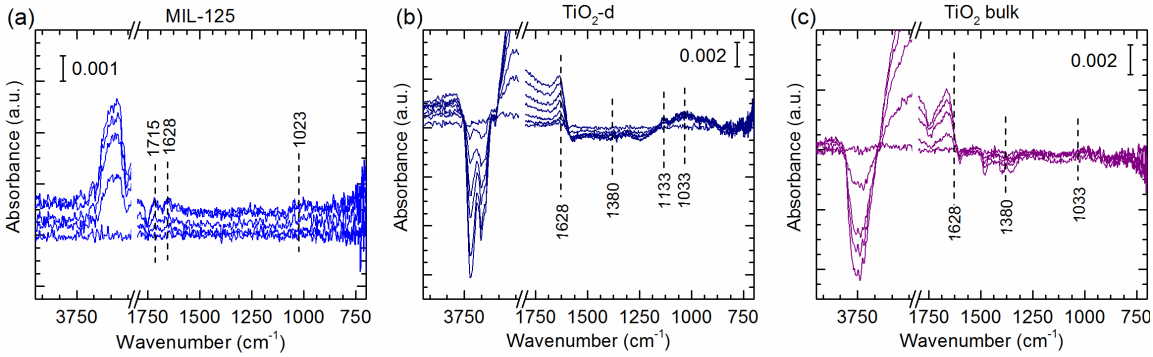

Figure 4.2. IR spectra during 15 minutes of SO_2 adsorption on MIL-125, TiO_2-d, and TiO_2 bulk at 25 ˚C.

Table 4.2: Assignment of IR bands observed upon room temperature CO_2 and SO_2 adsorption on cerium and titanium containing samples.

Species	Band Assignment
sulfates	1424, 1380, 1340, 1233, 1194, 1133, 1110, 1064, 1033 1018, 897, 849
sulfites	1133, 1018,989
physisorbed SO_2	1166

Species	Band Assignment
bicarbonates	1674, 1606, 1496, 1429, 1245, 1221, 1215, 1025, 980
carbonates	1588, 1402, 1284, 1237, 1165, 1131, 1025, 997

The preparation method for CeO_2-d is hypothesized to produce a material that possesses a large number of defects in addition to the porosity retained from CeBTC. The defect ratio (see Table 4.A.1) calculated for freshly prepared CeO_2-d from Raman spectrum is quite similar to that calculated for the CeO_2 wires; however, after SO_2 exposure the ratio drops 33.9%, indicating a large loss of oxygen vacancies, likely due to a large number of SO_x species occupying these sites. Comparison of the IR spectra on CeO_2 wires with the spectra on CeO_2-d shown in Figure 4.1(b) shows a similar multitude of peaks at 1424, 1340, 1233, 1194, 1110, 898, and 849 cm^{-1} indicating the formation of surface sulfates, and the peak at 980 cm^{-1} indicating the formation of surface sulfites during SO_2 adsorption.[11-19,25] The surface sulfate peaks at 1110 and 849 cm^{-1} are not observed for the CeO_2 wires, and the 1110 cm^{-1} peak can be attributed to adsorption on an exposed (100) face as seen in our ongoing studies.[26] In addition to these unique sulfate species, a difference is observed in the intensity of the negative peaks characteristic of the disturbed carbonates (1398, 1289, and 1218 cm^{-1}); these features are much more intense for CeO_2-d. The increase in intensity suggests the carbonate species are in higher abundance on CeO_2-d than on CeO_2 wires, which is supported by the higher intensity of CO_2 observed during SO_2 TPD for CeO_2-d shown in Figure 4.A.3 and calculated in Table 4.A.2.

SO_2 adsorption on CeBTC has not previously been investigated; however, the species observed over the CeO_2-d allow the assignment of the species observed for the MOF. The IR spectra shown in Figure 4.1(a) on CeBTC during SO_2 adsorption exhibited a characteristic peak at 1166 cm^{-1} indicating the presence of physisorbed species, similar to that observed during SO_2 adsorption over MOFs.[27] Peaks observed at 1027 and 983 cm^{-1} can be correlated with bands indicating the formation of similar surface sulfite species occurring at the location

of oxygen vacancies seen on CeO_2 wires. CeBTC possesses trivalent cerium atoms and the uncoordinated metal sites closely resemble cerium at sites with an oxygen vacancy; therefore, it can be determined that the formation of the observed sulfite species on CeBTC is occurring at the coordinatively-unsaturated metal sites. The peaks exhibited at 891 and 853 cm^{-1} mirror those seen on CeO_2-d characteristic of the formation of surface sulfates species. The formation of these sulfates likely occurs between the oxygens connecting the tricarboxylate ligands and cerium atoms, as seen in other MOFs.[27] In addition, it is hypothesized that the observed sulfate species may form polynuclear species with the sulfites adsorbed on the open metal sites. No peaks characteristic of perturbation of adsorbed carbonates are observed on CeBTC during SO_2 adsorption. In a study of co-adsorption of CO_2 and SO_2 on another open-metal site MOF, Tan et al. discovered that the replacement of adsorbed CO_2 by SO_2 is slow,[28] which supports the lack of peaks characteristic of disturbed carbonates during the short time the sample is exposed to low concentration SO_2. Monitoring of the CO_2 evolved during SO_2 TPD indicates a significant release of CO_2 as the temperature rises above 250 ˚C. A temperature of 300 ˚C has been identified as the necessary temperature to fully expose the open metal sites present in CeBTC;[4] therefore, these carbonate species remained adsorbed throughout the previous TPD and their bonds with the open metal sites have been slightly weakened by adsorbed SO_2, allowing their displacement during SO_2 TPD.

As expected, comparison of the amount and maximum desorption temperature of SO_2 evolved during TPD (Figure 4.A.5) for the three cerium containing samples reveals CeBTC adsorbs the largest amount of SO_2 due to its high surface area, with continual release of physisorbed SO_2 (indicated by the IR band at 1166 cm^{-1}) beginning at 30 ˚C. A peak in intensity is observed at 275 ˚C

for CeBTC, correlated with the previously mentioned temperature required during activation to remove adsorbed species from open metal sites. A similar peak at 280 ˚C has been observed on CeO_2 rods in current work,[26] correlated with the release of sulfite species adsorbed at oxygen vacancies. Therefore, these similar peaks observed during TPD further support the hypothesis that the surface sulfite species observed at 1027 and 983 cm^{-1} for CeBTC occur at open metal sites mirroring the oxygen vacancies present in CeO_2 wires. CeO_2-d and CeO_2 wires both exhibit a maximum in intensity at 65 ˚C, with CeO_2-d exhibiting a slightly higher amount of evolved SO_2, as calculated in Table 4.A.2. The lack of a second maximum similar to that observed for CeBTC leads to the hypothesis that species remaining after the primary CO_2 adsorption stage of the experiment occupy the most strongly adsorbing sites in the oxide materials, which is further supported by the release of CO_2 at temperatures greater than 150 ˚C for both oxide materials, shown in Figure 4.A.3.

Figure 4.2 shows the IR spectra during SO_2 adsorption on MIL-125, TiO_2-d, and TiO_2 bulk at room temperature as a function of time. All samples exhibit weak interactions with SO_2, in agreement with previous studies demonstrating TiO_2 has weak interactions with SO_2 in comparison to other metal oxides due to having weak and few Lewis base sites.[29] TiO_2-d and TiO_2 bulk exhibit an intense characteristic peak at 1628 cm^{-1}, which, combined with a significant increase in intensity of the negative peak between 3800-3600 cm^{-1}, indicates the reaction of SO_2 with surface hydroxyl groups to form adsorbed H_2O.[30] Both TiO_2 materials also exhibit characteristic peaks at 1380 and 1033 cm^{-1} indicating the formation of surface sulfate and sulfite species, respectively, on the anatase phase of titania.[16] In addition to these similar peaks, TiO_2-d exhibits a peak at 1133 cm^{-1} also characteristic of adsorbed surface sulfite species on anatase titania.[16] This feature

is lost in the background of the spectra of TiO_2 bulk due to the mixture of anatase and rutile phases. While the IR spectra for both TiO_2 samples resemble each other, an analysis of the SO_2 TPD (Figure 4.A.5) reveals a difference in the strength of adsorbed species. TiO_2-d exhibits a slow release of SO_2 reaching a maximum at 100 ˚C, while TiO_2 bulk reaches a maximum at 100 ˚C and a second maximum at 290 ˚C, indicating strongly adsorbed SO_2 species. The lack of this second increase in intensity in TiO_2-d is explained by monitoring of CO_2 evolved during SO_2 TPD (Figure 4.A.3). Only TiO_2-d releases CO_2 during SO_2 TPD, with a large amount of CO_2 released at 50 ˚C, with smaller peaks observed at 220 ˚C and 290 ˚C. Carbonate species present from the initial CO_2 adsorption stage likely occupy the strongest adsorbing defect sites in the material, while physisorbed CO_2 displaced by SO_2 adsorption is trapped in the high porosity of the material until TPD is performed.

As with CeBTC, SO_2 adsorption has not been studied on MIL-125; however, the knowledge of adsorbed species on TiO_2-d allows for the assignment of the weak features observed on the metal-organic framework. The formation of surface sulfites, indicated by the characteristic peak at 1023 cm^{-1}, likely occurs at the metal clusters where titanium-bridging oxygen atoms resemble the structure of anatase titania. The characteristic peak indicating an interaction of SO_2 with surface hydroxyls to form adsorbed surface water, at 1628 cm^{-1}, is also observed on MIL-125, a possible assignment given each titanium atom in the metal node possesses a hydroxyl group. However, the corresponding decrease in the region between 3800-3600 cm^{-1} is not observed. Instead, a steady increase in this region is observed during SO_2 adsorption. This increase is explained by the presence of uncoordinated carboxylates as the material is degraded by reaction with SO_2 leading to the evolution of bands corresponding to the hydroxyl (3700-3600 cm^{-1})

and corresponding carbonyl groups (1715 cm^{-1}) of the uncoordinated carboxylic acid linker. Furthermore, it is hypothesized that the formation of water by interaction of SO_2 with the surface hydroxyls serves to further degrade the material and lead to a drastic loss of surface area, as shown in Table 4.1.

4.2.3 Effect of SO_2 exposure on adsorbed species during CO_2 adsorption

In situ IR spectroscopy during CO_2 adsorption was performed before and after in situ IR SO_2 adsorption to evaluate (i) the differences in adsorbed species between materials, and (ii) the effect of SO_2 exposure on adsorbed CO_2 species for each material. Figure 4.3 shows the IR spectra during CO_2 adsorption before and after in situ SO_2 experiments on CeBTC, CeO_2-d, and CeO_2 wires at room temperature as a function of time. The IR spectra shown in Figure 4.3(b) of CeO_2-d during CO_2 adsorption before SO_2 adsorption exhibited peaks characteristic of bicarbonate, bridged carbonate, bidentate carbonate, and monodentate carbonate species summarized in Table 4.2.[22-24,31-34] Ceria wires exhibited similar peaks; however, several peaks differed between the two samples. Notably, CeO_2-d exhibits peaks characteristic of carbonate species at 1237, 1131, 997 cm^{-1},[24,34] while the CeO_2 wires exhibit a peak characteristic of bidentate and monodentate carbonates at 1588 cm^{-1} not observed for CeO_2-d.[22] The difference in observed species is likely due to the retained porosity of CeO_2-d. This hypothesis is further supported by comparison of the IR spectra for both samples after SO_2 experiments. The monodentate carbonate peak that is unique to the CeO_2-d remains, but the unique bicarbonate species are no longer present on the CeO_2-d sample, indicating the loss of these unique adsorption sites either through occupation by adsorbed sulfates or through degradation; a hypothesis supported by the 33.9% reduction in defect sites after SO_2 exposure observed

through Raman spectroscopy (Table 4.A.1). In addition, the IR spectra on CeO_2-d very closely resembles the spectra on ceria wires after SO_2 experiments, suggesting CeO_2-d has transformed into a material possessing facets and defects very similar to those found on the ceria wires. Further investigation of this hypothesis with SEM and BET is discussed in the following section. The IR spectra shown in Figure 4.3(a) of CeBTC during CO_2 adsorption before SO_2 adsorption exhibited characteristic peaks at 1165, 1048, 980 cm^{-1} similar to those observed on CeO_2-d indicating the formation of bicarbonate and carbonate species during CO_2 adsorption.[22] After exposure to SO_2, CeBTC exhibits a single carbonate peak at 1123 cm^{-1}.[34] The loss of the peaks observed before SO_2 exposure is correlated with the 100% loss of surface area, leaving only surface sites available for adsorption.

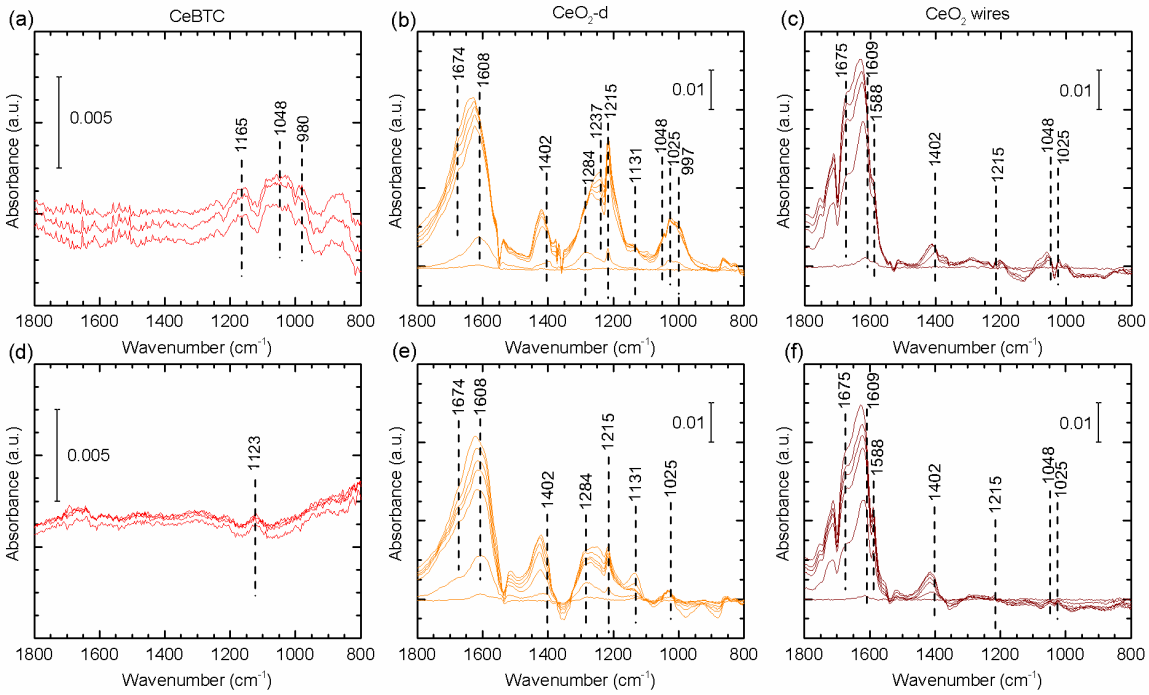

Figure 4.3. IR spectra during 15 minutes of CO_2 adsorption on (a,d) CeBTC, (b,e) CeO_2-d, and (c,f) CeO_2 wires on pristine sample (a-c) and after in situ SO_2 exposure (d-f) at 25 ˚C.

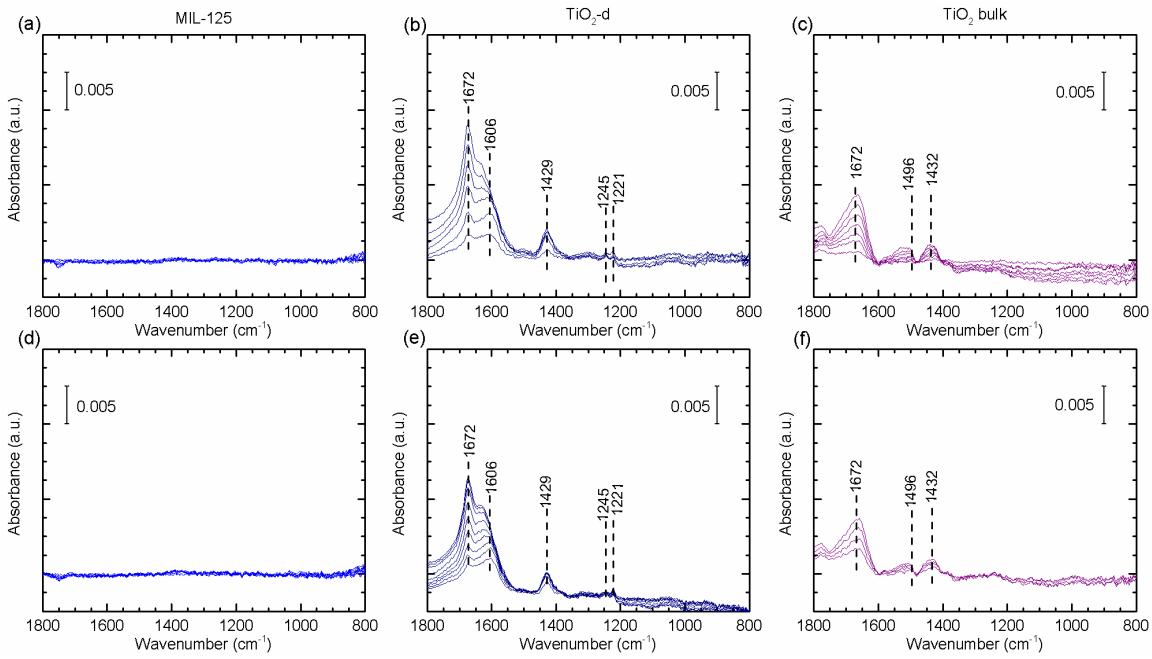

Figure 4.4. IR spectra during different time intervals of CO_2 adsorption on MIL-125, TiO_2-d, and TiO_2 bulk on pristine sample (top) and after in situ SO_2 exposure (bottom) at 25 ˚C.

Figure 4.4 shows the IR spectra during CO_2 adsorption on MIL-125, TiO_2-d, and TiO_2 bulk at room temperature as a function of time both before and after the in situ IR SO_2 experiment. The IR spectra on MIL-125 during CO_2 adsorption exhibits no characteristic adsorption peaks due to the lack of open metal sites. TiO_2-d and TiO_2 bulk exhibit characteristic peaks at 1672 and 1429 cm^{-1} indicating the formation of mono- and bidentate bicarbonates, respectively, originating from the reaction of CO_2 with residual hydroxyl groups.[35] In addition, TiO_2-d exhibits peaks at 1221 and 1245 cm^{-1} indicative of monodentate bicarbonates and a peak at 1606 cm^{-1} that slowly shifts to 1635 cm^{-1} with increasing surface coverage indicative of bidentate bicarbonates not observed for the TiO_2 bulk sample.[35] These species are likely more intense and able to be observed on TiO_2-d due somewhat to the sample being pure anatase, but more importantly the presence of defects inherited through synthesis from the parent MIL-125. The TiO_2 bulk

sample also possesses a band at 1496 cm^{-1} characteristic of bidentate bicarbonates adsorbed on a rutile phase titania,[36,37] demonstrating the mixed-phase titania results in the formation of slightly different species than the pure phase TiO_2-d. There is no loss of species observed for TiO_2-d or TiO_2 bulk after exposure to SO_2; however, the intensity of the adsorbed species does decrease 31% and 14%, respectively, after exposure, indicating a loss of adsorption sites after SO_2 exposure. TiO_2-d possesses double the overall intensity of adsorption over TiO_2 bulk, and experiences approximately double the decrease in intensity due to the loss of retained mesoporosity; a loss directly tied to the degradation of the MOF-like particles observed with SEM and discussed in the following section.

4.2.4 Material stability after SO_2 adsorption

After in situ IR studies, the effect of acid gas exposure was first explored through PXRD analysis. As is known from literature, MOFs are often unstable upon exposure to certain gases and vapors,[38,39] rapidly losing porosity and crystallinity. Comparison of the PXRD patterns taken before and after IR studies for MIL-125 and CeBTC (Figure 4.5) reveals that both materials have not retained their crystallinity and no longer resemble the as-synthesized patterns. The instability of these materials is further confirmed by comparing BET surface areas calculated from N_2 physisorption before and after IR experiments. Both materials experience a drastic loss in surface area attributed to a degradation and loss of the material structure and porosity, 86% for MIL-125 and 100% for CeBTC, as shown in Table 4.1.

Analysis of the oxide materials; however, did not mimic the loss of stability observed for the MOF materials. Comparison of the PXRD patterns for all oxides

revealed no change between the as-synthesized patterns and those taken before IR experiments. Although there was no observed change in the PXRD patterns after acid gas exposure, analysis of the materials' BET surface area revealed changes did occur for the MOF-derived oxide samples. The surface area of CeO_2 wires and TiO_2 bulk did not change after exposure; however, CeO_2-d and TiO_2-d experience a loss in surface area of 10% and 65%, respectively. The large loss in surface area without a corresponding change in the diffraction pattern indicates a loss of the retained porosity in the MOF-derived oxide particle, as illustrated in Figure 4.A.2, reducing the surface area without greatly affecting the crystal structure.

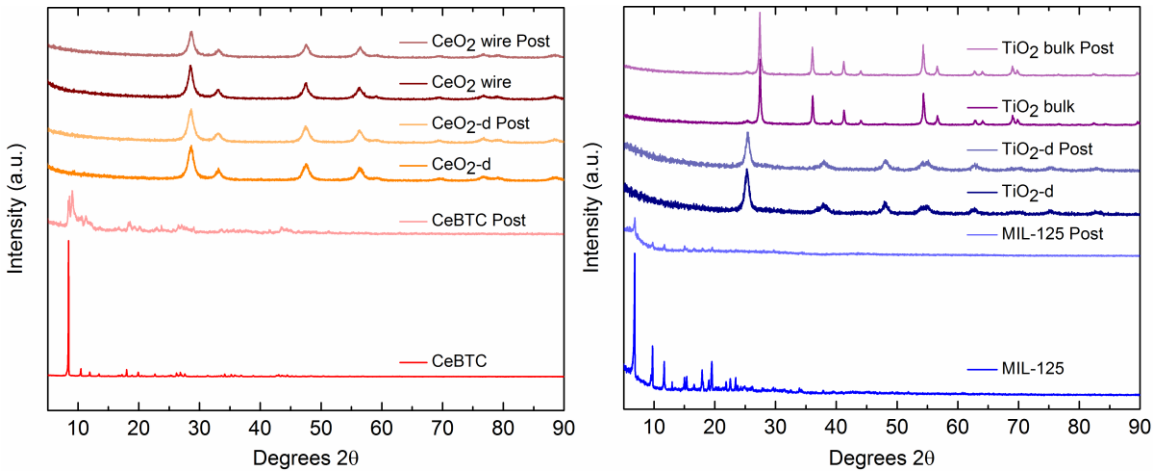

Figure 4.5. PXRD patterns of (left) CeBTC as-synthesized, CeBTC after SO_2 exposure, CeO_2-d as-synthesized, CeO_2-d after SO_2 exposure, CeO_2 wire as-synthesized, CeO_2 wires after SO_2 exposure, and (right) MIL-125 as-synthesized, MIL-125 after SO_2 exposure, TiO_2-d as-synthesized, TiO_2-d after SO_2 exposure, TiO_2 bulk, TiO_2 bulk after SO_2 exposure.

In order to explore if a visual change to the particles could further confirm this hypothesis, SEM and TEM images were taken of all samples before and after in situ IR experiments. Figure 4.6 shows the SEM images of titanium containing samples before and after in situ IR experiments, while Figure 4.A.6-8 contains

TEM images for these samples before and after in situ IR experiments. Figure 4.6(a) and Figure 4.A.6(a,d) show the characteristic terminated octahedral crystal

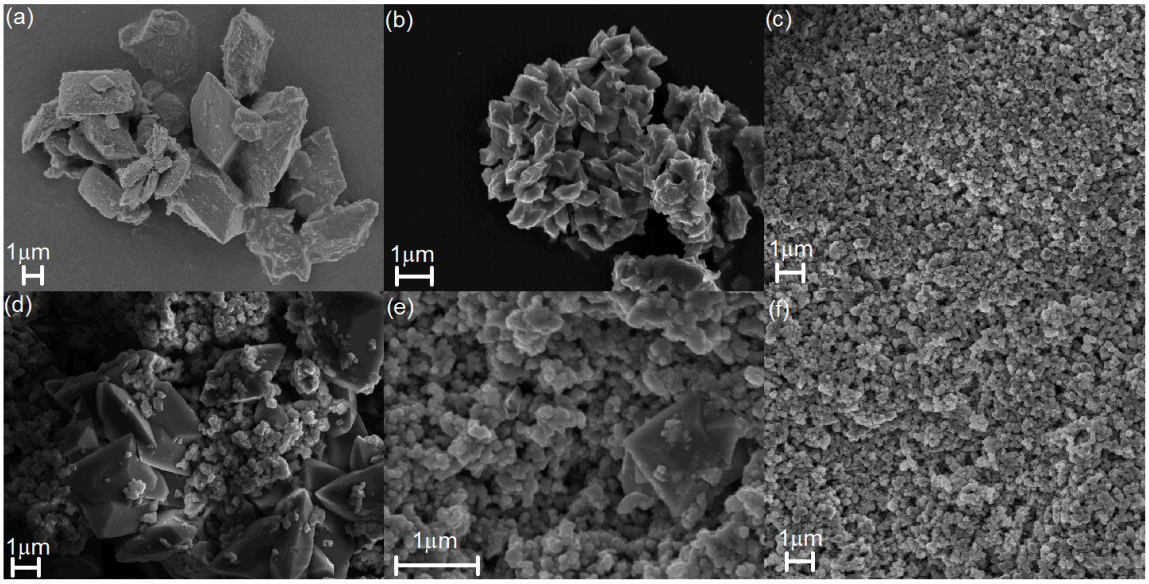

Figure 4.6. SEM images of (a) MIL-125, (b) TiO_2-d, (c) TiO_2 bulk before IR experiments, and (d) MIL-125, (e) TiO_2-d, (f) TiO_2 bulk after IR experiments.

of MIL-125. TiO_2-d retains this overall particle structure in Figure 4.6(b) and Figure 4.A.7(a,d) as seen in literature.[5,10] While the macroscopic particle morphology is retained, a loss of volume is observed upon preparation of the MOF-derived oxide, as expected. Figure 4.6(c) and Figure 4.A.8(a,d) show TiO_2 bulk is composed of small agglomerates. Figure 4.6(d-f) are SEM images of the titanium containing samples after in situ IR experiments. It can be observed from comparison of Figure 4.6(c,f) that the TiO_2 bulk sample does not undergo any change to the overall particle structure after acid gas exposure, further supporting the hypothesis that the TiO_2 bulk is not degraded by exposure to SO_2. Instead, the 22% reduction in CO_2 capacity (calculated in Table 4.A.2) is likely due to retention of strongly bound SO_x species even after desorption and TPD in He. A comparison of the images before and after exposure for MIL-125 yields the observation of the evolution of small agglomerates resembling the morphology of

bulk TiO_2 particles. In addition, close inspection of the SEM and TEM images reveals several instances of the creation of cavity defects in the MIL-125 crystal. These cavity defects are centered on the crystal edges where the surface is the most uncoordinated and presumably allows for the strongest surface adsorption of acid gas molecules. The creation of these defects leads to an increase in uncoordinated sites where SO_2 can strongly adsorb, allowing the degradation to propagate throughout the crystal. Furthermore, the degradation can be observed at different stages of progression in the image. In the upper right hand corner of Figure 4.6(d), a crystal can be seen with a cavity defect that has begun at the corner of the particle and propagated along the face, while to the left, a particle is seen that has undergone much more degradation and has formed many more small agglomerates. This degradation and loss of material structure results in a loss in CO_2 adsorption capacity as illustrated by the reduction in quantity adsorbed after IR experiments shown by the isotherms in Figure 4.A.9. It is observed for TiO_2-d that the retained particle structure has been lost upon exposure to acid gases as the sample is mainly comprised of the agglomerates seen in the bulk TiO_2 sample. However, observation of one of the few remaining particles gives a glimpse into the degradation of the macroscopic particle and it is seen to be identical to the mechanism observed for a MIL-125 crystal. A small cavity defect has formed at the corner of the octahedral particle as well as a small agglomerate as the structured particle dissolves upon exposure. Additional SEM images shown in Figure 4.A.10(a-e) illustrate the almost complete degradation of the TiO_2-d particles to form small agglomerates after exposure to SO_2 during in situ IR experiments. One important difference to note between the agglomerates observed in the MIL-125 sample after exposure and those in the TiO_2 samples is that those observed in the MOF sample cannot yet be identified, while those in the

TiO_2-d are crystalline TiO_2. Although visually similar, this difference is supported by the lack of evolution of any reflections characteristic of TiO_2 in the PXRD pattern of MIL-125 after IR experiments. However, these reflections might be low in intensity and hidden by the still relatively intense reflections of degraded MIL-125.

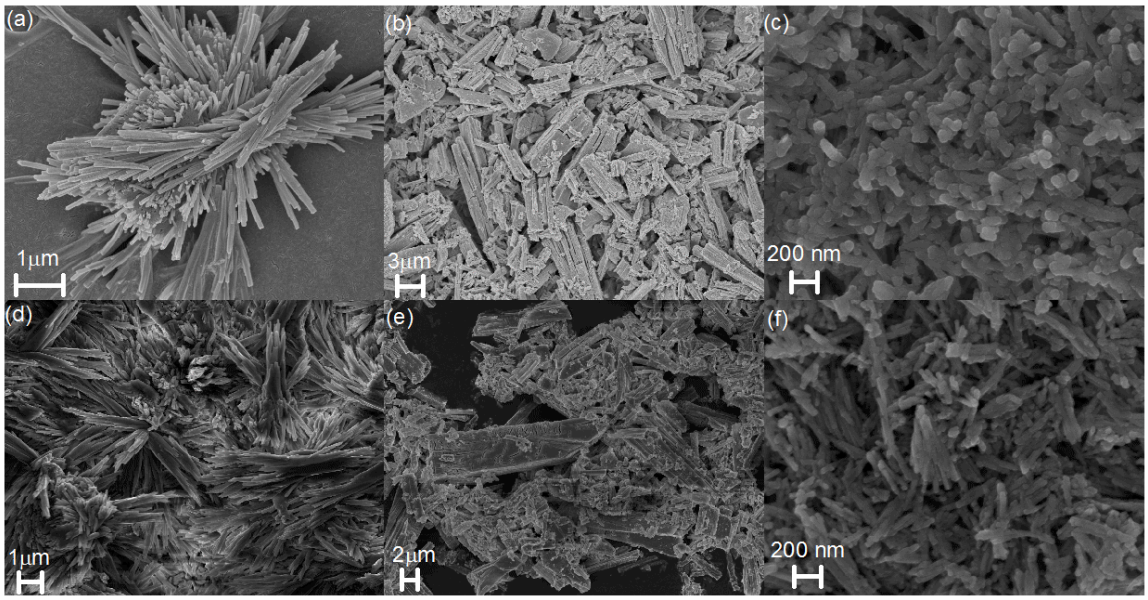

Figure 4.7. SEM images of (a) CeBTC, (b) CeO_2-d, (c) CeO_2 wires before IR experiments, and (d) CeBTC, (e) CeO_2-d, (f) CeO2 wires after IR experiments.

SEM and TEM images of cerium containing samples before and after in situ IR experiments are shown in Figure 4.7 and Figure 4.A.11-13, respectively. Figure 4.7(a) shows rod shaped crystals characteristic of CeBTC. The CeO_2-d species is seen to retain this overall particle structure in Figure 4.7(b), but as with TiO_2-d the macroscopic particle structure is retained with a corresponding loss of volume. Figure 4.7(c) shows the CeO_2 wires, displaying characteristic small wire shaped particles. SEM images of the cerium containing samples after in situ IR experiments are shown in Figure 4.7(d-f). As with the bulk TiO_2, comparison of the CeO_2 wires in Figure 4.7(c,f) and in the TEM images in Figure 4.A.13 shows that the sample does not undergo any change to the overall particle structure after

acid gas exposure, supporting the hypothesis that the synthesized oxides are not degraded by exposure to SO_2. Instead, the 10.9% reduction in CO_2 adsorption capacity (Table 4.A.2) is likely due to retention of SO_x species even after desorption and TPD in He. CeBTC particles after SO_2 exposure in Figure 4.7(d) resemble the overall morphology of the original material; however, the particles have agglomerated and have softened edges, suggesting a mechanism for degradation similar to MIL-125, where the most uncoordinated edge sites are attacked by SO_2 during adsorption. Figure 4.A.11(b,e) display the degradation of the CeBTC particle edges, with small fissures forming after SO_2 exposure. CeO_2-d particles, on the other hand, seem to retain a somewhat rod-like morphology even after acid gas exposure, and only a 2.3% reduction in CO_2 capacity is observed (Table 4.A.2) with little to no change in the CO_2 breakthrough time shown in Figure 4.A.14. The retention of this morphology is probable given that rod shaped ceria has been synthesized previously.[22,32] However, comparison of CeO_2-d before and after experiment reveals the formation of cracks and fissures in the rod shaped particles and that some of the larger rod shaped particles have broken apart after exposure to form smaller rod shaped particles. This observation is explained by the high number of defects in the MOF-derived oxide allowing numerous sites for SO_2 adsorption and the propagation of already existing cracks to break apart the larger rods and form smaller particles. It is important to note that the degradation of the samples is unlikely solely due to the TPD step during each segment of the experiment. The oxide materials showed less than 2 wt.% loss during TGA as shown in Figure 4.A.15. For the MOF materials, the chosen TPD temperature is well below the known upper stability limit, illustrated by a large wt.% loss in Figure 4.A.15. However, the addition of heat and the presence of adsorbed SO_2 species likely hasten the degradation process. Additional studies

are necessary to determine the kinetics of the degradation mechanism and how the addition of heat or additional acid gases will affect the speed of the degradation.

4.2.5 Effect of water adsorption on material stability

Material stability and degradation in the presence of water vapor has been a widely explored topic within MOF literature.[39] Therefore, in order to explore similarities between degradation observed during acid gas exposure presented in the previous section and that observed during water exposure, each sample was characterized as above after water adsorption isotherms were collected. Water adsorption isotherms for cerium and titanium containing samples are shown in Figure 4.A.16. As expected, the oxide materials do possess the high water adsorption observed for the MOF materials. The difference in adsorbed amount is due to the high porosity of the MOF materials and the ability of water to cluster in the pores. Both MOF materials possess an approximately linear increase in adsorption as the relative water pressure is increased; however, MIL-125 desorbs the majority of the water adsorbed during the experiment while CeBTC possesses a much larger hysteresis and retains 17 mmol/g of water after desorption. As CeBTC possesses open metal sites, water is strongly adsorbed and will not desorb during evacuation without heating.

SEM and TEM images of both cerium and titanium containing samples after water adsorption experiments are shown in Figure 4.A.17 and Figure 4.A.6-12 (c,f), respectively. Figure 4.A.17(a) and Figure 4.A.11(c,f) show that the rod shaped crystals of CeBTC become softened after water adsorption; however, the change in morphology is not as drastic as observed after SO_2 exposure. N_2 physisorption and PXRD analysis after water adsorption revealed a drastic loss of

surface area, 93%, and a reduction in the intensity of reflections during diffraction experiments supporting the similar effects of water exposure and SO_2 exposure for CeBTC. The CeO_2-d sample shown in Figure 4.A.17(b) possesses numerous cracks and fissures in particles as well as a corresponding loss of surface area attributed to a loss of porosity after water exposure (Table 4.1); however, as with the CeBTC sample, the degree to which degradation has occurred is seemingly less than with SO_2 as there is much less formation of smaller rod shaped particles. CeO_2 wires continue to maintain their morphology after water exposure, confirming the particles are stable after water exposure due to their preparation via hydrothermal treatment.

MIL-125 after water adsorption is shown in Figure 4.A.17(d) and Figure 4.A.6(c,f). The crystals do not display the cavities seen in the sample after SO_2 exposure, but instead a roughening and etching of the crystal surface is observed. This observation suggests that, similar to the CeBTC crystals, the degradation of the MIL-125 particles is proceeding at a much slower rate upon exposure to water over the day long isotherm run than that observed after 15 minutes of 15 ppm SO_2 exposure. This hypothesis is further supported by PXRD and BET analysis, where some crystallinity is retained (Figure 4.A.18, A19) and a less drastic loss of surface area is observed (Table 4.1). The TiO_2-d species; however, does possess the cavities seen to evolve after exposure to SO_2 as well as the corresponding decrease in surface area, 133 to 51 m^2/g, suggesting the degradation mechanism proceeds through the same pathway for both SO_2 and H_2O adsorption for the derived titania sample. Furthermore, the majority of TiO_2-d has transformed from the octahedral shaped particles to the small agglomerates observed for the bulk TiO_2. As was expected, the bulk TiO_2 did not undergo any change in morphology, surface area, or diffraction pattern after water adsorption experiments.

4.3 Conclusions

In conclusion, we have investigated the effect of acid gas adsorption on a set of cerium and titanium MOFs, MOF-derived oxides, and oxides with IR spectroscopy, SEM, and TEM imaging. MOF-derived oxides were studied to create a link between the morphology of the parent MOF and the composition of the oxide, and gain insight into adsorbed species and possible degradation mechanisms. Adsorbed species on both parent MOFs could be directly correlated with observed adsorbed species on the MOF-derived oxide material. The retained porosity and inherent defects of CeO_2-d changed the nature of species adsorbed, as well as enhanced the overall strength of adsorption of both SO_2 and CO_2. Although neither TiO_2-d nor the bulk TiO_2 strongly adsorbed SO_x species, an increase in overall adsorption of the acid gases studied was observed for TiO_2-d, explained by the retained porosity during formation of the MOF-derived oxide. Insight into the degradation mechanism was developed through SEM and TEM imaging of samples before and after acid gas exposure. For MIL-125 and TiO_2-d samples, exposure to SO_2 or H_2O resulted in the formation of cavity defects on the particle edge. It is hypothesized that the formation of these defects is due to the porous nature of the samples, the attack and degradation of the material begins at an uncoordinated edge and quickly propagates through the particle as the acid gas is able to penetrate into the particle. For CeBTC and CeO_2-d samples, similar exposure resulted in a softening of particle edges, and for the MOF-derived oxide the breaking of particles into smaller particles along pre-existing cracks and fissures.

4.4 References

(1) Wu, Z.; Li, M.; Howe, J.; Meyer, H. M.; Overbury, S. H. *Langmuir* **2010**, *26*, 16595.

(2) Im, J. H.; Ko, N.; Yang, S. J.; Park, H. J.; Kim, J.; Park, C. R. *New J. Chem.* **2014**, *38*, 2752.

(3) Vaesen, S.; Guillerm, V.; Yang, Q.; Wiersum, A. D.; Marszalek, B.; Gil, B.; Vimont, A.; Daturi, M.; Devic, T.; Llewellyn, P. L.; Serre, C.; Maurin, G.; De Weireld, G. *Chem. Commun.* **2013**, *49*, 10082.

(4) Mu, W.; Huang, X.; Zhong, R.; Xia, W.; Liu, J.; Zou, R. *CrystEngComm* **2015**, *17*, 1637.

(5) Im, J. H.; Kang, E.; Yang, S. J.; Park, H. J.; Kim, J.; Park, C. R. *Bull. Korean Chem. Soc.* **2014**, *35*, 2477.

(6) Walton, K. S.; Snurr, R. Q. *J. Am. Chem. Soc.* **2007**, *129*, 8552.

(7) Wu, Z.; Dai, S.; Overbury, S. H. *J. Phys. Chem. C* **2010**, *114*, 412.

(8) Gustafsson, M.; Bartoszewicz, A.; Martín-Matute, B.; Sun, J.; Grins, J.; Zhao, T.; Li, Z.; Zhu, G.; Zou, X. *Chem. Mater.* **2010**, *22*, 3316.

(9) Dan-Hardi, M.; Serre, C.; Frot, T.; Rozes, L.; Maurin, G.; Sanchez, C.; Férey, G. *J. Am. Chem. Soc.* **2009**, *131*, 10857.

(10) Wang, Z. Q.; Li, X.; Xu, H.; Yang, Y.; Cui, Y. J.; Pan, H. G.; Wang, Z. Y.; Chen, B. L.; Qian, G. D. *J. Mater. Chem. A* **2014**, *2*, 12571.

(11) Cotton, F. A.; Wilkinson, G.; Bochmann, M.; Murillo, C. A. *Advanced Inorganic Chemistry*; Wiley, 1999.

(12) Luo, T.; Gorte, R. J. *Appl. Catal., B* **2004**, *53*, 77.

(13) Waqif, M.; Bazin, P.; Saur, O.; Lavalley, J. C.; Blanchard, G.; Touret, O. *Appl. Catal., B* **1997**, *11*, 193.

(14) Luo, T.; Vohs, J. M.; Gorte, R. J. *J. Catal.* **2002**, *210*, 397.

(15) Morrow, B. A.; McFarlane, R. A.; Lion, M.; Lavalley, J. C. *J. Catal.* **1987**, *107*, 232.

(16) Saur, O.; Bensitel, M.; Saad, A. B. M.; Lavalley, J. C.; Tripp, C. P.; Morrow, B. A. *J. Catal.* **1986**, *99*, 104.

(17) Morterra, C.; Cerrato, G.; Bolis, V. *Catal. Today* **1993**, *17*, 505.

(18) Morterra, C.; Cerrato, G.; Emanuel, C.; Bolis, V. *J. Catal.* **1993**, *142*, 349.

(19) Liu, J.; Li, X. Y.; Zhao, Q. D.; Hao, C.; Wang, S. B.; Tade, M. *ACS Catal.* **2014**, *4*, 2426.

(20) Colthup, N. B.; Daly, L. H.; Wiberley, S. E. *Introduction to Infrared and Raman Spectroscopy*; Elsevier Science, 1990.

(21) Lavalley, J. C. *Catal. Today* **1996**, *27*, 377.

(22) Wu, Z.; Mann, A. K. P.; Li, M.; Overbury, S. H. *J. Phys. Chem. C* **2015**, *119*, 7340.

(23) Binet, C.; Daturi, M.; Lavalley, J.-C. *Catal. Today* **1999**, *50*, 207.

(24) Vayssilov, G. N.; Mihaylov, M.; Petkov, P. S.; Hadjiivanov, K. I.; Neyman, K. M. *J. Phys. Chem. C* **2011**, *115*, 23435.

(25) Lu, Z.; Müller, C.; Yang, Z.; Hermansson, K.; Kullgren, J. *J. Chem. Phys.* **2011**, *134*, 184703.

(26) Tumuluri, U.; Li, M.; Cook, B. G.; Sumpter, B.; Dai, S.; Wu, Z. *J. Phys. Chem. C* **2015**, *119*, 28895.

(27) Tan, K.; Canepa, P.; Gong, Q.; Liu, J.; Johnson, D. H.; Dyevoich, A.; Thallapally, P. K.; Thonhauser, T.; Li, J.; Chabal, Y. J. *Chem. Mater.* **2013**, *25*, 4653.

(28) Tan, K.; Zuluaga, S.; Gong, Q.; Gao, Y.; Nijem, N.; Li, J.; Thonhauser, T.; Chabal, Y. J. *Chem. Mater.* **2015**, *27*, 2203.

(29) Ziolek, M.; Kujawa, J.; Saur, O.; Aboulayt, A.; Lavalley, J. C. *J. Mol. Catal. A: Chem.* **1996**, *112*, 125.

(30) Xu, W.; He, H.; Yu, Y. *J. Phys. Chem. C* **2009**, *113*, 4426.

(31) Finos, G.; Collins, S.; Blanco, G.; del Rio, E.; Cíes, J. M.; Bernal, S.; Bonivardi, A. *Catal. Today* **2012**, *180*, 9.

(32) Wu, Z.; Li, M.; Overbury, S. H. *J. Catal.* **2012**, *285*, 61.

(33) Li, C.; Sakata, Y.; Arai, T.; Domen, K.; Maruya, K.-i.; Onishi, T. *J. Chem. Soc., Faraday Trans.* **1989**, *85*, 1451.

(34) Li, C.; Sakata, Y.; Arai, T.; Domen, K.; Maruya, K.-i.; Onishi, T. *J. Chem. Soc., Faraday Trans.* **1989**, *85*, 929.

(35) Mino, L.; Spoto, G.; Ferrari, A. M. *J. Phys. Chem. C* **2014**, *118*, 25016.

(36) Jackson, P.; Parfitt, G. D. *J. Chem. Soc., Faraday Trans.* **1972**, *68*, 896.

(37) Liao, L. F.; Lien, C. F.; Shieh, D. L.; Chen, M. T.; Lin, J. L. *J. Phys. Chem. B* **2002**, *106*, 11240.

(38) Han, S. G.; Huang, Y. G.; Watanabe, T.; Nair, S.; Walton, K. S.; Sholl, D. S.; Meredith, J. C. *Micro. Meso. Mater.* **2013**, *173*, 86.

(39) Burtch, N. C.; Jasuja, H.; Walton, K. S. *Chem. Rev.* **2014**, *114*, 10575.

APPENDIX 4.A

Ce AND Ti MATERIAL CHARACTERIZATION

Experimental Section

Chemicals: Cerium nitrate hexahydrate ($Ce(NO_3)_3 \cdot 6H_2O$, Sigma Aldrich, 99%), 1,3,5 benzene-tricarboxylic acid (Sigma Aldrich, 98%), TiOiPr (Sigma Aldrich, 99%), benzene-1,4-dicarboxylic acid (Sigma Aldrich, 98%), MeOH (methanol, Sigma Aldrich, 99.5%), DMF (*n,n*-dimethylformamide, Sigma Aldrich, 99%), and deionized water were used as received.

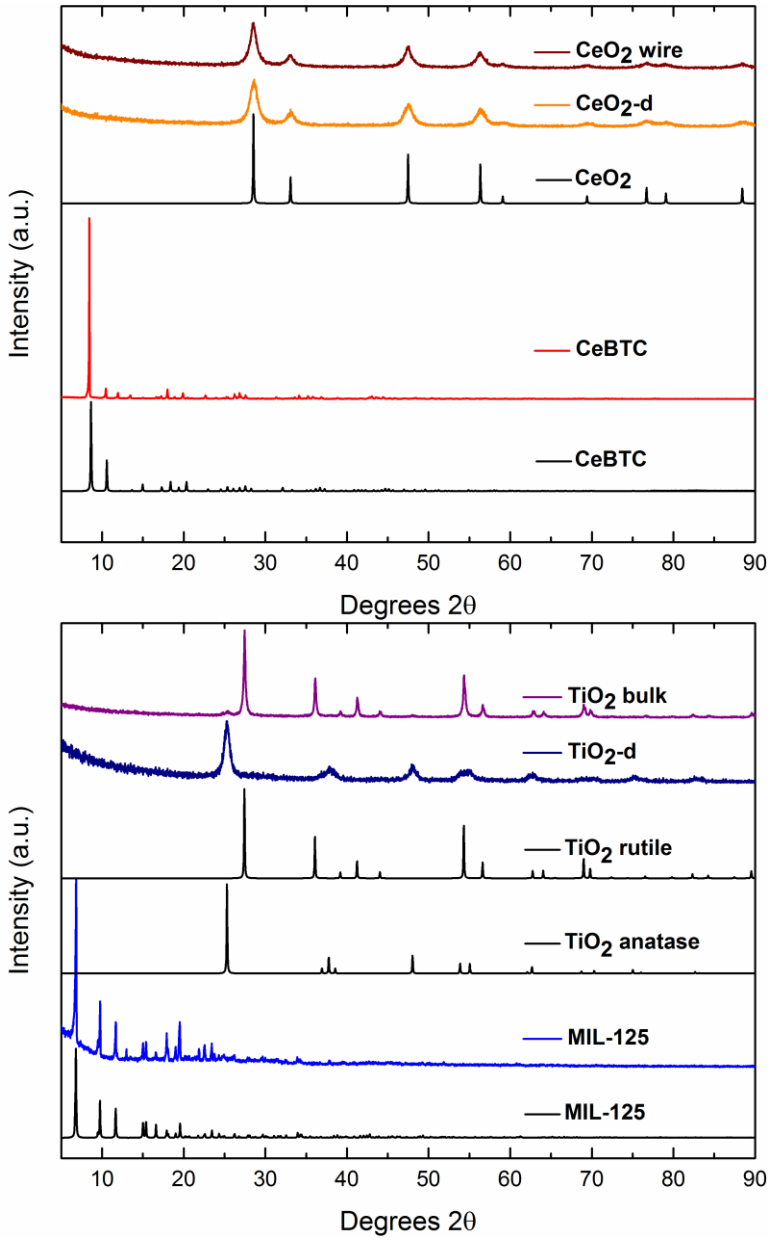

Figure 4.A.1. PXRD patterns of CeBTC simulated (black), CeBTC as-synthesized (red), CeO_2 simulated (black), CeO_2-d as-synthesized (orange), CeO_2 wire as-synthesized (dark red), MIL-125 simulated (black), MIL-125 as-synthesized (blue), TiO_2 anatase simulated (black), TiO_2 rutile simulated (black), TiO_2-d as-synthesized (navy), TiO_2 bulk (purple).

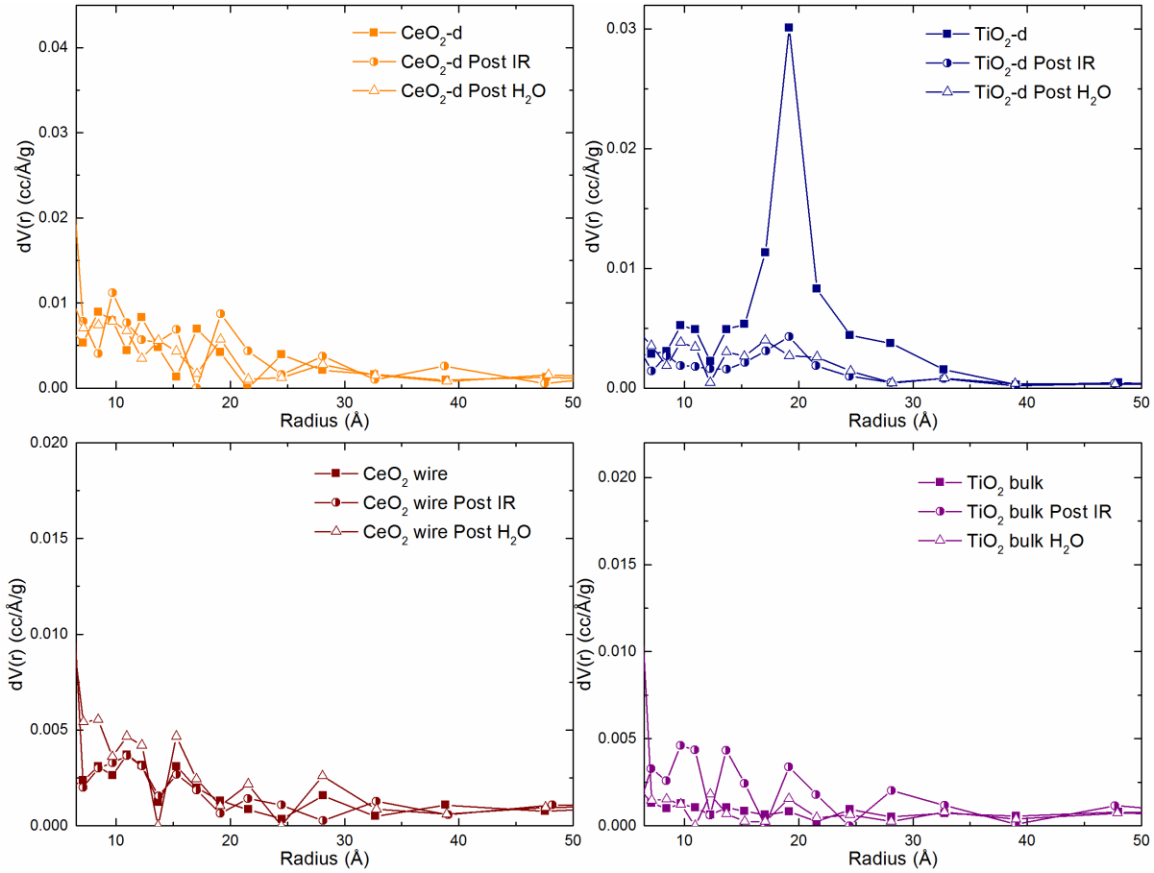

Figure 4.A.2. Pore size distribution for CeO_2-d, CeO_2 wires, TiO_2-d, and bulk TiO_2.

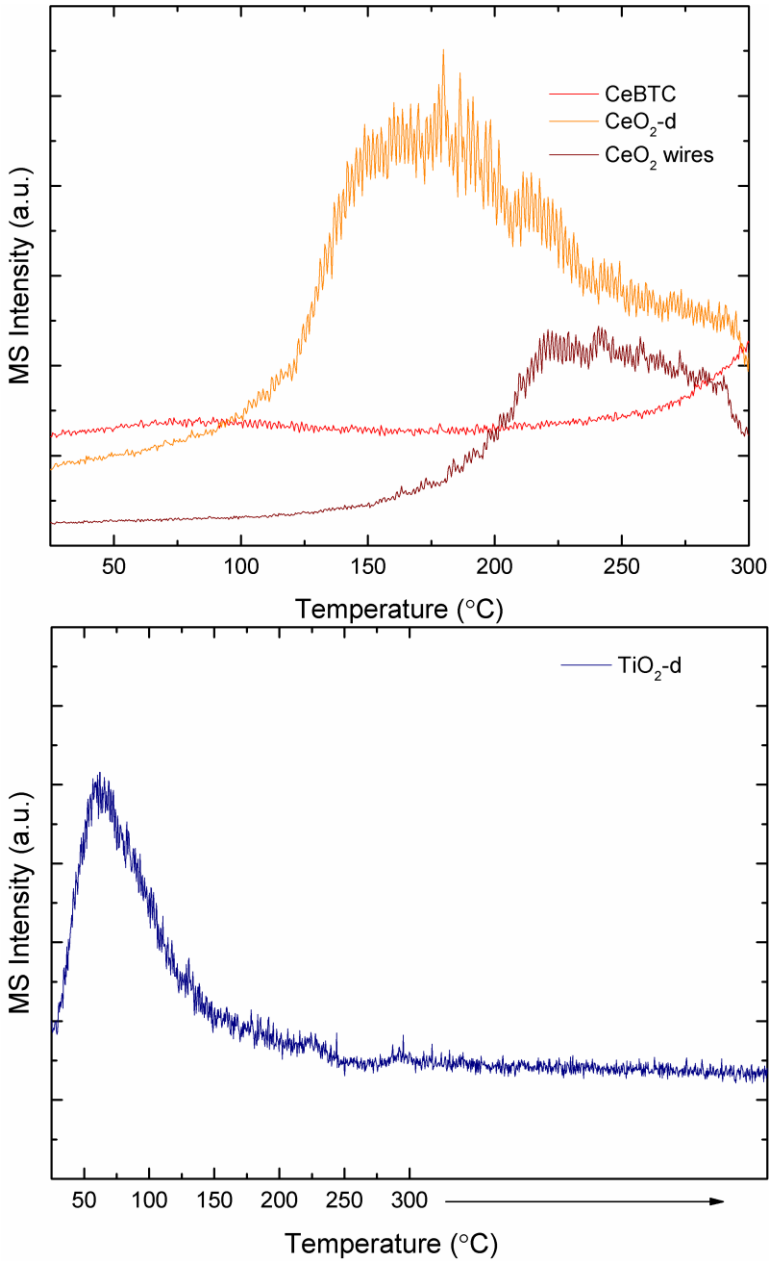

Figure 4.A.3. MS intensity for CO_2 during SO_2 TPD for CeBTC, CeO_2-d, CeO_2 wires and TiO_2-d.

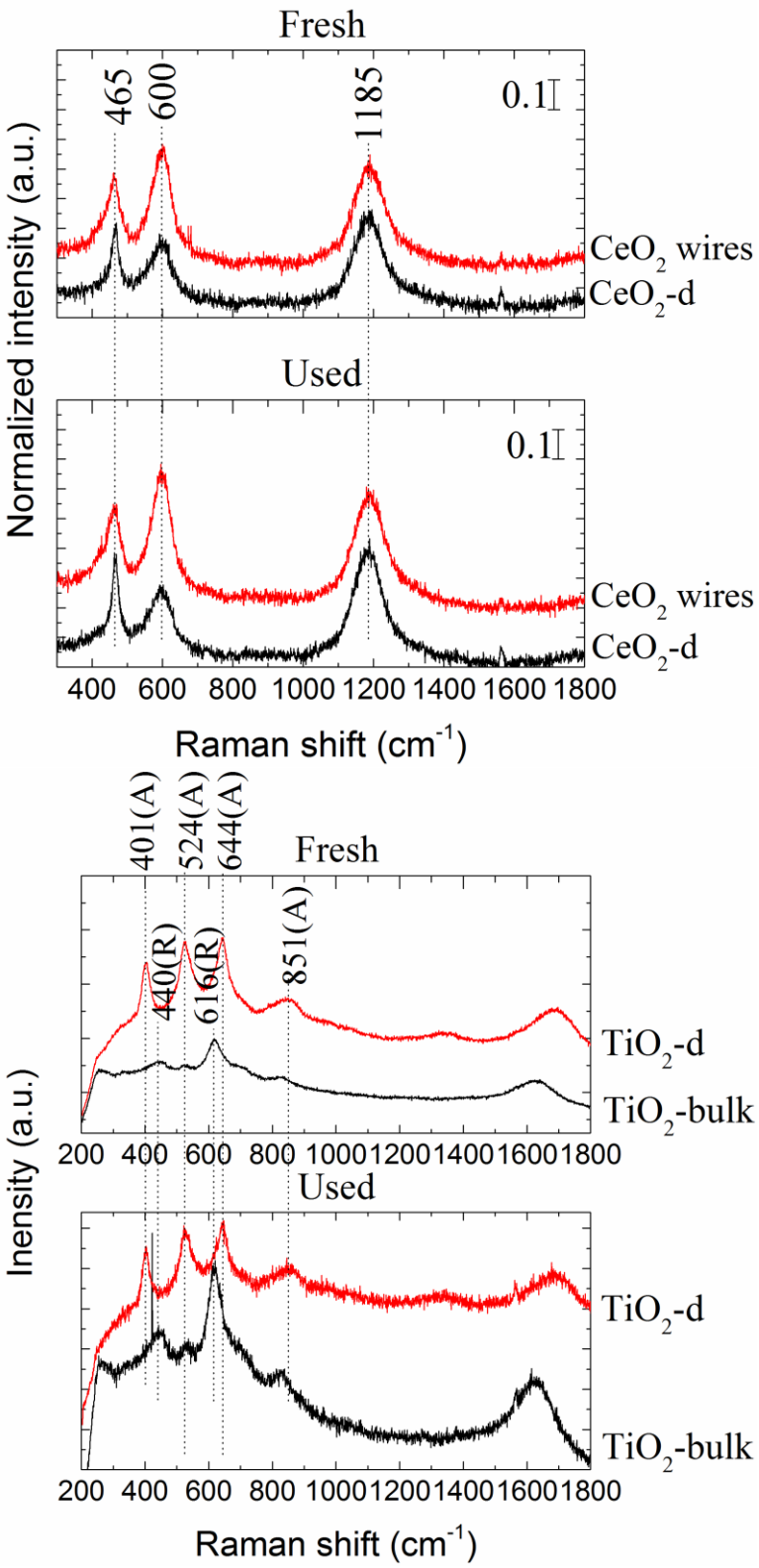

Figure 4.A.4. Raman spectra (λ=532 nm) for CeO_2-d, CeO_2 wires and TiO_2-d, TiO_2 bulk before and after SO_2 exposure.

Table 4.A.1. Analysis of material defects from Raman spectra

Material	465 cm^{-1}	600 cm^{-1}	Defect Ratio	%Change in Defect Ratio
CeO_2-d Pre	5.50431	12.09849	2.20	
CeO_2-d Post	9.27486	13.47688	1.45	33.89205
CeO_2 wires Pre	10.28294	23.53605	2.29	
CeO_2 wires Post	11.09493	23.6817	2.13	6.74502

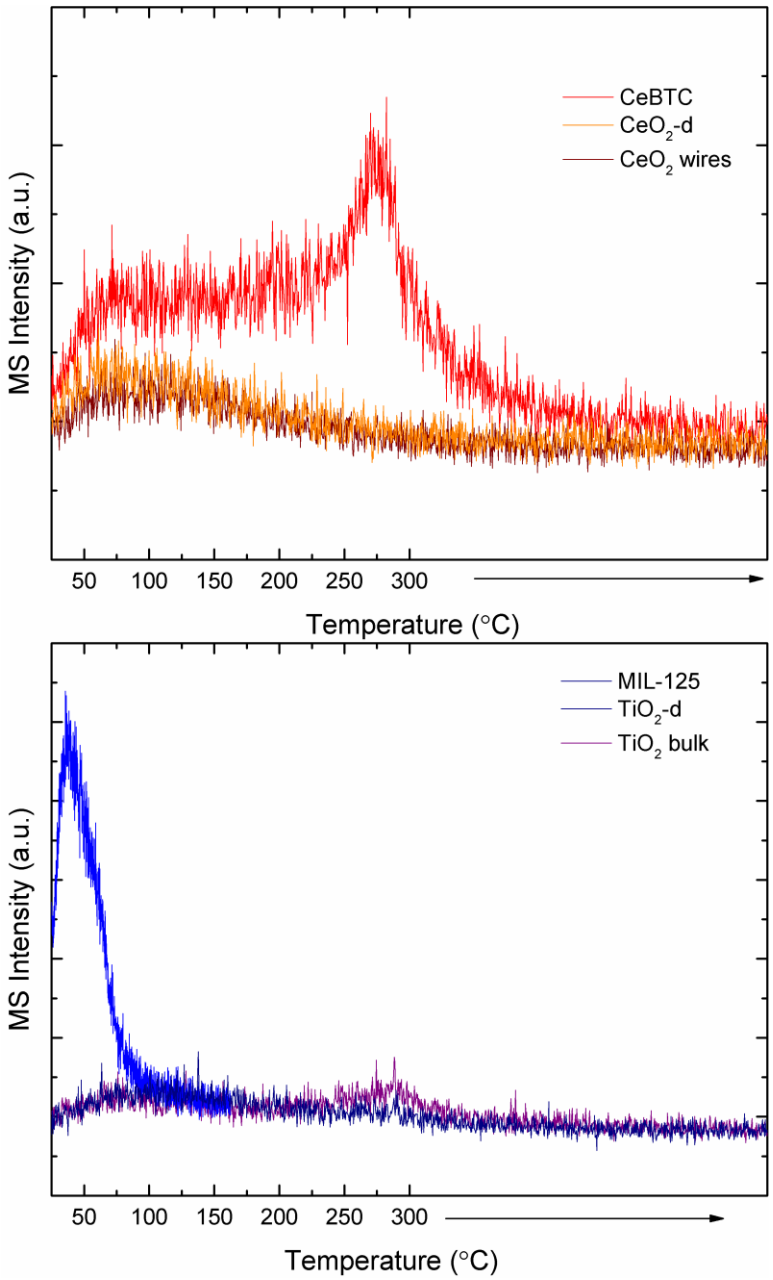

Figure 4.A.5. SO_2 TPD curves for CeBTC, CeO_2-d, CeO_2 wires and MIL-125, TiO_2-d, TiO_2 bulk.

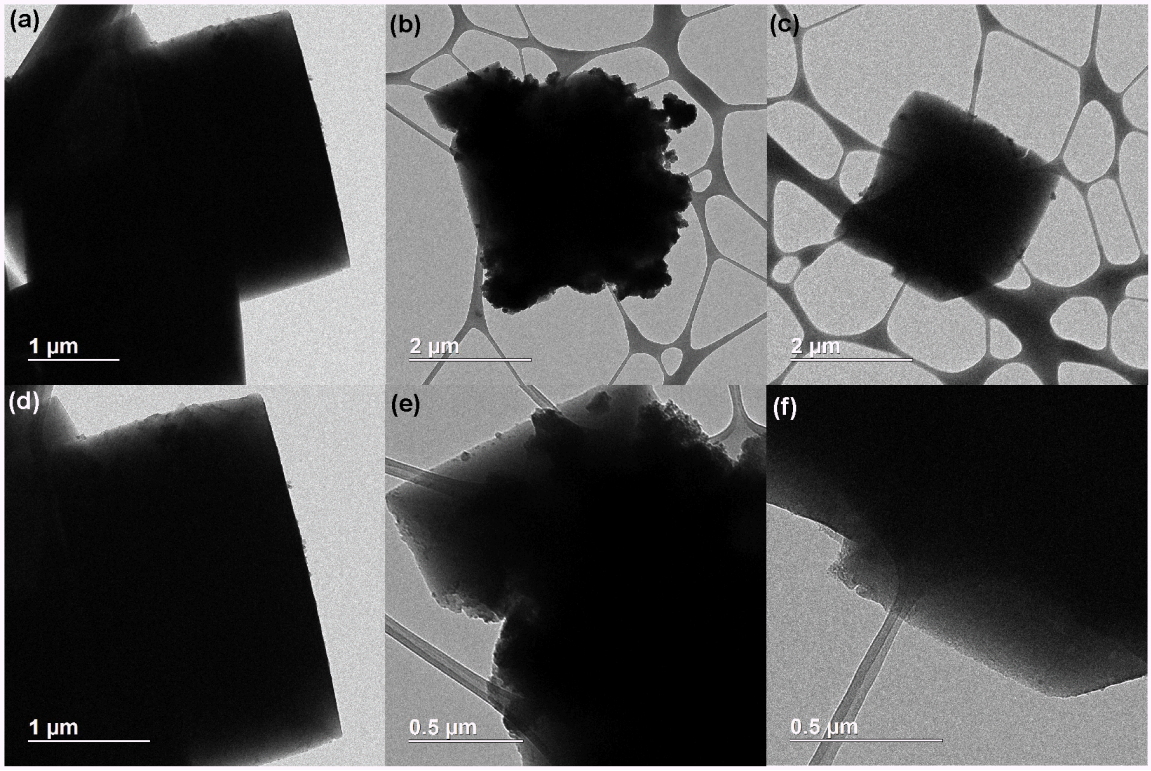

Figure 4.A.6. TEM images of MIL-125. (a,d) fresh sample, (b,e) post CO_2/SO_2 exposure, (c,f) after water adsorption experiments.

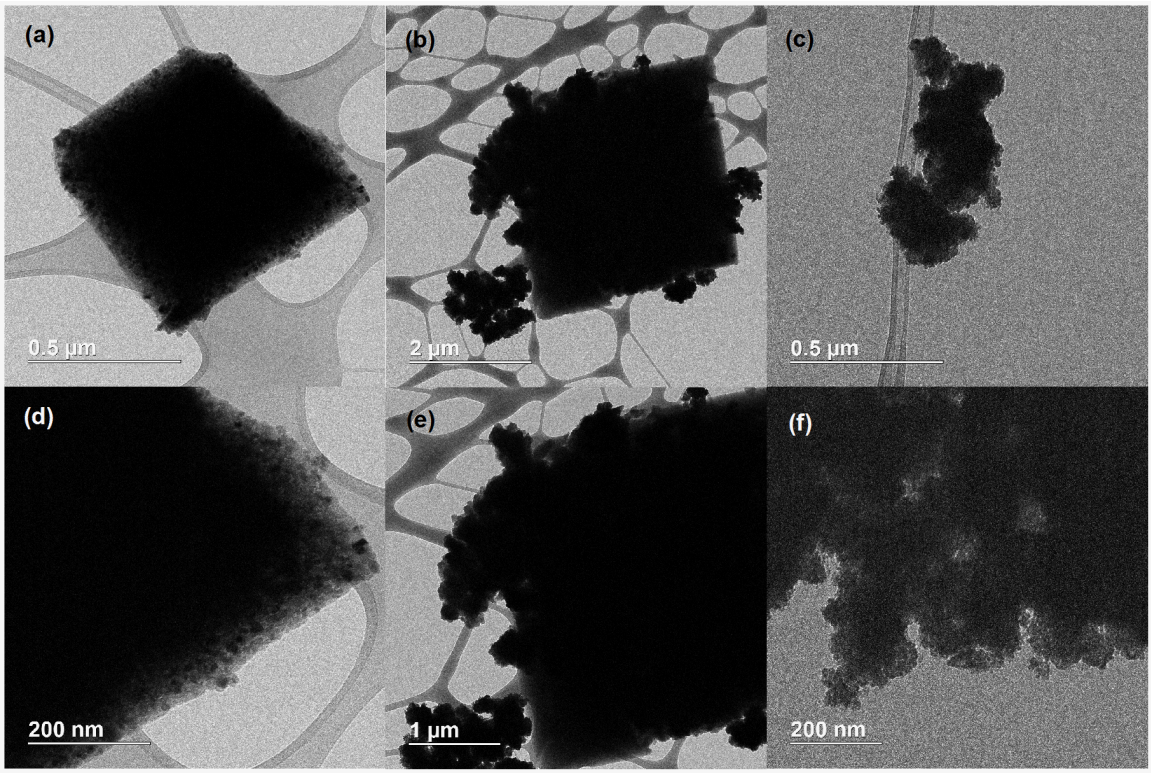

Figure 4.A.7. TEM images of TiO_2-d. (a,d) fresh sample, (b,e) post CO_2/SO_2 exposure, (c,f) after water adsorption experiments.

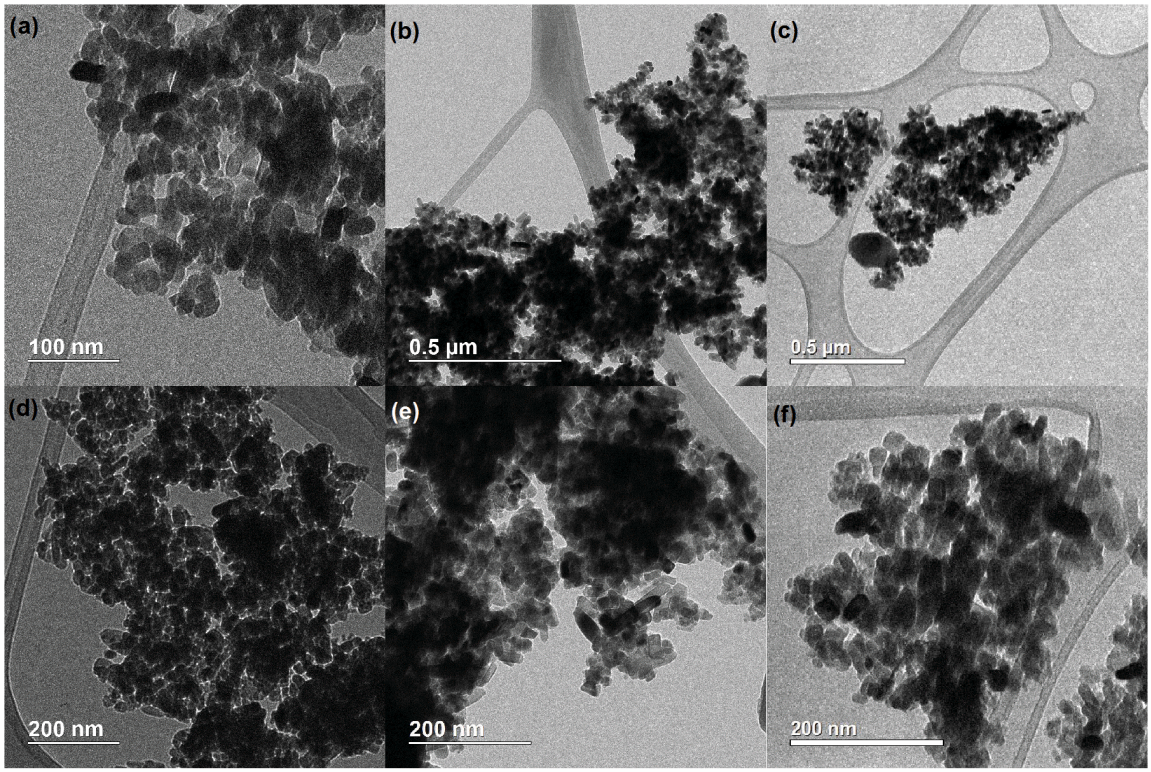

Figure 4.A.8. TEM images of TiO_2 bulk. (a,d) fresh sample, (b,e) post CO_2/SO_2 exposure, (c,f) after water adsorption experiments.

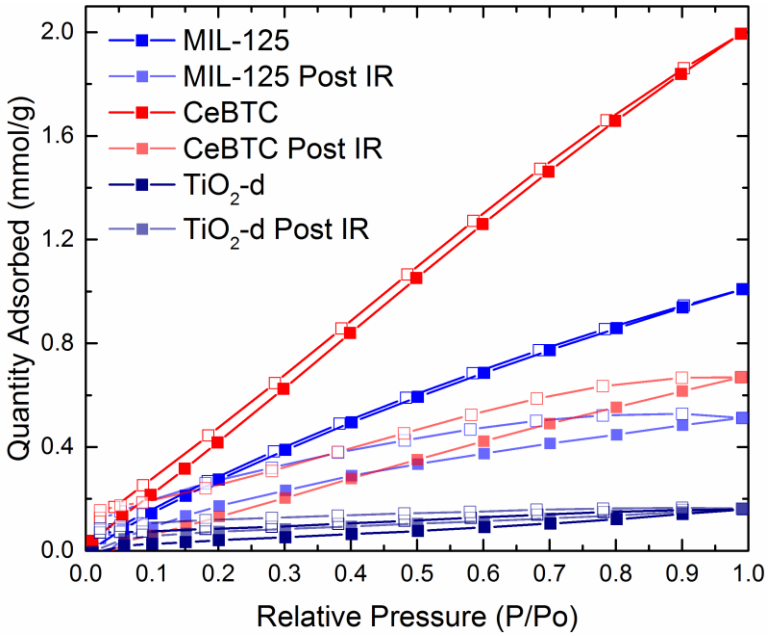

Figure 4.A.9. CO_2 adsorption isotherms for MIL-125, TiO_2-d, and CeBTC before (squares) and after (light squares) IR experiments. Closed symbols are adsorption points, open symbols are desorption points. P_0 = 760 mmHg

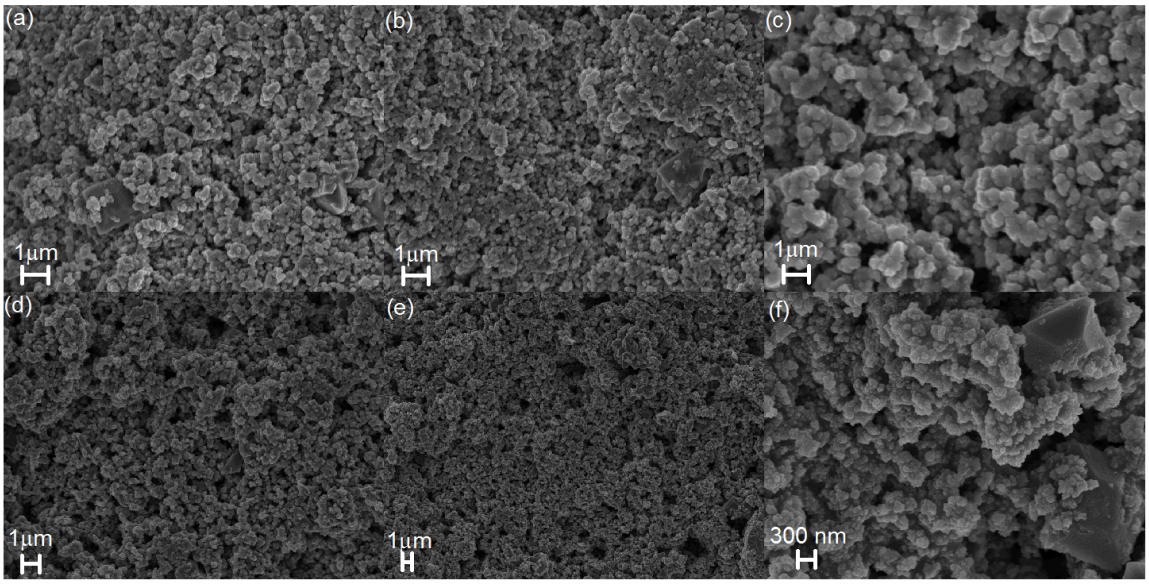

Figure 4.A.10. SEM images of TiO_2-d after (a-e) CO_2/SO_2 exposure, (f) after water adsorption experiments.

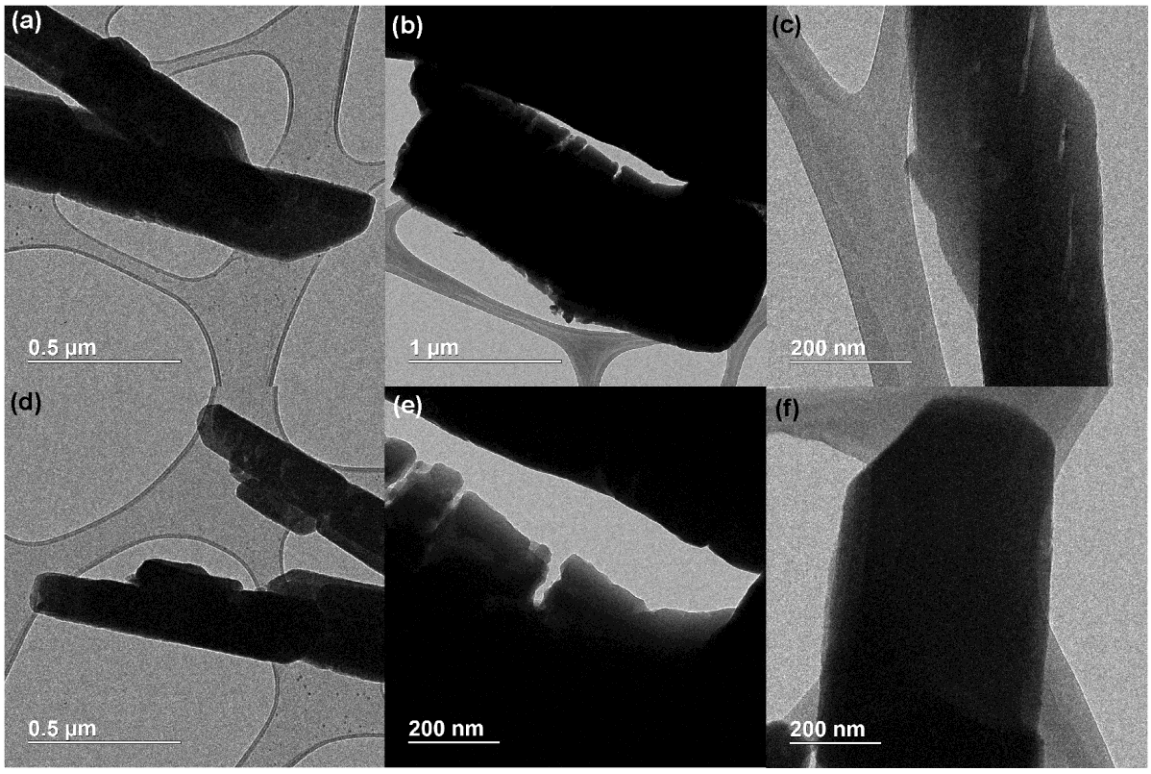

Figure 4.A.11. TEM images of CeBTC. (a,d) fresh sample, (b,e) post CO_2/SO_2 exposure, (c,f) after water adsorption experiments.

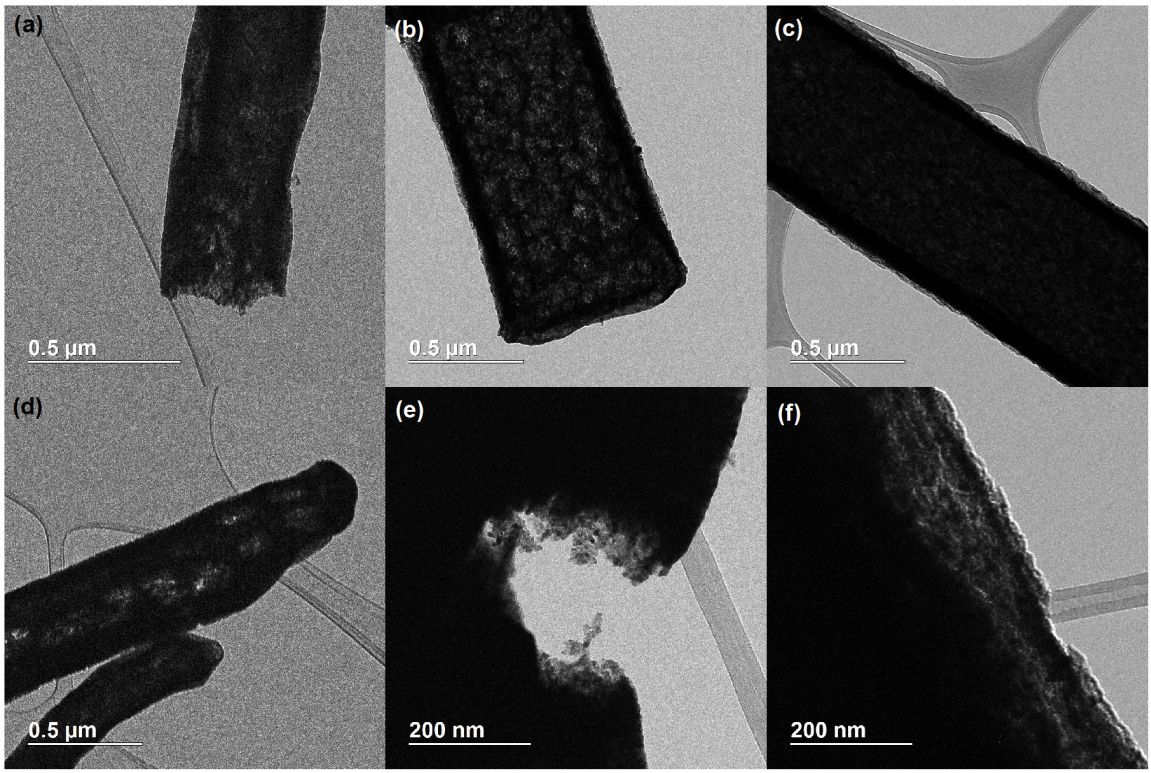

Figure 4.A.12. TEM images of CeO_2-d. (a,d) fresh sample, (b,e) post CO_2/SO_2 exposure, (c,f) after water adsorption experiments.

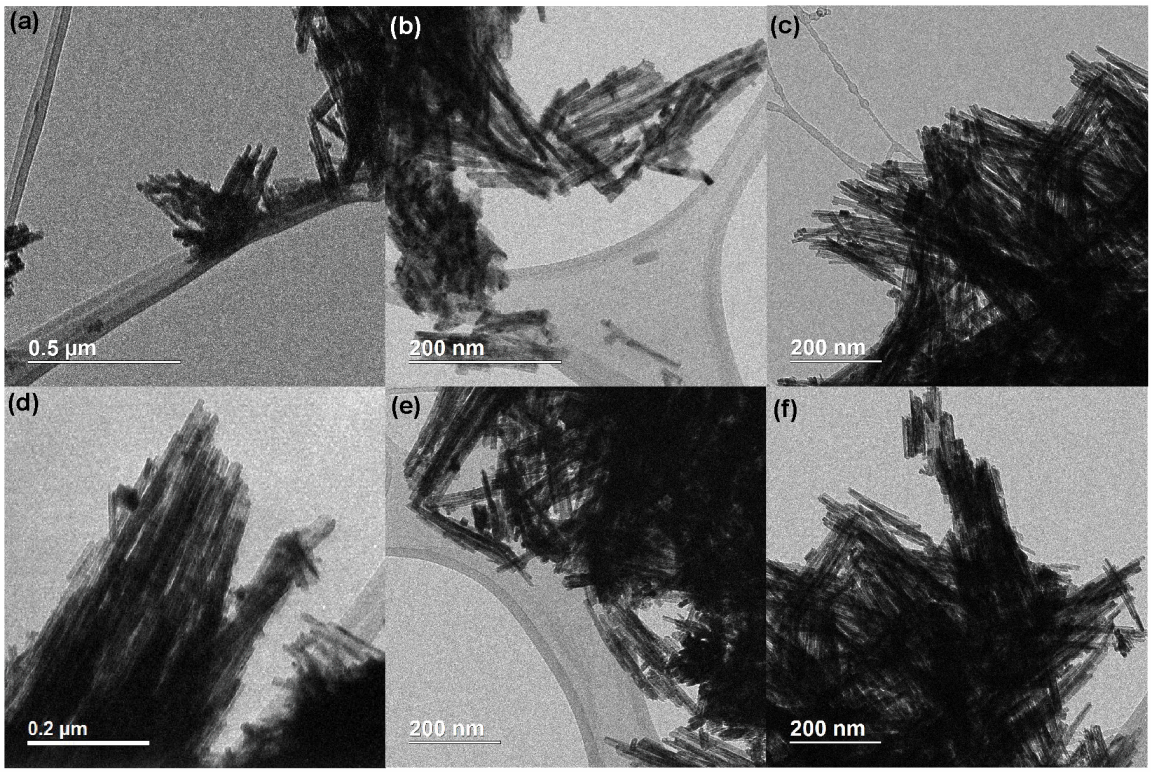

Figure 4.A.13. TEM images of CeO_2 wires. (a,d) fresh sample, (b,e) post CO_2/SO_2 exposure, (c,f) after water adsorption experiments.

Table 4.A.2. Calculated CO_2 and SO_2 TPD for all samples

Material	Sample Weight (mg)	TPD SO_2 (µmol/g)	TPD CO_2 Pre SO_2 (µmol/g)	TPD CO_2 Post SO_2 (µmol/g)	CO_2 during SO_2 TPD (µmol/g)	% Change in CO_2 TPD
CeBTC	25.39	5.41	140.28	105.26	88.04	24.96
CeO_2-d	21.88	2.12	173.93	170.02	134.76	2.25
CeO_2 wires	50.29	1.11	130.65	116.45	40.26	10.86
MIL-125	28.33	6.34	4.85	3.72	0.00	23.28
TiO_2-d	52.24	1.23	7.82	6.99	1.86	10.58
TiO_2 bulk	23.77	2.33	10.36	8.06	0.06	22.13

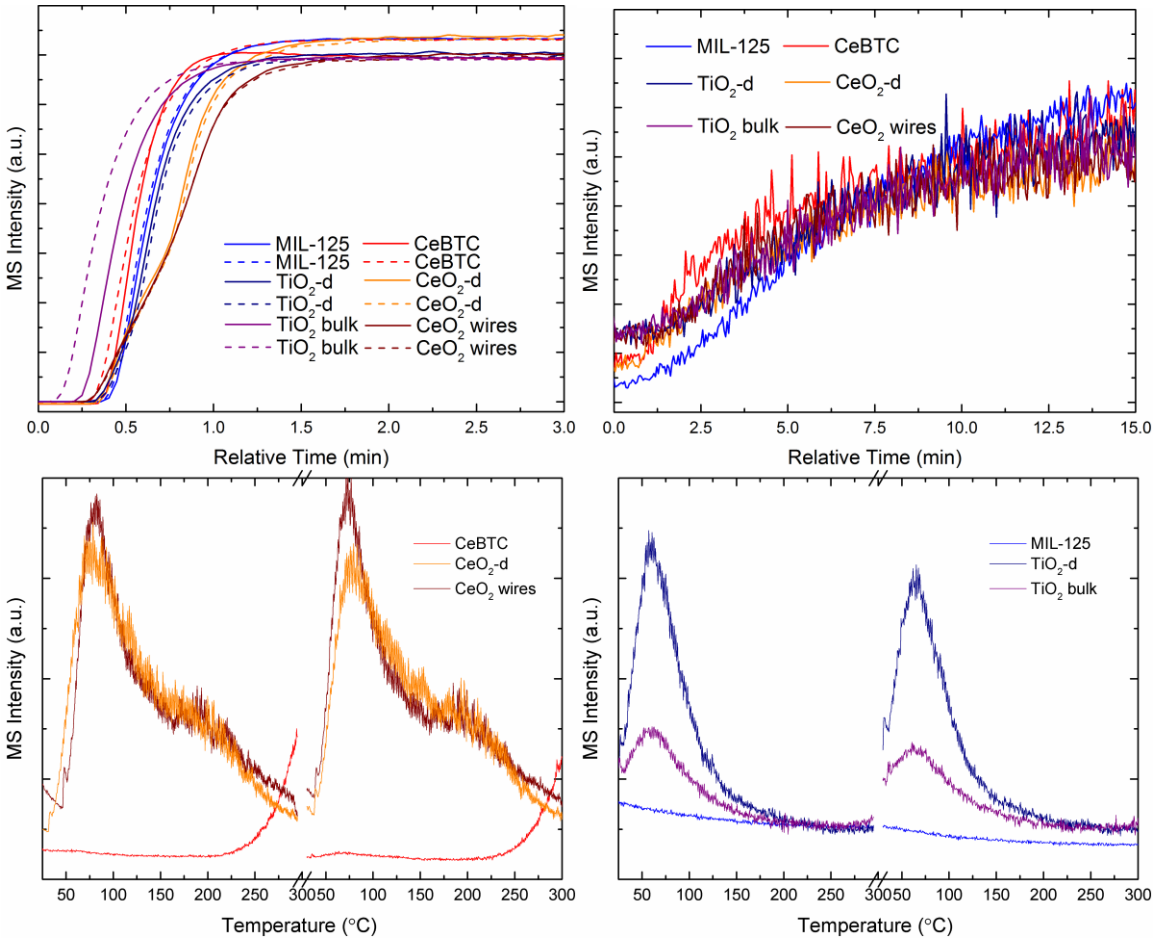

Figure 4.A.14. CO_2, SO_2 adsorption profiles (top), CO_2 TPD curves (bottom) for all samples.

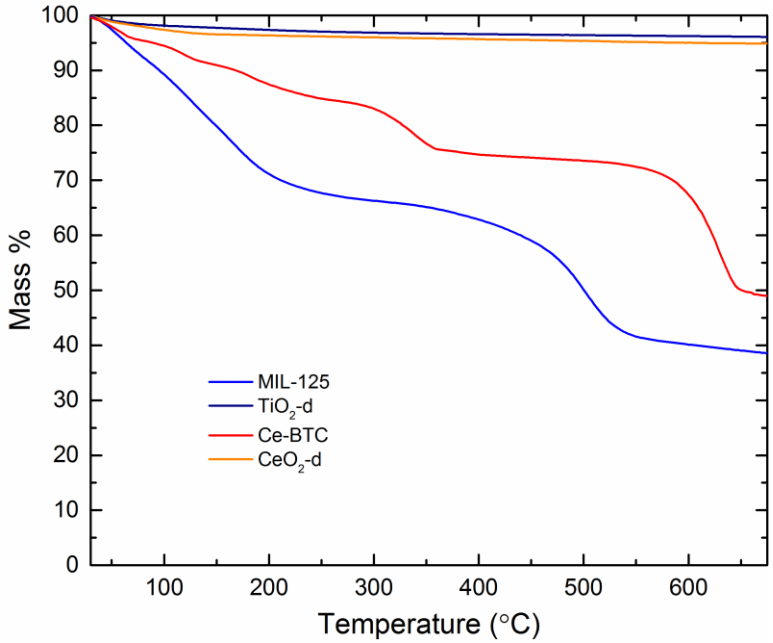

Figure 4.A.15. TGA curves of CeBTC, MIL-125, CeO_2-d, TiO_2-d as-synthesized.

Thermo gravimetric analysis (TGA) was carried out in the temperature range of 30-710 ˚C on a NETZSCH STA 449 F1 Jupiter® under helium with a heating rate of 5 ˚C / min and flow rate of 20 mL/min. The TGA curve for MIL-125 as-synthesized exhibits two main events between room temperature and 700 °C. The first between 0-210 °C is the departure of free terephthalic acid and DMF, while the second, above 450 °C corresponds to the elimination of the terephthalate linkers from the framework. The TGA curve for CeBTC as-synthesized exhibits three main events between room temperature and 700 °C. The first between 0-200 °C is the departure of water molecules, free trimesic acid, and DMF while the second, above 300 °C is the removal of DMF from the open metal sites. The third event above 600 °C corresponds to the elimination of the trimesic linkers from the framework. A slow removal of water molecules is seen for both derived oxides resulting in less than 2% mass loss.

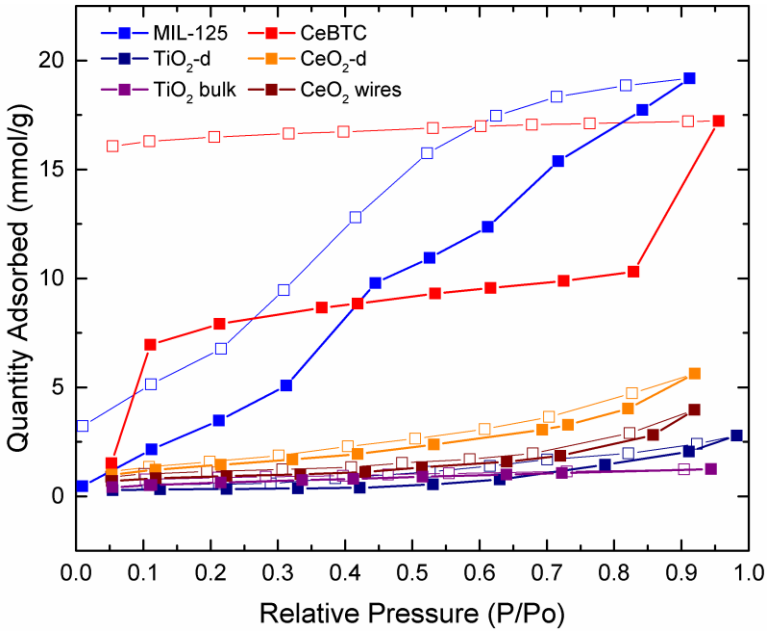

Figure 4.A.16. Water adsorption isotherms for CeBTC, CeO_2-d, CeO_2 wires, MIL-125, TiO_2-d, TiO_2 bulk. Closed symbols are adsorption points, open symbols are desorption points.

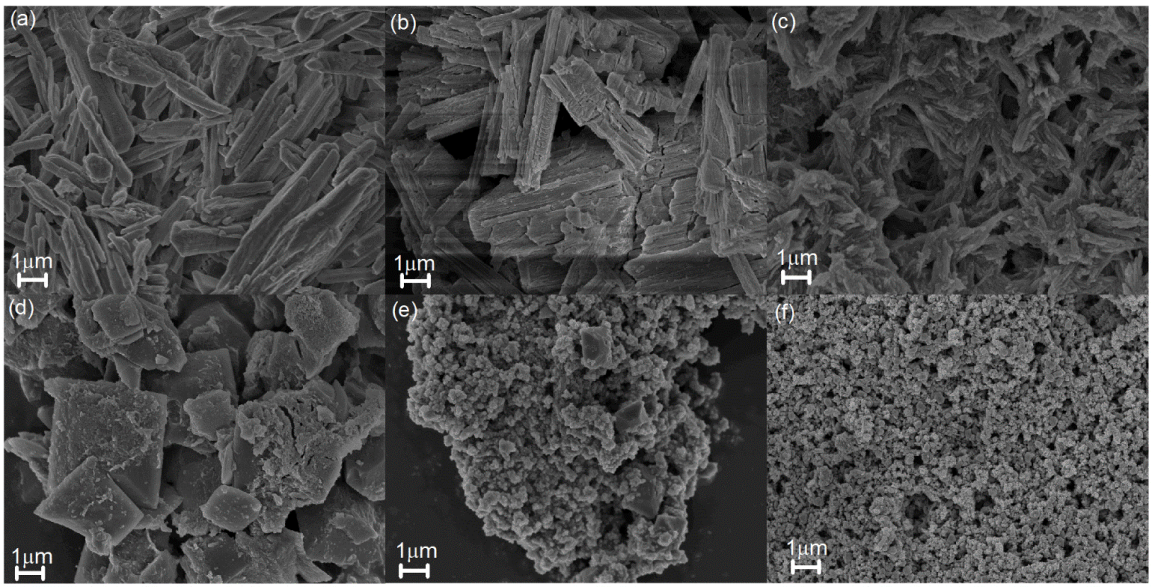

Figure 4.A.17. SEM images of (a) CeBTC, (b) CeO_2-d, (c) CeO_2 wires, (d) MIL-125, (e) TiO_2-d, and (f) TiO_2 bulk after water adsorption experiments.

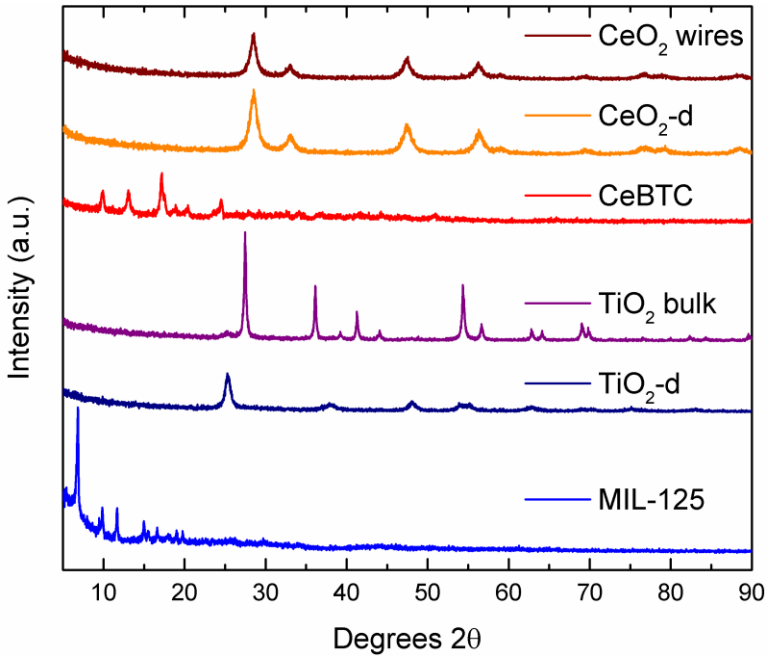

Figure 4.A.18. PXRD patterns of MIL-125, TiO_2-d, TiO_2 bulk, CeBTC, CeO_2-d, CeO_2 wires after water adsorption experiments.

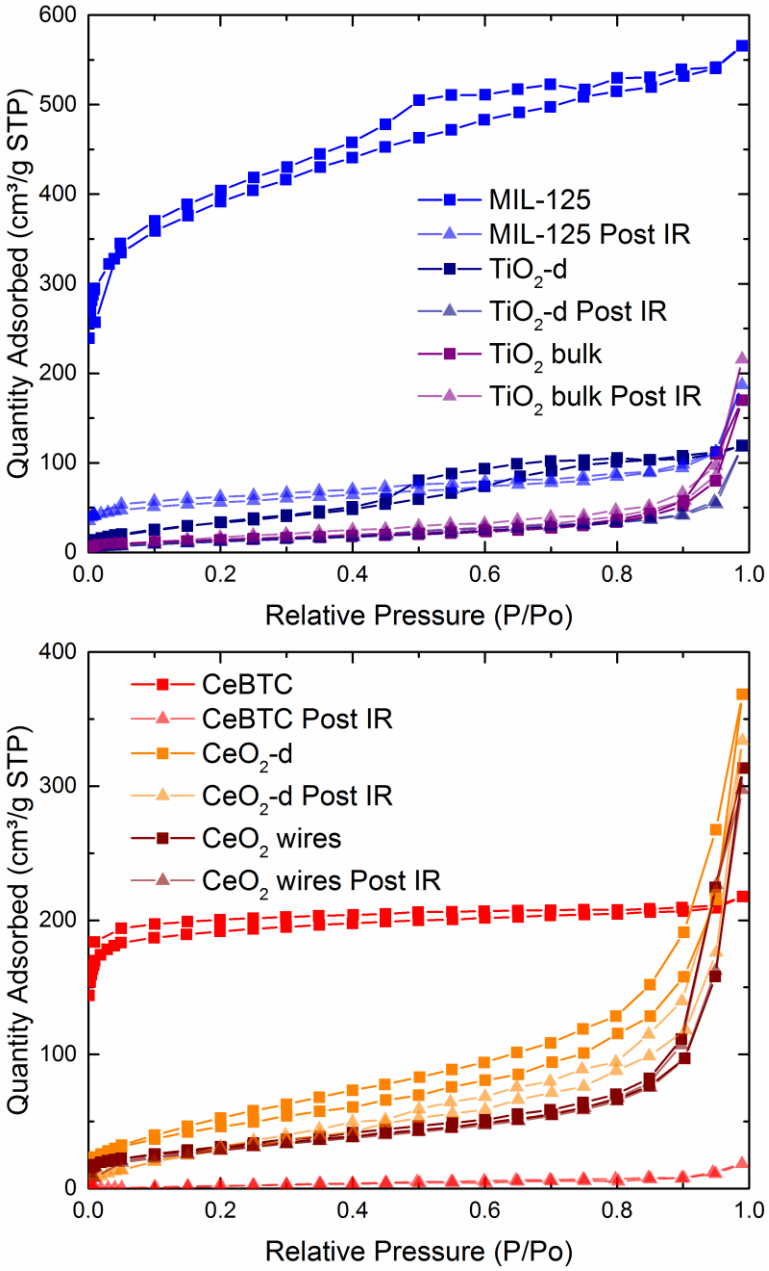

Figure 4.A.19. N_2 adsorption isotherms for MIL-125, TiO_2-d, TiO_2 bulk, CeBTC, CeO_2-d, CeO_2 wires before (squares) and after (triangles) IR experiments.

CHAPTER 5

SYNERGISTIC EFFECTS OF WATER AND SO_2 ON DEGRADATION OF MIL-125 IN THE PRESENCE OF ACID GASES

In the previous chapter, the effect of acid gases was investigated over Ti and Ce MOFs and MOF-derived oxides with an emphasis on understanding the adsorbed species present in the materials. A degradation during SO_2 exposure was observed in the titanium MOF, MIL-125, through a loss of surface area, powder X-ray pattern, and the visual appearance of cavities in the particles. This chapter focuses on an experimental and computational investigation of the degradation mechanism in MIL-125 to gain a deeper understanding of the degradation process and inform future efforts increasing the stability of this and other MOF materials. This Chapter was adapted with permission from W.P. Mounfield, III; C. Han; S.H. Pang; U. Tumuluri; Y. Jiao; S. Bhattacharyya; M.R. Dutzer; S. Nair; Z. Wu; R.L. Lively; D.S. Sholl; K.S. Walton, "Synergistic Effects of Water and SO_2 on Degradation of MIL-125 in the Presence of Acid Gases," Journal of Physical Chemistry C, DOI: 10.1021/acs.jpcc.6b09264. Copyright 2016 American Chemical Society. Several collaborators contributed to the work presented in Chapter 5: computational simulations and analysis were performed by C.H.; aqueous SO_2 exposure, XPS experiments and data analysis were performed by S.H.P.; in situ IR spectra were collected by U.T.; SEM imaging was performed by Y.J.; humid SO_2 exposure was performed by S.B.; dry SO_2 exposure isotherms were collected by M.R.D.

MIL-125 and MIL-125-NH_2 were studied in dry, humid, and aqueous SO_2 environments to gain insight into degradation mechanisms during acid gas exposure. Material stability and textural properties were evaluated using N_2

physisorption at 77 K, scanning electron microscopy (SEM), and powder X-ray diffraction (PXRD) after timed, concentration-controlled exposure to adsorbing gases. The study of the amine functionalized MIL-125 allowed for the investigation into the effect of ligand functionalization on acid gas stability and degradation mechanism. In situ IR experiments tracked sulfur-based species arising during the degradation of the MOF materials. Computational simulations were coupled with the experimental results to investigate and evaluate several potential reaction mechanisms leading to degradation of the MOF crystal structures. This method allowed the examination of the degradation effects on MIL-125 from the combination of water with SO_2 to form acidic species in several environments. In addition, the effect of the amine functionality on the extent of degradation of MIL-125-NH_2 in these environments was investigated using the combined computational and experimental approach.

5.1 Experimental Procedure

Synthesis of MIL-125. MIL-125 was synthesized following the procedure detailed in previous work.[1] Benzene-1,4-dicarboxylic acid (BDC) (2.75 mmol) was added to a mixture of DMF (6.5 mL) and methanol (6.5 mL). Acetic acid (22.5 mmol, 1.4 mL) was then added before the addition of titanium isopropoxide (0.75 mmol, 0.22 mL) to prevent the titanium precursor from hydrolyzing. The solution was placed in a 60 mL scintillation vial and heated in an isothermal oven at 110 °C for 24 h. The resultant white product was thrice rinsed with DMF and once with methanol. The dry powder was collected and stored in a vial in a desiccator.

Synthesis of MIL-125-NH_2. MIL-125-NH_2 was synthesized following a similar procedure to that detailed in previous work for the unfunctionalized material.[1] 2-aminobenzene-1,4-dicarboxylic acid (BDC-NH_2) (2.75 mmol) was

added to a mixture of DMF (6.5 mL) and methanol (6.5 mL). Acetic acid (22.5 mmol, 1.4 mL) was added before the addition of titanium isopropoxide (0.75 mmol, 0.22 mL) to prevent the titanium precursor from hydrolyzing. The solution was placed in a 60 mL scintillation vial and heated in an isothermal oven at 110 °C for 24 h. The resultant yellow product was thrice rinsed with DMF and once with methanol. The dry powder was collected and stored in a vial in a desiccator.

Aqueous SO_2 exposure. MIL-125 and MIL-125-NH_2 were exposed to aqueous solutions of SO_2 at a concentration of 2.5×10^{-5} mol/L, which was determined to be the concentration in equilibrium with 20 ppm in the vapor phase by Henry's law. A solution of the desired concentration was introduced into a 60 mL glass vial with approximately 200 mg of sample and sealed. The mixture was sonicated briefly to ensure good dispersion. After the desired length of time, the particles were centrifuged and washed copiously with DI water and methanol and finally dried under vacuum at 60 °C. The dry powder was stored in a vial in a desiccator before characterization. For aqueous SO_2 exposure units of ppm-h are calculated by the multiplication of vapor phase equivalent concentration, 20 ppm, by the time exposed.

Humid SO_2 exposure. MIL-125 and MIL-125-NH_2 were exposed to the humid SO_2 environment at 25 °C at the concentration 27 ppm ± 6 ppm in 86 ± 5 %RH, as measured by a Dräger PAC 7000 SO_2 electrochemical sensor and an Ambient Weather humidity probe. SO_2 was generated by bubbling air at 60 mL/min through a 400 mL aqueous solution of 0.5 mg/mL $NaHSO_3$ at a pH of 3.7 at 45 °C into a Secador mini-desiccator. Approximately 50 mg of sample was placed in a 250 mL beaker within the exposure chamber. The glass crystallization dish was removed to allow the desired length of exposure. After the desired length of time exposed, the particles were removed from the exposure chamber and

washed with methanol and finally dried under vacuum at 60 °C. The dry powder was stored in a vial in a desiccator before characterization. For humid SO_2 exposure units of ppm-h are calculated by the multiplication of the concentration by the time exposed.

Dry SO_2 isotherms. SO_2 (Airgas, Anhydrous, 99.98% Purity) isotherms were measured using a lab-built volumetric system. Approximately 30 mg of sample were outgassed under dynamic vacuum at 150 °C for approximately 16 h. Adsorption isotherms were measured for pressures ranging from 0 to 2.7 bar (P/P_0 = 0 to 0.69, P_0 = 3.92 bar) at 25 °C. The SO_2 adsorption loading was calculated by measuring the pressure drop in the sample cell, and converting from pressure to moles using the Peng-Robinson equation of state. The dry powder was stored in a vial in a desiccator before characterization.

Powder X-ray diffraction. Powder X-ray diffraction patterns were recorded at room temperature on an X'Pert X-ray PANalytical diffractometer with an X'accelerator module using Cu Kα (λ = 1.5418 Å) radiation with a step size of 0.02˚ in two theta (2θ).

N_2 physisorption. Nitrogen physisorption isotherms were measured at 77 K using the Quantachrome Quadrasorb SI for samples exposed to aqueous SO_2 activated at 423 K for 12 h under vacuum using the Quantachrome FloVac. Nitrogen physisorption isotherms were measured at 77 K for samples exposed to humid and dry SO_2 activated at 423 K for 12 h under vacuum using the 3Flex Surface Characterization Analyzer from Micromeritics. Nitrogen adsorption analysis was performed on all resulting products, and surface areas were determined by applying BET theory over a range of data points applicable to microporous materials.[2] N_2 isotherms showed typical Type I behavior as per the IUPAC classification.

X-ray photoelectron spectroscopy (XPS). X-ray photoelectron spectra were obtained on a Thermo K-Alpha XPS with Al Kα radiation. Prior to spectra acquisition, samples were dried under vacuum at 60 °C overnight. High-resolution spectra for the O1s binding region were acquired from 525-545 eV in 0.1 eV steps over 8 scans; peaks were fit in OriginPro using a Gaussian-Lorentzian and controlling the FWHM of peaks between samples for consistency.

In situ infrared spectroscopy. MIL-125 and MIL-125-NH_2 were activated at 423 K for 12 h in vacuum prior to the IR experiments. Samples were pretreated at 150 ˚C at the rate of 10 ˚C/min and held for 1 h in He flow at 50 cm^3/min. The in situ spectroscopic studies consisted of the following steps: (i) adsorption of SO_2, (ii) He purge, and (iii) temperature programmed desorption (TPD). During the first step, the material was exposed to 260 ppm SO_2/He flow at 50 cm^3/min for 30 min at 25 ˚C. During the second step, the He purge, the residual gas was purged by He flow at 50 cm^3/min for 10 min at 25 ˚C. For the final step, temperature programmed desorption was performed, during which the material was heated to 150 ˚C at the rate of 10 ˚C/min; the temperature of the material was held at 150 ˚C for 30 min, followed by cooling the material to 25 ˚C at the rate of 10 ˚C/min.

IR spectra were collected continuously through the entire measurement cycle using a Thermo Nicolet Nexus 670 spectrometer in Diffuse Reflectance mode (DRIFTs); the outlet gases from the DRIFTs cell (Pike Technologies HC-900) were analyzed using a quadrupole mass spectrometer (Omnistar GSD-301 O_2, Pfeiffer Vacuum). Absorbance spectra during SO_2 adsorption were calculated as $Abs = -log(I/Io)$, where I is the single beam spectrum during adsorption and I_o is the single beam spectrum before adsorption.

Scanning electron microscopy (SEM). Samples were imaged on a Zeiss Ultra60 FE-SEM instrument with a high-efficiency in-lens SE detector at a working

distance of 7-8 mm and accelerating voltage of 5 kV. Prior to SEM imaging, samples were sonicated for 10 s in methanol and dispersed on a flat Al sample holder with two-sided adhesive conductive carbon tape. Samples were then coated with carbon for 30 s at 4.4 V using a Cressington 108A Carbon Coater to exclude the charging effect. Several images were taken for each sample with varying levels of magnification.

Water vapor adsorption. A 3Flex Surface Characterization Analyzer from Micromeritics was used to collect water vapor isotherms at 25 ˚C for all samples. Isotherms were collected with fresh, unexposed samples. Prior to water adsorption measurements, MIL-125 and MIL-125-NH_2 were activated at 150 ˚C for 12 h under dynamic vacuum. All water vapor isotherms were measured to P/P_0 = 0.95, P_0 = 23.76 mmHg to avoid water condensation.

Density functional theory simulations. A periodic model of MIL-125 was constructed from the X-ray diffraction (XRD) crystal structure as the initial crystal geometry and optimized by Density Functional Theory (DFT) calculations.[3] The DFT calculations were performed using the Vienna Ab initio Simulation Package (VASP)[4,5] with the projected augmented wave (PAW) method and a plane-wave energy cutoff of 600 eV.[6] All calculations were performed using the PBE exchange-correlation functional[7] and semi-empirical dispersion correlations by the DFT-D2 method,[8] sampling k—space at the Gamma-point with total energy and ionic force convergence criteria for energy minimization of 10^{-4} eV and 0.03 eV/Å, respectively.

The DFT-optimized MIL-125 lattice constants (a=b=18.984 Å and c=18.092 Å) were in good agreement with experimental values (a=b=18.654 Å and c=18.144 Å).[3] The lattice constants were then fixed during the structural optimizations for MIL-125 with one or two water or H_2SO_3 molecules per unit cell.

The geometry of MIL-125-NH_2 was obtained by adding a NH_2 group to each BDC ligand and optimizing by the same method as that applied to MIL-125. The formation energy of defects formed by water or H_2SO_3 molecules are defined as

$$\Delta E = E_{defect} - E_{perfect} - \sum E_{molecule} ,$$

where E_{defect} and $E_{perfect}$ are the energy of a defective and perfect MIL-125(-NH_2) unit cell, respectively, and $E_{molecule}$ is the energy of an isolated water or H_2SO_3 molecule. With this conversion, a negative formation energy is enthalpically favorable. The reaction pathways were calculated by the climbing-image nudged elastic band (CI-NEB) method[9] on a periodic MIL-125 or MIL-125-NH_2 unit cell.

The simulated IR spectra of perfect and defective MIL-125 were calculated by the Gaussian09 package with B3LYP functional and 6-31G(d,p) basis set.[10] Finite cluster models cut from the optimized periodic MIL-125 structures with dangling BDC ligands replaced by COOH groups were used as the initial structures of MIL-125 for geometry optimization and subsequent analysis of vibrational modes (Figure 5.A.1).

5.2 Results and Discussion

5.2.1 Material characterization and acid gas exposure

The structures of MIL-125 and MIL-125-NH_2 were verified with powder X-ray diffraction (PXRD) after synthesis. Figure 5.A.2 shows the as-synthesized patterns of MIL-125, MIL-125-NH_2, and the simulated MIL-125 pattern obtained from the structure reported by Dan-Hardi et al.[3] Both materials match the simulated pattern, indicating the unfunctionalized and functionalized forms have identical topology to the literature structure. Surface areas of the pristine materials were determined from N_2 physisorption isotherms. The surface areas obtained for both materials, shown in Table 5.A.1, are higher than those observed in literature[3,11-14] and our previous study,[1] and lie closer to

the theoretical values calculated by Vaesen et al.,[11] suggesting the synthesis and activation method allowed for complete removal of residual ligand or solvent after synthesis.

Pure component SO_2 and water isotherms were collected for both materials, with pre- and post-adsorption characterization to assess the stability of the materials in the presence of these individual adsorbates. The SO_2 isotherms shown in Figure 5.A.3 illustrate the adsorption capacity of MIL-125 and MIL-125-NH_2 for SO_2, reaching a loading of 10.9 and 10.3 mmol/g at 2.7 bar (P/P_0 = 0.69), respectively. Previous breakthrough studies with 1.0 % SO_2 reported low SO_2 adsorption capacity, less than 0.5 mmol/g, for several MOFs and high capacity in MOF-74, ~3.0 mmol/g.[15] Interpolation of the SO_2 isotherms in Figure 5.A.3 at the corresponding pressure (0.01 bar) yields low to moderate adsorption capacities for MIL-125 and MIL-125-NH_2, 0.3 mmol/g and 1.0 mmol/g, respectively. The stronger adsorption in the low pressure region for MIL-125-NH_2 results from the strong interaction of SO_2 with the amine functional group. Sun et al. simulated SO_2 adsorption isotherms for several MOFs and zeolites in the 0-1 bar pressure range.[16] The adsorption capacity of MIL-125 and MIL-125-NH_2 lies slightly below that of the open-metal site MOFs studied by Sun et al., yet well above other MOFs and zeolites lacking open-metal sites.

N_2 physisorption after dry SO_2 adsorption revealed minimal change in surface area for MIL-125 and a 10% decrease for MIL-125-NH_2 (Table 5.A.1), suggesting both MOFs are stable in the presence of SO_2 and minimal degradation occurs due to the presence of the dry acid gas. A decrease in the micropore volume from 0.68 cm^3/g to 0.60 cm^3/g was observed for MIL-125-NH_2 after dry SO_2 exposure. Additionally, no measureable change in the PXRD pattern was observed for either material after dry SO_2 exposure, as seen in Figure 5.A.4. The high adsorption capacity and minimal degradation of these materials suggests they may offer a stable alternative to the often

unstable open-metal site MOFs without sacrificing a large amount of SO_2 adsorption capacity.

Water adsorption in MIL-125 and MIL-125-NH_2 has been investigated previously in several studies,[1,13,17,18] where the unfunctionalized material is seen to exhibit a loss of surface area and degradation after exposure to water vapor, and the amine functionalized material is stable. The adsorption isotherms presented in Figure 5.A.5 are in agreement with those presented in previous studies, with MIL-125 and MIL-125-NH_2 exhibiting a strong step increase in adsorption at P/P_0 = 0.3 and 0.2, respectively, and a similar maximum loading of 30 mmol/g at P/P_0 = 0.95. However, the previously reported drastic loss of surface area after water adsorption was not observed for MIL-125, as shown in Table 5.A.1. This observation is likely associated with differences in the experimental conditions of previous studies[1,17] in comparison to this study. In other studies the sample was removed from the adsorption instrument before transferring to a separate instrument for N_2 physisorption. This method would expose the material to humid air. In our previous study, we also conducted the measurement in a similar fashion and observed an approximately 70% loss of surface area.[1] In contrast, the experiments presented in this study were performed by determining the surface area through N_2 physisorption before and after water adsorption in the same instrument. Thus, the sample tube was never removed from the system, ensuring water was the only adsorbate to which the material was exposed. This observation explains the stability observed in our experiments with water vapor, although the instability of the material when exposed to water and ambient air obviously present concerns about whether this material could be used in practical applications. Completely reversible isotherms were observed for both materials, indicating no retention of water vapor and that degradation had likely not occurred.[19,20] Furthermore, similar to the observation after SO_2 adsorption,

no change in the PXRD pattern was observed for either material after water exposure (Figure 5.A.4).

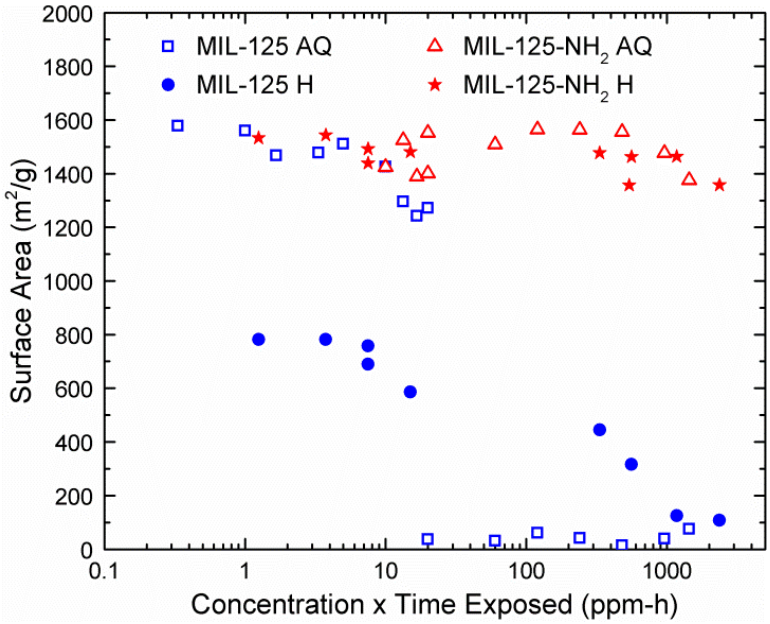

Figure 5.1. BET surface areas for MIL-125 and MIL-125-NH_2 samples plotted against concentration x time exposed in ppm-h for aqueous (AQ) or humid (H) SO_2 exposure.

The stability of MIL-125 in the presence of dry SO_2 was initially puzzling, as degradation was observed after exposure to 15 ppm SO_2 in our previous study.[1] However, an analysis of the MS data from our previous work revealed trace amounts of water in the SO_2 stream. This observation led to the hypothesis that the combination of water and SO_2 caused the degradation of the material. To this end, the textural properties of the materials were studied after exposure to SO_2 in aqueous or humid environments. Figure 5.1 shows the BET surface area for MIL-125 and MIL-125-NH_2 after exposure in either an aqueous (AQ) or humid (H) environments. MIL-125 displayed little change in surface area in an aqueous environment until after 20 ppm-h of exposure, where a complete loss of surface area(>95%) was observed. For all subsequent times after this point, a complete loss of surface area was also observed. The surface area loss is correlated directly with a disappearance of the PXRD pattern after 20 ppm-h of

exposure, with the pattern retained before this time, as shown in Figure 5.2 and Figure 5.A.6a. However, MIL-125-NH_2 displays complete stability throughout aqueous exposure, with little change in surface area or PXRD pattern after exposure (Figure 5.1-2 and Figure 5.A.6c).

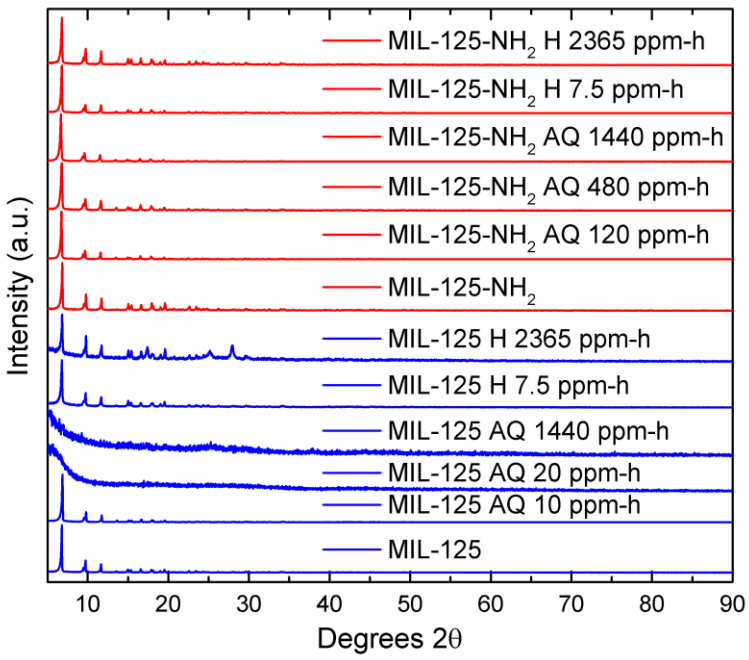

Figure 5.2. PXRD patterns for selected MIL-125 and MIL-125-NH_2 samples after timed exposure to aqueous (AQ) or humid (H) SO_2 environment. All patterns are normalized to the most intense peak.

Humid exposure resulted in a larger degree of initial degradation for MIL-125, with nearly a 50% loss in surface area after 1.25 ppm-h of exposure and a gradual loss in surface area observed thereafter until a complete loss of surface area was observed after 960 ppm-h of exposure. Although complete surface area loss was observed, little change in PXRD pattern was observed after 2365 ppm-h of exposure, suggesting the bulk structure of the particles are retained while surface degradation has led to pore-blocking and higher diffusional resistance from displaced or dangling ligands preventing the adsorption of N_2. As with aqueous exposure, little change in the surface area or PXRD pattern was observed for the amine-functionalized MIL-125 after humid

exposure, suggesting the addition of the amine functionality resulted in a considerable stabilization of the framework in the presence of this acid gas mixture. Motivated by these observations, experimental techniques were coupled with computational simulations to gain insight into the variances in stability and degradation mechanism(s) in different exposure environments for MIL-125 and MIL-125-NH_2.

5.2.2 Elucidation of acid gas degradation mechanism

5.2.2.1 Structural investigation

SEM imaging was employed to visually observe the degradation of the materials after exposure and gain insight into the differences observed after exposure for each material and exposure environment. As shown in Figure 5.A.7a and Figure 5.A.8a, cavities do not form on MIL-125 or MIL-125-NH_2 after exposure to H_2O or dry SO_2, as expected from the stability observed through surface area results and PXRD patterns. This result further supports the necessity of the combination of SO_2 and water to initiate the degradation of the framework. Figure 5.3 and Figure 5.A.7 show SEM images of MIL-125 after aqueous and humid SO_2 exposure. After exposure to aqueous SO_2 for 1.67 ppm-h (Figure 5.3a), MIL-125 particles began to display cavities, indicative of the degradation that was observed in our previous study.[1] These cavities increased in number and size through 10 ppm-h of exposure, and after 20 ppm-h of exposure through 1440 ppm-h of exposure, a complete degradation of the particle was observed. Only small agglomerates remained, indicating a complete destruction of the framework, as explained by the loss of the PXRD pattern and surface area. Furthermore, after 960 ppm-h of exposure, peaks attributed to rutile and anatase TiO_2 appeared, suggesting the small particles observed in the SEM images in Figure 5.3 are agglomerations of metal oxide clusters released from the framework after the displacement and removal of the BDC ligands. It is important to note that before 480 ppm-h, no PXRD peaks for TiO_2

were observed, as the TiO_2 particles were either amorphous or crystalline and small, leading to very broad peaks that were hidden below the background of the pattern.

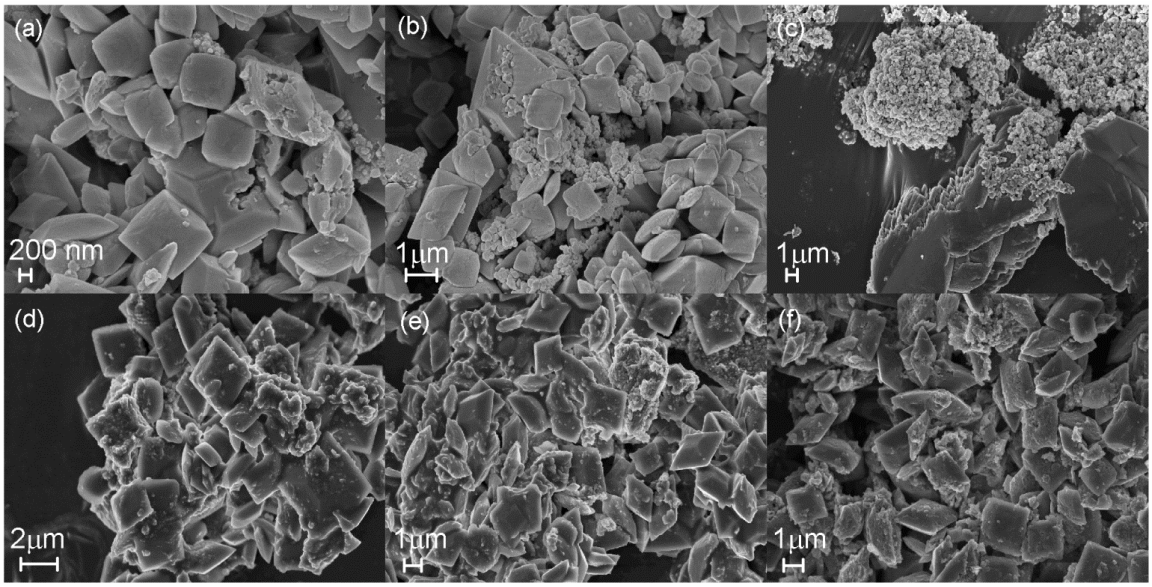

Figure 5.3. SEM images of MIL-125 after aqueous SO_2 exposure for (a) 1.67 ppm-h, (b) 10 ppm-h, (c) 20 ppm-h, and after humid SO_2 exposure for (d) 1.25 ppm-h, (e) 15 ppm-h, (f) 2365 ppm-h.

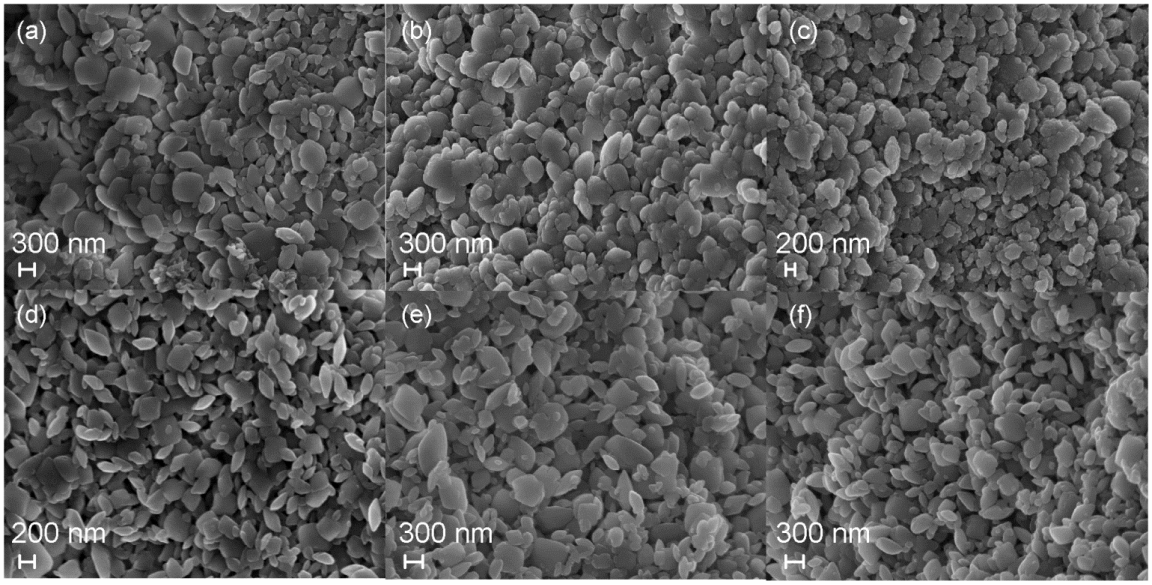

Figure 5.4. SEM images of MIL-125-NH_2 after aqueous SO_2 exposure for (a) 20 ppm-h, (b) 240 ppm-h, (c) 1440 ppm-h, and after humid SO_2 exposure for (d) 1.25 ppm-h, (e) 15 ppm-h, (f) 2365 ppm-h.

After humid SO_2 exposure, cavities were observed after 1.25 ppm-h of exposure, as shown in Figure 5.3d. A gradual increase in the number and size of these cavities was observed through 2365 ppm-h of exposure (Figure 5.A.7b). This observation is consistent with the gradual decrease in surface area and eventual complete loss of porosity of the sample despite retention of the PXRD pattern (Figure 5.A.6b). After exposure for 2365 ppm-h, the bulk particle shape was retained, with a large number of cavities scattered on the surface, suggesting that dangling or displaced ligands on the surface blocked the pores and prevented diffusion of gaseous or liquid species into the particle. We hypothesize that this pore blocking does not occur in the aqueous environment due to the large concentration of water that results in the dissolution of the displaced/dangling surface ligands and allows water to displace ligands within the framework (reaction discussed below with computational simulations). SEM imaging of the MIL-125-NH_2 framework (Figure 5.4 and Figure 5.A.8) revealed no visual change in the particles and a lack of cavity formation in either environment for all exposure times, consistent with the retention of the material's surface area and PXRD pattern, and further indicating that the amine functionality yields an acid-gas resistant framework.

5.2.2.2 Surface chemistry investigation

Investigation of the changes in the chemistry of the near-surface region for each framework after exposure to different environments was performed using XPS. Though the frameworks are porous, the particle sizes are large enough that it is expected that the sampling depth for photoelectrons is limited to the near-surface region of several tens of nanometers. The spectra shown in Figure 5.A.9 illustrate the change in the O1s spectra for selected SO_2 exposure times in aqueous and humid environments. The peaks observed can be assigned to the bridging oxygen in the titanium oxide nodes (530.2 eV), coordinating carboxylate oxygens in the linkers (531.7 eV), and

polyester-like species, likely arising from oligomerization of linkers released from the framework after degradation (533.6 eV).[21] The pristine MIL-125 framework only contains the former two peaks in an approximately 1:2 area ratio, indicative of the stoichiometry of the parent framework. Figure 5.A.9 shows a relative increase in peak intensity of the bridging oxygen species after aqueous exposure with a corresponding decrease in the intensity of the peak associated with carboxylates. This supports the hypothesis that structural degradation proceeds through the displacement of linkers and formation of additional TiO_2 clusters, as seen in SEM images shown in Figure 5.3 and Figure 5.A.7.

A third peak at 533.6 eV appeared after 20 ppm-h of exposure of MIL-125 to aqueous SO_2 (the exposure time corresponding to the complete loss in surface area), possibly corresponding to polyester-like species, suggesting that the displaced ligands have undergone oligomerization or polymerization.[22] The lack of this peak prior to 20 ppm-h of exposure supports the hypothesis that the initial degradation under aqueous conditions occurs slowly and only at the surface. After a sufficient number of ligands are fully displaced, the interior of the particle can be accessed by acidic species, resulting in complete loss of surface area and structure. The intensity of this third peak decreases steadily after 20 ppm-h, likely due to the dissolution of a majority of the displaced ligands, both oligomerized and monomeric, into the aqueous phase.

After humid SO_2 exposure, similar changes in the relative intensities of the oxide carboxylate oxygen peaks were observed. Additionally, the spectra lack the peak indicative of ligand polymerization at all time points. These observations suggest that degradation initially occurred through a similar pathway of displacing ligands. However, due to the inability to wash away displaced ligands in the humid environment, the surface area loss after the first 1.25 ppm-h of exposure was more rapid than for the aqueous exposure.

XP spectra for MIL-125-NH_2 after aqueous and humid SO_2 exposure are shown in Figure 5.A.10, where the oxide oxygen and carboxylate oxygen peaks are both present. Analysis of the spectra reveals a slight change in the relative intensities of these two oxygen species, similar to that observed for MIL-125. However, the oxygen species associated with oligomerized linkers was not observed at any exposure time for MIL-125-NH_2. In combination with the retention of surface area, this suggests that any structural changes that could have occurred would only be on the surface of the particle and no degradation of the inner structure occurring. Additionally, essentially no change in relative intensity of the oxide and carboxylate oxygen peaks was observed after humid SO_2 exposure, in agreement with SEM images illustrating the retention of the MIL-125-NH_2 structure (Figure 5.4 and Figure 5.A.8).

One potential reason for the lack of degradation of the amine-functionalized MIL-125 is due to adsorption of SO_2 on the amine, which would reduce the number of acidic species available for degradation. A small peak near 169 eV can be seen above the noisy background in the S2p spectra for MIL-125-NH_2 after exposure to humid SO_2 (Figure 5.A.11d), indicative of bound sulfur on this sample. In comparison, very little to no sulfur is detected in XPS after aqueous SO_2 exposure on the MIL-125 sample, suggesting that the presence of the amine groups offers a favorable binding site for SO_2 that are not dissolved under humid exposure conditions.

5.2.2.3 Simulation of reaction mechanisms

Several reaction mechanisms were proposed for evaluation with computational techniques to further elucidate the degradation mechanism of MIL-125. The reaction mechanisms ranged from degradation occurring due to the presence of water to more complex mechanisms involving sulfurous acid, as depicted in Scheme 1. Calculations were performed on periodic MIL-125 and MIL-125-NH_2 structures to determine the

change in energy with each mechanism. The two mechanisms (Figure 5.5) involving water, and sulfurous acid and water are the most favorable, with formation energies of -1.21 eV and -1.28 eV, respectively. For the same reaction mechanism, MIL-125-NH_2 displays lower formation energies of -0.54 eV and -0.50 eV, respectively, supporting the experimental observation that the addition of the amine functional group has resulted in a higher degree of stability. The reaction involving solely SO_2 was found to be unfavorable in both structures, an observation that supports the stability of the frameworks in a dry SO_2 environment.

Scheme 5.1. Proposed degradation mechanisms involving water vapor, the dissociation of water, sulfurous acid, sulfurous acid and water.

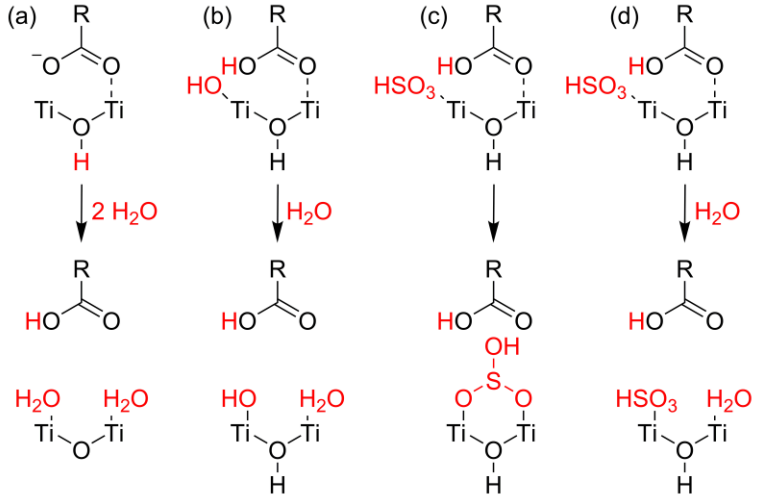

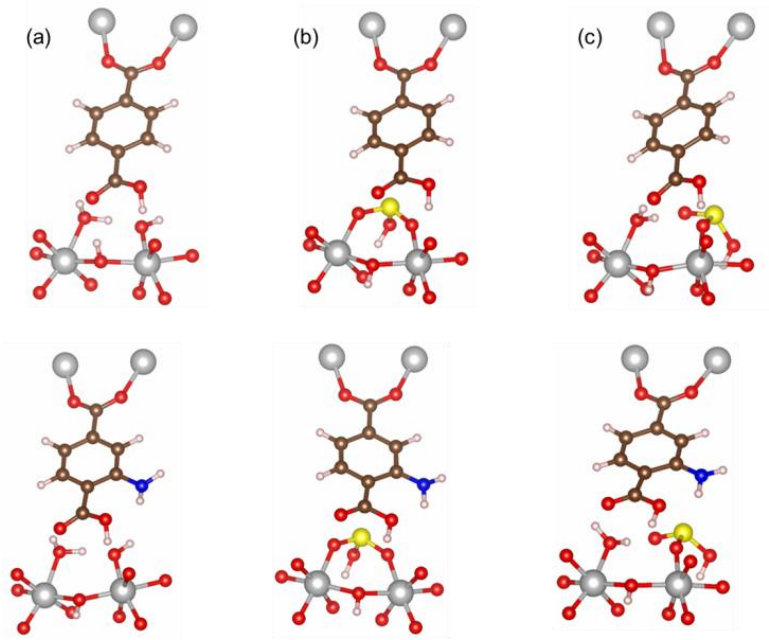

Figure 5.5. DFT optimized geometries of dangling BDC ligands, which are formed by breaking 2 Ti-O bonds with 2 water molecules (a), a H_2SO_3 molecule (b), or a water and a H_2SO_3 molecule (c), in MIL-125 (top) and MIL-125-NH_2 (bottom). Ti, O, C, H, and N are represented by grey, red, brown, white, and blue spheres, respectively.

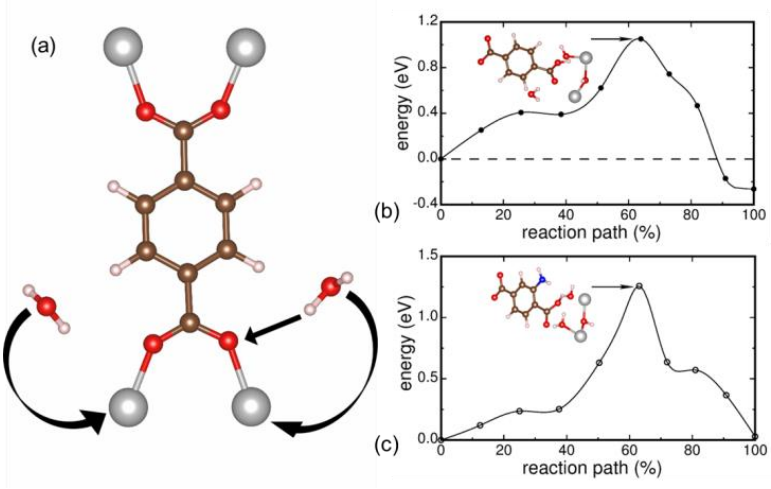

Figure 5.6. (a) Reaction pathway (in the directions of arrows) of two water molecules simultaneously breaking two Ti-O bonds in MIL-125 frameworks, in which one water molecule dissociates into a proton, which is bound to the oxygen atom of a BDC ligand, and a hydroxyl group, which is bound to a Ti atom, and the other water molecule moves towards another Ti atom and finally coordinates with it; (b) Energy barrier (1.05 eV) for (a) in MIL-125; (c) Energy barrier (1.26 eV) for (a) in MIL-125-NH_2. The transition state structures are shown in the insets in (b) and (c).

The support of both favorable reaction pathways and the stability of MIL-125-NH_2 by the calculated formation energies provide only partial insight into the complex nature of degradation. Therefore, reaction energy barriers were calculated to give a more complete understanding of the favorability of potential reactions and stability of the frameworks in acid gas conditions. Reaction energy barriers for the reaction involving solely water in MIL-125 and MIL-125-NH_2 are 1.05 eV and 1.26 eV, respectively, as depicted in Figure 5.6. Note that the energy difference between initial and final images on the pathway (-0.26 eV and 0.03 eV for MIL-125 and MIL-125-NH_2, respectively) is smaller than the formation energy (-1.21 eV and -0.54 eV for MIL-125 and MIL-125-NH_2, respectively) because the reactant molecules are initially adsorbed by the framework in the calculations of pathways, while the formation energies are calculated using non-interacting molecules and frameworks. The adsorption energy of a water molecule in the MIL-125 framework is in the range of 0.4 to 0.8 eV varying between the adsorption sites, thus two adsorbed water molecules in the framework result in a lower initial energy (lowered by ~ 1 eV). It is reasonable to expect that the activation energy barrier is related to the formation energy, and a higher formation energy is directly correlated to a higher energy barrier. Therefore, without calculating the energy barriers we predict that the barrier for the mechanism involving solely water is higher than the other favorable mechanisms as the reactions involving solely water have higher formation energies. This hypothesis supports the experimental observation that the combination of SO_2 and water is needed to effect a change in the structure. Furthermore, the energy barrier for MIL-125-NH_2 is higher than the barrier for the identical reaction occurring in MIL-125, giving insight into one potential source of the stability of the functionalized framework.

It is important to note that reactions involving the formation of sulfuric acid and sulfuric-sulfurous acid complexes occur readily in the humid experiments and that the formation of sulfurous acid in the gas phase is thermodynamically unfavorable under the

exposure conditions.[23,24] A hypothesized route for the formation of sulfurous acid in the humid experiments is the dissolution in and reaction of SO_2 with a water film formed in the pores of MIL-125. The formation of this water film is supported by the high hydrophilicity of the framework[13,17] and complete saturation at the conditions of these experiments. Other routes have been explored for a hydrophobic material, ZIF-8, in a separate study.[25] The reaction of sulfuric acid with the framework likely represents a more favorable degradation pathway than that with sulfurous acid. Therefore, the above results for sulfurous acid support the favorability of framework degradation by sulfuric acid in the humid experiments, as well as give insight into potential degradation occurring through the formation of sulfurous acid in a water film within the material.

5.2.2.4 Investigation of adsorbed species

In situ IR experiments with 260 ppm SO_2 and trace amounts of water were performed to further investigate these reaction mechanisms and correlate with simulated IR spectra of proposed adsorbed species shown in Scheme 1. The IR spectra during SO_2 adsorption at room temperature as a function of time for MIL-125 and MIL-125-NH_2 and simulated spectra for H_2SO_3 and H_2SO_3+H_2O adsorbed species are shown in Figure 5.7. The formation of bridged bisulfites over MIL-125 (Scheme 1.c), indicated by the characteristic peaks of asymmetric S-O stretching at 988 cm^{-1},[26] likely occurs at the metal oxide cluster between two titanium atoms. In addition, the formation of monodentate bisulfite over MIL-125 at the metal oxide cluster with a compensating water molecule, the species hypothesized stretching at 904, 953, and 1037 cm^{-1} and symmetric S-O in Scheme 1.d, is indicated by the characteristic peaks at 1071 and 1143 cm^{-1} of S=O stretching and (S-)O-H bending, respectively.[26] These observed species are quite similar to those observed in the simulated spectra for the species associated with the reactions from Scheme 1.c,d, as shown in Figure 5.7c and tabulated in Table 5.A.2.

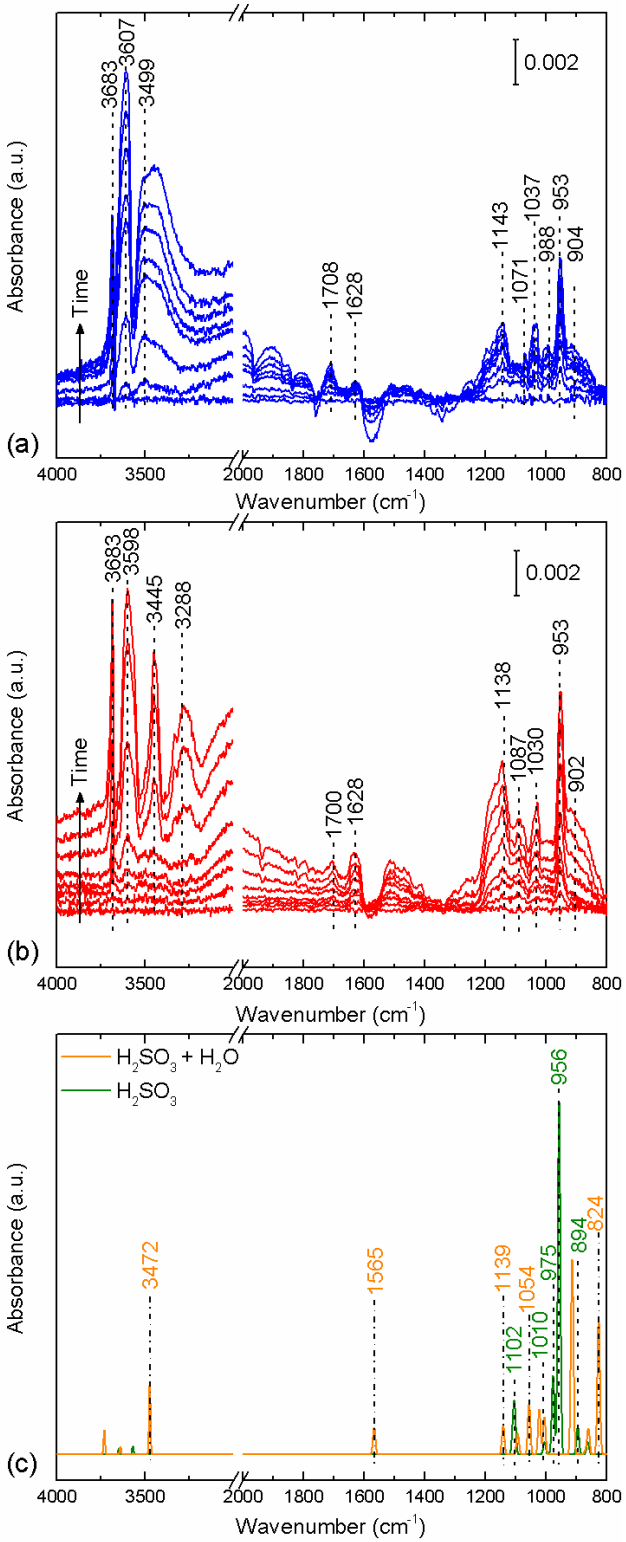

Figure 5.7. IR spectra during 30 min of 260 ppm SO_2 adsorption on (a) MIL-125 and (b) MIL-125-NH_2 at 25 ˚C. (c) Simulated IR spectra for H_2SO_3 + H_2O and H_2SO_3 species adsorbed within MIL-125.

The simulated spectra show characteristic peaks for asymmetric S-O stretching at 894, 956, and 1010 cm^{-1}, symmetric S-O stretching at 975 cm^{-1}, S=O stretching at 1054 cm^{-1}, (S-)O-H bending at 1102 and 1139 cm^{-1}, and O-H stretching of the bisulfite species at 3472 cm^{-1}. The presence of these species over MIL-125 supports the favorability of these reactions, as indicated by the simulation results discussed in the previous section. Furthermore, as in our previous study,[1] a peak at 1708 cm^{-1}, indicative of the carbonyl group on the carboxylic acid ligand, increased simultaneously with an increase in the hydroxyl stretching region (3700-3200 cm^{-1}) over the time of exposure, as ligands were displaced by reaction of the bisulfite ion and free water was adsorbed within the framework. An increase in adsorbed surface water generated from the reaction of SO_2 with surface hydroxyls or adsorption of free water in the system is observed by an increase in the peak at 1628 cm^{-1}, assigned to H-O-H bending.[1,27] The several peaks in the hydroxyl stretching region that increased during adsorption may also be attributed to adsorbed surface water, O-H stretching of the bisulfite ion, hydroxyl groups formed from the dissociation of water, or compensating water adsorbed after reaction of the bisulfite ion with the opposing titanium atom.

The amine-functionalized material displays similar sulfur-based species during SO_2 adsorption, with peaks characteristic of asymmetric S-O stretching at 902, 953, and 1030 cm^{-1}. However, the peak characteristic of symmetric S-O stretching was absent from the spectra, likely hidden by the level of noise of the measurement. Monodentate bisulfite species similar to those formed over MIL-125 were also observed with characteristic peaks at 1138 and 1087 cm^{-1} of (S-)O-H bending and S=O stretching, respectively. The presence of these species aligns with two of the proposed reaction schemes, and a slight peak in the carbonyl stretch region was observed at 1700 cm^{-1}. No other signs of degradation were observed for MIL-125-NH_2 in the aqueous and humid SO_2 environments through other characterization techniques, and it is likely that any

degradation occurring was associated with the displacement of surface ligands, with little to no degradation occurring within the bulk structure.

Two peaks are observed at 3288 and 3445 cm^{-1} in the MIL-125-NH_2 spectra that are absent from the unfunctionalized MIL-125 spectra. These peaks result from a perturbation of the symmetric and asymmetric N-H stretch due to interaction with adsorbed sulfur species similar to the effect observed for MIL-125-NH_2 after H_2S exposure.[11] The perturbation of these peaks suggests the amine functional group offers an additional binding site preventing access and reaction of sulfur species with the framework and likely aids in stabilizing the material in humid SO_2 conditions.

5.4. Conclusions

The degradation mechanism of MIL-125 in the presence of SO_2 and water was investigated with a combined experimental and computational approach. Both amine-functionalized and unfunctionalized MIL-125 materials were found to be stable after exposure to either dry SO_2 or SO_2-free water, while degradation of MIL-125 occurred rapidly upon exposure to humid SO_2 and aqueous SO_2. The use of the amine-functionalized BDC ligand stabilized the framework in all environments and exposure times with no measurable change in surface area or PXRD pattern of MIL-125-NH_2. The degradation of the framework was hypothesized to occur through the reaction of SO_2 with water to form an acidic sulfur species and subsequent formation of a dangling, uncoordinated ligand upon reaction with the framework. In situ IR experiments confirmed the presence of bisulfite species and in combination with computational simulation of formation energies of these adsorbed species, indicated the degradation of the framework likely proceeds through the hypothesized mechanism in the aqueous phase and through either a reaction involving sulfuric or sulfurous acid in the humid experiments. Simulation of reaction energy barriers suggests the stability of

the MIL-125-NH_2 framework is due to the degradation reaction pathway being unfavorable and requiring a significant energy barrier to occur. We hypothesize the reaction mechanisms discussed in this study can be abstracted to other MOFs, particularly those containing BDC as the ligand. Additional studies focusing on exploring the degradation mechanism of other materials with acid gases are required to determine the scope of the applicability of this mechanism. Furthermore, the stability of the framework due to the addition of the amine functional group has provided an avenue for engineering MOF materials that are stable in the presence of acid gases.

5.5. References

(1) Mounfield III, W. P.; Tumuluri, U.; Jiao, Y.; Li, M.; Dai, S.; Wu, Z.; Walton, K. S. *Micro. Meso. Mater.* **2016**, *227*, 65.

(2) Walton, K. S.; Snurr, R. Q. *J. Am. Chem. Soc.* **2007**, *129*, 8552.

(3) Dan-Hardi, M.; Serre, C.; Frot, T.; Rozes, L.; Maurin, G.; Sanchez, C.; Férey, G. *J. Am. Chem. Soc.* **2009**, *131*, 10857.

(4) Kresse, G.; Furthmüller, J. *Phys. Rev. B* **1996**, *54*, 11169.

(5) Kresse, G.; Furthmiiller, J. *Comput. Mater. Sci.* **1996**, *6*, 15.

(6) Blöchl, P. E. *Phys. Rev. B* **1994**, *50*, 17953.

(7) Perdew, J. P.; Burke, K.; Ernzerhof, M. *Phys. Rev. Lett.* **1996**, *77*, 3865.

(8) Grimme, S. *J. Comput. Chem.* **2006**, *27*, 1787.

(9) Henkelman, G.; Uberuaga, B. P.; Jónsson, H. *J. Chem. Phys.* **2000**, *113*, 9901.

(10) Frisch, M. J.; Trucks, G. W.; Schlegel, H. B.; Scuseria, G. E.; Robb, M. A.; Cheeseman, J. R.; Montgomery, J. A., Jr.; Vreven, T.; Kudin, K. N.; Burant, J. C.; Millam, J. M.; Iyengar, S. S.; Tomasi, J.; Barone, V.; Mennucci, B.; Cossi, M.; Scalmani, G.; Rega, N.; Petersson, G. A.; Nakatsuji, H.; Hada, M.; Ehara, M.; Toyota, K.; Fukuda, R. H., J.; Ishida, M.; Nakajima, T.; Honda, Y.; Kitao, O.; Nakai, H.; Klene, M.; Li, X.; Knox, J. E.; Hratchian, H. P.; Cross, J. B.; Bakken, V.; Adamo, C.; Jaramillo, J.; Gomperts, R.; Stratmann, R. E.; Yazyev, O.; Austin, A. J.; Cammi, R.; Pomelli, C.; Ochterski, J. W.; Ayala, P. Y.; Morokuma, K.; Voth, G. A.; Salvador, P.; Dannenberg, J. J.; Zakrzewski, V. G.; Dapprich, S.; Daniels, A. D.; Strain, M. C.; Farkas, O.; Malick, D. K.; Rabuck, A. D.; Raghavachari, K.; Foresman, J. B.; Ortiz, J. V.; Cui, Q.; Baboul, A. G.; Clifford, S.; Cioslowski, J.; Stefanov, B. B.; Liu, G.; Liashenko, A.; Piskorz, P.; Komaromi, I.; Martin, R. L.; Fox, D. J.; Keith, T.; Al-Laham, M. A.; Peng, C. Y.; Nanayakkara, A.; Challacombe, M.; Gill, P. M. W.; Johnson, B.; Chen, W.; Wong, M. W.; Gonzalez, C.; Pople, J. A. *Gaussian Revision E.01*; Gaussian, Inc.: Wallingford, CT, 2004.

(11) Vaesen, S.; Guillerm, V.; Yang, Q.; Wiersum, A. D.; Marszalek, B.; Gil, B.; Vimont, A.; Daturi, M.; Devic, T.; Llewellyn, P. L.; Serre, C.; Maurin, G.; De Weireld, G. *Chem. Commun.* **2013**, *49*, 10082.

(12) Fu, Y.; Sun, D.; Chen, Y.; Huang, R.; Ding, Z.; Fu, X.; Li, Z. *Angew. Chem. Int. Ed. Engl.* **2012**, *51*, 3364.

(13) Canivet, J.; Bonnefoy, J.; Daniel, C.; Legrand, A.; Coasne, B.; Farrusseng, D. *New J. Chem.* **2014**, *38*, 3102.

(14) Zlotea, C.; Phanon, D.; Mazaj, M.; Heurtaux, D.; Guillerm, V.; Serre, C.; Horcajada, P.; Devic, T.; Magnier, E.; Cuevas, F.; Ferey, G.; Llewellyn, P. L.; Latroche, M. *Dalton Trans.* **2011**, *40*, 4879.

(15) Britt, D.; Tranchemontagne, D.; Yaghi, O. M. *Proc. Natl. Acad. Sci. U. S. A.* **2008**, *105*, 11623.

(16) Sun, W.; Lin, L.-C.; Peng, X.; Smit, B. *AIChE J.* **2014**, *60*, 2314.

(17) Kim, S.-N.; Kim, J.; Kim, H.-Y.; Cho, H.-Y.; Ahn, W.-S. *Catal. Today* **2013**, *204*, 85.

(18) Jeremias, F.; Lozan, V.; Henninger, S. K.; Janiak, C. *Dalton Trans.* **2013**, *42*, 15967.

(19) Liang, Z.; Marshall, M.; Chaffee, A. L. *Micro. Meso. Mater.* **2010**, *132*, 305.

(20) Jasuja, H.; Walton, K. S. *Dalton Trans.* **2013**, *42*, 15421.

(21) Naumkin, A. V.; Kraut-Vass, A.; Gaarenstroom, S. W.; Powell, C. J. *X-ray Photoelectron Spectroscopy Database Version 4.1*; National Institute of Standards and Technology (NIST): Gaithersburg, MD, 2000-2012.

(22) Briggs, D.; Beamson, G. *Anal. Chem.* **1993**, *65*, 1517.

(23) Liu, J.; Fang, S.; Liu, W.; Wang, M.; Tao, F.-M.; Liu, J.-y. *J. Phys. Chem. A* **2015**, *119*, 102.

(24) Liu, J.; Fang, S.; Wang, Z.; Yi, W.; Tao, F.-M.; Liu, J.-y. *Environ. Sci. Technol.* **2015**, *49*, 13112.

(25) Bhattacharayya, S.; Pang, S. H.; Dutzer, M. R.; Lively, R. P.; Jones, C. W.; Walton, K. S.; Sholl, D. S.; Nair, S. *J. Phys. Chem. C* **2016**.

(26) Nanayakkara, C. E.; Pettibone, J.; Grassian, V. H. *Phys. Chem. Chem. Phys.* **2012**, *14*, 6957.

(27) Xu, W.; He, H.; Yu, Y. *J. Phys. Chem. C* **2009**, *113*, 4426.

APPENDIX 5.A

MIL-125 COMPUTATIONAL SIMULATIONS AND CHARACTERIZATION

The cluster models for the calculations of vibrational frequencies were constructed by cutting the appropriate fragments from the periodic structures. To examine our proposed degraded structures with sulfur species (Scheme 1), we used charge neutral clusters $Ti_8O_8(OH)_4(COOH)_{12}$ to represent perfect MIL-125, $Ti_8O_8(OH)_4(COOH)_{11}(HSO_3)$ defective MIL-125 with a bridged bisulfite ion and $Ti_8O_8(OH)_4(COOH)_{11}(H_2O)(HSO_3)$ defective MIL-125 with a coordinated water molecule and a bisulfite ion, respectively (Figure 5.A.1). In the cluster models we did not include BDC ligands, which exist in perfect and all the proposed defective MIL-125 structures, because they would not result in the difference in the calculated vibrational modes over all kinds of MIL-125 structures. The geometries of the clusters were optimized with the protons of the terminated COOH groups fixed, and then the optimized structures were used to calculate the vibrational frequencies. To examine the new IR peaks brought by the sulfur species, for the defective MIL-125 clusters shown in Figure 5.A.1, we relax the atoms of local fragments, which have two neighbor Ti atoms, the O atoms bound to the two Ti atoms, the bridging OH group between the two Ti atoms, the HSO3 group, and the water molecule for the analysis of vibrational modes. For comparison, we relax the similar atoms in the perfect MIL-125 cluster structure, in which a COOH group between the two Ti atoms was also allowed to relax. All the calculations were performed by Gaussian09 package with B3LYP functional and 6-31G(d,p) basis set.[1] The calculated vibrational modes were scaled by a factor of 0.9611 to be better compared with experimental IR spectra.[2]

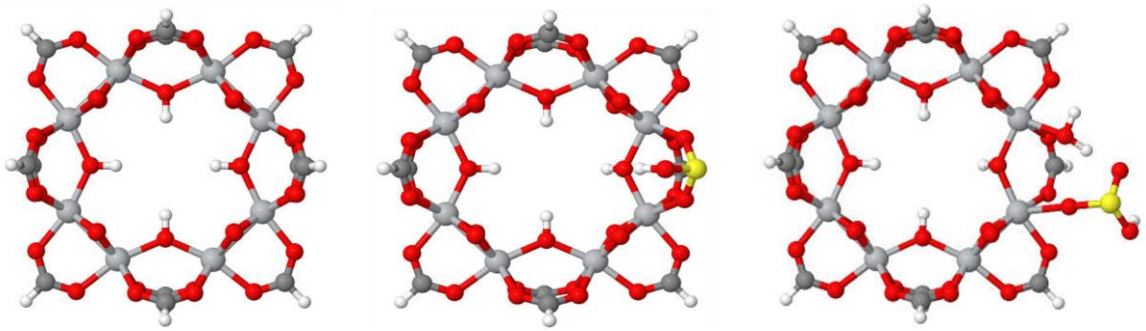

Figure 5.A.1. Cluster models of perfect (left) and defective MIL-125 with sulfite ions (middle and right) for vibrational frequency calculations.

Table 5.A.1. BET surface area in m^2/g for as-synthesized, humid (H) SO_2, aqueous (AQ) SO_2, dry SO_2 and water exposed MIL-125 and MIL-125-NH_2 samples.

Exposure Time (min)	Concentration x Time (ppm-h)	Concentration x Time (ppm-h)	MIL-125 AQ	MIL-125-NH_2 AQ	MIL-125 H	MIL-125-NH_2 H
1	0.33	--	1578	--	--	--
3	1	--	1560	--	--	--
5	1.67	1.25	1468	--	782	1533
10	3.33	--	1478	--	--	--
15	5	3.75	1511	--	782	1544
30	10	7.5	1426	1425	690/758	1439/1492
40	13.33	--	1296	1525	--	--
50	16.67	--	1243	1389	--	--
60	20	15	1272/37	1552/1401	586	1481
180	60	--	32	1509	--	--
360	120	--	61	1565	--	--
540	--	333	--	--	445	1477
720	240	--	42	1563	--	--
960	--	560	--	--	317	1463
1440	480	--	15	1555	--	--
2160	--	540	--	--	--	1357
2880	960	1176	40	1477	125	1464
4320	1440	--	76	1376	--	--
6480	--	2365	--	--	108	1358

	MIL-125	MIL-125-NH_2
As-synth.	1527	1861
Dry SO_2	1591	1667
H_2O	1317	1553

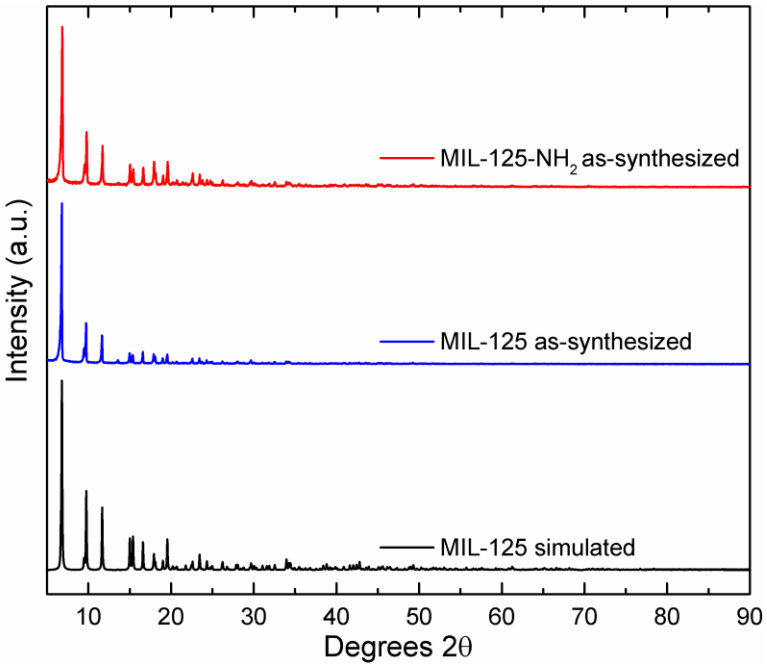

Figure 5.A.2. PXRD patterns for simulated MIL-125, MIL-125 as-synthesized and MIL-125-NH_2 as-synthesized.

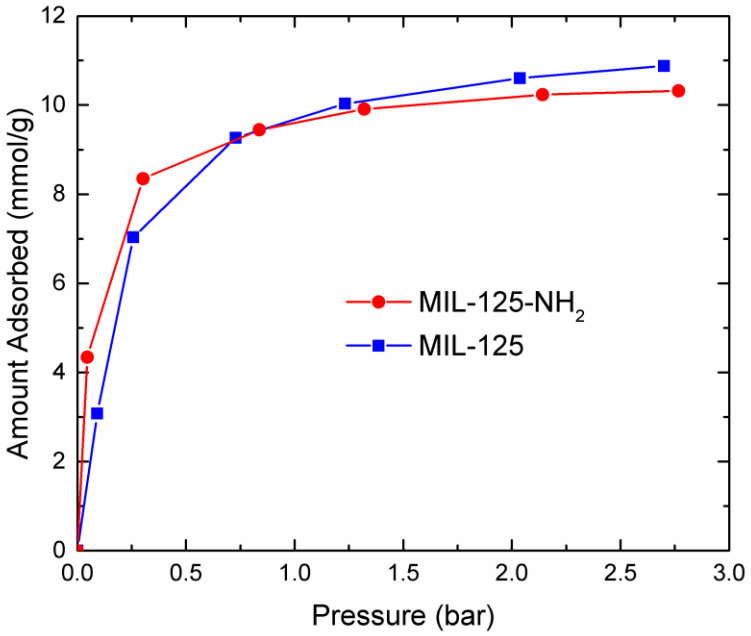

Figure 5.A.3. SO_2 adsorption isotherms for MIL-125 and MIL-125-NH_2.

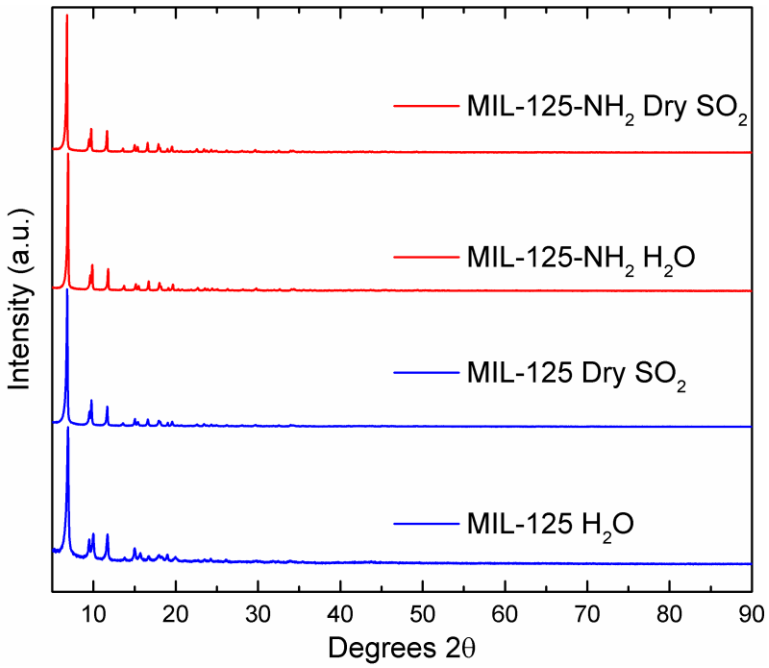

Figure 5.A.4. PXRD patterns for MIL-125 and MIL-125-NH_2 after water vapor and dry SO_2 exposure. All patterns are normalized to the most intense peak.

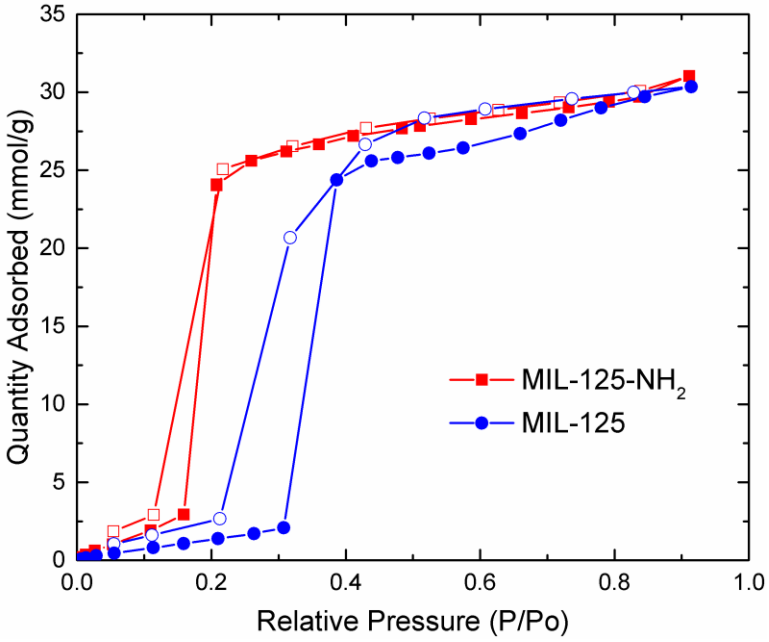

Figure 5.A.5. Water adsorption isotherms for MIL-125 and MIL-125-NH_2. Solid symbols indicate adsorption, open symbols indicate desorption.

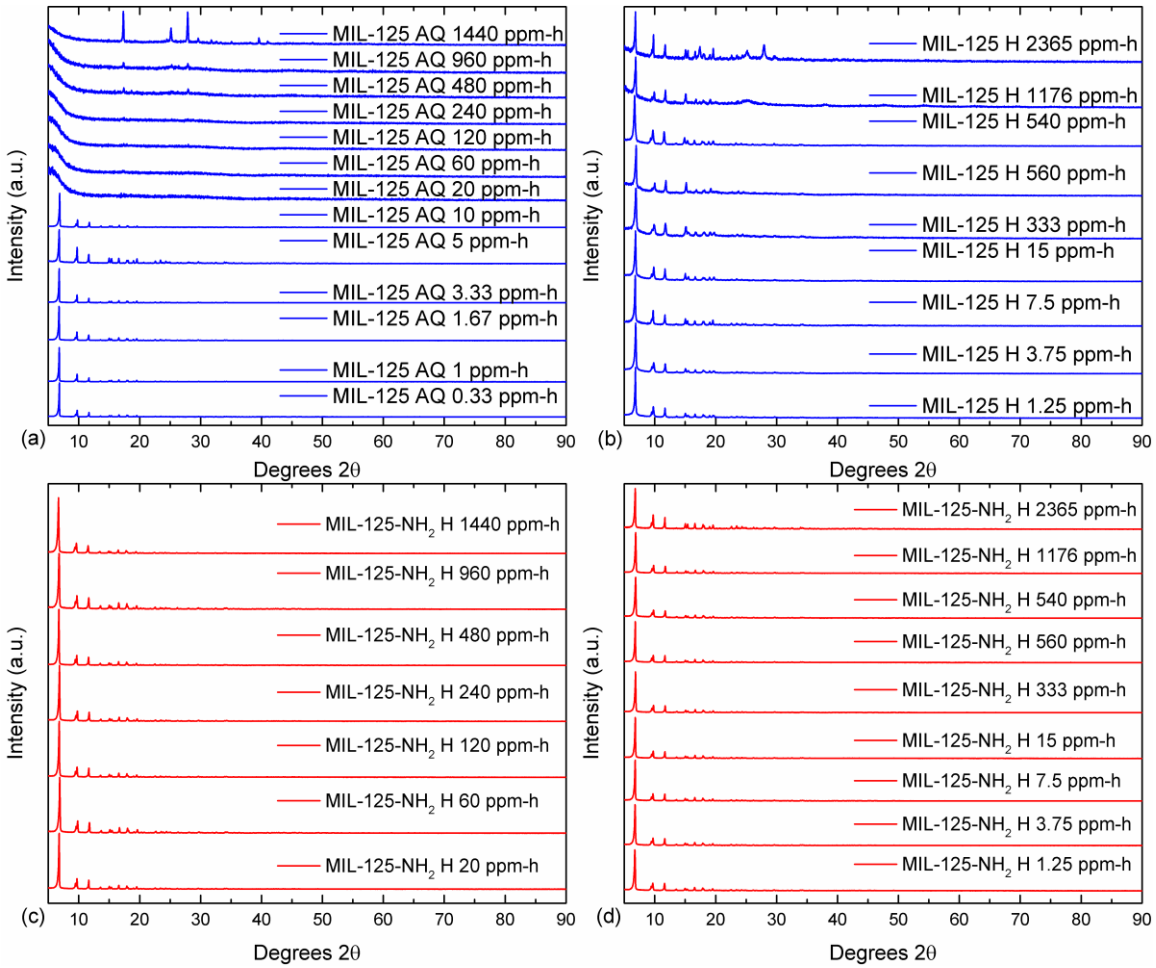

Figure 5.A.6. PXRD patterns for MIL-125 (top) and MIL-125-NH_2 (bottom) after timed exposure to aqueous (AQ) or humid (H) SO_2 environment. All patterns are normalized to the most intense peak.

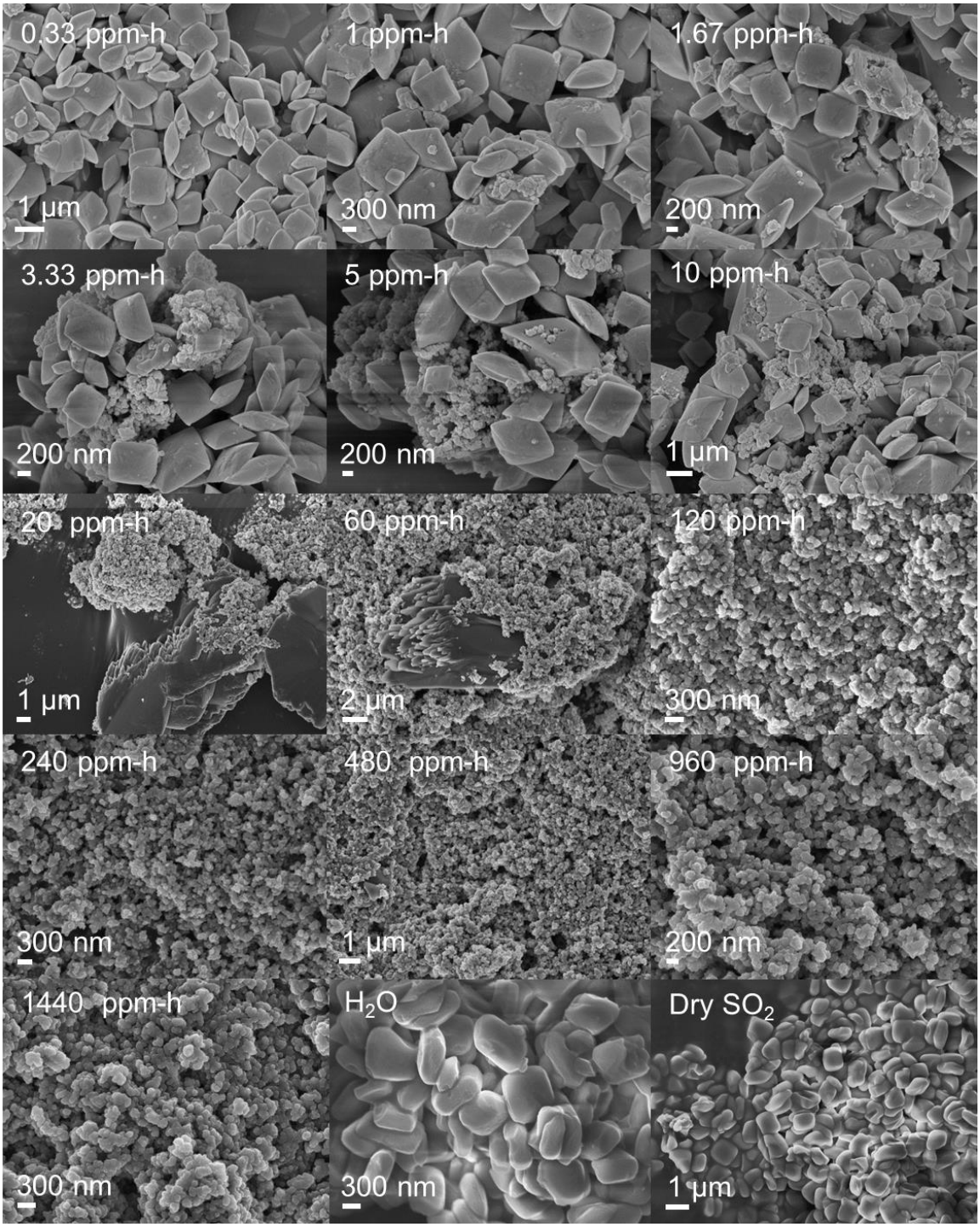

Figure 5.A.7a. SEM images of MIL-125 after timed exposure to aqueous SO_2 environment, water, and dry SO_2.

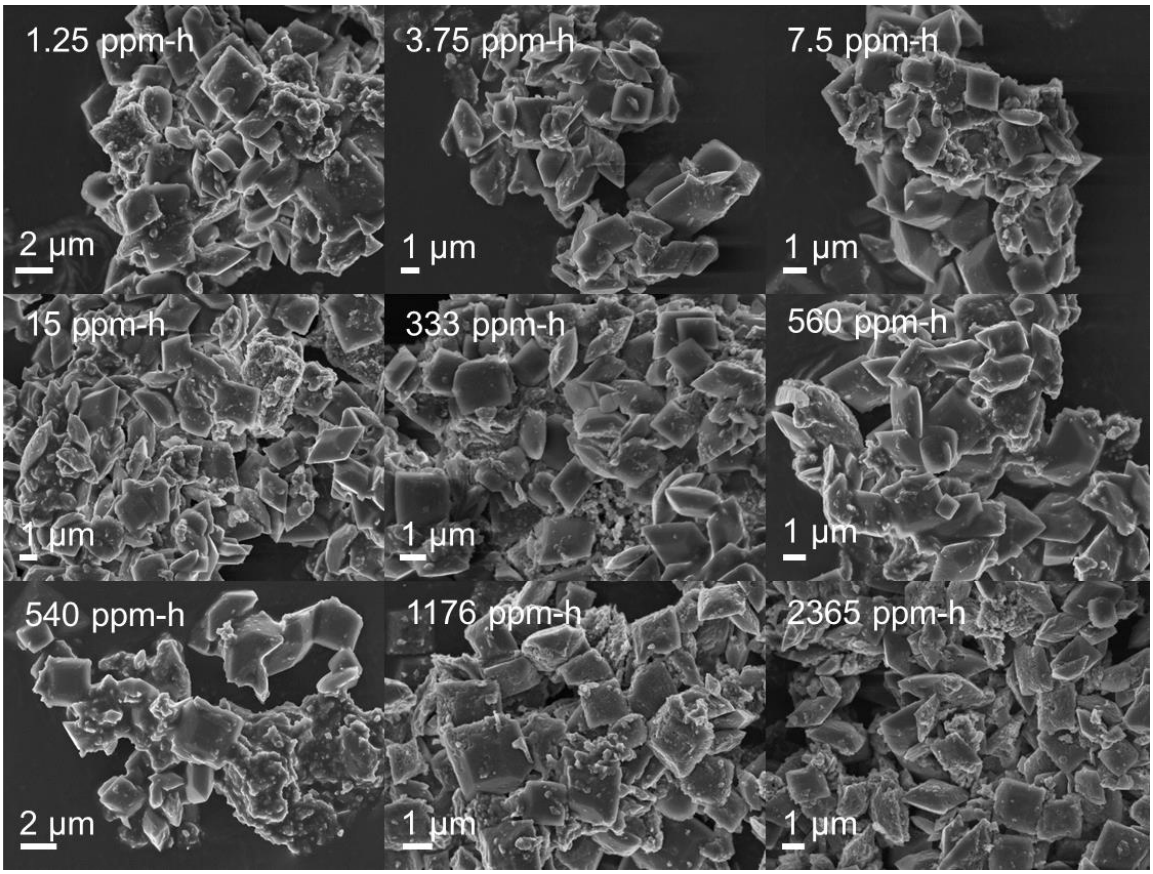

Figure 5.A.7b. SEM images of MIL-125 after timed exposure to humid SO_2 environment.

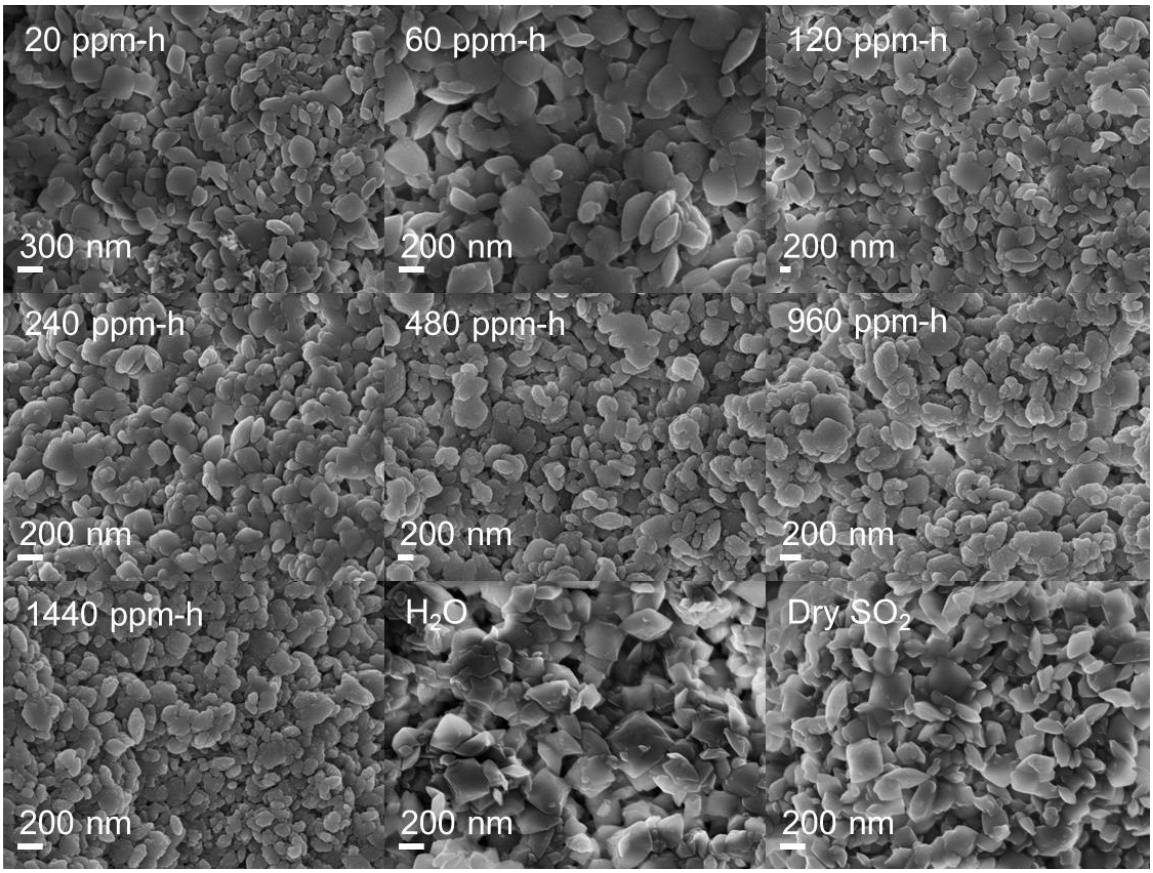

Figure 5.A.8a. SEM images of MIL-125-NH_2 after timed exposure to aqueous SO_2 environment, water, and dry SO_2.

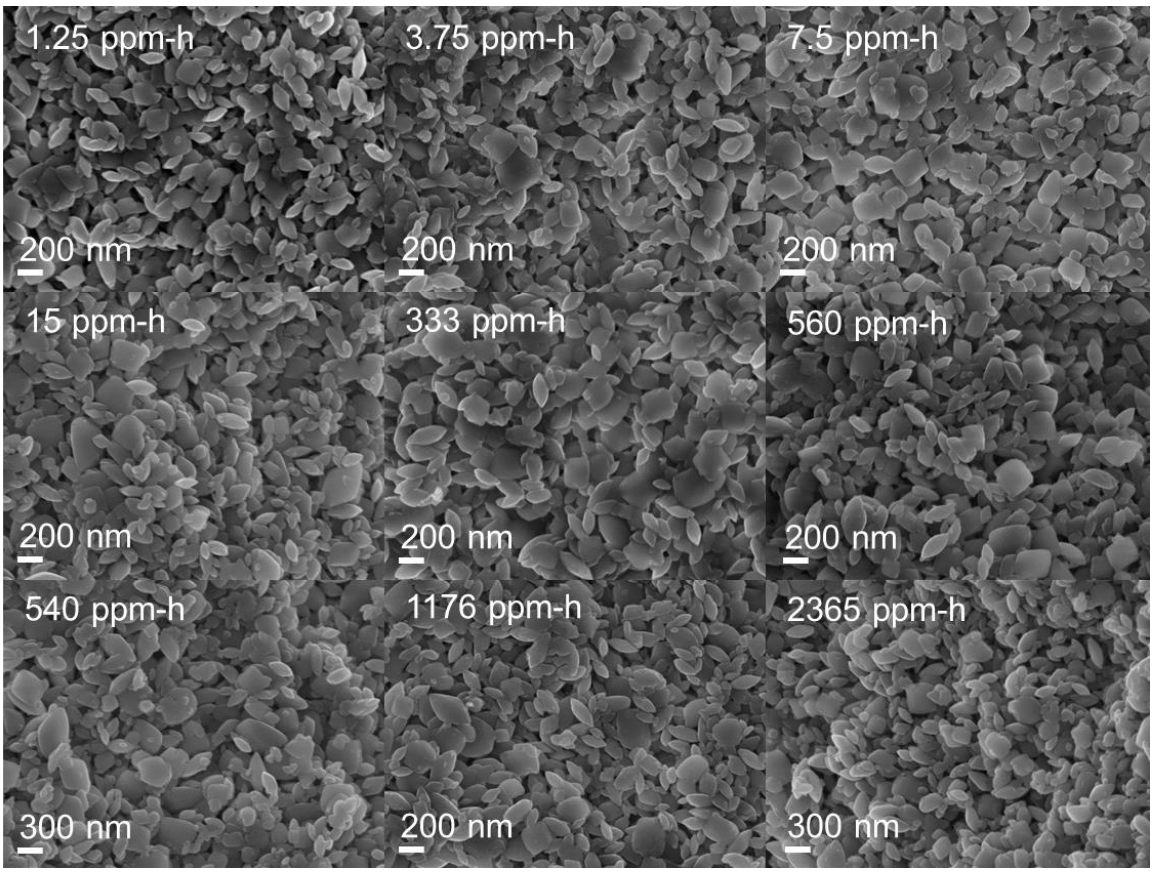

Figure 5.A.8b. SEM images of MIL-125-NH_2 after timed exposure to humid SO_2 environment.

Table 5.A.2. Calculated vibrational modes of the cluster models shown in Figure 5.A.1

Wavenumber (cm^{-1})	Vibrational mode	cluster
446	Ti-OH stretching	$Ti_8O_8(OH)_4(COOH)_{12}$
656	Ti-O stretching	$Ti_8O_8(OH)_4(COOH)_{12}$
715	S-OH stretching	$Ti_8O_8(OH)_4(COOH)_{11}(HSO_3)$
723	Asy. O-S-OH stretching, Ti-O stretching	$Ti_8O_8(OH)_4(COOH)_{11}(H_2O)(HSO_3)$
742	S-OH stretching, Ti-O stretching	$Ti_8O_8(OH)_4(COOH)_{11}(HSO_3)$
750	Sym. O-S-OH stretching, Ti-O stretching	$Ti_8O_8(OH)_4(COOH)_{11}(H_2O)(HSO_3)$
824	S-O(-Ti) stretching	$Ti_8O_8(OH)_4(COOH)_{11}(H_2O)(HSO_3)$
894	Asy. S-O stretching (weak)	$Ti_8O_8(OH)_4(COOH)_{11}(HSO_3)$
956	Asy. S-O stretching (strong)	$Ti_8O_8(OH)_4(COOH)_{11}(HSO_3)$
975	Sym. S-O stretching	$Ti_8O_8(OH)_4(COOH)_{11}(HSO_3)$
1010	Asy. S-O stretching (very weak)	$Ti_8O_8(OH)_4(COOH)_{11}(HSO_3)$
1054	S=O stretching	$Ti_8O_8(OH)_4(COOH)_{11}(H_2O)(HSO_3)$
1102	S-O-H bending	$Ti_8O_8(OH)_4(COOH)_{11}(HSO_3)$
1139	S-O-H bending	$Ti_8O_8(OH)_4(COOH)_{11}(H_2O)(HSO_3)$
1369	Sym. C-O stretching	$Ti_8O_8(OH)_4(COOH)_{12}$
1565	Water (adsorbed by Ti) bending	$Ti_8O_8(OH)_4(COOH)_{11}(H_2O)(HSO_3)$
1580	Asy. C-O stretching	$Ti_8O_8(OH)_4(COOH)_{12}$
2839	O-H (of water) stretching	$Ti_8O_8(OH)_4(COOH)_{11}(H_2O)(HSO_3)$
3472	O-H (of HSO_3) stretching	$Ti_8O_8(OH)_4(COOH)_{11}(H_2O)(HSO_3)$

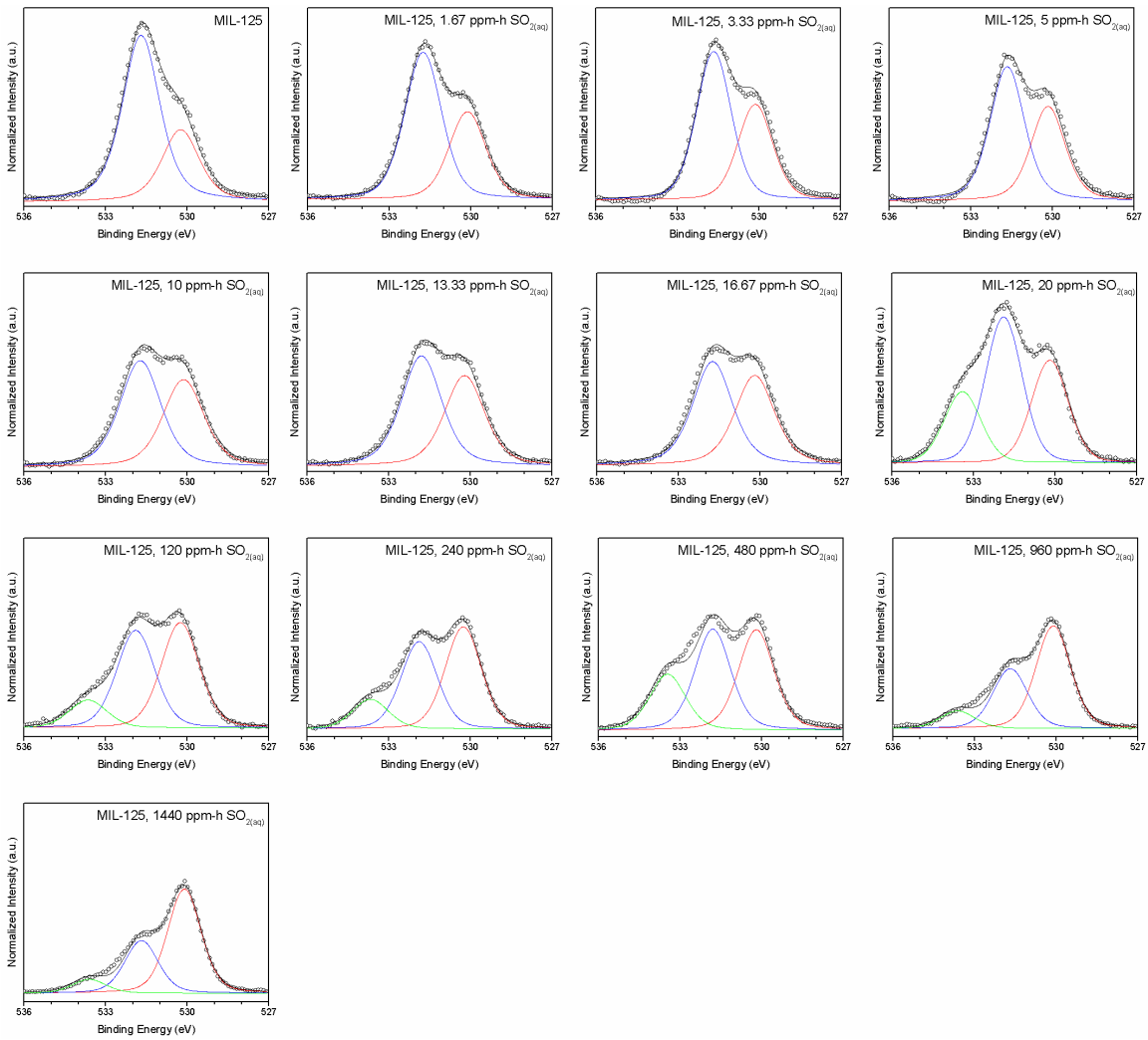

Figure 5.A.9a. High-resolution O1s XP spectra of MIL-125 after timed exposure to aqueous SO_2 environment.

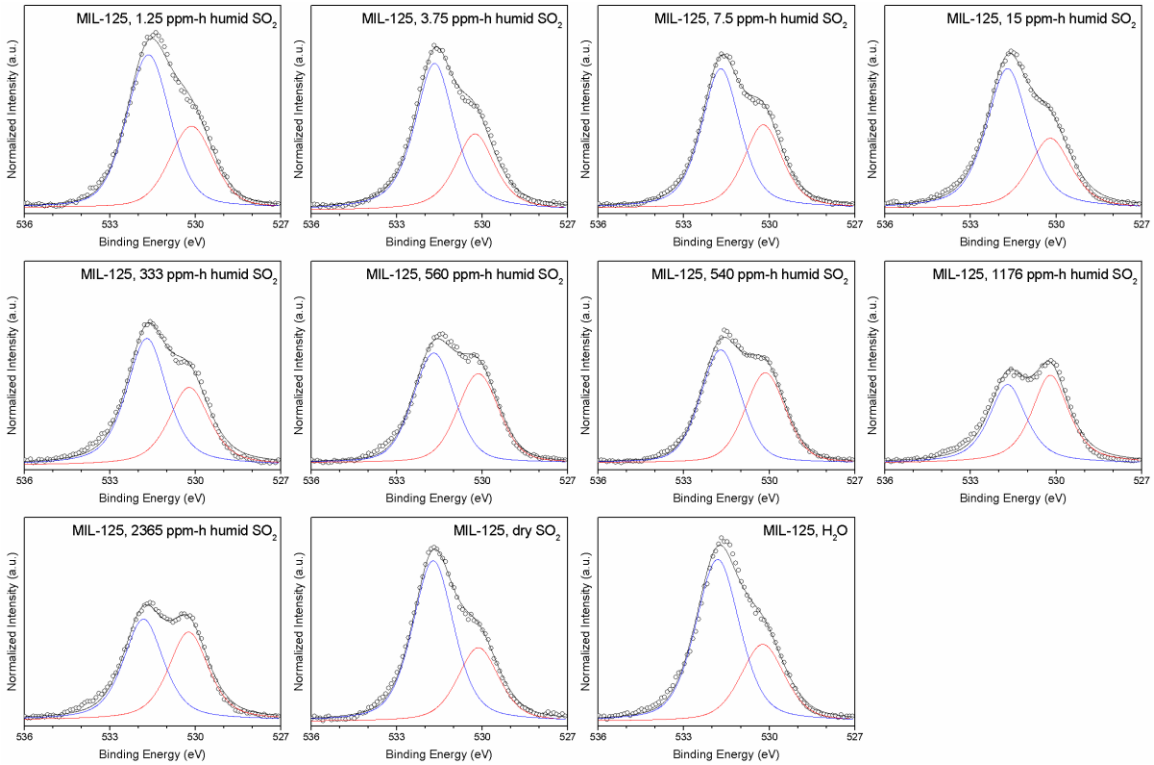

Figure 5.A.9b. High-resolution O1s XP spectra of MIL-125 after timed exposure to humid SO_2 environment, dry SO_2, and water vapor.

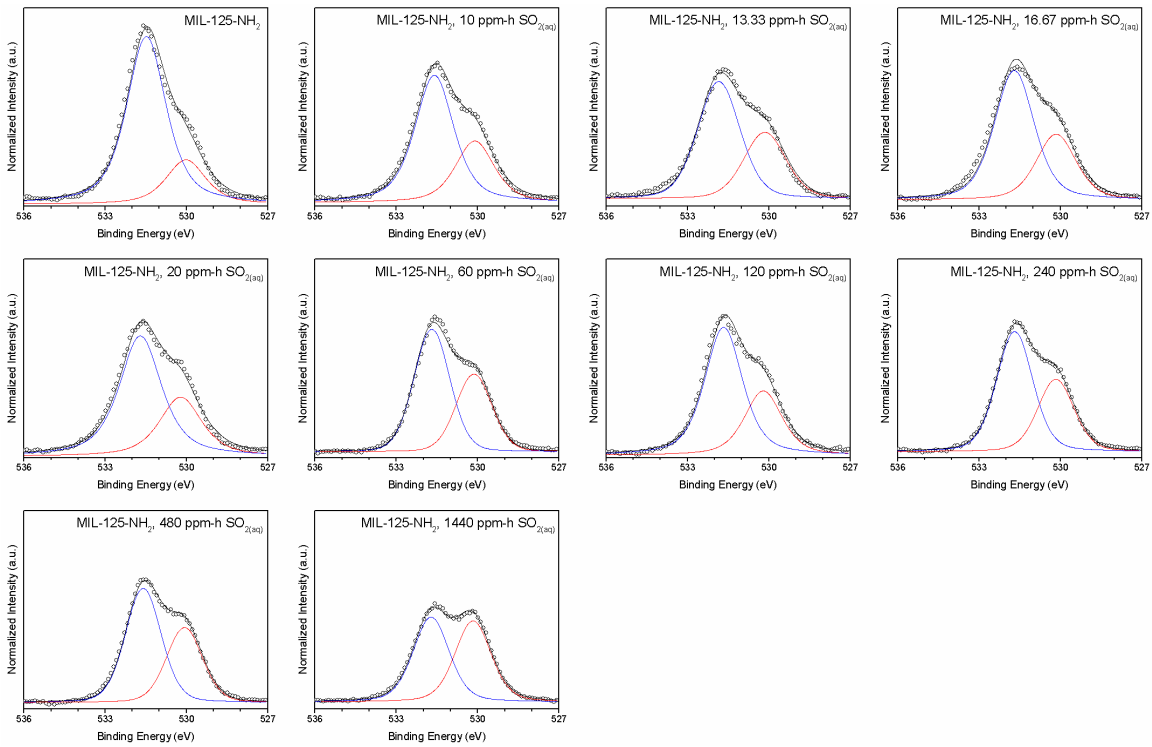

.

Figure 5.A.10a. High-resolution O1s XP spectra of MIL-125-NH_2 after timed exposure to aqueous SO_2 environment.

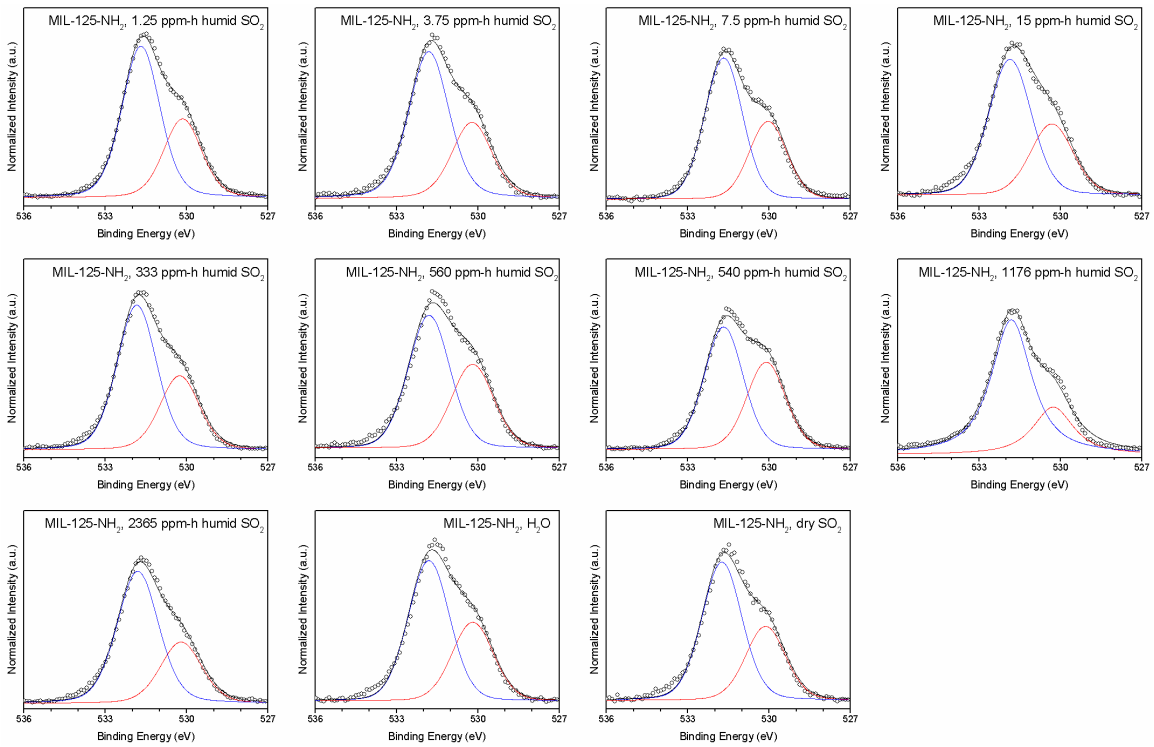

Figure 5.A.10b. High-resolution O1s XP spectra of MIL-125-NH_2 after timed exposure to humid SO_2 environment, dry SO_2, and water vapor.

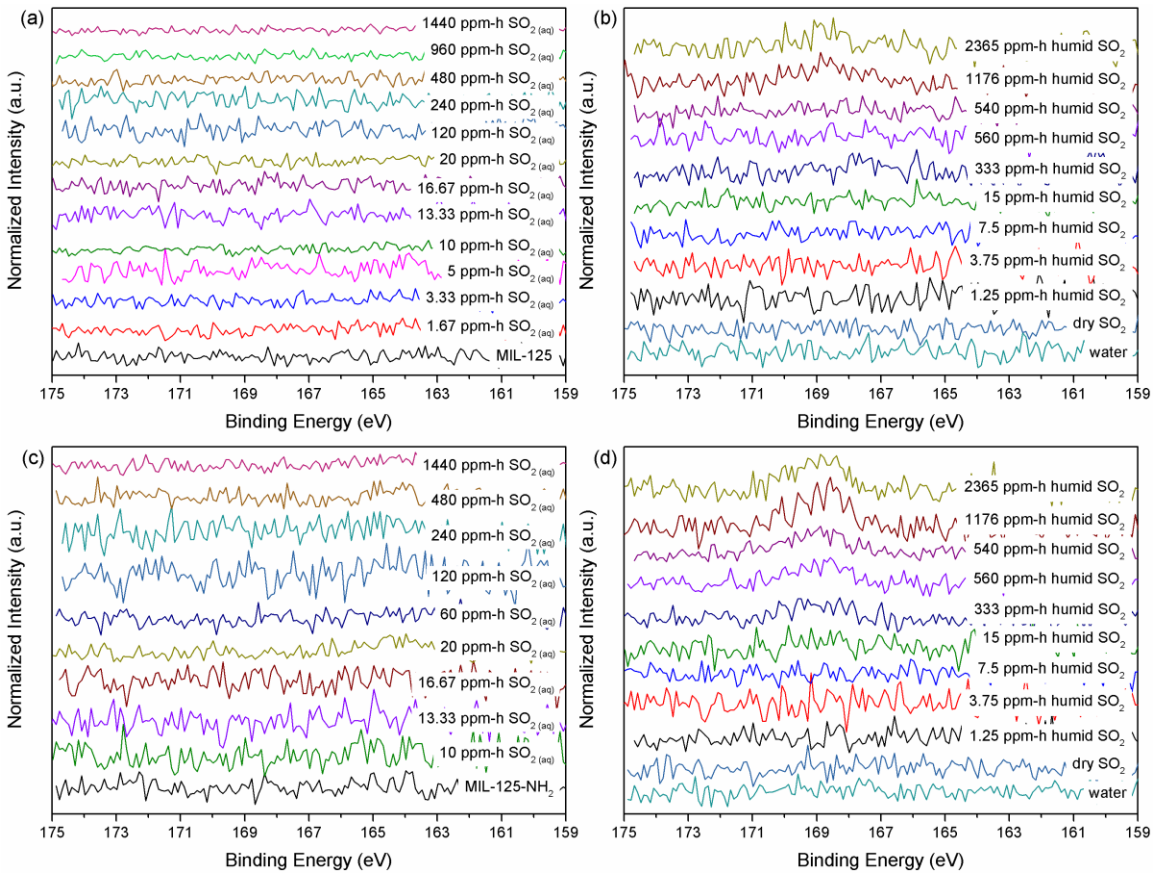

Figure 5.A.11. High-resolution S2p XP spectra of MIL-125 (top) and MIL-125-NH_2 (bottom) after timed exposure to (a,c) aqueous and (b,d) humid SO_2 environment, dry SO_2, and water vapor.

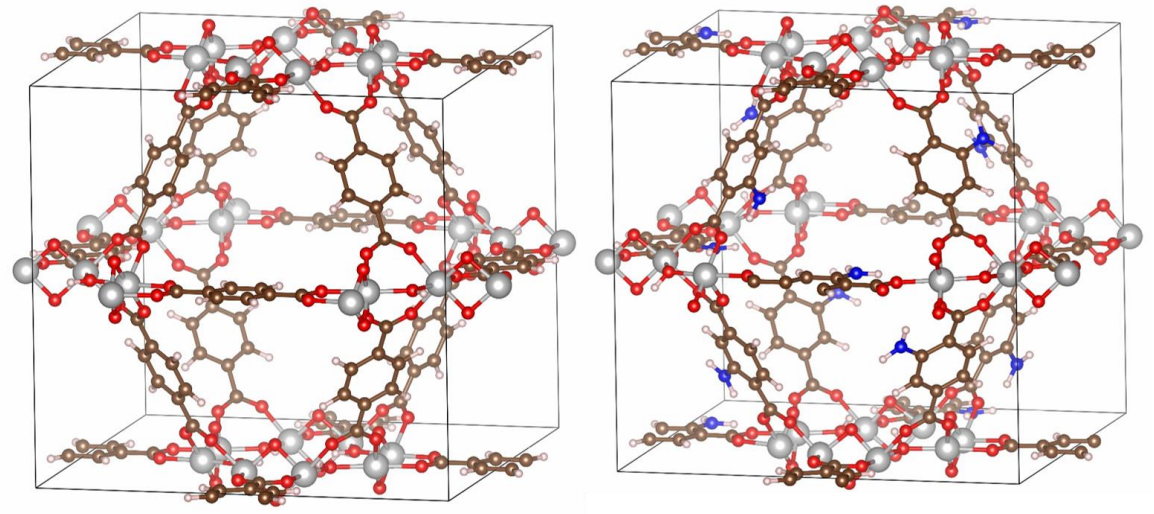

Figure 5.A.12. DFT optimized unit cells of MIL-125 (left) and MIL-125-NH_2 (right). Ti, O, C, H, and N are represented by grey, red, brown, white, and blue balls, respectively.

References

(1) Frisch, M. J.; Trucks, G. W.; Schlegel, H. B.; Scuseria, G. E.; Robb, M. A.; Cheeseman, J. R.; Montgomery, J. A., Jr.; Vreven, T.; Kudin, K. N.; Burant, J. C.; Millam, J. M.; Iyengar, S. S.; Tomasi, J.; Barone, V.; Mennucci, B.; Cossi, M.; Scalmani, G.; Rega, N.; Petersson, G. A.; Nakatsuji, H.; Hada, M.; Ehara, M.; Toyota, K.; Fukuda, R. H., J.; Ishida, M.; Nakajima, T.; Honda, Y.; Kitao, O.; Nakai, H.; Klene, M.; Li, X.; Knox, J. E.; Hratchian, H. P.; Cross, J. B.; Bakken, V.; Adamo, C.; Jaramillo, J.; Gomperts, R.; Stratmann, R. E.; Yazyev, O.; Austin, A. J.; Cammi, R.; Pomelli, C.; Ochterski, J. W.; Ayala, P. Y.; Morokuma, K.; Voth, G. A.; Salvador, P.; Dannenberg, J. J.; Zakrzewski, V. G.; Dapprich, S.; Daniels, A. D.; Strain, M. C.; Farkas, O.; Malick, D. K.; Rabuck, A. D.; Raghavachari, K.; Foresman, J. B.; Ortiz, J. V.; Cui, Q.; Baboul, A. G.; Clifford, S.; Cioslowski, J.; Stefanov, B. B.; Liu, G.; Liashenko, A.; Piskorz, P.; Komaromi, I.; Martin, R. L.; Fox, D. J.; Keith, T.; Al-Laham, M. A.; Peng, C. Y.; Nanayakkara, A.; Challacombe, M.; Gill, P. M. W.; Johnson, B.; Chen, W.; Wong, M. W.; Gonzalez, C.; Pople, J. A. *Gaussian Revision E.01*; Gaussian, Inc.: Wallingford, CT, 2004.

(2) Irikura, K. K.; Johnson, R. D.; Kacker, R. N. *The Journal of Physical Chemistry A* **2005**, *109*, 8430.

CHAPTER 6

SYNERGISTIC EFFECT OF MIXED OXIDE ON THE ADSORPTION OF AMMONIA WITH METAL-ORGANIC FRAMEWORKS

In the previous chapters, the effects of acid gases on MOF adsorption and structural properties were studied to gain insight into the degradation mechanism of MIL-125 and drive the improvement of future MOF materials for applications in harsh environments. This chapter presents an approach to create functional MOF composites with increased adsorption capacity by leveraging favorable properties of a mixed oxide binding material. This Chapter was adapted from W.P. Mounfield, III; M. Taborga Claure; C.W. Jones; K.S. Walton, "Synergistic Effect of Mixed Oxide on the Adsorption of Ammonia with Metal-Organic Frameworks," Industrial & Engineering Chemical Research, 55, 6492-6500 DOI**:** 10.1021/acs.iecr.6b01045. Synthesis of MMO in Chapter 6 was performed by M.T.C.

In this chapter, a hydotalcite-derived MgAl oxide (MMO) with acid-base pairs, previously investigated as a catalyst support,[1-4] was evaluated as a binding material in composites with two promising MOF materials for ammonia adsorption applications. Due to its acid-base sites[5] and known transformation to meixnerite during rehydration,[6] it is hypothesized that MMO/MOF composites will possess additional ammonia capacity. Ammonia adsorption performance was evaluated through ammonia breakthrough experiments in dry and humid conditions to

determine the effect of the addition of the MMO on the MOF materials' performance. UiO-66 and the amine functionalized UiO-66-NH_2 were chosen as the MOF materials for these experiments as they have displayed promising adsorption under dry and humid conditions as well as exhibiting good stability in the harsh ammonia environment.[7,8] In addition to these breakthrough experiments, material stability and textural properties were evaluated through PXRD analysis, FTIR spectroscopy, and N_2 physisorption before and after ammonia exposure. It is expected that the strong water affinity of the MMO, due to its propensity to transform to meixnerite and acid sites, will allow for greater ammonia capacity in wet conditions for the mixed adsorbents over the pure MOF adsorbents. In addition, the origin of an observed synergistic effect on ammonia adsorption performance in humid conditions for the MOF:MMO composites was investigated through water adsorption isotherms.

6.1 Experimental Procedure

Synthesis of UiO-66. The synthesis of UiO-66 was performed using the procedure reported previously by Schoenecker, et al.[9] $ZrCl_4$ (2.73 mmol) and benzene dicarboxylic acid (BDC) (2.73 mmol) were dissolved in 100 mL of DMF. The solution was divided equally between ten 20 mL scintillation vials. The vials were heated in an isothermal oven at 120 °C for 20 hours. The resultant product was rinsed with DMF three times and methanol one time.

Synthesis of UiO-66-NH_2. The synthesis of UiO-66-NH_2 was performed by mixing $ZrCl_4$ and 2-amino terephthalic acid (BDC-NH_2) in DMF in the same molar ratio as the un-functionalized material. The solution was divided equally between ten 20 mL scintillation vials. The vials were heated in an isothermal oven at 120 °C for 20 hours. The resultant product was rinsed with DMF three times and methanol one time.

Synthesis of hydrotalcite and MMO. Hydrotalcite and MMO were synthesized using the same method described in previous studies[1,3,4] by coprecipitation of magnesium nitrate hexahydrate (Alfa Aesar, 98–102%), and aluminum nitrate nonahydrate (Alfa Aesar, 98–102%) aqueous solutions with a Mg:Al molar ratio of 7:3 (0.6 M in metal ions) together with a 1.2 M NaOH (EMD, 97.0%) and 0.15 M Na_2CO_3 (Aldrich, 99.5+%) at 65 °C and a pH of 9.5. The resulting solution was stirred for 48 h, filtered, washed with deionized water, dried overnight at 105 °C to yield hydrotalcite (HT). A portion of the resulting HT was then calcined at 450 °C for 2 h to yield MgAl oxide (MMO).

Preparation of MOF:MMO and MOF:HT composites. UiO-66 and UiO-66-NH_2 were activated at 150 °C overnight under vacuum prior to preparation of composites. Each composite was prepared in a 5:1 ratio by weight of MOF:oxide. 5 mg of MOF and 1 mg of either MMO or HT were ground for 15 minutes to ensure good contact between MOF and oxide particles then stored in a vial in a desiccator prior to characterization or ammonia breakthrough. Prior to fixing the MOF:MMO ratio at 5:1, the performance of three separate compositions were evaluated, as shown in Figure 6.A.1, under dry ammonia breakthrough conditions: 1:1, 9:1, 5:1, and it was determined that a ratio of 5:1 provided the best performance.

Powder X-ray diffraction. Powder X-ray diffraction patterns were recorded on an X'Pert X-ray PANalytical diffractometer with an X'accelerator module using Cu Kα (λ = 1.5418 Å) radiation at room temperature, with a step size of 0.02˚ in two theta (2θ).

N_2 physisorption. Nitrogen physisorption isotherms were measured at 77 K for samples activated at 423 K for 5 h before and after ammonia exposure using the Quadrasorb system from Quantachrome instruments (Figure 6.A.2-3). Nitrogen adsorption analysis was performed on all resulting products, and surface areas were determined by applying BET theory over a range of data points applicable to

microporous materials.[10] N_2 isotherms showed typical Type II behavior for MMO and HT and Type I behavior up to P/P_0=0.95 for all other materials as per the IUPAC classification.

Ammonia breakthrough. The experiment setup schematic can be seen in Scheme S1. Materials in powder form were packed into a quartz bed oriented vertically with an inner diameter of 4 mm against a quartz frit with a bed volume of 20 mm^3. All samples were activated ex situ in an isothermal vacuum oven at 150 °C overnight and then allowed to cool back down to room temperature for 30-45 minutes under vacuum. After cooling, the materials were weighed and loaded into the packed bed. The dry adsorption run was started by switching a N_2 stream to a stream of 1500 ppm NH_3 in air (Airgas) at a rate of 20 ml min^{-1}. For a wet breakthrough run, a humidified stream was created by flowing air at 16 ml min^{-1} through a bubbler, and then combining it with a concentrated NH_3 stream (7155 ppm) at a flow rate of 4 ml min^{-1}. The total mixed stream flowed through the packed bed at a rate of 20 ml min^{-1} with a measured relative humidity of 75% and a calculated NH_3 concentration of 1431 ppm. Time was started as soon as the dilute NH_3 stream was switched on, and data points are taken until the NH_3 returns close to 0 ppm during desorption. The effluent stream was analyzed using an Analytical Technology H10-15 ammonia electrochemical sensor. After the electrochemical sensor reached a reading of 500 ppm NH_3, the NH_3 is switched off to preserve the life of the sensor. The N_2 flow was maintained again at 50 ml min^{-1} to capture the desorption behavior of the bed. An inert bed of sand was used to calculate the dead time within the system, and was subtracted from the total breakthrough time. No significant pressure drop is noted for these conditions. The experimental procedure for wet and dry conditions is identical. The adsorption capacity of each material in mmol of NH_3 per g of adsorbent or per g of MOF was determined by integration of the area above the

breakthrough curve, accounting for the inlet NH_3 concentration, flow rate, breakthrough time, and mass of adsorbent following the method of previous studies.[11,12]

Ammonia temperature programmed desorption (NH_3-TPD). NH_3-TPD experiments were carried out using a Micromeritics AutoChem II 2920 to probe the strength of acidic sites on select MOF:MMO composites. 40 mg of each material was inserted, and each sample was pretreated in flowing He at 200 °C to remove adsorbed H_2O. After cooling, the sample was exposed to 20 ml/min of 2000 ppm NH_3 in He for 2 hours. To obtain the NH_3-TPD profile, the flow was then switched to He and the temperature ramped to 500 °C for the MOF materials and 800 °C for the oxide materials at a rate of 10 °C/min. The effluent stream was analyzed by a Thermal Conductivity Detector (TCD). "Blank" runs were performed for each material to determine the TCD signal resulting from a degradation of the material or loss of compensating anions during heating. The ammonia capacity for each material was calculated by finding the difference in peak area for the NH_3-TPD curve and the blank curve.

FTIR spectroscopy. FTIR spectra were recorded on samples before and after ammonia exposure on a Magna 560 FTIR (Nicolet Instruments) equipped with a DTGS detector in transmission geometry. Samples were prepared in a 1:100 sample:KBr 13 mm pellet. The spectra were collected with an accumulation of 40 scans and a resolution of 4 cm^{-1}. A flow of N_2 at 20 mL/min was maintained during the measurement. The spectra were recorded at room temperature without any pre-treatment of the samples.

Water Vapor Adsorption Isotherms. A 3Flex Surface Characterization Analyzer from Micromeritics was used to collect water vapor isotherms at 22 ˚C for all samples. Prior to water adsorption measurements, samples were activated in a Smart VacPrep from Micromeritics at 175 °C for 12 h under dynamic vacuum. All water vapor isotherms were measured up to $P/P_0 = 0.95$ to avoid water condensation.

6.2 Results and Discussion

6.2.1 Material characterization

Powder X-ray diffraction (PXRD) was used to verify the structures of the MOFs and oxides after synthesis. Figure 6.1 shows the as-synthesized patterns for UiO-66, UiO-66-NH_2, and the hydrotalcite-derived mixed metal oxide (MMO); magnified patterns are shown in Figure 6.A.4. Both unfunctionalized and functionalized UiO-66 materials match the patterns shown in literature.[13] After calcination the crystalline HT (Figure 6.A.5) transforms into MMO with two diffraction peaks at 44° and 64° characteristic of MgO as seen in previous studies.[1] PXRD patterns for the MOF:MMO composites shown in Figure 6.1 closely resemble the MOF patterns, as the intensity of the MOF reflections prevents the observation of MMO reflections. N_2 physisorption isotherms (Figure 6.A.2-3) were collected for each material to determine the surface area and confirm the MOFs were properly activated prior to the preparation of composites for breakthrough experiments. UiO-66 and UiO-66-NH_2 exhibited surface areas (Table 6.1) similar to those observed in literature,[7,8,14] suggesting the washing and activation material allowed for complete removal of any remaining ligand or solvent after synthesis. Furthermore, analysis of FTIR spectra shown in Figure 6.A.6 taken after activation of the materials lacks any band characteristic of the carbonyl group of DMF, supporting the complete removal of the solvent molecules during activation.[14] MMO also possessed a surface area similar to that observed in previous investigations.[1,3] The surface area of the MOF:MMO composites was determined in order to investigate the effect of ammonia adsorption on the adsorbent composites after breakthrough experiments, discussed below. For all composites, a 25-30% reduction in surface area was observed which is associated with the addition of relatively low surface area material (MMO). This observation is consistent with the work of Kim et al.[15] who observed the addition of poly(vinyl alcohol) as binder in MOF composites resulted in over a 40% decrease in the

observed surface area. Moreira et al.[16] made a similar observation noting more than a 20% drop in surface area for graphite/UiO-66 composites.

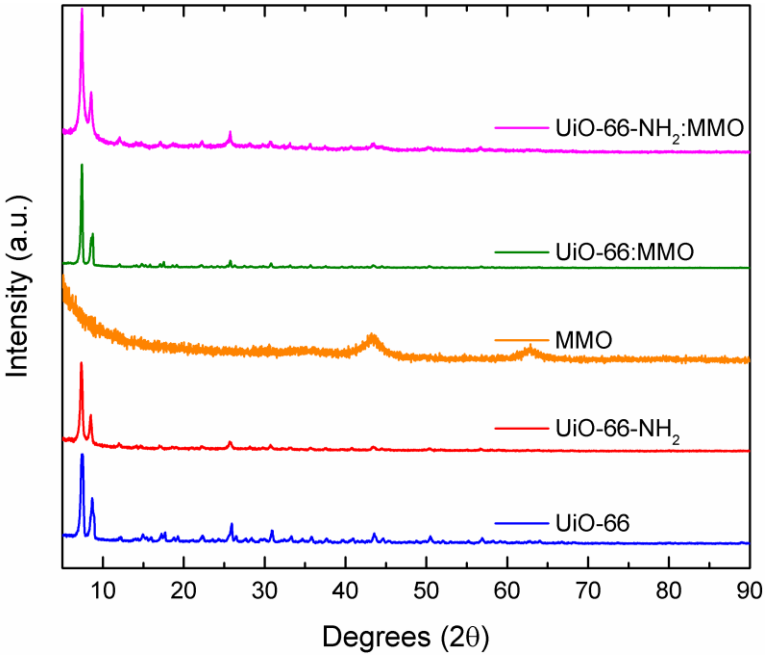

Figure 6.1. PXRD patterns of UiO-66, UiO-66-NH_2, MMO, UiO-66:MMO, and UiO-66-NH_2:MMO composites after synthesis.

Table 6.1. BET surface areas for samples as-synthesized, after dry NH_3 breakthrough experiments, and after wet NH_3 breakthrough experiments.

	No NH_3 exposure	Dry NH_3 exposure	Wet NH_3 exposure
Material	SA_{BET} (m^2/g)	SA_{BET} (m^2/g)	SA_{BET} (m^2/g)
UiO-66	1425	1091	967
UiO-66-NH_2	1232	1138	819
MMO	172	113	143
HT	80	83	69
UiO-66:MMO	1000	826	843
UiO-66:HT	845	824	793
UiO-66-NH_2:MMO	929	779	733

6.2.2 Ammonia breakthrough adsorption experiments

Ammonia breakthrough experiments performed in dry conditions at 25 °C are presented in Figure 6.2(a). Unfunctionalized and functionalized UiO-66 both yielded similar capacities (Table 6.2) to those reported in previous studies.[7,8] UiO-66-NH_2 exhibits a higher ammonia capacity than UiO-66; as expected from a computational investigation of lowest binding energy for various functional groups by Snurr and coworkers.[17] Analysis of the materials' performance on a per mass basis does not yield a decrease in capacity for both MOF:MMO composites, different from what was observed in literature, as a decrease in capacity is often observed with the addition of low surface area binder materials that have little to no adsorption capacity when combined with MOFs.[15,18] MMO itself possesses poor adsorption performance, 0.68 mmol/g, and a linear combination of the MOF and MMO capacity would suggest a loss in performance. The fact that this loss in capacity is not observed is the first indication that MMO can provide a synergistic effect for the adsorption of ammonia in combination with MOFs, an effect discussed further below. Figure 6.2(b) illustrates the effect of the addition of MMO by normalizing the capacity on a per volume basis. While MMO displays weak adsorption with instantaneous breakthrough of ammonia upon adsorption, when combined with UiO-66 the composite possesses a measurable positive shift in breakthrough time and capacity. A similar, albeit less emphasized increase is observed for the combination of MMO and UiO-66-NH_2 illustrating the non-negative influence of adding the MMO to the composite. It is hypothesized that the synergistic effect (no decrease in capacity with the addition of MMO) observed in dry conditions is the result of cooperative interactions between adsorbed ammonia molecules in the MMO and UiO-66, as discussed below.

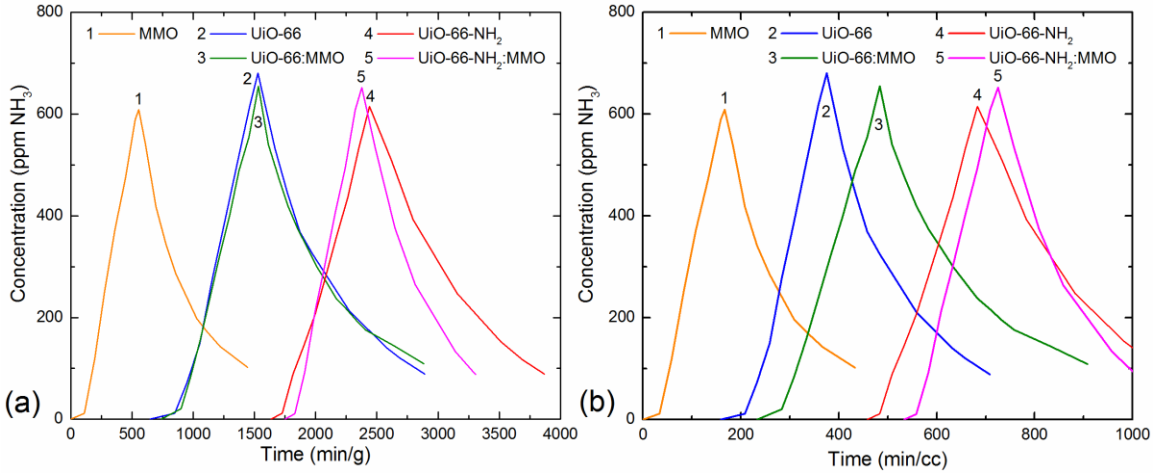

Figure 6.2. Breakthrough and desorption curves for MMO, UiO-66, UiO-66-NH_2, UiO-66:MMO, and UiO-66-NH_2:MMO under dry conditions. Time is normalized either by (a) gram of total adsorbent mass in g or (b) total bed volume in cm^3.

Performing ammonia breakthrough experiments in wet conditions allows assessment of the materials' performance in conditions that simulate real-world application as well as further insight into the synergistic effect of the addition of MMO. Humid experiments performed at 80 %RH and 25 °C are presented in Figure 6.3. Unfunctionalized and functionalized UiO-66 again yielded similar capacities (Table 6.2) to those reported in previous studies.[7,8] MMO displayed a similar, almost instantaneous breakthrough, but slower adsorption than observed in dry conditions. This slower adsorption, present for all materials, has been observed in other breakthrough studies[7,19] and is hypothesized to be due to slower diffusion through the composite due to the presence of water and strong ammonia-water-framework interactions. The mixture of MMO and unfunctionalized UiO-66 results in a large measurable increase in the breakthrough time and associated ammonia capacity, 2.63 to 5.06 mmol/g, as illustrated in Figure 6.3 and Table 6.2. The functionalized composite also experiences a similar increase in adsorption capacity, 3.18 to 4.06 mmol/g. It is hypothesized that the observed increase in capacity is the result of cooperative interactions between adsorbed water and ammonia in MMO, but also the ability of MMO to act as a water adsorbent and

leave open adsorption sites in UiO-66 and UiO-66-NH_2 that are occupied by water in the pure material. This hypothesis is investigated further with water adsorption experiments and discussed below.

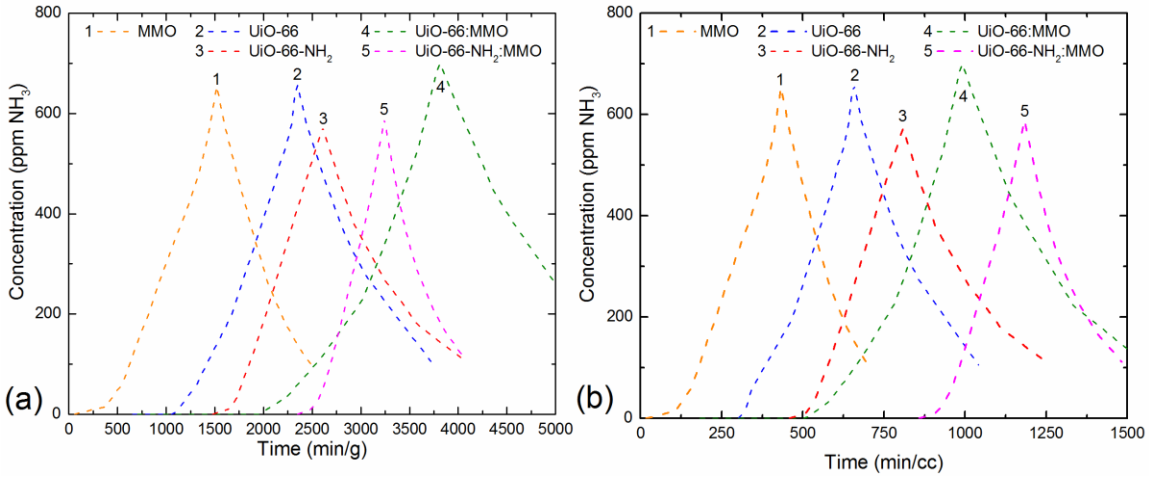

Figure 6.3. Breakthrough and desorption curves for MMO, UiO-66, UiO-66-NH_2, UiO-66:MMO, and UiO-66-NH_2:MMO under wet conditions. Time is normalized either by (a) gram of total adsorbent mass in g or (b) total bed volume in cm^3.

Table 6.2. Calculated dynamic ammonia capacity for all materials and composites. Breakthrough capacity is calculated by extrapolation and integration to 1500 ppm/1483 ppm, respectively. Values shown in parentheses are normalized per gram of MOF.

	Dry NH_3 exposure	Wet NH_3 exposure
Material	Capacity (mmol/g)	Capacity (mmol/g)
UiO-66	1.84	2.63
UiO-66-NH_2	3.25	3.18
MMO	0.68	1.50
HT	0.66	1.25
UiO-66:MMO	1.89 (2.26)	5.06 (6.07)
UiO-66:HT	1.51 (1.81)	2.00 (2.40)
UiO-66-NH_2:MMO	3.48 (4.18)	4.06 (4.87)

6.2.3 Characterization of materials after ammonia adsorption

A multiple use ammonia adsorbent must not only display strong adsorption but retain its textural properties after exposure. Therefore, all materials and composites were characterized via powder X-ray diffraction to verify the retention of structure of the MOFs and MMO after synthesis. Figure 6.4 shows the patterns for UiO-66, UiO-66-NH_2, MMO and the composites thereof after exposure to wet and dry ammonia. Both the unfunctionalized and functionalized UiO-66 materials and MOF:MMO composites match the as-synthesized patterns shown. As noted previously, MMO has a poorly crystalline pattern that does not exhibit strong diffraction peaks and therefore is not discernable in the composite patterns. However, it is important to note that the MMO after wet ammonia exposure has not experienced the “memory” effect seen in literature, where, upon extended exposure to water, MMO transforms to the highly crystalline meixnerite.[6,20,21] This memory effect is likely not observed in the samples containing MMO as they are not exposed to the humidified stream for a sufficient time to effect the restructuring of MMO into meixnerite.

In addition to analysis of the PXRD patterns, N_2 physisorption isotherms (Figure 6.A.2-3) were collected for each material after exposure to determine changes in porosity upon ammonia adsorption. UiO-66 and UiO-66-NH_2 exhibited a 23% and 7% decrease, respectively, in surface area after dry exposure (Table 6.1), while a 32% and 33% decrease was observed after wet exposure indicating the co-adsorption of ammonia and water leads to either a degradation of the material or more likely the presence of strongly adsorbed species that are unable to be removed at the chosen activation temperature.[7,8] MMO experienced a 34% decrease in surface area upon dry exposure; however, a less significant, 17%, decrease was observed after wet exposure. This leads to the hypothesis that MMO under wet conditions primarily adsorbs a large amount of water (consistent with the beginning of a transformation to meixnerite),[6] with

additional ammonia adsorption occurring due to interactions with this adsorbed water.[22] The ammonia species formed due to interaction with adsorbed water are likely weakly adsorbed species compared to the directly adsorbed ammonia species formed during dry exposure, and these species are then more easily removed under the chosen activation conditions leading to less decrease in the surface area after wet exposure. Composites of UiO-66/UiO-66-NH_2 and MMO experienced a drop in surface area corresponding to a linear combination of the decrease observed for each material, further suggesting that the decrease in surface area observed after ammonia adsorption is the result of strongly adsorbed species rather than a degradation of the materials. If degradation was occurring, a more drastic decrease in surface area would be observed for the composites due to degradation of the structure by the large amount of ammonia and water, an effect observed in less stable MOF materials during water adsorption but not in the UiO-66 materials.[23,24]

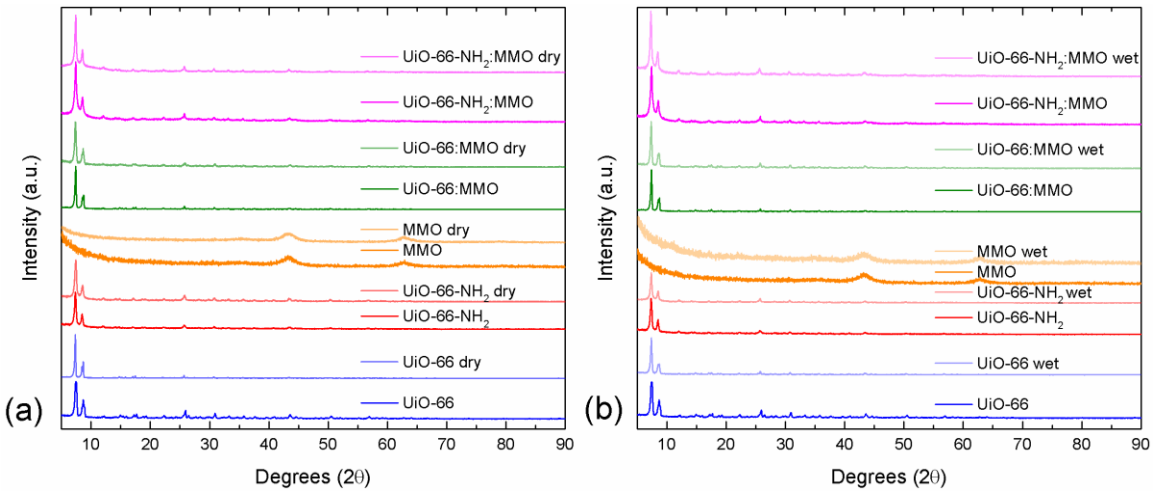

Figure 6.4. PXRD patterns for materials and composites after (a) dry and (b) wet ammonia adsorption experiments.

In addition to X-ray diffraction and N_2 physisorption, FTIR spectroscopy was used to further examine changes in the materials after exposure to ammonia. As shown in Figure 6.A.6, the FTIR spectra for UiO-66 and UiO-66-NH_2 match those spectra found in

literature,[8,13,25] and do not undergo any change after exposure to dry or wet ammonia, suggesting there is little or no change in the structure or functionalization of the material. Neither MMO, HT nor their composites with UiO-66 or UiO-66-NH_2 display any change in spectra after exposure, suggesting the oxide materials are also largely unaffected by ammonia exposure. Any potential residual ammonia molecules that could give insight into the reduction in surface area observed after exposure are present in concentrations too low to be measured accurately with this method. Subsequent studies should be performed using in situ IR techniques to determine adsorbed ammonia species on these materials.

6.2.4 Synergistic effect of MMO

As stated previously, the combination of MMO and UiO-66 results in a measureable increase in ammonia adsorption in humid conditions, while maintaining performance in dry conditions when normalized on a per gram basis. This observation leads to a hypothesis that the synergistic effect of MMO is two-fold, where MMO serves to prevent a portion of the water present during humid experiments from adsorbing in the MOF framework, thereby allowing additional ammonia to be adsorbed therein, as well as having cooperative interactions between adsorbed water and ammonia in the MMO. This hypothesis is consistent with the work of Pérez-Ramírez et al., who reported the transformation from a hydrotalcite-derived MgAl oxide to meixnerite in 2 vol% water stream would occur in approximately 30 min.[6] These findings support the strong affinity and rapid uptake of water into the MMO structure and imply that given a sufficient exposure time and water concentration level, MMO would transform to meixnerite. However, as UiO-66 also possesses strong affinity for water,[9] MMO likely slowly incorporates hydroxyl ions during the humid breakthrough experiments, which will interact with ammonia molecules, but are not present in sufficient quantities to change

the structure to meixnerite during the course of the experiment. As mentioned above, water that is adsorbed in the MMO can have cooperative interactions with ammonia in the form of hydrogen bonding and strengthen the interaction of the MMO with ammonia,[22] also increasing adsorption. To investigate the validity of this hypothesis, ammonia adsorption was performed in both wet and dry conditions for the HT parent material. As seen in Figure 6.A.7, the ammonia adsorption for HT is very similar to that of MMO in dry conditions with almost instantaneous breakthrough observed, indicating that this material itself has poor interaction with ammonia in dry conditions. In wet conditions, MMO has slightly higher adsorption than HT; this is likely due to MMO's strong affinity for water adsorption[6] and subsequent water-hydrogen bonding with ammonia. HT possesses carbonate anions that are removed upon calcination to obtain MMO; the abundant presence of these carbonate anions leads to less available sites for adsorption of ammonia and the prevention of cooperative effects observed in MMO. In addition, HT has a similar (almost instantaneous) breakthrough time (Figures 6.A.7, 6.A.8) for both dry and wet conditions, with breakthrough under wet conditions occurring at a slightly slower rate due to additional interactions between adsorbed water and ammonia. A composite of HT and unfunctionalized UiO-66 was tested under dry and wet ammonia breakthrough conditions. Figures 6.A.7, 6.A.8 and Table 6.2 illustrate that UiO-66 under dry conditions experiences a drop in capacity from 1.84 mmol/g for the pure UiO-66 to 1.51 mmol/g for the composite with HT, and normalizing the breakthrough capacity per gram of MOF yields a value of 1.81 mmol/g, similar to that of the pure UiO-66, supporting the notion that the HT material has very weak interactions with ammonia and does not provide any synergistic effect after mixing with UiO-66. Furthermore, the breakthrough time for the composite in wet conditions is almost identical to that under dry conditions, further supporting the hypothesis that the presence of the carbonate anions in HT reduces the amount and strength of water and

subsequently ammonia adsorbed and thereby prevents the same level of cooperative effects as seen with MMO from occurring.

The addition of a poorly performing material such as MMO should result in a measurable decrease in ammonia adsorption capacity for the UiO-66:MMO composite; instead the capacity is maintained. It is hypothesized that this effect is caused by the close proximity of the MMO and MOF. To investigate this effect, ammonia TPD experiments were performed on UiO-66, UiO-66-NH_2, MMO, and HT.[1] As shown in Figure 6.A.9, UiO-66 displays weak peaks at 95 °C and 250 °C with a strong peak at 490 °C. The strong peak observed at 490 °C and a portion of the peak at 250 °C for all UiO-66 containing samples are attributed to the degradation of the framework as the same peaks are observed for an experiment without an ammonia adsorption step (the temperature approaches the thermal stability limit of UiO-66 in helium).[14] UiO-66-NH_2 displays a similar weak peak at 95 °C with a second peak shifted from 250 °C to 350 °C indicating stronger adsorption of ammonia in the amine-functionalized framework; supported by the increase in dry breakthrough capacity over the unfunctionalized UiO-66. Due to the lack of open metal sites in UiO-66, the majority of ammonia-framework interactions are physical in nature;[23] therefore, it is hypothesized that the addition of MMO is able to enhance and strengthen the interaction of ammonia with UiO-66 by strengthening the hydrogen bonding between ammonia molecules[26] and in the case of humid adsorption, promote and strengthen ammonia-water hydrogen bonding.[22] This hypothesis is consistent with the findings of Van Humbeck et al.[26], who reported an increase in ammonia adsorption due to cooperative hydrogen bonding in MOF frameworks and Nijem et al.[22], who reached similar conclusions studying water-ammonia interactions and subsequent effects on ammonia adsorption observed with the presence of co-adsorbed water on CuBTC. The large, intense peak centered at 315 °C for HT is attributed to a loss of the compensating carbonate anions, confirmed by

TPD experiments performed without ammonia adsorption. The total ammonia adsorbed from TPD for HT shown in Table 6.A.1 is very small, 0.077 mmol/g, suggesting HT has weak interaction and has only physical adsorption of ammonia. The amount of ammonia adsorbed over MMO is much higher than HT and similar to values reported in literature for MgAl oxides;[27] however, as shown in Table 6.2, the capacity of these materials during dry ammonia breakthrough experiments (accounting for both physisorbed and chemisorbed species rather than solely chemisorbed) is similar. Therefore, MMO possesses a higher degree of chemisorption than HT and contributes to the synergistic effect between UiO-66 and MMO by strongly binding ammonia and strengthening ammonia-ammonia interactions in the UiO-66:MMO composite under dry conditions.

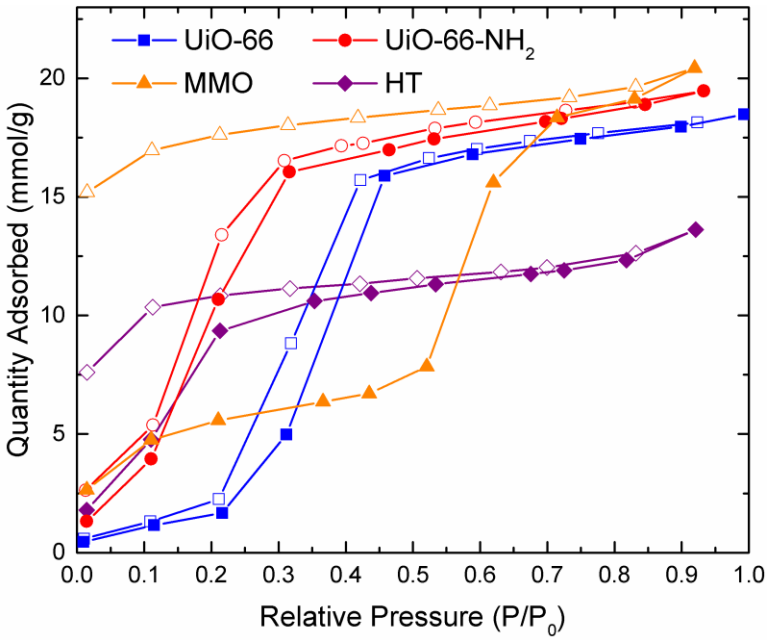

Figure 6.5. Water adsorption isotherms for UiO-66, UiO-66-NH_2, MMO, and HT. Solid symbols indicate adsorption, open symbols indicate desorption. P_0 = 20.5 mmHg

In addition to ammonia adsorption experiments with HT and ammonia TPD studies, water adsorption experiments were performed on each material to elucidate the materials' water adsorption affinity. Figure 6.5 illustrates the water adsorption isotherms for each material. HT adsorbs the least amount of water due to carbonate anions

occupying likely adsorption sites and retains 7.6 mmol/g after desorption, due to the strong interaction of the carbonate anions and water molecules. MMO adsorbs the largest amount of water, 20.4 mmol/g; however, the adsorption at low relative pressure ($P/P_0 < 0.5$) is less than the parent HT material. The large step increase in adsorption observed at $P/P_0 > 0.5$ is explained by the presence of mesopores in MMO, where at low relative pressure, water experiences only interactions with the pore wall and at high relative pressure, water is able to cluster within the pore and the adsorption increases drastically, and effect that has been observed and explored in computational and experimental studies.[28-31] Similar to the parent HT material, MMO retains a large amount of water upon desorption, 15.2 mmol/g, illustrating the strong interaction of MMO with water. As shown in previous studies,[9] UiO-66 and UiO-66-NH_2 adsorb large amounts of water, considerably more than HT, 18.5 and 19.5 mmol/g, respectively, yet retain less than 2.6 mmol/g after desorption indicating weak and reversible interactions with water. It is evident from the UiO-66 and UiO-66-NH_2 isotherms that the prevention or reduction of water adsorption at high humidity levels will be beneficial for adsorption and leave additional open sites for ammonia adsorption. It is important to note that MMO adsorbs a larger quantity of water than either UiO-66 material under the high relative pressure conditions that ammonia adsorption experiments are conducted under, suggesting it can be effective in withdrawing the water from the MOF material and allowing additional adsorption to take place at the now unoccupied adsorption sites. In addition, the water adsorbed in the MMO would leverage the solubility of ammonia in the adsorbed water within the pore and result in additional ammonia adsorption, an effect that has been previously observed by measuring surface pH after ammonia adsorption in layered graphitic oxides.[11]

A series of three ammonia breakthrough experiments were performed on the UiO-66:MMO composite to determine if the synergistic effect is retained after

reactivation and to evaluate the composites for multi-use applications. Wet conditions were chosen to elucidate the effect of regeneration on the synergistic effect observed under these conditions for a single breakthrough test. Ammonia TPD experiments in Figure 6.A.9 show that the majority of ammonia is desorbed for all materials before 200 °C; therefore, after each run, the composite was regenerated in situ at 200 °C under flowing N_2. As shown in Figure 6.A.10, the initial breakthrough time remains the same for the composite after each regeneration, suggesting the synergistic effect is preserved for the composite after multiple exposures. It is hypothesized that after reactivation the remaining strongly adsorbed water and ammonia species result in a decrease of mass transfer resistance within the sample, as a sharper breakthrough curve is observed for each subsequent cycle.[32] The presence of these strongly adsorbed species is expected to shift the breakthrough curve to shorter times; however, the initial breakthrough time for this composite is preserved as these species promote cooperative interactions with additional adsorbed species, as discussed above. The presence of these strongly adsorbed species is supported by an 11.6% decrease in surface area of the composite after three exposures (745 m^2/g) from the surface area of the composite after one exposure (843 m^2/g). The 11.6% decrease in surface area is less than the 15.7% decrease experienced after initial exposure, suggesting the surface area of the composite and; therefore, the available adsorption sites, are reaching equilibrium.

6.3 Conclusions

The synergistic effect on ammonia adsorption performance observed for the combination of hydrotalcite-derived mixed MgAl oxide, MMO, with UiO-66 was investigated. Addition of MMO to UiO-66 in a 5:1 MOF:MMO ratio resulted in almost a two-fold increase in wet ammonia adsorption performance above the pure MOF capacity, although the MMO alone possesses poor performance. The effect in humid

conditions is hypothesized to be two-fold, benefiting from a water withdrawing effect allowing adsorption sites to remain open for ammonia adsorption and the solubility of ammonia in the water adsorbed on the MMO. In dry conditions, the addition of MMO did not negatively affect adsorption performance, usually the case with the addition of a poorly adsorbing binding material. The traditional stability of UiO-66 was maintained with the addition of MMO with no change observed in PXRD patterns or FTIR spectra and the observed drop in surface area attributed to the presence of strongly bound ammonia species that were not removed during reactivation. These composites showed promise as multi-use adsorbents, as the initial breakthrough capacity and synergistic effect was preserved through three consecutive exposures for the UiO-66:MMO composite in wet conditions. Additional studies focusing on the cyclic stability of these composites will be important to elucidate their application as multi-use adsorbents. UiO-66 and UiO-66-NH_2 have proven to be stable ammonia adsorbents;[7,8] therefore, the cyclic stability of these composites will depend largely on the ability of the process to delay the memory effect of the MMO and maintain the synergistic effect of the composite. Additional investigations focusing on ammonia adsorbed species with in situ IR techniques could confirm the hypotheses presented above. The ability to maintain or improve performance while maintaining material stability with the addition of a binding material presents a promising outlook for development of engineered forms of MOF materials.

6.4 References

(1) Taborga Claure, M.; Chai, S.-H.; Dai, S.; Unocic, K. A.; Alamgir, F. M.; Agrawal, P. K.; Jones, C. W. *J. Catal.* **2015**, *324*, 88.

(2) Taborga Claure, M.; Morrill, M. R.; Goh, J. W.; Chai, S.-H.; Dai, S.; Agrawal, P. K.; Jones, C. W. *Catal. Sci. Technol.* **2016**.

(3) Morrill, M. R.; Thao, N. T.; Shou, H.; Davis, R. J.; Barton, D. G.; Ferrari, D.; Agrawal, P. K.; Jones, C. W. *ACS Catal.* **2013**, *3*, 1665.

(4) Morrill, M. R.; Thao, N. T.; Agrawal, P. K.; Jones, C. W.; Davis, R. J.; Shou, H.; Barton, D. G.; Ferrari, D. *Catal. Lett.* **2012**, *142*, 875.

(5) Kozlowski, J. T.; Davis, R. J. *ACS Catal.* **2013**, *3*, 1588.

(6) Perez-Ramirez, J.; Abello, S.; van der Pers, N. M. *Chem.--Eur. J.* **2007**, *13*, 870.

(7) Jasuja, H.; Peterson, G. W.; Decoste, J. B.; Browe, M. A.; Walton, K. S. *Chem. Eng. Sci.* **2015**, *124*, 118.

(8) Peterson, G. W.; DeCoste, J. B.; Fatollahi-Fard, F.; Britt, D. K. *Ind. Eng. Chem. Res.* **2014**, *53*, 701.

(9) Schoenecker, P. M.; Carson, C. G.; Jasuja, H.; Flemming, C. J. J.; Walton, K. S. *Ind. Eng. Chem. Res.* **2012**, *51*, 6513.

(10) Walton, K. S.; Snurr, R. Q. *J. Am. Chem. Soc.* **2007**, *129*, 8552.

(11) Seredych, M.; Bandosz, T. J. *Langmuir* **2010**, *26*, 5491.

(12) Bashkova, S.; Bandosz, T. J. *J. Colloid Interface Sci.* **2014**, *417*, 109.

(13) Garibay, S. J.; Cohen, S. M. *Chem. Commun.* **2010**, *46*, 7700.

(14) Jasuja, H.; Walton, K. S. *J. Phys. Chem. C* **2013**, *117*, 7062.

(15) Kim, J.; Kim, S.-H.; Yang, S.-T.; Ahn, W.-S. *Micro. Meso. Mater.* **2012**, *161*, 48.

(16) Moreira, M. A.; Santos, J. C.; Ferreira, A. F. P.; Loureiro, J. M.; Ragon, F.; Horcajada, P.; Shim, K.-E.; Hwang, Y.-K.; Lee, U. H.; Chang, J.-S.; Serre, C.; Rodrigues, A. E. *Langmuir* **2012**, *28*, 5715.

(17) Kim, K. C.; Yu, D.; Snurr, R. Q. *Langmuir* **2013**, *29*, 1446.

(18) DeCoste, J. B.; Denny, J. M. S.; Peterson, G. W.; Mahle, J. J.; Cohen, S. M. *Chem. Sci.* **2016**.

(19) Peterson, G. W.; Wagner, G. W.; Balboa, A.; Mahle, J.; Sewell, T.; Karwacki, C. J. *J. Phys. Chem. C* **2009**, *113*, 13906.

(20) Takehira, K.; Shishido, T.; Shoro, D.; Murakami, K.; Honda, M.; Kawabata, T.; Takaki, K. *Catal. Commun.* **2004**, *5*, 209.

(21) Nunan, J. G.; Herman, R. G.; Klier, K. *J. Catal.* **1989**, *116*, 222.

(22) Nijem, N.; Fürsich, K.; Bluhm, H.; Leone, S. R.; Gilles, M. K. *J. Phys. Chem. C* **2015**.

(23) DeCoste, J. B.; Peterson, G. W.; Schindler, B. J.; Killops, K. L.; Browe, M. A.; Mahle, J. J. *J. Mater. Chem. A* **2013**, *1*, 11922.

(24) Burtch, N. C.; Jasuja, H.; Walton, K. S. *Chem. Rev.* **2014**, *114*, 10575.

(25) Kandiah, M.; Usseglio, S.; Svelle, S.; Olsbye, U.; Lillerud, K. P.; Tilset, M. *J. Mater. Chem.* **2010**, *20*, 9848.

(26) Dixit, M.; Mishra, M.; Joshi, P. A.; Shah, D. O. *J. Ind. Eng. Chem.* **2013**, *19*, 458.

(27) Di Cosimo, J. I.; Apesteguía, C. R.; Ginés, M. J. L.; Iglesia, E. *J. Catal.* **2000**, *190*, 261.

(28) Bellarosa, L.; Calero, S.; López, N. *Phys. Chem. Chem. Phys.* **2012**, *14*, 7240.

(29) De Toni, M.; Jonchiere, R.; Pullumbi, P.; Coudert, F. X.; Fuchs, A. H. *ChemPhysChem* **2012**, *13*, 3497.

(30) Tan, K.; Nijem, N.; Canepa, P.; Gong, Q.; Li, J.; Thonhauser, T.; Chabal, Y. J. *Chem. Mater.* **2012**, *24*, 3153.

(31) Mounfield III, W. P.; Walton, K. S. *J. Colloid Interface Sci.* **2015**, *447*, 33.

(32) Ruthven, D. M. *Principles of adsorption and adsorption processes*; John Wiley & Sons, 1984.

APPENDIX 6.A

MOF:MMO COMPOSITE CHARACTERIZATION AND PERFORMANCE EVALUATION

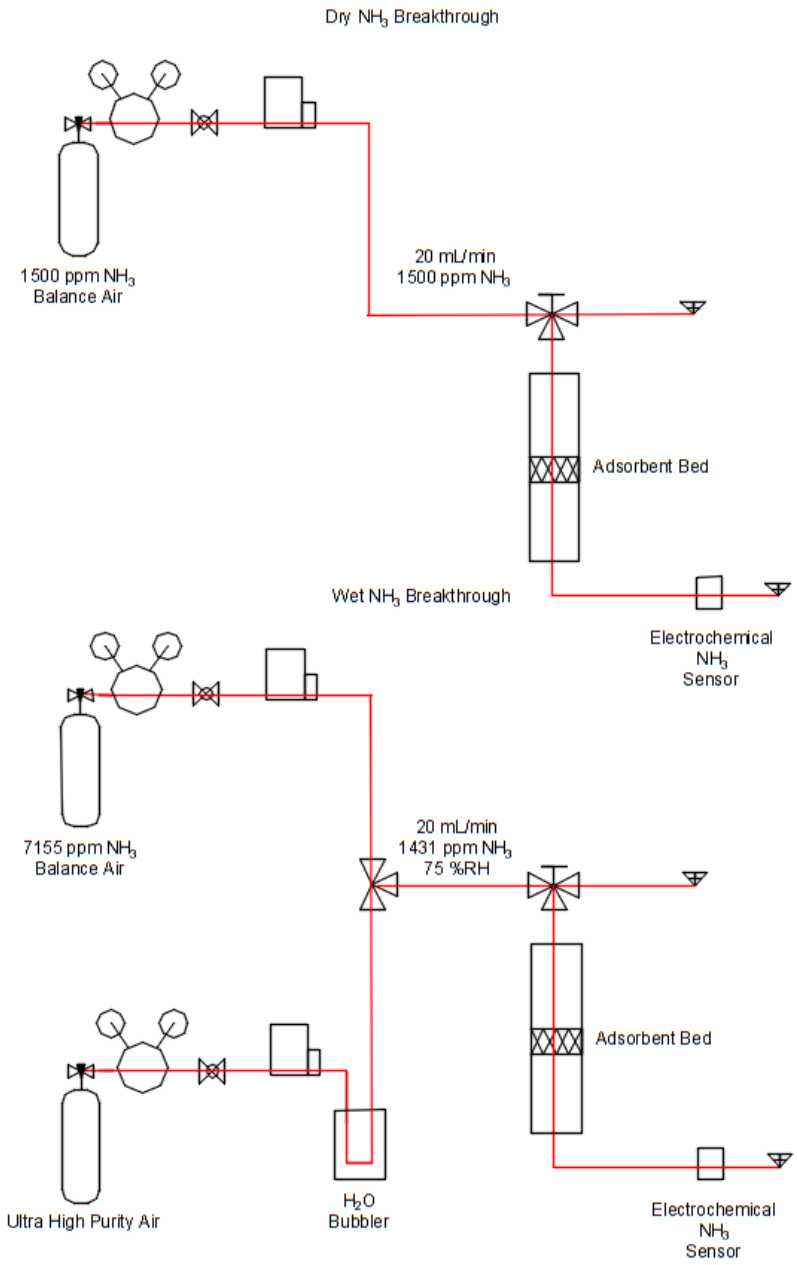

Scheme 6.A.1. P&ID diagram of the breakthrough system apparatus under (top) dry conditions (bottom) humid conditions

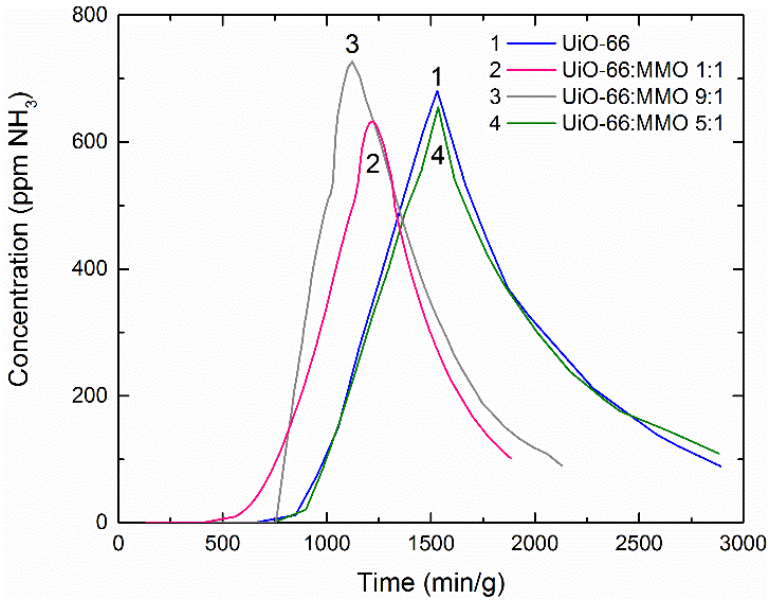

Figure 6.A.1. Breakthrough and desorption curves for UiO-66 and UiO-66:MMO in 1:1, 9:1, and 5:1 ratios under dry conditions. Time is normalized by gram of total adsorbent mass in g.

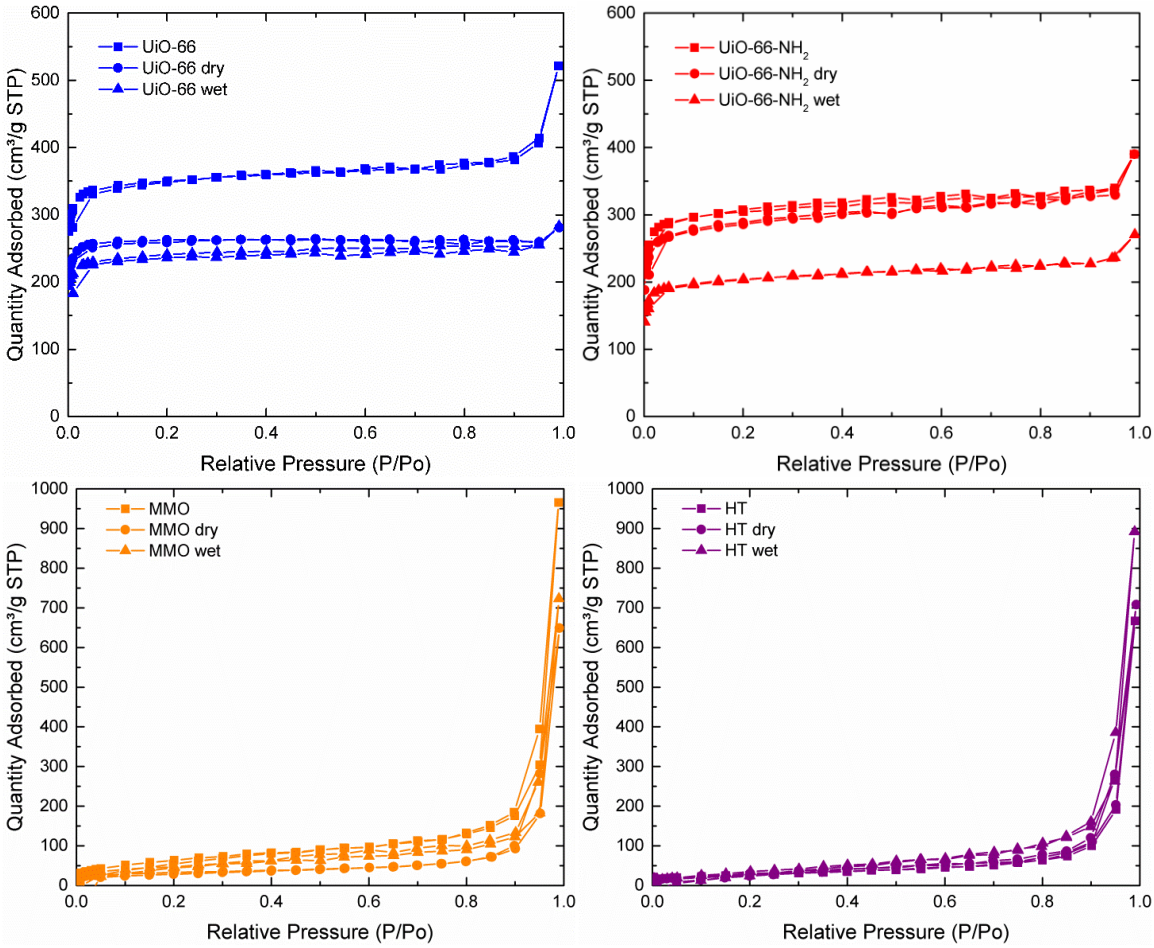

Figure 6.A.2. N_2 adsorption isotherms for UiO-66, UiO-66-NH_2, MMO, and HT after synthesis and after dry and wet ammonia breakthrough experiments.

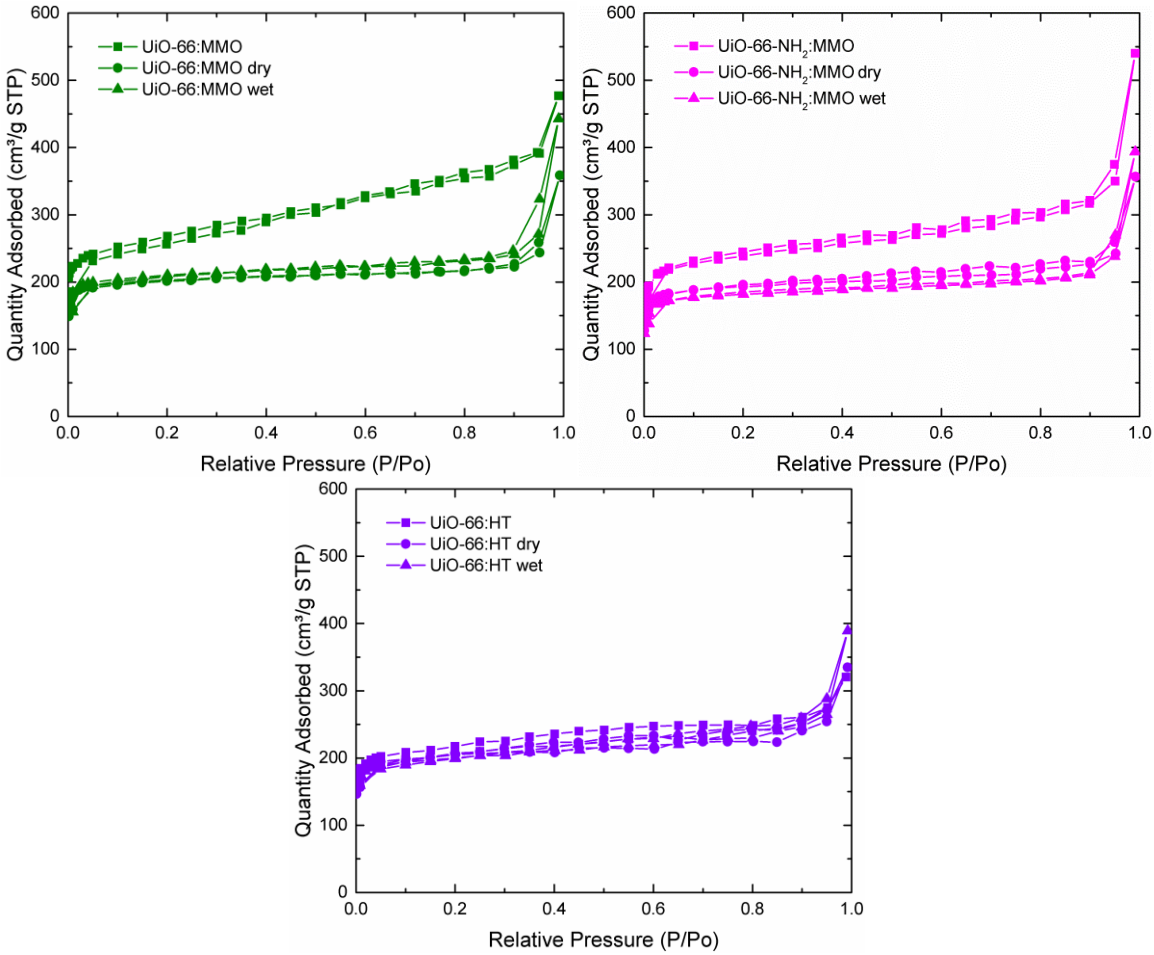

Figure 6.A.3. N_2 adsorption isotherms for UiO-66:MMO, UiO-66-NH_2:MMO, and UiO-66:HT after synthesis and after dry and wet ammonia breakthrough experiments.

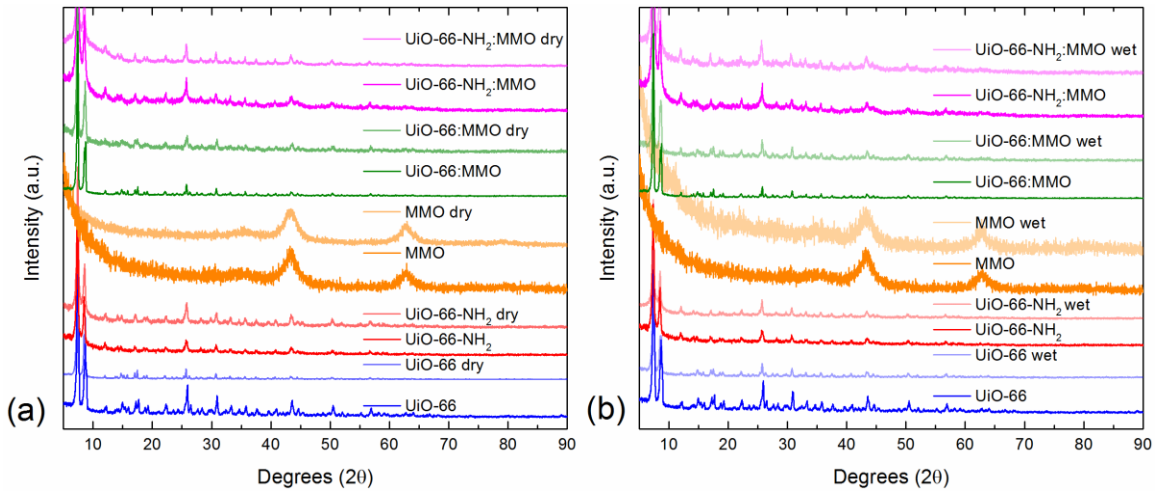

Figure 6.A.4. Magnified PXRD patterns for materials and composites after (a) dry and (b) wet ammonia adsorption experiments.

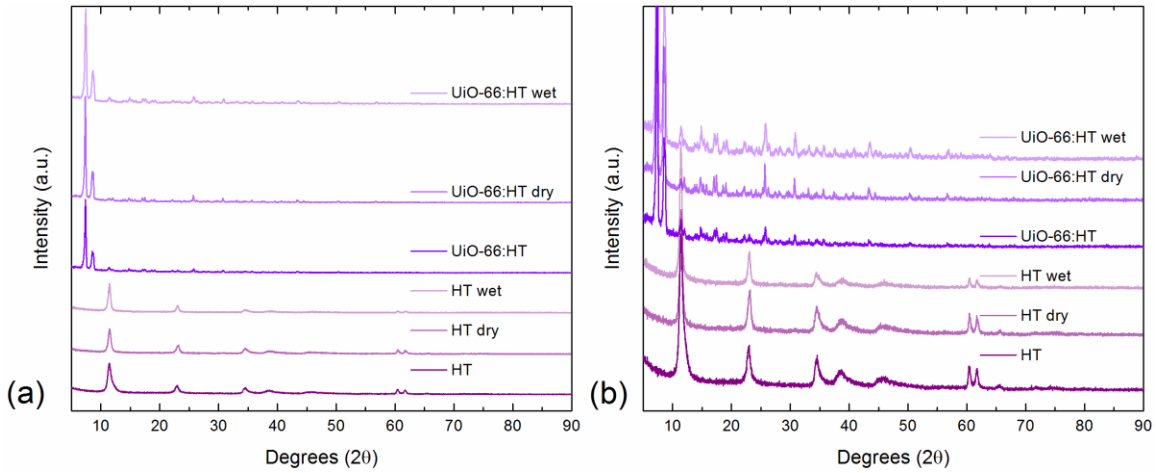

Figure 6.A.5. PXRD patterns of HT and UiO-66:HT composite (a) after synthesis and after dry and wet NH_3 breakthrough experiments and (b) magnified patterns after synthesis and after dry and wet NH_3 breakthrough experiments.

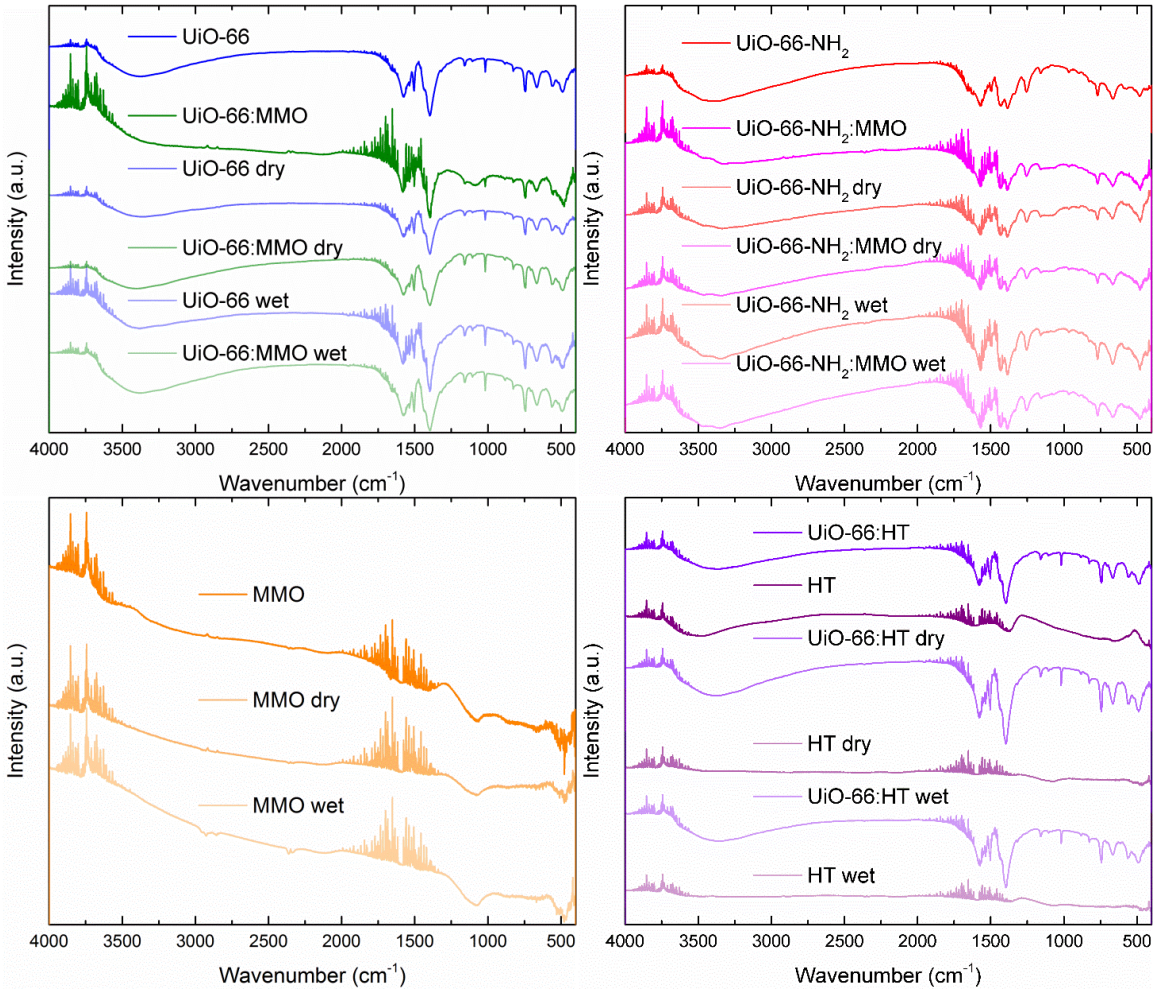

Figure 6.A.6. FTIR spectra for UiO-66 (top left), and UiO-66-NH_2 (top right), MMO (bottom left), and hydrotalcite (HT) (bottom right) after synthesis and initial activation, and dry and wet ammonia breakthrough experiments.

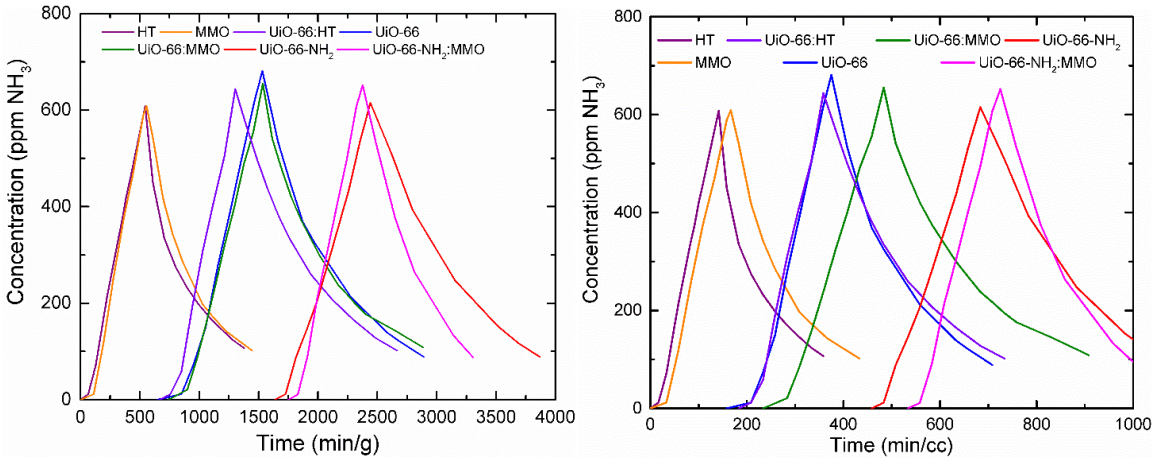

Figure 6.A.7. Breakthrough and desorption curves for HT, MMO, UiO-66, UiO-66-NH_2, UiO-66:MMO, UiO-66:HT, and UiO-66-NH_2:MMO under dry conditions. Time is normalized by (left) gram of total adsorbent mass in g or (right) total bed volume in cm^3.

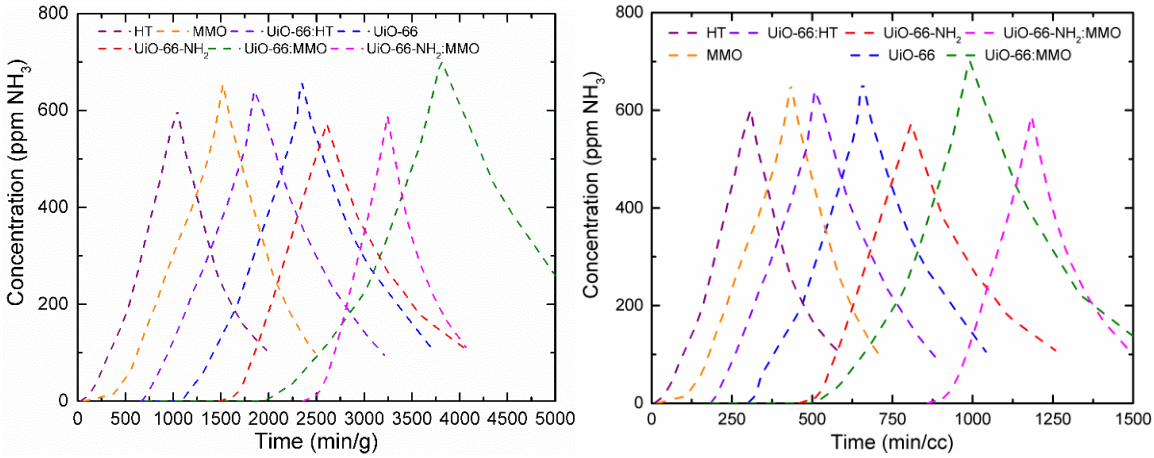

Figure 6.A.8. Breakthrough and desorption curves for HT, MMO, UiO-66, UiO-66-NH_2, UiO-66:MMO, UiO-66:HT, and UiO-66-NH_2:MMO under wet conditions. Time is normalized by (left) gram of total adsorbent mass in g or (right) total bed volume in cm^3.

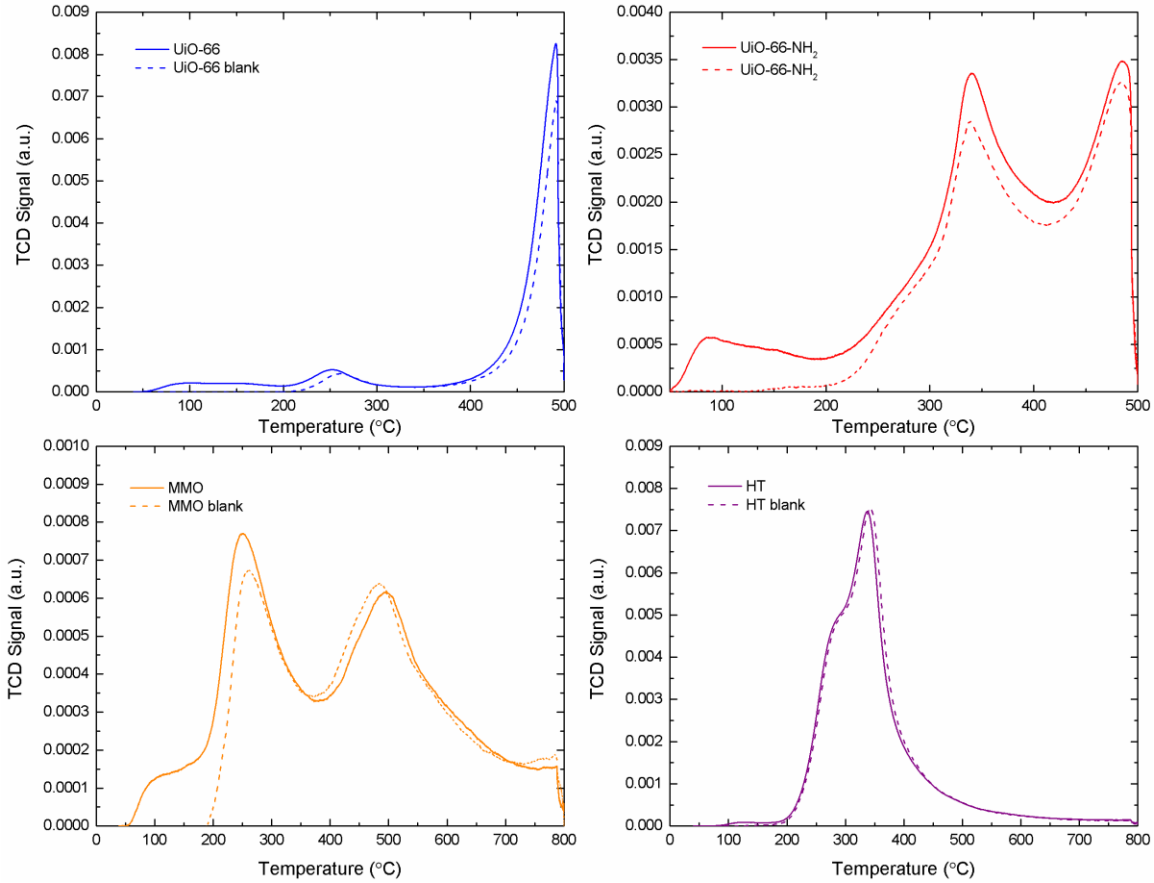

Figure 6.A.9. NH_3-TPD curves of UiO-66, UiO-66-NH_2, MMO, and HT. Solid lines indicate NH_3-TPD experiments, dashed lines indicate "blank" experiments where no NH_3 is adsorbed and only the change in TCD signal due to degradation of the material or release of compensating anions is recorded to determine accurate amounts adsorbed. TCD signal is normalized per mg of sample.

Table 6.A.1. Calculated NH_3 capacities of UiO-66, UiO-66-NH_2, MMO, and HT from NH_3 TPD.

Material	Sample Weight (g)	NH_3 capacity (mmol/g)
UiO-66	0.0426	0.273
UiO-66-NH_2	0.0151	0.625
MMO	0.0435	0.248
HT	0.0404	0.077

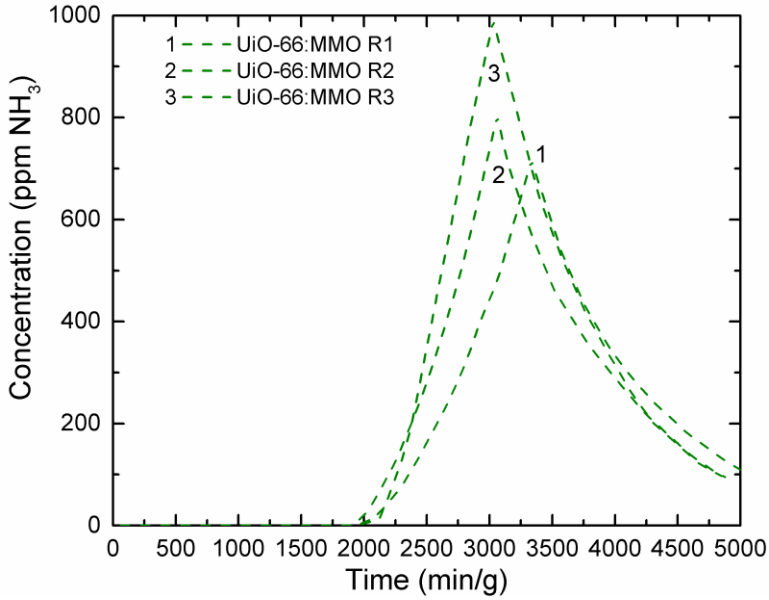

Figure 6.A.10. Breakthrough and desorption curves for UiO-66:MMO under wet conditions. The sample was regenerated in situ at 200 °C with flowing N_2 at 50 mL/min after an initial run (R1), exposed under identical conditions (R2), and regenerated again in situ before being exposed a third time (R3). Time is normalized by gram of total adsorbent mass in g.

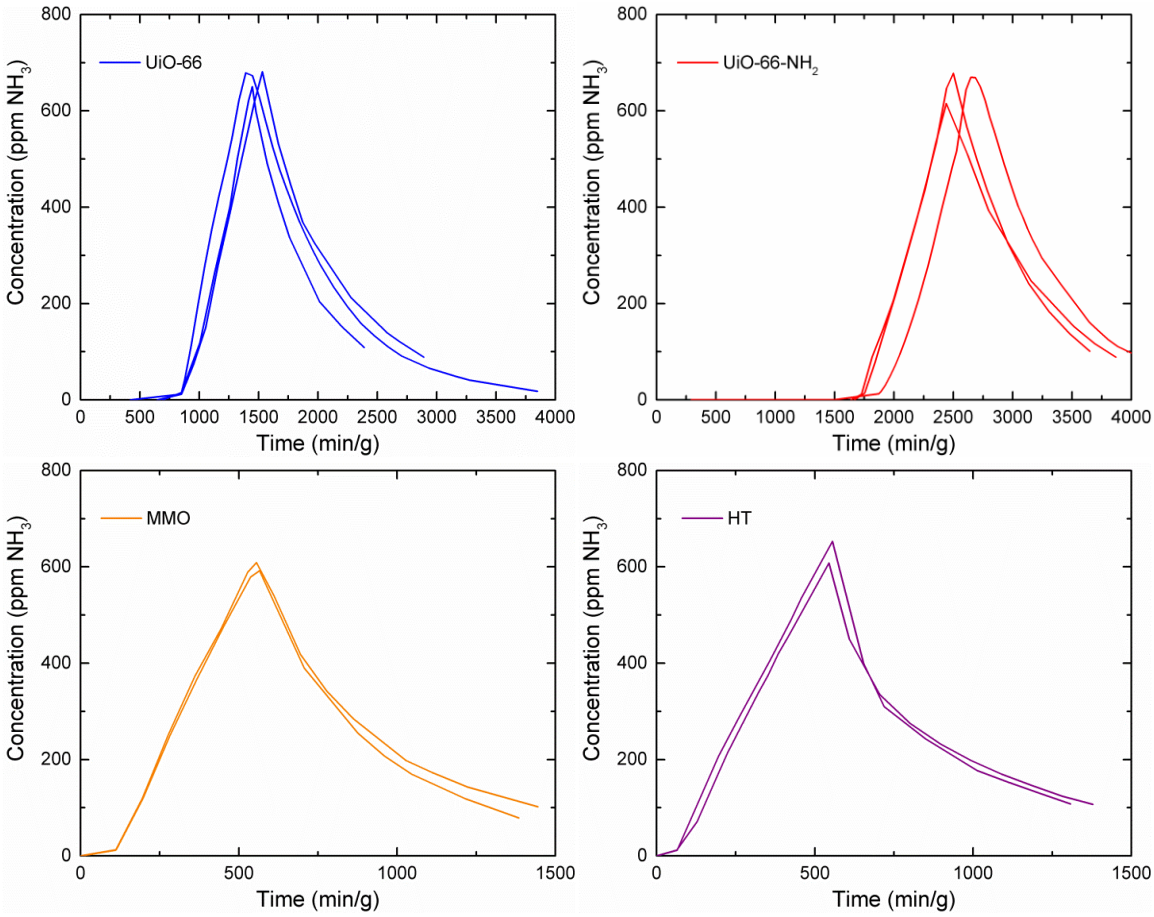

Figure 6.A.11. Breakthrough and desorption curves for UiO-66, UiO-66-NH_2, MMO, and HT under dry conditions. Time is normalized by gram of total adsorbent mass in g.

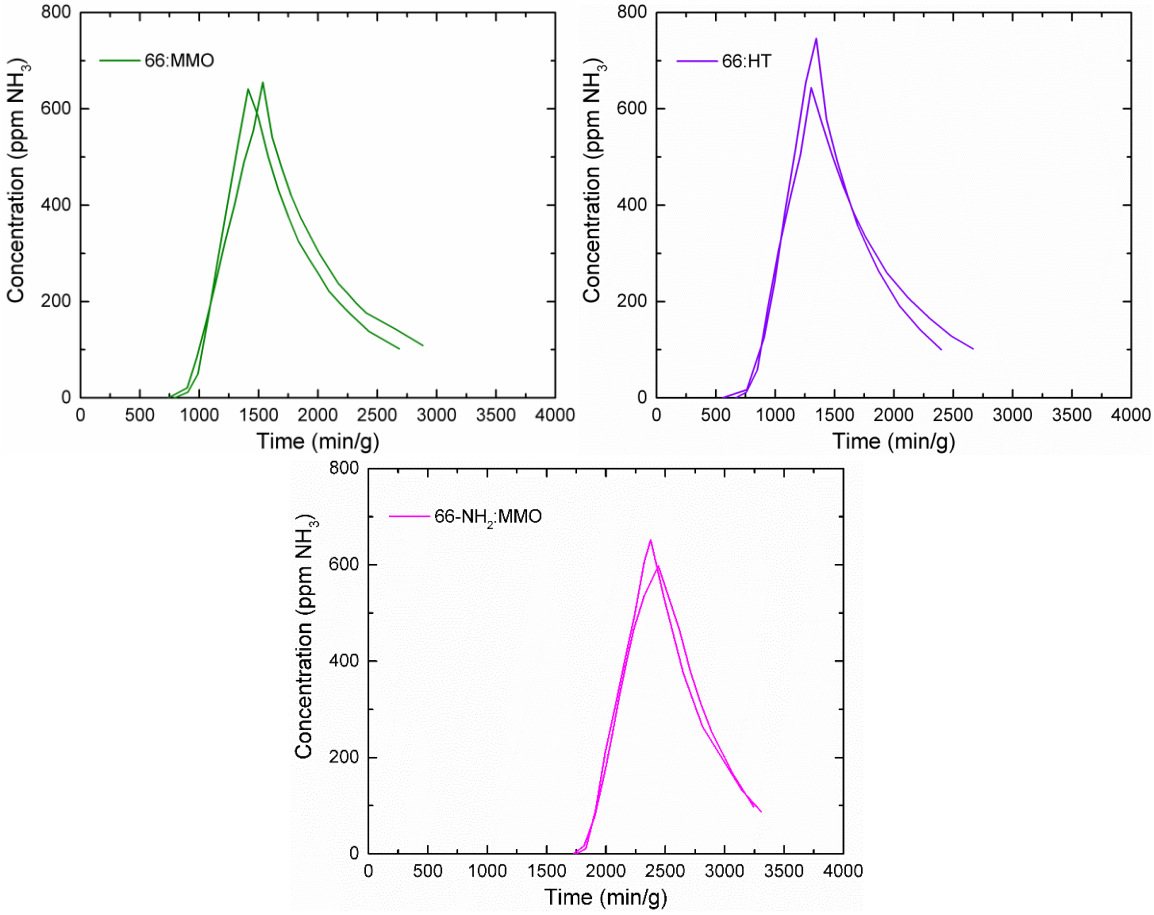

Figure 6.A.12. Breakthrough and desorption curves UiO-66:MMO, UiO-66:HT, and UiO-66-NH_2:MMO under dry conditions. Time is normalized by gram of total adsorbent mass in g.

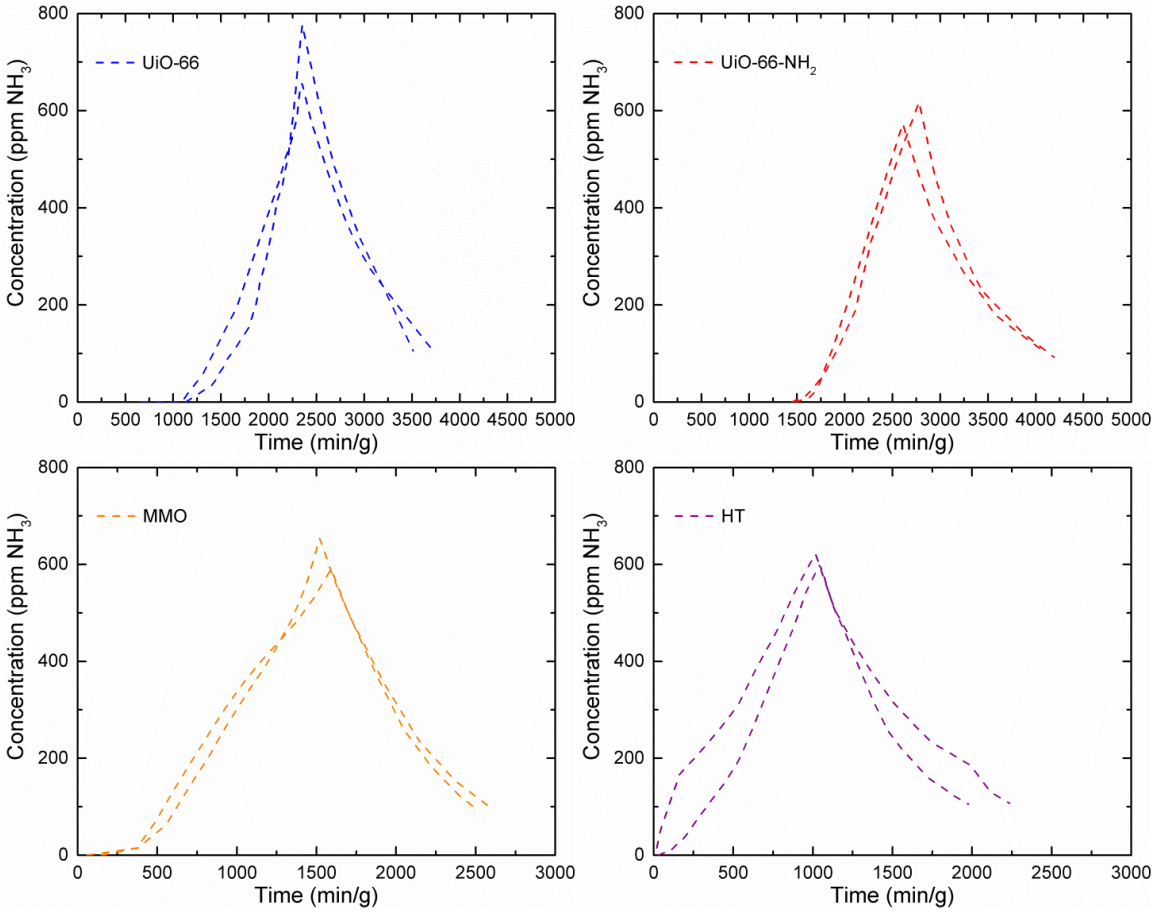

Figure 6.A.13. Breakthrough and desorption curves for UiO-66, UiO-66-NH_2, MMO, and HT under wet conditions. Time is normalized by gram of total adsorbent mass in g.

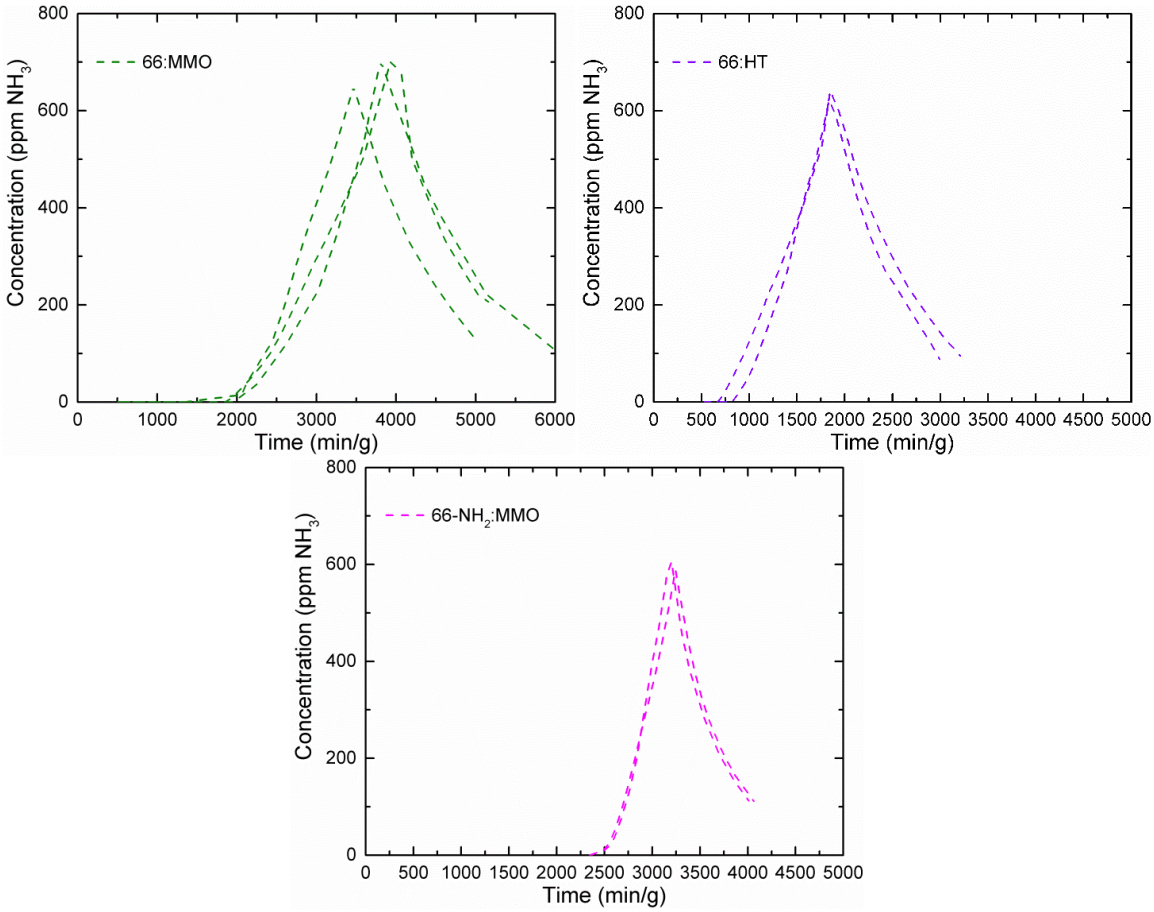

Figure 6.A.14. Breakthrough and desorption curves UiO-66:MMO, UiO-66:HT, and UiO-66-NH_2:MMO under wet conditions. Time is normalized by gram of total adsorbent mass in g.

Scanning Electron Microscopy. Samples were imaged on a Zeiss Ultra60 FE-SEM instrument with a high-efficiency in-lens SE detector at a working distance of 7-8 mm and accelerating voltage of 5 kV. The samples were sonicated for 10 s in methanol and then dispersed on a flat Al sample holder with two-sided adhesive conductive carbon tape. Prior to SEM observations, samples were coated with carbon for 30 s at 4.4 V using a Cressington 108A Carbon Coater to exclude the charging effect. Several images were captured for each sample with varying levels of magnifications.

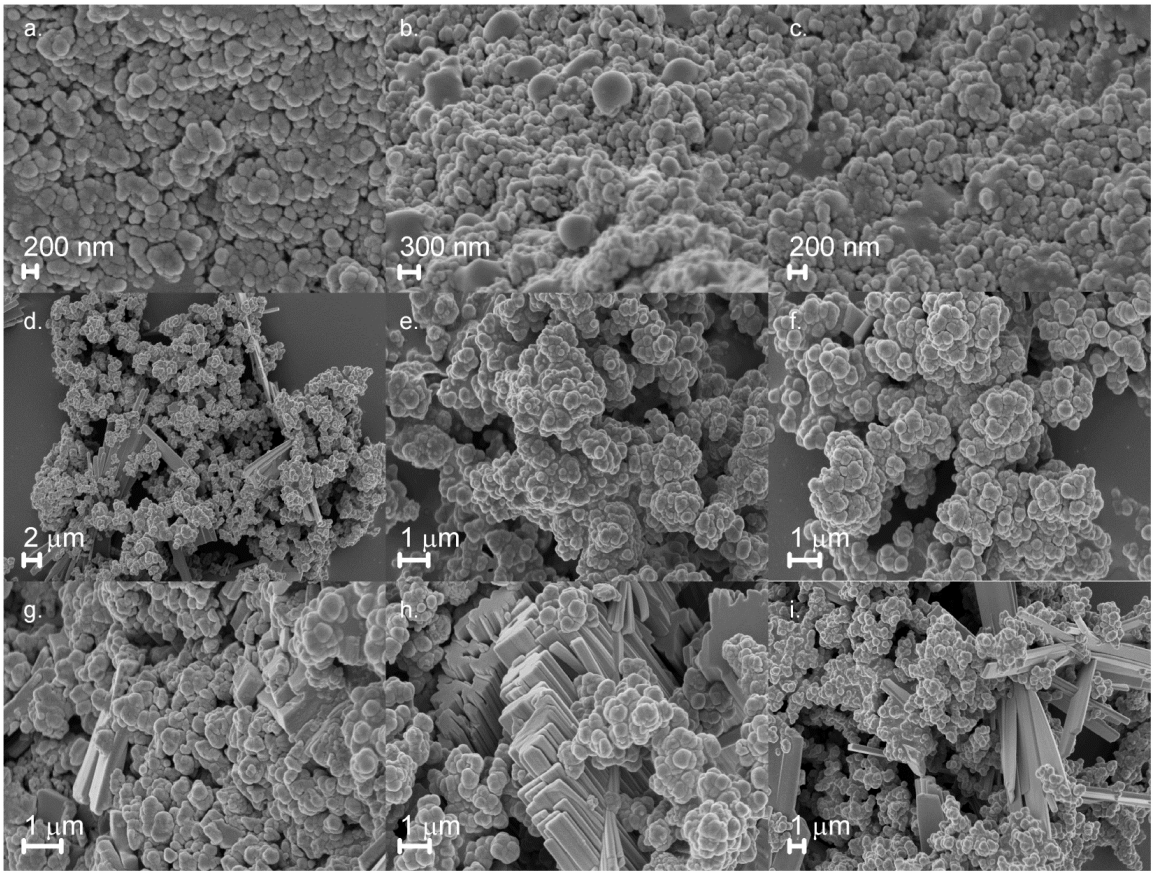

Figure 6.A.15. SEM images of (a-c) MMO, (d-f) UiO-66, (g-i) UiO-66:MMO after mixture preparation (left), after dry NH_3 exposure (middle), and wet NH_3 exposure (right).

The SEM images shown above in Figure 6.A.15 illustrate that no change is observed in the materials after exposure to ammonia and that no discernable cooperative effect can be made visually beyond the observation that the materials are present in a physical mixture.

CHAPTER 7

CONCLUSIONS AND RECOMMENDATIONS

7.1 Conclusions

The content of this dissertation focused on developing insight into several challenging areas of MOF material chemistry and engineering. Specifically addressed herein were the effects of synthesis solvent and corrosive gases on specific MOFs' structural and adsorption properties. The key findings of this work are:

(i) Solvothermal syntheses of large-pore stabilized MIL-53(Al) that do not possess the standard breathing behavior found in literature can be accomplished through synthesis at 120 °C in DMF, and synthesis at 220 °C in DMF results in a material with a gradual, slight breathing behavior.

(ii) The increased stability of the large-pore form in the structures synthesized in DMF allows for a large increase in CO_2 adsorption in the 1-5 bar region.

(iii) Choice of synthesis solvent can have an impact on the resulting structure, allowing synthesis of polymorphic materials with a simple solvent change. Understanding and modulating the breathing behavior of metal-organic frameworks offers the opportunity to increase capacity or tune selectivity for adsorption applications.

(iv) TiO_2 and CeO_2 MOF-derived oxides link between the morphology of the parent MIL-125 and CeBTC and the composition of the oxide allowing insight into adsorbed species on the MOFs. The adsorbed species on both parent MIL-125 and Ce-BTC are directly correlated with observed adsorbed species on the MOF-derived oxide materials.

(v) The retained porosity and inherent defects of CeO_2-d and TiO_2-d changed the nature of species adsorbed and enhanced the overall adsorption of both SO_2 and CO_2.

(vi) A mechanism involving the formation of an acidic sulfur species and subsequent formation of a dangling, uncoordinated ligand upon reaction with the framework leading to the degradation of MIL-125 in the presence of SO_2 and water was developed and investigated through a combined experimental and computational approach.

(vii) Both amine-functionalized and unfunctionalized MIL-125 materials were stable after exposure to either dry SO_2 or SO_2-free water, while degradation of MIL-125 occurred rapidly upon exposure to humid SO_2 and aqueous SO_2.

(viii) The amine-functionalized BDC ligand stabilized the framework in all environments and exposure times with no measurable change in surface area or PXRD pattern of MIL-125-NH_2.

(ix) In situ IR experiments confirmed the presence of bisulfite species and in combination with computational simulation of formation energies of these adsorbed species, indicated the degradation of the framework proceeds through the hypothesized mechanism.

(x) Simulation of reaction energy barriers suggests the stability of the MIL-125-NH_2 framework is due to the degradation reaction(s) being unfavorable and requiring a significant energy barrier to occur.

(xi) Addition of hydrotalcite-derived mixed MgAl oxide, MMO to UiO-66 in a 5:1 MOF:MMO ratio resulted in a synergistic effect and a 92% increase in wet ammonia adsorption performance above the pure MOF capacity. In dry conditions, the addition of MMO did not negatively affect adsorption performance, usually the case with the addition of a poorly adsorbing binding material.

(xii) The synergistic effect in the UiO-66:MMO composite in humid conditions is hypothesized to be two-fold, benefiting from a water withdrawing effect allowing adsorption sites to remain open for ammonia adsorption and the solubility of ammonia in the water adsorbed on the MMO.

(xiii) The UiO-66:MMO composite remained stable after exposure with no change observed in PXRD patterns or FTIR spectra and the observed drop in surface area attributed to the presence of strongly bound ammonia species that were not removed during reactivation.

(xiv) The UiO-66:MMO composite showed promise as a multi-use adsorbent, as the initial breakthrough capacity and synergistic effect was preserved through three consecutive exposures for the UiO-66:MMO composite in wet conditions.

This research provides a methodology and strong basis for analysis and determination of MOF reaction mechanisms in the presence of corrosive gases, and an avenue for engineering MOF materials that are stable in the presence of these gases. Furthermore, this research has demonstrated the ability to maintain or improve performance while maintaining material stability with the addition of a beneficial binding material that presents a promising outlook for development of engineered forms of MOF materials.

7.2 Recommendations

The work presented herein provides a basis for the further elucidation of degradation pathways and routes to engineering MOFs with higher degrees of chemical stability. There are still many challenging areas that would be beneficial to address in the progression of MOF materials toward widespread use and application.

7.2.1 Investigation of MOF water stability in humid air

Many investigations have been performed to evaluate and characterize water stability in MOFs[1-11] as most potential applications contain concentrations from a few ppm to several percent in the case of flue gas capture.[12,13] While many literature investigations have focused on investigating the stability of frameworks in humid conditions, little attention has been given to components other than water itself, such as CO_2. During the investigations of Chapters 4 and 5, where the stability of MIL-125 in environments containing water and SO_2 was investigated, it was discovered that MIL-125 is stable in pure water vapor. However, dosing CO_2 into a sample saturated with water in varying concentrations led to a loss of surface area, as illustrated by the N_2 isotherms shown in Figure 7.1.

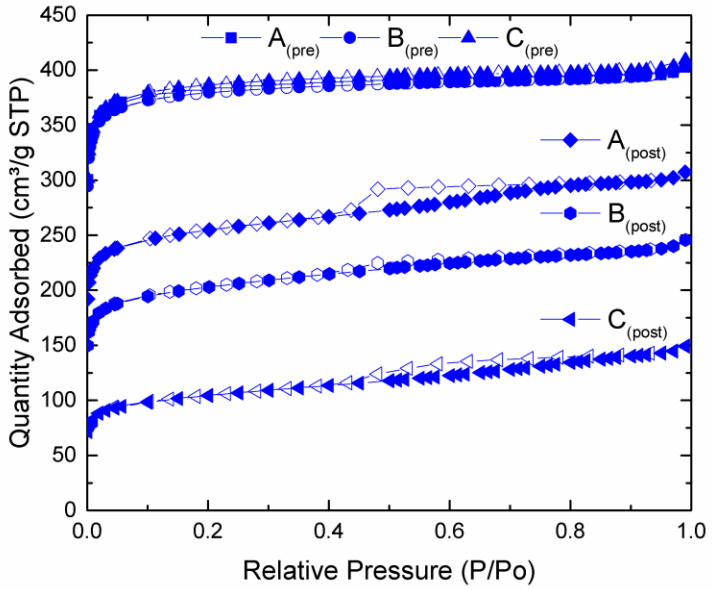

Figure 7.1. Nitrogen isotherms for MIL-125 before and after exposure to water and CO_2 at varying concentrations. A, 0.304 mmHg (400 ppm); B, 114 mmHg (15%); C, 760 mmHg. Closed symbols represent adsorption, open symbols represent desorption.

A similar hypothesis was presented for ZIF-8 materials by Mottillo et al., where humid CO_2 led to a degradation of the framework as evaluated by PXRD measurements.[14] Therefore, a study of the effects of CO_2 and water together could be

carried out to evaluate the stability of materials in humid environments. Furthermore, such a study would provide valuable information on a material's potential application in environments with high concentrations of CO_2 and water, such as flue gas capture. A study of materials considered to be unstable in water, such as UiO-67, HKUST-1, and Ni-MOF-74, would allow some consensus to be developed as to the effects of pure water and water and acid gases, respectively.

As discussed in Chapter 5 for MIL-125, the addition of a functional group to a ligand can have a measureable impact on the acid gas stability of a MOF material. The effect of ligand functionalization has been explored for DMOF-X by Jasuja et al.,[15,16] where the addition of tetra-methyl functionality resulted in considerable stabilization of the framework. These effects could be explored in future studies for other materials to gain a better understanding of the source(s) of the stabilization and all design of future stable frameworks for these harsh environments.

7.2.2 Development and use of advanced in situ analysis techniques

Development of in situ analysis techniques would allow a better understanding of degradation mechanisms, effects of defects, and adsorption of acid gases beyond the limits of ex situ PXRD, surface area measurements, and ex situ imaging. In Chapters 4 and 5 these ex situ techniques combined with ex situ surface techniques such as XPS allowed for the characterization of acid gas stability and the effects of exposure on MOF materials. However, the use of in situ IR allowed the confirmation of the presence of adsorbed species and strong support of potential reaction mechanisms.

The development and use of in situ techniques such as in situ PXRD, single crystal diffraction, or solid state NMR in the presence of acid gases could allow a much deeper understanding of the adsorption or reaction mechanisms, and degradation or stability of the framework. Furthermore, the use of in situ surface area/adsorption

measurements similar to those suggested in Section 7.2.1 for humid CO_2 exposure allows precise control of the concentration and time of exposure for each sample and eliminates the effects of sample removal, transportation, and storage, which are often overlooked in stability studies.

7.2.3 Engineering functional forms with beneficial binding materials

Chapter 6 presented a unique approach to production of MOF functional forms with increased ammonia adsorption by leveraging cooperative interactions between a mixed metal oxide, water, and ammonia instead of the traditional approach (for engineering materials for humid environments) of exploring hydrophobic materials, resulting in reduced adsorption. Future studies could explore the effect of modifying the acid-base character of the mixed MgAl oxide (MMO) through synthesis and the resulting effect on ammonia capacity. Furthermore, this binding material could provide a beneficial effect for acid gas adsorption applications, withdrawing water or acidic species from the MOF framework and increasing stability and/or performance of the composite. This approach could also be explored for materials that are unstable in humid conditions, such as HKUST-1 or MIL-125, as the water withdrawing effect of the mixed oxide could increase the stability of the framework in humid conditions. Developing functional composites that contain materials that can selectively adsorb separate species in a particular application stream would allow unique applications and ease engineering constraints for many of the potential industrial applications where cost and energy penalties are major concerns.

7.2.4 Outlook

Performing the experiments described above would expand the knowledge base of how MOF materials could perform in industrial environments and allow that understanding to move beyond laboratory single-component analysis. There are many

challenges/opportunities that exist in the MOF field, such as defect engineering, that should be addressed to push the field forward. The development of in situ analysis techniques would increase the chemical intuition in these areas and be the beginning of understanding how to tune MOF materials. The steps beyond those suggested involve leveraging this insight into how acid gases and other harsh adsorbates interact with MOFs to develop stable materials and materials that are ultimately tuned for a given application. In addition, the production of composite forms that maintain or minimize performance loss will allow these tuned MOFs to be translated to industrial applications.

7.3 References

(1) Sholl, D. S.; Lively, R. P. *J. Phys. Chem. Lett.* **2015**, *6*, 3437.

(2) Zhang, C.; Han, C.; Sholl, D. S.; Schmidt, J. R. *J. Phys. Chem. Lett.* **2016**, *7*, 459.

(3) Zuluaga, S.; Fuentes-Fernandez, E. M.-A.; Tan, K.; Xu, F.; Li, J.; Chabal, Y. J.; Thonhauser, T. *J. Mater. Chem. A* **2016**, *4*, 5176.

(4) Jiao, Y.; Morelock, C. R.; Burtch, N. C.; Mounfield III, W. P.; Hungerford, J. T.; Walton, K. S. *Ind. Eng. Chem. Res.* **2015**, *54*, 12408.

(5) Im, J. H.; Ko, N.; Yang, S. J.; Park, H. J.; Kim, J.; Park, C. R. *New J. Chem.* **2014**, *38*, 2752.

(6) Jasuja, H.; Burtch, N. C.; Huang, Y. G.; Cai, Y.; Walton, K. S. *Langmuir* **2013**, *29*, 633.

(7) Burtch, N. C.; Jasuja, H.; Walton, K. S. *Chem. Rev.* **2014**, *114*, 10575.

(8) DeCoste, J. B.; Denny, J. M. S.; Peterson, G. W.; Mahle, J. J.; Cohen, S. M. *Chem. Sci.* **2016**.

(9) Mounfield III, W. P.; Walton, K. S. *J. Colloid Interface Sci.* **2015**, *447*, 33.

(10) Schoenecker, P. M.; Carson, C. G.; Jasuja, H.; Flemming, C. J. J.; Walton, K. S. *Ind. Eng. Chem. Res.* **2012**, *51*, 6513.

(11) DeCoste, J. B.; Peterson, G. W.; Schindler, B. J.; Killops, K. L.; Browe, M. A.; Mahle, J. J. *J. Mater. Chem. A* **2013**, *1*, 11922.

(12) Granite, E. J.; Pennline, H. W. *Ind. Eng. Chem. Res.* **2002**, *41*, 5470.

(13) Sumida, K.; Rogow, D. L.; Mason, J. A.; McDonald, T. M.; Bloch, E. D.; Herm, Z. R.; Bae, T. H.; Long, J. R. *Chem. Rev.* **2012**, *112*, 724.

(14) Mottillo, C.; Friščić, T. *Angewandte Chemie International Edition* **2014**, *53*, 7471.

(15) Jasuja, H.; Walton, K. S. *J. Phys. Chem. C* **2013**, *117*, 7062.

(16) Jasuja, H.; Huang, Y.-g.; Walton, K. S. *Langmuir* **2012**, *28*, 16874.